Functional characterization of peroxisomal transport protein in *Arabidopsis thaliana* – role in stress adaptation and redox homeostasis

Inaugural dissertation

for the attainment of the title of doctor
in the Faculty of Mathematics and Natural Sciences
at the Heinrich Heine University Düsseldorf

submitted by

Katarzyna Krawczyk
from Pajęczno, Poland

Düsseldorf, August 2025

from the Institute for Plant Biochemistry
at the Heinrich Heine University Düsseldorf

Published by permission of the
Faculty of Mathematics and Natural Sciences at
Heinrich Heine University Düsseldorf

Supervisor: Prof. Dr. Nicole Linka
Co-supervisor: Prof. Dr. Andreas Weber

Date of the oral examination: 19.01.2026

This PhD is supported by funding from the German Academic Exchange Service (DAAD) under the Graduate School Scholarship Programme.

Deutscher Akademischer Austauschdienst
German Academic Exchange Service

As a member of International Graduate Program for Plant Science (iGRAD plant), this PhD Project is funded by the German Research Foundation (DFG).

iGRAD*plant*
International
Graduate
Program
for Plant Science

Deutsche
Forschungsgemeinschaft
German Research Foundation

Part of this PhD Project was conducted during an 8-month research stay at Michigan State University in East Lansing, MI, USA.

MICHIGAN STATE
UNIVERSITY

Statement of Authorship and AI Assistance

I hereby declare that I have written this dissertation independently and without unauthorized help in compliance with the principles of "Good Research Practice". This dissertation has not been submitted in the same or similar form to any other institution.

I have not made any unsuccessful attempts to obtain a doctorate.

I acknowledge that AI-based Assistance was used for improving grammar, clarity and readability of this thesis. The content, ideas and scientific interpretations presented remain my own.

Düsseldorf, 22.08.2025

_____

Katarzyna Krawczyk

Acknowledgements

Conducting PhD research has been an incredibly enriching experience. I have learned a great deal, grown as scientist and developed as a person. Over the years, it was inevitable to change and grow – and I truly did. However, none of my achievements would have been possible without the support of many wonderful people. From the bottom of my heart, I want to thank **everyone** I met along the way – during my PhD and even before it. You have shaped me into who I am today, and I am deeply grateful for this journey. There are few people I would especially like to acknowledge.

First and foremost, I want to express my deepest gratitude to my supervisor and biggest supporter, **Nicole Linka**. You believed in me from the very beginning, and I am incredibly thankful for all your understanding, patience and encouragement throughout every stage of this journey. I truly appreciate you were always available for me and that you dedicated your time so generously. I loved our brainstorming sessions, which not only helped me solve scientific challenges but also left me feeling motivated and inspired. I also cherished our simple, relaxed talks, that made our collaboration feel natural and enjoyable. I am truly grateful to have you as my to-go person, and I wish everybody had such a cool person to work with.

I would also like to thank **Andreas Weber** for building such a powerful research group. I am proud to have been part of the *Biochemistry of Plants* lab under your leadership and always amazed by the depth of knowledge one person can have. Thank you for this opportunity.

Thank you, **Shizue Matsubara**, for supporting me from the very beginning, starting with my interview talk. I am grateful for having you in my Thesis Advisory Committee and for bringing light and positive energy to our interactions.

I am thankful to all the people that supported me scientifically, especially **Philipp Westhoff** from **CMML** and the whole group for their help with metabolic analyses. Thank you, **Josemi,** for teaching me statistics and for performing phylogenetic analyses together. A big thank you to my collaborator **Javier Corpas** for our always very friendly talks and for your research support on *PERTL6*.

I want to thank the whole **AG Weber, CPGE, AG Fichtner** and **AG Jahns** for the daily cooperation and help. My work would not have been possible without the technical support of **Sam** and **Kirsten**, as well as dedicated work of **gardeners**.

There were many people I interacted with during my PhD as part of the **iGRAD Plant Graduate School,** and I am incredibly thankful for the friendships I made and the mental support I received. Thanks to the iGRAD, I also had a chance to complete a research stay at Michigan State University, where I was fortunate to be part of the wonderful community at the **Plant Research Laboratory,** that I am deeply grateful to everyone I met there who made my time so enriching.

In particular, I want to thank **Jianping Hu** and the whole **Hu Lab** for hosting me with such warmth and hospitality. I really felt part of your group. I especially appreciate **Amanda's** help with microscopy and **Xiaotong's** support in everyday lab life.

I am also thankful to **Berkley Walker** for making me feel welcome in your lab. My gratitude extends to the entire **Walker lab,** and especially **Luke Gregory** for introducing me to everyone and making sure I was doing well, and for the friendship and kindness you all shared with me.

Thank you, **Susanne** and **Christoph,** for always being there for me and supporting me in every possible way while I was so far away from home. You truly made me feel like I had home there.

Moreover, thank you **Melinda** from the Center for Advanced Microscopy and **Xinyu Fu** and people from MSU Mass Spectrometry and Metabolomics Core Facility for your scientific support, which helped me grow and develop as a scientist.

To my mentors, **Francesca** and **Edyta,** thank you for always giving me the very best of your time, guidance and encouragement. I appreciate all the invaluable advice you shared.

Last but not least, I want to thank **all my friends and family** not mentioned earlier – especially **Kasia, Picha, Laia, Jasmin, Debora, Luke S., Paulina and Patryk**. You made this journey brighter and filled it with lots of joy and laughter and unforgettable memories.

Summary

Plant peroxisomes play a central role in metabolism, cellular redox homeostasis, and stress adaptation. Many antioxidative processes occur in peroxisomes, thus understanding their function is crucial for mitigating the negative effects of environmental stress and preventing loss of crop yield. While many peroxisomal enzymes have been already characterized, only a few membrane transporters are known, limiting our understanding how plans regulate metabolite exchange during stress. Therefore, this thesis focuses on PERTL6 (peroxisomal-transport like protein 6) in *Arabidopsis thaliana*. PERTL6 belongs to the mitochondrial carrier family and was found to be upregulated upon heat stress. Given the role of peroxisomes in antioxidative defense and the gap in knowledge regarding peroxisomal transporter facilitating antioxidants, the aim of this thesis was to determine the role PERTL6 a plant physiology, with a particular emphasis on oxidative stress response.

An integrative approach was employed to fully portray the role of PERTL6. Subcellular localization was determined by using fusion with fluorescent proteins, revealing that contrastingly with previous predictions, PERTL6 is indeed localized to peroxisomal membrane. Phylogenetic studies identified PERTL6 as land-specific protein encoded by a single gene in *Arabidopsis thaliana*. *In silico* promoter region analysis revealed multiple cis elements related to stress, which was consistent with co-expression network data linking PERTL6 to genes encoded heat shock proteins or proteins involved in proteolysis. Physiological experiments were conducted utilizing several *pertl6* lines, including established CRISPR/Cas9-generated knockouts. Physiological assays included growth assessments, photosynthetic efficiency (Fv/Fm) measurements, CO_2 assimilation, germination assays or transcript quantification under various oxidative stress-inducing conditions such as heat shock, prolonged warming, salt stress, photorespiratory stress and extended darkness. Metabolites profiling was used to identify shifts in metabolites induced by stress.

Although *pertl6* mutants did not show severe growth defects, they displayed altered metabolic responses. Notably, mutants accumulated higher levels of ornithine and arginine and showed disruption in TCA cycle intermediates, supporting the hypothesis PERTL6 exacerbates redox imbalance and metabolic flexibility. The accumulation of arginine, ornithine, points to a potential role in amino acid transport, potentially linking the urea cycle, polyamine biosynthesis and central carbon metabolism.

In conclusion, this work provides the first functional characterization of PERTL6, identifying it as a candidate for peroxisomal ornithine/arginine transporter. The results suggest that PERTL6 supports the peroxisomal antioxidative machinery and plays a role in nitrogen metabolism, particularly under stress conditions. These findings contribute to a broader understanding of how peroxisomes integrate into plant metabolic networks and allocate resources during stress adaptation.

Table of Contents

1. Introduction

1.1. Climate change negatively affects crop yield

Plants as sessile organisms are constantly exposed to changing environmental conditions. Unlike animals, they cannot escape from unfavorable situations and must cope with them by adapting their physiological and molecular responses. These challenges arise from both biotic threats, such as pathogen attack, or abiotic stresses like heat, high light, drought, heavy metals and salinity (Xu et al., 2022).

Climate change has become a major concern in nowadays agriculture. Rising temperatures, elevated CO_2 concentration and more frequent droughts threaten global food security by impairing plant growth and development (Chaudhry & Sidhu, 2021; Mittler et al., 2022). Under extreme conditions, crop yield losses have been simulated from 7% to as much as 23%. At the same time, the global population is expected to increase by 30% - 62% by 2050, further intensifying the demand for food and making plants more resilient a critical agricultural challenge (Rezaei et al., 2023).

To survive in disadvantageous conditions, plants have evolved a wide range of defense mechanisms and strategies. A widespread physiological response to various biotic and abiotic stresses is the production of reactive oxygen and nitrogen species (ROS/RNS). They serve as signaling molecules but also lead to oxidative stress when accumulate in excess (Kerchev & Van Breusegem, 2022a; Nadarajah, 2020). Understanding how plants sense and alleviate the negative effect of oxidative stress has become a central theme in plant biology, as it plays a vital role in maintaining cellular homeostasis under stress.

1.2. Oxidative and nitrosative stress

Oxidative stress arises from an imbalance between production of reactive oxygen species (ROS) and the efficiency of ROS scavenging mechanisms, leading to harmful ROS accumulation and disruption of cellular redox homeostasis. Reactive oxygen species such as superoxide ($O_2^{\bullet-}$), hydrogen peroxide (H_2O_2), hydroxyl radical ($OH^{\bullet}$), and singlet oxygen ($^1O_2$) are highly reactive molecules produced as toxic by-products of aerobic metabolism (Kerchev & Van Breusegem, 2022b; Mittler, 2017a).

Reduction-oxidation (redox) reactions are integral part of any cellular component. At basal levels, ROS are necessary for plant life acting as signaling molecules that regulate multiple

processes, including activation of plant defense responses against stress, control of development and differentiation, maintenance of redox balance, and even cell death (Mittler, 2017). However, when concentration for ROS exceeds the non-toxic basal threshold, they become detrimental to cellular components and functions (Apel & Hirt, 2004).

Environmental stressors such as high light and heat increase electron leakage from the photosynthetic electron transport chain, leading to increased ROS accumulation (Sharma & Ahmad, 2014). Both long-term warming and acute short-term heat shock promote ROS accumulation. Acute heat stress impairs photosynthetic efficiency and respiration due to structural and functional changes in thylakoid membranes. Long-term warming decreases stomatal conductance and alters metabolism, including increased photosynthetic electron transport rate or inhibited TCA cycle, while triggering activation of acclimation responses (Jagadish et al., 2021; L. Wang et al., 2020). Similarly, salt stress contributes to oxidative stress by causing ionic and osmotic imbalance which destabilizes membranes and promotes ROS formation (H. Zhou et al., 2024). Photorespiration also contributes to ROS production, as the oxygenation of rubisco leads to the production of glycolate, which is metabolized in peroxisomes and generates hydrogen peroxide as a by-product of glyoxylate oxidase activity (GOX) (Bao et al., 2021). Although ROS generation is often associated with light reactions, extended darkness can also induce oxidative stress, particularly in mitochondria and peroxisomes (Rosenwasser et al., 2011).

In addition to ROS, reactive nitrogen species (RNS) such as nitric oxide (NO•), S-nitrosoglutathione (GSNO) or peroxynitrite ($ONOO^-$) are generated in plants (Corpas et al., 2021). Like ROS, they have dual functions involved in both signaling and stress. RNS may be produced through oxidative pathways – e.g. from arginine via nitric oxide synthase (NOS) or from polyamine catabolism – or through reductive pathways from nitrite via the nitrate reductase activity (Sami et al., 2018). At basal levels, RNS contribute to processes such as seed and pollen germination, root development, stomatal closure, senescence, fruit ripening as well as stress adaptation. In excess, however, they contribute to nitrosative stress by modifying proteins through tyrosine nitration or S-nitrosylation, leading to exacerbating oxidative damage (Corpas et al., 2020). Moreover, RNS and ROS can interact to further cause cellular damage (Corpas et al., 2021).

Excessive ROS and RNS accumulation can result in lipid peroxidation, protein oxidation and nitration, DNA damage leading to enzymes inactivation and eventually cell death (Corpas et al., 2021; Kerchev & Van Breusegem, 2022b). As ROS and RNS are primarily formed in

organelles such as chloroplasts, mitochondria, and peroxisomes, these organelles, and especially the latter one play a central role in maintaining redox homeostasis and mitigating oxidative and nitrosative stress (Del Río & López-Huertas, 2016).

1.3. Peroxisomes as a hub for oxidative stress and antioxidative mechanisms

Peroxisomes are eukaryotic organelles surrounded by a lipid bilayer. Although historically discovered as the last major organelles, they are now recognized as essential for numerous metabolic processes in plant cells. These include fatty acids β-oxidation, photorespiration, polyamine catabolism and metabolism of reactive oxygen and nitrogen species. Many of these processes are highly oxidative, making peroxisomes both a prominent source and a target of oxidative stress (Hu et al., 2012; R. Kumar et al., 2024).

Among the key peroxisomal enzymes contributing to ROS production are glycolate oxidase (involved in photorespiration), acyl-Co oxidase (in fatty acid β-oxidation), urate oxidase (linked to purine degradation during senescence) or polyamine oxidase (involved in stress-related polyamines catabolism). These enzymes generate hydrogen peroxide, one of the most abundant ROS in plant cells (Eastmond, 2007; Pan et al., 2020). In parallel, abiotic stresses strongly affect photosynthesis, where the oxygen-evolving system of photosystem II becomes damaged, repair mechanisms are impaired, and both rubisco activity and ATP synthase function are inhibited (Allakhverdiev et al., 2008; T. Liu et al., 2021). Moreover, under environmental stress conditions the peroxisomal reactions are often upregulated leading to increased ROS generation. Consequently, peroxisomes become major source of ROS in stressed plant cells (Del Río & López-Huertas, 2016). Together, these processes intensify oxidative stress resulting in significant losses in crop yield (Figure 1.1).

To prevent oxidative damage and preserve cellular function, peroxisomes evolved a robust antioxidative machinery. In fact, they host the most comprehensive ROS-scavenging systems in plant cells. This dual nature – as both generator and modulators of oxidative stress – peroxisomes play crucial role in maintaining cellular redox balance, particularly under stress conditions (Pan et al., 2020). Understanding how these defense systems are organized and regulated is essential to decipher how plants manage oxidative challenges especially in the context of increasing environmental stress due to climate change.

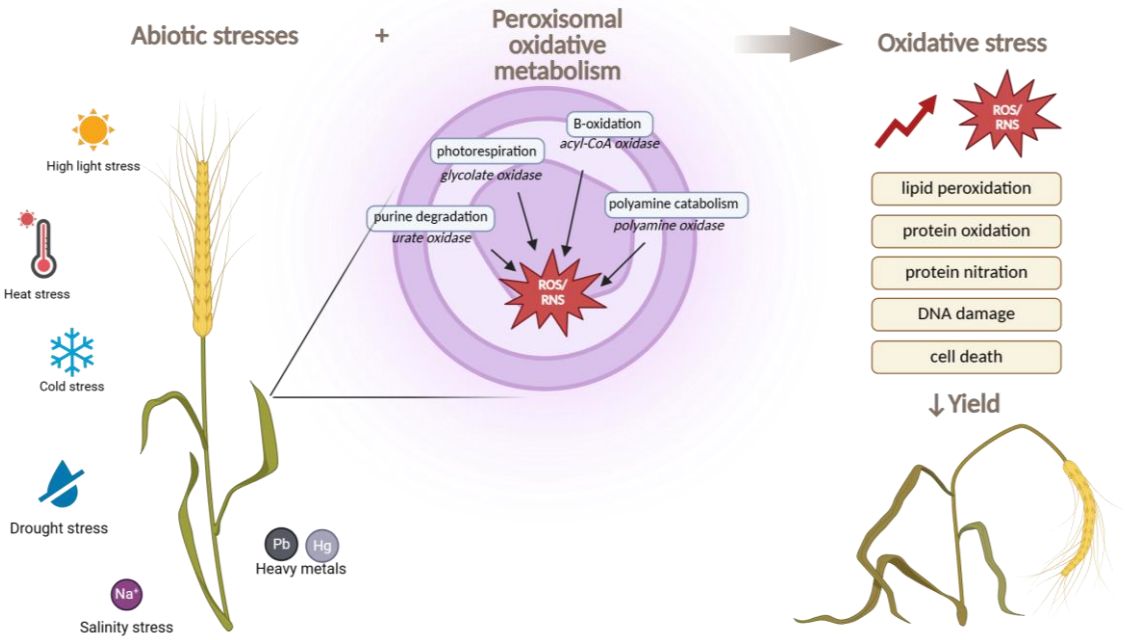

Figure 1.1 Oxidative stress sources in plants

Abiotic stresses such as high light, heat, cold, drought, salinity, and heavy metals together with peroxisomal highly oxidative metabolism lead to increased ROS/RNS production. Their accumulation causes oxidative stress, which compromises plant performance and ultimately limit crop yield.

1.4. Antioxidative mechanisms

Maintaining cellular redox homeostasis under fluctuating environmental conditions relies on a complex antioxidative machinery, composed of both enzymatic and non-enzymatic components. Catalase (CAT), ascorbate peroxidase (APX), glutathione reductase (GR) and superoxide dismutase (SOD) belong to the enzymatic part of the antioxidative system, while non-enzymatic antioxidants are represented by ascorbate (ASC) and glutathione (GSH) (Corpas et al., 2020).

Catalase is the primary ROS-scavenging enzyme in peroxisomes. In *Arabidopsis thaliana*, three peroxisomal isoforms (*CAT1-CAT3*) have been identified. Only *CAT2* is expressed in photosynthetic tissues, which makes this isoform to play major role in hydrogen peroxide scavenging under stress in leaves. Catalase catalyzes the dismutation of hydrogen peroxide into water and oxygen without requiring an electron donor making it especially effective under high concentration of ROS (Mhamdi, Queval, et al., 2010).

Ascorbate-glutathione cycle (also known as Foyer-Asada-Halliwell pathway) is a complex system that contributes significantly to ROS detoxification. This complex system scavenges

ROS through well-orchestrated action of ascorbate peroxidase (APX), monodehydroascorbate reductase (MDAR), dehydroascorbate reductase (DHAR), and glutathione reductase (GR). APX reduces hydrogen peroxide to water using ascorbate (ASC) as an electron donor. The oxidized form ascorbate-monodehydroascorbate (MDA) is further recycled back to ASC by MDAR using NADH. Additionally, dehydroascorbate (DHA) is regenerated to ASC by DHAR using glutathione (GSH) resulting in oxidized glutathione (GSSG), which is subsequently reduced to GSH by GR using NADPH. This cycle is not only present in peroxisomes, but also in chloroplasts and mitochondria, plays a critical role in sustaining redox balance without net loss of antioxidants, requiring only two NAD(P)H per H_2O_2 molecule reduced (Halliwell & Foyer, 1976; Noctor, 2025). NADPH, critical cofactor for normal cell growth and proliferation, can be regenerated in peroxisomes by several dehydrogenases and well as through the oxidative pentose phosphate pathway (OPPP). The OPPP pathway plays a particularly important role under stress conditions, as it provides the reducing power for ROS detoxification and supports antioxidant systems, but also is involved in ROS/RNS signaling (Corpas & Barroso, 2018; Pan et al., 2020).

Another important layer of antioxidative defenses involves polyamines (PAs) metabolism, closely linked to arginine catabolism. Polyamines, such as putrescine, spermidine and spermine are small aliphatic amines that enhance stress tolerance through both direct and indirect actions (Pál et al., 2015). In *Arabidopsis,* polyamines can be synthesized from arginine and contribute to synthesis of nitric oxide and hydrogen peroxide, probably through nitric oxide synthase-like activity (NOS) (Astier et al., 2018). Within peroxisomes, polyamine oxidases (PAOs) catalyze PA catabolism, producing hydrogen peroxide and γ-aminobutyric acid (GABA). This reaction therefore contributes to the GABA pool. GABA acts as a signaling molecule and participates in nitrogen metabolism during senescence caused by abiotic stress (Ramos-Ruiz et al., 2019). Moreover, GABA can be synthesized in cytosol from glutamate or from proline catabolism under oxidative stress. GABA is metabolized via the GABA shunt into succinate, linking amino acid and energy metabolism through TCA cycle and helping maintain metabolic flux under stress conditions (Michaeli & Fromm, 2015; Ramos-Ruiz et al., 2019).

This ROS/RNS crosstalk underscores the importance of PAs metabolism in modulating redox signaling under stress. While PA catabolism generates ROS, its overall effect might be protective through triggering redox signaling activation under stress (Blázquez, 2024).

Superoxide dismutase (SOD), present in multiple organelles including peroxisomes, catalyze the dismutation of superoxide radicals ($O_2^{\bullet-}$) into H_2O_2. SOD vary in their metal cofactors and subcellular localizations – Cu/Zn-SOD in peroxisomes, chloroplasts and cytosol, Fe-SOD in chloroplasts, and Mn-SOD in mitochondria – contributing to compartment-specific protection against superoxide toxicity (Del Río & López-Huertas, 2016; G. Zhou et al., 2022).

Importantly, the antioxidative system in plants is distributed across organelles and not limited to one of them, forming intracellular redox network. Plastids, mitochondria, cytosol and peroxisomes each harbor unique but complementary sets of enzymes and metabolites, collectively allowing coordinated responses to oxidative stress. In this context, peroxisomes are the major hub for ROS detoxification and redox signaling (Del Río & López-Huertas, 2016; Suzuki et al., 2012).

However, the effectiveness of peroxisomal antioxidative machinery relies not only on enzymatic activity but also on the dynamic exchange of key metabolites across the peroxisomal membrane. Efficient ROS detoxification requires the import of substrates like ascorbate, glutathione and possibly amino acids like arginine, as well as export of signaling molecules and second messengers like GABA, hydrogen peroxide or nitric oxide (Figure 1.2). The lipid bilayer surrounding peroxisomes creates a barrier for these small molecules, highlighting the crucial role of peroxisomal transporters.

ASC is synthesized in mitochondria and cytosol (Smirnoff & Wheeler, 2024), GSH in chloroplasts, cytoplasm and mitochondria (Hasanuzzaman et al., 2017), and arginine and ornithine in chloroplasts (G. Winter et al., 2015). Since all these metabolites are required in peroxisomes, transport across cellular compartments is essential. Supporting this, several transporters for these molecules have been characterized in carious organelles: mammalian mitochondrial GSH transporter SLC25A39 (Shi et al., 2022; Y. Wang et al., 2021), the *Arabidopsis* chloroplast ASC transporter AtPHT4;4 (Miyaji et al., 2015), the mitochondrial ASC transporter in rat liver and potato proteoliposomes (Scalera et al., 2018), the yeast ornithine/citrulline shuttle ARG11/ORT1 (Crabeel et al., 1996; L. Palmieri et al., 1997), human mitochondrial ornithine transporter ORC1/ORC2 (Fiermonte et al., 2003), the yeast arginine transporter Can1 (Tanahashi et al., 2023), and *Arabidopsis* polyamine transporters PUT1-PUT3 (Tong et al., 2016). Despite evidence for some low affinity transport activity (Bachhawat et al., 2013) so far, no transporters for these molecules have been yet characterized in plant peroxisomes. Their existence is likely essential, as they would enable

substrate availability, redox cofactor exchange between cellular compartments and signal molecule trafficking, thereby positioning peroxisomal transporters as key regulators of cellular redox homeostasis and stress tolerance in plants. The presence of analogous transporters in plastids and mitochondria underscores that such membrane transport system must exist in peroxisomes to coordinate the overall cellular metabolism.

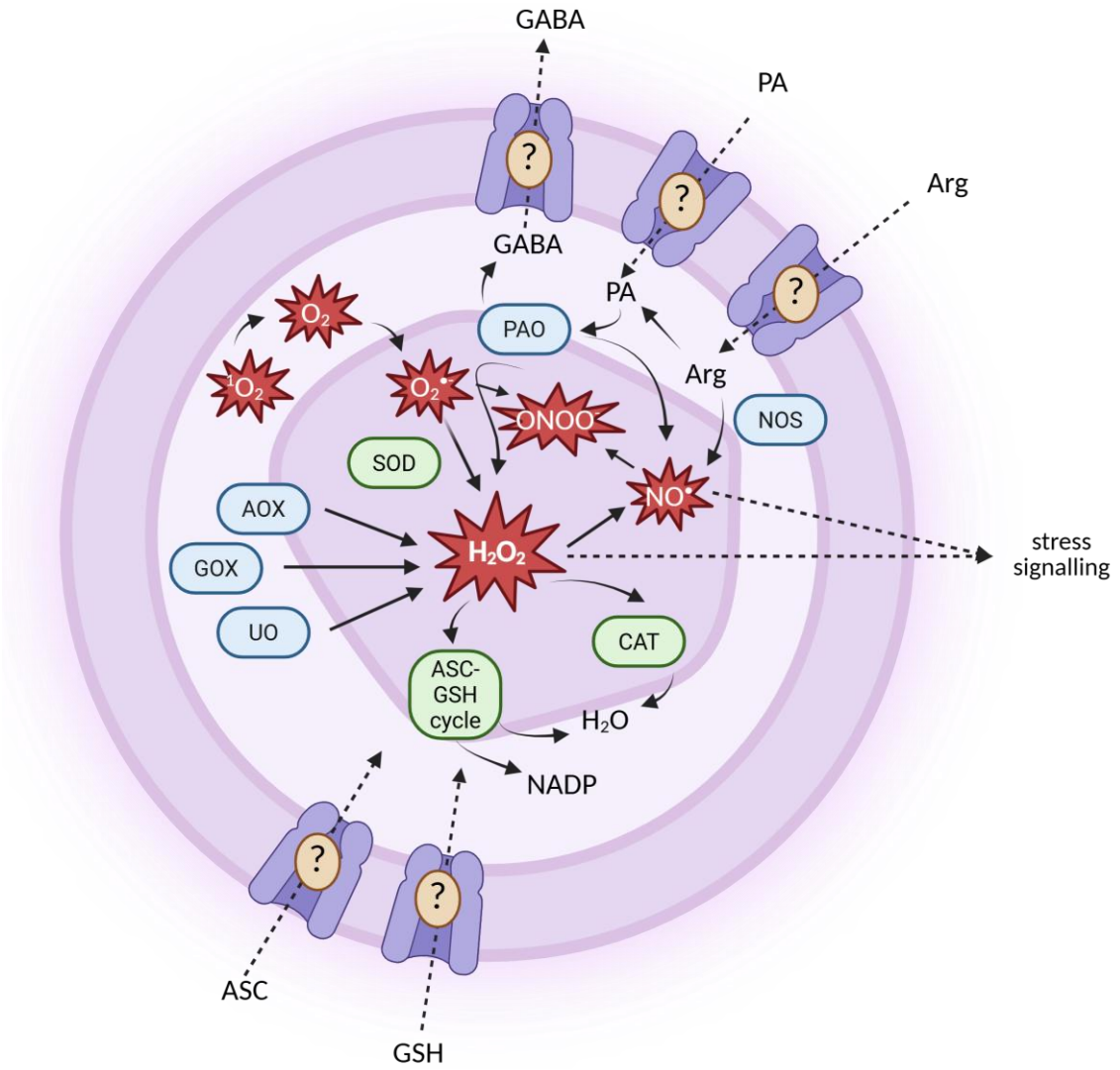

Figure 1.2 Redox mechanisms in plant peroxisomes with yet unidentified transporters

Plant peroxisomes are hubs for oxidative and antioxidative processes, relying on continuous exchange of redox-related metabolites across the peroxisomal membrane. Efficient function requires the exchange of cofactors and substrates such as ascorbate (ASC), glutathione (GSH), Arginine (Arg), Polyamines (PA) and γ-aminobutyric acid (GABA) and ROS/RNS. However, to date, no such peroxisomal transporters have been characterized. Other abbreviations: AOX – acyl-CoA oxidase, CAT – catalase, GOX – glycolate oxidase, NOS – nitric oxide synthase, PAO – polyamine oxidase, SOD-superoxide dismutase, UO – urate oxidase

1.5. Peroxisomal Transporters

Given the complexity of the antioxidative system and the compartmentalization of plant cells, transport through membrane is essential for enabling metabolic fluxes during stress adaptation. Peroxisomes, highly dynamic and metabolically active organelles, require efficient import and export of various solutes, including redox cofactors, signaling molecules and metabolic intermediates to sustain functions such as lipid metabolism, photorespiration, redox homeostasis (Charton et al., 2019; Hu et al., 2012).

Peroxisomal proteins are encoded in nucleus and then imported to peroxisomes post-translationally. Matrix proteins are recognized and translocated by the peroxisomal targeting signal (PTS) by peroxins (PEX proteins). However, less is known about the substrate specificity of the peroxisomal membrane proteins (PMP), particularly those facilitating molecules exchange across the lipid bilayer (Brown & Baker, 2008; Reumann & Bartel, 2016).

Peroxisomal membrane transporters described in plants, mammals and yeast belong to either mitochondrial carrier family (MCF) or to the ATP-binding cassette (ABC) transporter family. MCF transporters mediate the diffusion of solutes along their electrochemical gradient, typically operating as antiporters, while ABC transporter facilitates the transport actively against their electrochemical gradient using ATP as energy source (Plett et al., 2020).

Among the best characterized peroxisomal transporters in *Arabidopsis thaliana* are peroxisomal NAD^+/AMP carrier (PXN) and the peroxisomal ATP/AMP carrier (PNC1 and PNC2), all MCF members. They, like other members of this family, contain tandem homologous repeats domain. PXN facilitate the antiport of NAD^+, NADH, AMP, ADP and CoA, thereby supplying peroxisomes with reducing cofactor for β-oxidation, photorespiration and redox reactions, including these in glutathione-ascorbate cycle. Knock out studies of PXN in *Arabidopsis* lines revealed only partial impairment in β-oxidation, suggesting the existence of alternative NAD-dependent pathways occurring in peroxisomes (Bernhardt et al., 2012; Charton et al., 2019; van Roermund et al., 2016). Similarly, PNC1 and PNC2 facilitate ATP uptake in exchange for AMP or ADP. This is necessary for β-oxidation, the process that occurs exclusively in peroxisomes. Double knockouts of PNC1 and PNC2 in *Arabidopsis* displayed impaired fatty acid catabolism, particularly leading to block in storage oil mobilization during early seedling development (Linka et al., 2008; Plett et al., 2020).

The peroxisomal ABC transporter also known as CTS (COMATOSE) acts as an ATP-dependent uniport for importing CoA esters of fatty acids. In plant peroxisomes, CoA is

required not only in import of fatty acids into peroxisomes but also is a substrate in peroxisome-localized synthesis of secondary metabolites such as jasmonic acid (Corpas & Barroso, 2018).

Besides these characterized transporters, the peroxisomal membrane contain also non-selective pores like channels that enable rapid passive diffusion by gradient of small hydrophilic molecules (<400 Da). For example, PMP22 forms channels that may allow passage of solutes or small proteins (max 22 Da) while peroxin 11 (PEX11) is involved in peroxisome proliferation but also in determining its size and number (Charton et al., 2019).

Despite extensive studies, no specific transporters have yet been identified for several metabolites involved in antioxidative defense, including glutathione, ascorbate, amino acids and polyamines. Given the crucial role of peroxisomes in maintaining cellular redox balance and mitigating the negative effects of oxidative stress, elucidating how peroxisomal transport of these molecules is integrated with stress signaling network has become an emerging field of interest. The absence of characterized transporters for these solutes leaves a significant gap in understanding of how peroxisomes contribute to resource allocation within a complex compartmentalized redox network of the plant cell.

Notably, recent studies have highlighted a stress-inducible member of MCF in *Arabidopsis*, which has emerged as a promising candidate due to its potential role in modulating peroxisomal function through metabolite exchange. In the following chapter, the focus will shift to PERTL6, exploring its putative potential function in the context of peroxisomal oxidative stress response.

1.6. PERTL6 as a candidate involved in supporting antioxidative machinery

Peroxisomal transport-like protein 6 (PERTL6) encoded by At1g74240 belongs to the group of MCF. Phylogenetic analysis of this family revealed that PERTL6 is closely related to the groups of transporters of negatively charged amino acids and positively like S-adenosylmethionine transporters and the recently characterized mammalian GSH transporter SLC25A39 (Figure 1.3).

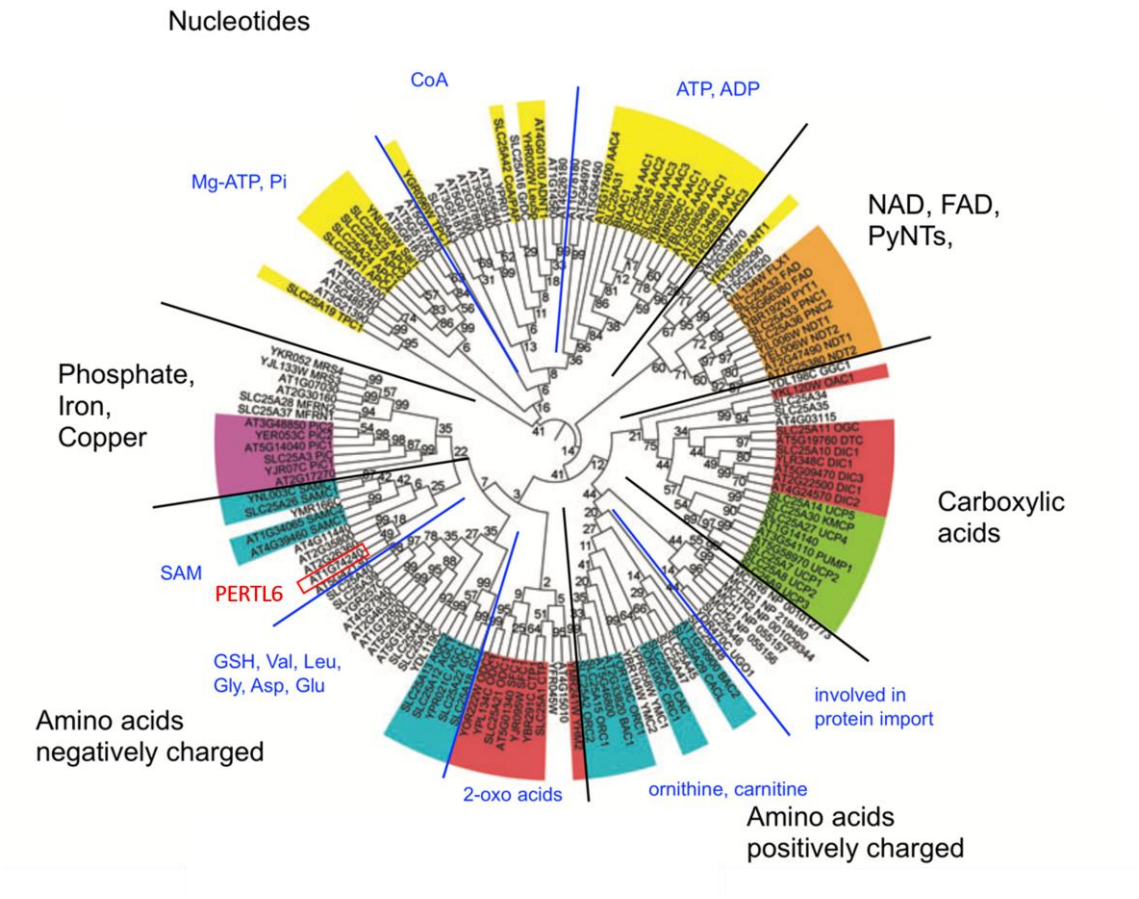

Figure 1.3 Phylogenetic tree of Mitochondrial Carrier Family

The tree of H. sapiens (53), S. cerevisiae (35) and A. thaliana (58) MCF originated from ClustalW multiple-sequence alignments by using the neighbor-joining method implemented in MEGA4 (modified from F. Palmieri et al., 2011)

Tissue specific gene expression analysis of At1g74240 demonstrates that *PERTL6* is ubiquitously expressed at low levels, with the highest expression observed in seeds, shoot apex inflorescence and in the early floral buds (Figure 1.4 A). Interestingly, PERTL6's expression is upregulated under heat stress, raising the possibility that PERTL6 may contribute to the cellular mechanisms involved in stress adaptation (Figure 1.4 B).

Thus, the central aim of this thesis is to elucidate the role of PERTL6 in stress responses in plants, with a particular focus in oxidative stress adaptation. It is hypothesized that PERTL6 supports antioxidative defense, potentially by transporting metabolites into peroxisomes, thereby influencing plant physiological responses under oxidative stress conditions.

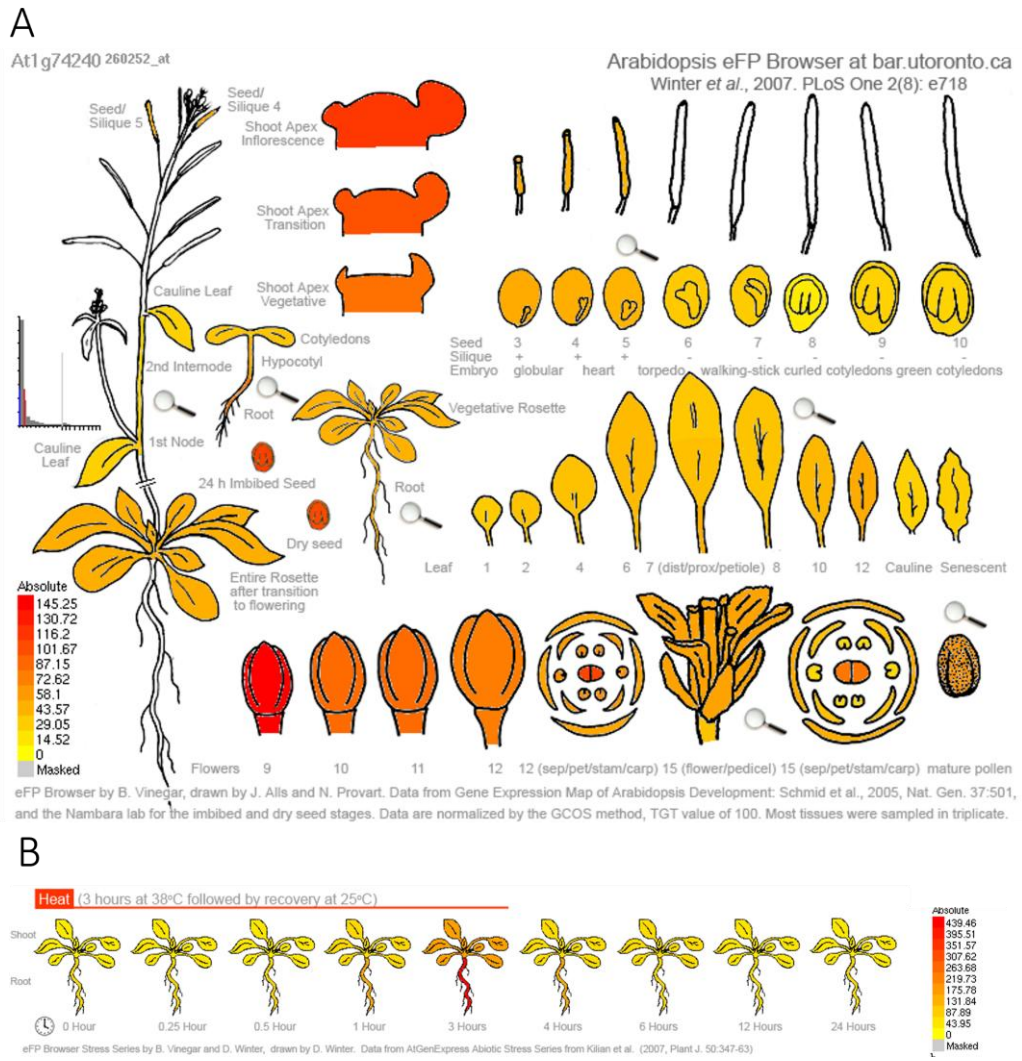

Figure 1.4 Expression patterns of *PERTL6* in *Arabidopsis thaliana*

Organ-specific PERTL6 gene expression map of *Arabidopsis thaliana* (A) Expression pattern of *PERTL6* under 3 h of heat stress followed by recovery (B) From eFB Browser (D. Winter et al., 2007a)

Studying the role of uncharacterized protein such as PERTL6 requires an integrative approach combining bioinformatics (sequence analysis, homology search), molecular biology, genetics (gene expression, localization studies and functional mutant analysis), and biochemistry. The experiments will be performed under both control and oxidative stress conditions to enhance the physiological relevance of these findings.

Overall, the study aims to shed light on the potential contribution of PERTL6 to the antioxidative machinery and its physiological role during oxidative stress. The results will broaden the understanding of peroxisomal metabolism and may give insights into improving plant resilience under environmental stress with implications for agriculture and food security in the context of ongoing climate change.

2. Materials and Methods

2.1. Materials

2.1.1. Laboratory equipment

The equipment used in this project is listed in Table 2.1.

Table 2.1. Laboratory equipment

EQUIPMENT	MODEL	MANUFACTURER
Air incubator	ICP500	Memmert
Air incubator	KT 53	Binder
Autoclave	VX-150	Systec
Blue-Green LED Flashlight	FG-11	NIPPON Genetics
Centrifuge	GS-6KR	Beckman Coulter
Centrifuge	5424, 5425	Eppendorf
Clean bench	Scanlaf	LaboGene
Confocal Laser Scanning Microscope	FluoView FV1000	Olympus
Dish washer	PG 8583	Miele
Electronic pipettes	Xplorer plus	Eppendorf
Electrophoresis system	Perfect Blue	Peqlab (vwr)
Electroporator	2510	Eppendorf
Imaging system FluorCam	FC 800-C/1010GFP	Photon Systems Instruments
GC-MS	Agilent 7890A	Agilent
Plant growth chamber	L2-TDLdual+	PolyKlima
LC-MS	1260 Bioinert	Agilent
Lyophiliser	Alpha 1-2 LDplus	CHRIST
Magnetic stirrer	MA-20A	Witeg
Nanodrop Spectrophotometer	One	Thermo Fisher Scientific (TFS)
pH meter	inoLab 720	WTW
Pipettes	Pipetman	Gilson
Planetary Ball Mill	MM 400	Retsch
Plate growth chamber	Percival CU-36L5	CLF
Porometer/Fluorometer	LI-600	LI-COR
Portable Photosynthesis System	LI-6800	LI-COR
Real-Time PCR System	StepOnePlus	Applied Biosystems (TFS)
Shaker	Multitron	Infors HT
Shaker	Innova 44	New Brunswick Scientific
Spectrophotometer	UVmini-1240	SHIMADZU
Thermocycler	Veriti 9902	Applied Biosystems (TFS)
Theromixer	Compact	Eppendorf
Tissue grinder	FastPrep-24	MP biomedicals
Ultracentrifuge	Avanti J-26 XP	Beckman Coulter
UV gel documentation system	UVP GelSolo	Analytic Jena
Vacuum pump	RZ 2.5	Vacuubrand
Votrex	VTX-3000L	LMS
Water purification system	PURELAB flex	ELGA

2.1.2. Reagents, Chemicals, and Commercial Kits

Unless otherwise noted, all chemicals and standard lab consumables (pipette tips, plastic tubes, plates etc.) were purchased from Merck Sigma-Aldrich (Munich, Germany), Carl ROTH (Karlsruhe, Germany) Sarstedt (Nümbrecht, Germany), Duchefa Biochemie (Haarlem, Netherlands), and VWR Avantor (Radnor, USA). Enzymes were provided by New England Biolabs (NEB) (Frankfurt am Main, Germany), Thermo Fisher Scientific (TSF) (Waltham, USA) and Promega (Fitchburg, USA). Specific kits used in this project are listed in Table 2.2 Commercial kits.

Table 2.2 Commercial kits

NAME	CATALOGUE NUMBER	MANUFACTURER
Luna Universal qPCR Master Mix	M3003L	New England Biolabs
LunaScript RT SuperMix Kit	E3010L	New England Biolabs
Phire Plant Direct PCR Master Mix	F160L	Thermo Fisher Scientific
RNeasy Plant Mini Kit (50)	74904	Qiagen
Wizard® Plus SV Minipreps DNA Purification System	A1460	Promega
Wizard® SV Gel and PCR Clean-up System	A9282	Promega

2.1.3. Software tools

Computational resources and software tools used during preparation of this dissertation are listed in Table 2.3 Software tools.

Table 2.3 Software tools

TOOL	PROVIDER
AGRIS	Grotewold et al.
Aramemnon	University of Cologne
ATTED-II v12	Obayashi et al.
Benchling	Benchling Inc.
BioRender	BioRender Inc.
CRISPOR	UC Santa Cruz
DNA Reverse Complement Calculator	Jamie McGowan
EnsemblPlants	EMBL-EBI
FluorCam 7 software	PSI
FV10-ASW software v4.2	Olympus Corporation
GraphPad Prism v10	GraphPad Software Inc.
ImageJ	Wayne Rasband at NIH
iTOL	Letunic & Bork, EMBL
JASPAR 2024	Rauluseviciute et al.
MEGA X	Kumar et al., Pennsylvania State Univ
Mendeley Reference Manager	Elsevier
Microsoft Office	Microsoft Corporation
MultAlin	Florence Corpet

New PLACE	Higo et al.
OrthoFinder	Erik J. Van Der Reijden et al.
Phytozome	University of California
PlantPAN 4.0	Chow et al.
PlantTFDB	Peking University
Primer-BLAST	NIH
PrimerQuest	IDT
RNAfold WebServer	University of Vienna
RStudio	RStudio, PBC
SHOOT.bio	David Emms & Steven Kelly
StepOne™ Software v2.x	Applied Biosystems (TFS)
TAIR	Phoenix Bioinformatics
Tm Calculator / NEBuilder	NEB

2.1.4. Primers

All primers named KKXX used in this project were designed using Primer-BLAST or PrimerQuest. Other primers sourced from the Primer Library at the Institute for Plant Biochemistry. A list of all the primers and their sequences can be found in Appendix, Table 6.1.

2.1.5. Vectors

Vectors created in this work, named pKK, are listed in Table 2.4. Other vectors and vector maps are listed in Appendix 6.5.

Table 2.4 pKK vectors

NAME	FEATURE	SELECTION MARKER	BACTERIA RESISTANCE
pKK1	CRISPR vector VEC 219 (pU6-26::tRNA-gRNA(PTG) with flanking RRS for BsaI)	None	Amp^R
pKK2	CRISPR vector VEC 249 (pU6-26::tRNA-gRNA(PTG) with flanking RRS for BpaI)	None	Amp^R
pKK3	CRISPR binary vector VEC 262 (NOS::barR::nos term, EC1::NLS::Cas9::rbcS E9 term, pU6-26::tRNA-gRNA(PTG), NapinA::Turbo GFP::osc term)	BASTA	Kan^R
pKK4	Binary vector pUBQ10::PERTL6-mCherry and 35S::mCerulean-PTS1 for subcellular localization studies	Kan	$Spec^R$

2.1.6. Microorganisms

The list of microorganisms used in this project is provided in Table 2.5.

Table 2.5 Microorganisms

STRAIN	GENOTYPE
Escherichia coli MACH1	F- φ80(*lacZ*)ΔM15 ΔlacX74 hsdR(rK-mK+) ΔrecA1398 endA1 tonA
Agrobacterium tumefaciens GV3101	C58 (Rif ^{R}) Ti pMP90 (pTiC58DT-DNA) (Gent^{R}) Nopaline

2.1.7. Plant material

Plant lines used in this thesis are listed in Table 2.6.

Table 2.6 Plant lines used in this project

Abbreviations: *cat2-1* – catalase 2, CL – complementation line, *gr1-1* – glutathione reductase 1, OEX – overexpressor, *pertl6* – peroxisomal transport-like protein 6, WT - wild type.

PLANT LINE	DESCRIPTION
Wild type (WT)	Columbia - 0
pertl6-1	SALK_030104, T-DNA for At1g74240
cat2-1	SALK_076998, T-DNA for At4g35090
pertl6-1 x cat2-1	double mutant of *pertl6-1* and catalase T-DNA lines
gr1-1	SALK_105794, T-DNA for At3g24170
pertl6-1 x gr1-1	double mutant of *pertl6-1* and glutathione reductase T-DNA lines
pertl6-6	CRISPR-Cas9 sgRNA multiplex system, T insertion in 1st exon in At1g74240
perlt6-1 CL	Complementation line in *pertl6-1* background
OEX	Overexpressor line in WT background

2.2. Methods

2.2.1. Plant work

2.2.1.1. Arabidopsis thaliana

In this project, wild-type (WT) *Arabidopsis thaliana* ecotype Columbia-0 was used, along with the lines indicated in Table 2.6. Sterilized seeds were plated on half- or full-strength Murashige & Skoog (MS) agar medium (Table 2.7) plates and stratified in the dark at 4 °C for 2 days prior to being placed in the growth chamber. For herbicide resistance selection, glufosinate ammonium (BASTA) was added to the MS medium at concentrations of 7.5 μg/ml.

Table 2.7 Full-strength Murashige & Skoog medium

SOLUTE	CONCENTRATION
MS salts	0.44% (w/v)
MES pH 5.7 (KOH)	5 mM
Plant agar	0.8% (w/v)
Sucrose (if needed)	1% (w/v)

Standard conditions in the growth chamber were as follows: day temperature 22 °C, night temperature 20 °C, normal day (ND) photoperiod (12 h light/12 h dark), light intensity ~100 µmol m^{-2} s^{-1}, 65% humidity, 410 ppm CO_2. Depending on the experiment, plants were also grown under short day (SD) (8 h light/16 h dark) conditions, to enhance vegetative growth for gas exchange measurements, or under long day (LD) (16 h light/8 h dark) conditions for rapid transition into the generative phase and seed production, as needed for establishing mutant lines.

2.2.1.1.1. Stress treatment

In this project, the influence of abiotic stress was investigated. The conditions tested are listed below. Unless stated otherwise, plants were grown in standard conditions described in 2.2.1.1. Specific experiments related to stress assessment are described further in Section 2.2.

A. For heat stress (HS) with seedlings, plants were grown for 2 weeks and then exposed to 40 °C for 1 or 4 hours, followed by a 4-hour recovery under standard conditions. In a separate HS experiment with mature plants, 5-week-old plants were exposed to 40 °C for 6 hours and then recovered for 24 hours.
B. For prolonged warming stress (PW), 5-week-old plants were subjected to increased temperature of 28°C during the day and 26°C during the night for an additional 7 days.
C. For salt stress treatment, seeds were placed on MS agar medium supplemented with 100 mM sodium chloride (NaCl) for 2 weeks under ND conditions.
D. For photorespiratory stress, plants were grown on ½ MS agar medium under ND photoperiod for 11 days in 3000 ppm CO_2, followed by 3 days in 390 ppm CO_2.
E. In the dark treatment, plants were grown under SD photoperiod for 4 weeks, then moved to dark for 6 days, followed by 3 days of recovery in SD conditions.
F. In the oxidative stress experiment, seeds were placed on medium supplemented with 0.5% (w/v) sucrose and 0.05 µM N,N'-dimethyl-4,4'-bipyridinium dichloride (methyl viologen, paraquat) and grown for 2 weeks.

2.2.1.1.2. Seeds sterilization

Seeds were aliquoted into 2 ml tubes and sterilized by washing them in 1 ml of 80% (v/v) ethanol supplemented with 0,05% (v/v) Tween-20, with subsequent shaking for 5 min at room temperature (RT) at 1400 rpm. The supernatant was removed, and the seeds were washed with 1 ml of absolute ethanol, with another 5 min shaking under the same conditions.

Afterwards, the supernatant was removed, and seeds were left to dry under the clean bench for at least 6 hours.

2.2.1.1.3. Stable transformation via Floral dip

A. thaliana transformation was performed using floral dip method (Clough & Bent, 1998; X. Zhang et al., 2006). Seeds were sterilized as described above and grown in ½ MS agar plates for 2 weeks in the growth chamber under 16 h light/8 h dark photoperiod at 22 °C. Germinated seedlings were transferred to pots with soil and grown for an additional 4 weeks. Four pots, each containing four plants, were used for each construct. Two days prior to plant transformation, transformed *Agrobacterium* were used to prepare a 5 ml preculture inoculum in liquid YEP medium with the appropriate antibiotics, and incubated overnight with shaking at 200 rpm at 28 °C. The following day, the preculture was used to prepare a 300 ml culture of YEP with the appropriate antibiotics and again incubated overnight with shaking at 200 rpm and at 28 °C. When the culture optical density (OD_{600}) reached 1.5 – 2.0, bacteria were centrifuged at 5500 x g for 10 min at RT. The resulting pink pellet was carefully resuspended using a suction ball on a glass stick in 300 ml of 5% (w/v) sucrose solution containing 0.02% Silwet L-77. All plant siliques were removed prior to dipping. Plants were inverted to dip the inflorescence shoots into the *Agrobacterium* suspension for 50 seconds, repeated twice. Afterward, the plants were placed horizontally in a covered tray containing wet cellulose cloth and incubated overnight in the dark to maintain humidity. The next day transformed plants were watered and transferred back to the growth chamber for another 2 weeks to allow for the formation of mature siliques.

Table 2.8 YEP medium

SOLUTE	CONCENTRATION
Yeast Extract	1.0% (w/v)
Peptone or Tryptone	1.0% (w/v)
Sodium chloride	0.5% (w/v)
Bacto agar (for plates only)	1.5% (w/v)

2.2.1.1.4. Genotyping transgenic plants

Arabidopsis thaliana plants were genotyped using the commercial Phire Plant Direct PCR Master Mix (Cat No. F160L, Thermo Fisher Scientific) according to the manufacturer's instructions. Plant lines were genotyped using primers as listed in the Table 2.9.

Table 2.9 Primer pair for genotyping plant lines

GENE	NAME	PRIMER COMBINATION	PRIMER PAIR	PCR PRODUCT
At5g09810	ACTIN 7	Gene specific gDNA	P067/P068	918 bp
At1g74240	*pertl6-1*	Gene specific	NL0509/NL0510	1165 bp
		T-DNA specific	P097/NL0509	712 bp
		T-DNA specific	P097/NL0510	841 bp
	pertl6-1 CL	pertl6 CDS	P098/P178	1611 bp
	OEX	pertl6 CDS	P098/P178	1611 bp
At4g35090	*cat2-1*	Gene specific	NL1062/NL1063	1019 bp
		T-DNA specific	P097/NL1062	338 bp
At3g24170	*gr1-1*	Gene specific	NL1064/NL1065	1224 bp
		T-DNA specific	P097/NL1065	676 bp

To check the T-DNA insertion size and position within the gene, Region of Interest (ROI) was amplified using *Taq* polymerase and cloned into pGEM-T Easy Vector (Promega) using TA cloning, followed by *E. coli* transformation. Positive clones were selected via α-complementation screening and confirmed by sequencing. Further details on cloning and selection procedures are provided in sections 2.2.2 and 2.2.3.

2.2.1.1.5. Crossing lines

Plants for crossing were grown in LD conditions for approximately 5-6 weeks. The female parent (the acceptor of pollen) was emasculated to prevent self-pollination by carefully removing all sepals, petals and stamens with forceps. Pollen from the male parent was then applied to the remaining stigma by gently rubbing. After pollination, all unpollinated flowers were removed, to ensure the desired cross occurred. The plants were then maintained in the growth chamber for further development. Once the seeds were collected, seedlings were genotyped to identify heterozygous plants. These T1 plants were subsequently used to generate a T2 generation of homozygous transgenic plants.

2.2.1.1. Nicotiana tabacum

For localization studies, *Nicotiana tabacum* plants were grown by gardeners in the growth chamber at 16 h light/8 h dark cycle at 22 °C.

2.2.1.1.1. Transient transformation via Agroinfiltration

Nicotiana tabacum transformation was carried out using tobacco infiltration method. Transformed *A. tumefaciens* were used to prepare 5 mL preculture inoculum in liquid YEP medium with the appropriate antibiotics, which was incubated for 2 days with shaking at 150 rpm at 28 °C. This starter culture was used to inoculate 25 mL medium containing the

appropriate antibiotics and 100 µM acetosyringone. After shaking at 150 rpm at 28 °C for approximately 2 hours, until the desired OD_{600} = 0.7, the culture was centrifuged for 10 min at 3500 x g. The bacterial pellet was resuspended in MMA resuspension buffer (Table 2.10) to the desired OD_{600} = 0.7. The resuspension was then incubated for 1 hour at RT. Infiltration of the bacterial resuspension was carried out using syringe to inject against the abaxial side of the tobacco leaf through the stomata until visible darkening of the leaf (usually 1-2 mL). After *Agrobacteria*-mediated transformation, the tobacco plants were grown for an additional 2 days before imaging.

Table 2.10 MMA resuspension buffer

SOLUTE	CONCENTRATION
MES	10 mM
Magnesium chloride	10 mM
acetosyringone	100 µM

2.2.2. Molecular Biology Techniques

2.2.2.1. DNA and RNA analysis

2.2.2.1.1. Polymerase Chain Reaction

Polymerase Chain Reaction (PCR) was used to amplify nucleic acid fragments for several purposes in this work. The primer sequences can be found in Table 6.1. Depending on the application, different polymerases were used. For cloning purposes, proof-reading Q5 High Fidelity DNA Polymerase (M0491, NEB) and Phusion High Fidelity DNA Polymerase (F630L, TFS) were employed, following the manufacturer's instructions. Homemade Taq Polymerase was used for standard applications such as Colony PCR, where instead of 1 µL of DNA template, 1 bacterial colony was used as the matrix for amplification. Annealing temperature and extension time were defined according to the primers sequence, length of the amplified fragment and specification of the polymerase, using Tm Calculator provided by NEB (https://tmcalculator.neb.com/#!/main). The standard protocol for Homemade Taq and PCR settings are in Table 2.11 PCR reaction mix for homemade Taq polymerase and Table 2.12 Homemade Taq PCR program settings.

Table 2.11 PCR reaction mix for homemade Taq polymerase

COMPONENT	VOLUME
DNA template	1 µL
5x Go Green Taq buffer	5 µL
10 mM dNTPs	0.5 µL

10 µM Primer Forward (PF)	1 µL
10 µM Primer Reverse (PR)	1 µL
Homemade Taq polymerase	0.625 µL
Nuclease-free water	15.875 µL

Table 2.12 Homemade Taq PCR program settings

STEP	TEMPERATURE	TIME	NUMBER OF CYCLES
Initial denaturation	95 °C	30 s	1
Denaturation	95 °C	10 s	
Annealing	Tm – 5 °C	45 s	35 cycles
Extension	72 °C	1 min / 1 kb	
Final extension	72 °C	5 min	1
Hold	20 °C	∞	1

2.2.2.1.2. Agarose gel electrophoresis

Agarose gel electrophoresis is used to separate DNA fragments by size in an electric field. The gel was prepared by dissolving 1% (w/v) agarose in 1x Tris-acetate-EDTA (TAE) buffer with peqGREEN. For fragments smaller than 300 base pairs (bp), 1.5% (w/v) or 2% (w/v) agarose solution was used. After solidification, samples were loaded into the wells along with a DNA ladder (1 kilobase (kb) or 100 bp) and electrophoresis was run at 120 V for 24 min, or for smaller fragments at 80 V for 90 min. Afterward, DNA/RNA bands were visualized using a UV gel documentation system (UVP GelSolo, Analytic Jena).

Table 2.13 TAE buffer for gel electrophoresis

SOLUTE	CONCENTRATION
Tris	40 mM
Glacial acetic acid	20 mM
EDTA	1 mM

2.2.2.1.3. DNA purification

DNA samples, either cut from agarose gel or directly from PCR reactions, were extracted and purified using the Wizard® SV Gel and PCR Clean-up System (A9282, Promega) according to the manufacturer's instructions. DNA concentration was measured using Nanodrop spectrophotometer.

2.2.2.1.4. DNA sequencing

All cloning inserts were verified via sequencing at Microsynth AG (Lindau, Germany) using the Sanger sequencing method. Sequencing results were analyzed using the Benchling platform.

2.2.2.2. Cloning strategies

2.2.2.2.1. Restriction digest

Restriction digests were performed to obtain fragments for cloning or to verify mutations. Depending on the specific requirement, different restriction enzymes (RE) were used. The pipetting is provided in Table 2.14. Digestion was carried out at 37 °C for 2 hours, followed by inactivation of the RE at 65 °C for 15 minutes.

Table 2.14 Restriction digest pipetting scheme

COMPONENT	VOLUME
Plasmid DNA (1µg)	1 µL
RE	0.5 µL
RE	0.5 µL
rCut Smart buffer (10x)	1 µL
Nuclease-free H_2O	7 µL

2.2.2.2.2. Ligation

Following the restriction digest, the backbone of a cut vector was ligated with the corresponding insert. The appropriate vector-to-insert ratio was calculated using the NEB Calculator (https://nebiocalculator.neb.com/#!/ligation). The ligation reaction was prepared according to the scheme in Table 2.15Table 2.15 Ligation pipetting scheme, and incubated overnight at 4 °C.

Table 2.15 Ligation pipetting scheme

COMPONENT	VOLUME
Vector DNA	x µL
Insert DNA	y µL
T4 or T7 DNA Ligase	1 µL
T4 DNA Ligase Buffer (10x)	1 µL
Nuclease-free H_2O	Up to 10 µL

2.2.2.2.3. TA cloning

TA cloning is used to insert PCR products into a vector with complementary T-overhangs. For this, homemade *Taq* polymerase was used, as it adds adenine (A) overhangs at 3' ends

of amplicons. In this thesis, TA cloning was used to confirm the T-DNA insertions in transgenic plant lines. The T-DNA-specific primers listed in Table 2.9 were used to amplify the ROI, generating the PCR fragments with A-overhangs. These amplicons were then gel-purified and ligated into the pGEM-T Easy Vector (A3600, Promega), which carries the complementary 3'-T overhangs, following the manufacturer's protocol. These overhangs enhance the ligation efficiency and prevent recircularization of the plasmid. The ligation mixture was then used to transform *E.coli*. pGEM-T Easy Vector (Chapter 6.5) contains lacZ gene that encodes β-galactosidase, an enzyme that hydrolyzes X-gal into a blue-colored product. When a plasmid with an intact lacZ cassette is transformed into bacteria, colonies will turn blue due to the β-galactosidase activity. However, if the lacZ cassette is disrupted by the insertion of foreign DNA, colonies will remain white, because β-galactosidase can no longer hydrolyze X-gal, indicating successful cloning. To enable this blue/white screening, transformed bacteria were spread on LB agar plates supplemented with ampicillin, X-gal and IPTG (an inducer of the lac operon). Subsequently, the proper insertion in white colonies was confirmed by Colony PCR followed by sequencing positive clones after plasmid isolation via miniprep.

2.2.2.2.4. Gibson Assembly

Gibson Assembly allows the ligation of multiple DNA fragments, regardless of their length or end compatibility. In this method, RE are used to create overhangs in the ligating fragments. An exonuclease generates single-stranded 3' overhangs, DNA polymerase fills in the gaps and DNA ligase seals any nicks in the assembled vector.

In this project, Gibson Assembly was used for subcellular localization studies. Primers for amplifying fragments with appropriate overhangs were designed using NEBuilder (https://nebuilder.neb.com/#!/). The pMG18 vector was used as a donor vector, carrying mCerulean fused to Peroxisomal Targeting Signal 1 (PTS1), as well as mCherry, which was fused to the PERTL6 CDS from pHHU 431, resulting in obtaining pKK4 vector (Figure 2.1).

Figure 2.1 Scheme of pKK4 binary vector for subcellular localization studies

Abbreviations: LB/RB – left/right border of T-DNA, pUBQ10 – Ubiquitin 10 promoter, p35S – promoter 35 S, kan – kanamycin resistance cassette, PTS1 – peroxisomal targeting signal 1

All the vectors used for this cloning, along with their maps, can be found in the Appendix under Section 6.5. RE AatII and PspXI were used to create 20 nt overhangs for the KK38 and KK39 primers (Table 6.1) which bind to the PERTL6 coding sequence (CDS) from the pHHU431 vector. The pMG18 vector was linearized by restriction digestion (as described in 2.2.2.2.1.) using these enzymes, run on a gel and purified (2.2.2.2.1). The concentrations of insert and vector were calculated using NEB Calculator to achieve 3:1 ratio and mixed with the Gibson Assembly master mix according to the Table 2.16. The reaction mix was then incubated at 50 °C for 60 minutes, followed by bacterial transformation.

Table 2.16 Gibson Assembly pipetting scheme for subcellular localization studies

COMPONENT	VOLUME
Linearized vector pMG18	2 µL
PERLT6 CDS insert	0.75 µL
Gibson Assembly master mix	15 µL
Nuclease-free H_2O	2.25 µL

Table 2.17 Gibson Assembly master mix

COMPONENT	CONCENTRATION
5x isothermal reaction buffer	1x
T5 exonuclease	5.2 U/mL
Phusion DNA Polymerase	30 U/mL
Taq DNA ligase	5000 U/mL
Nuclease-free H_2O	To final volume

Table 2.18 5x Isothermal reaction buffer

COMPONENT	CONCENTRATION
Tris base pH 7.5 (HCl)	500 mM
Magnesium chloride	50 mM
dATP	1 mM
dCTP	1 mM
dGTP	1 mM
dTTP	1 mM
DTT red	50 mM
NAD	5 mM
PEG 8000	25% (w/v)
Nuclease-free H_2O	To final volume

2.2.2.2.5. Golden Gate Modular Cloning

Overview of Golden Gate Modular Cloning

In this thesis, the Golden Gate Modular Cloning method was used to establish CRISPR/Cas9 mutant line in *PERTL6* gene. The Golden Gate Assembly relies on the use of type IIS restriction enzymes, which unlike traditional RE, cut outside of their restriction recognition sites (RRS). This allows for the creation of custom overhangs that facilitate the scarless assembly of multiple DNA fragments (Engler et al., 2008). In this project, the Golden Gate Modular Cloning (MoClo) system was applied, which follows a hierarchical assembly system approach. In this system each modular standard part (such as promoter, CDS, target signal peptide or terminator) can be combined in multiple steps to build complex genetic constructs (Engler et al., 2014; Marillonnet & Grützner, 2020).

Genes of interest are designed with flanking RRS for BpiI and BsaI, ensuring that the respective cutting sites are oriented inward relative to the RRS. This design removes the RRS of RE upon digestion, preventing repetitive cleavage after correct ligation into a vector, and enabling single-step cloning reaction. Ligation and subsequent cloning are facilitated by destination vectors (Level 0, 1 or 2), which contain the corresponding RRS for these enzymes.

Vectors of different levels used for cloning were obtained from Golden Gate MoClo Plant Parts Kit from AddGene repository. Figure 2.5 presents all the vectors that were used as plasmid backbones, and exact vector maps are included in Appendix 6.5.

Guide RNA design and annealing into PTG

Vector 423 (Level -1) contains a guide RNA scaffold (gRNA scaffold) and precursor transfer RNA (pre-tRNA), both essential for proper gRNA transcription and processing, as well as Cas9 binding to the target sequence. To knock out the *PERTL6* gene, Cas9 had to be directed to the specific target sites, which were identified using CRISPOR software (https://crispor.gi.ucsc.edu/crispor.py). The genomic DNA (gDNA) of *PERTL6* gene was used to avoid selecting a guide that spans two exons separated by intron. Preferred guides were located in early exons, with GC content between 40-70%, about 20 nt long, ideally with 0 off-targets and 0 mismatches, containing RRS and a protospacer adjacent motif (PAM) at the end (5'-NGG-3'), where N could be any nucleobase followed by two guanine (G) nucleobases. The gRNA guides Cas9 to the target locus in the genome and Cas9 cuts 3 nucleotides upstream of the recognized PAM sequence. The presence of RRS within the gRNA allows for screening and selection via restriction digest in subsequent steps of plant line establishment. Additionally, specific nucleotides location within guides were scored as

good or not good, based on factors such as presence or absence of TTT in the guide, C downstream of PAM, G at position -2 of PAM, G or A at the beginning of the gRNA, and G but not C at 20th position. To ensure that gRNA would create the appropriate secondary structure with the gRNA scaffold, RNAfold software was used (http://rna.tbi.univie.ac.at/cgi-bin/RNAWebSuite/RNAfold.cgi). An example of a preferred secondary structure is shown in Figure 2.2, where gRNA 7 is presented as an example of proper secondary structure of the gRNA and gRNA scaffold.

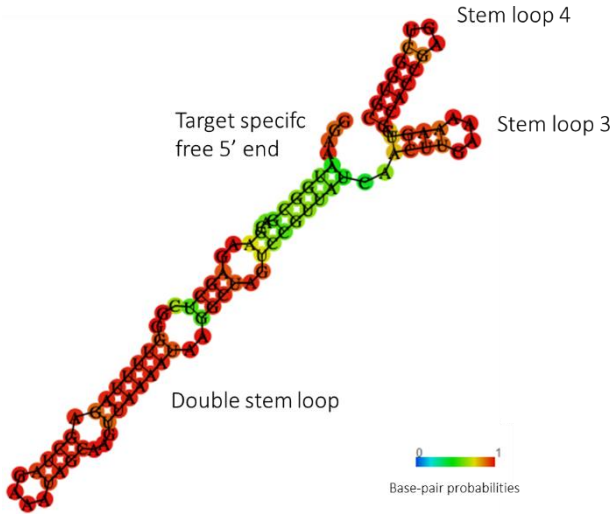

Figure 2.2 gRNA 7 as an example of proper II-structure or gRNA+gRNA scaffold

The four selected target sites within the *PERLT6* gene are shown in the schematic representation in Figure 2.3. The Cas9 cleavage site is located within exons 1, 3, 4, and 5 for guides 7, 2, 8, and 13, respectively.

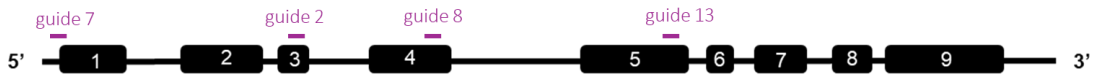

Figure 2.3 Position of targeted gRNA sequences on *PERTL6* gene map

In the next step, CRISPR primers were designed to create a tRNA-gRNA array. The DNA Reverse Complement Calculator (https://jamiemcgowan.ie/bioinf/complement.html) was used to generate complementary strands for the selected gRNA sequences. The KK primers were designed to bind to the selected target sites, while also containing overhangs with RRS for BsaI and overhangs corresponding to either gRNA scaffold (for FP) or pre-tRNA (for RP). Primers P155 and P156 included recognition sites for BpiI on the outer regions and BsaI in the inside regions. This design enabled the assembly of all parts into a single polycistronic tRNA-gRNA (PTG) array in downstream step. All primer pairs used for this

purpose can be found in Tab. 2.18 and their exact sequences provided in Appendix 6.4. A schematic representation of all amplified PTG parts is shown in Fig. 2.4. To facilitate primer design, guide RNA sequences were divided into two halves (gX_A and gX_B). Amplification was performed using VEC 423 (Figure 2.5) as a template, with Q5 polymerase, following the protocol described earlier in 2.2.2.1.1.

Table 2.19 Primers used for creating PTG parts for Golden Gate Modular Cloning

LEVEL 1 PART NO.	PRIMER FORWARD	PRIMER REVERSE	PRODUCT LENGTH
1	P155	KK04	123 bp
2	KK03	KK10	195 bp
3	KK09	KK12	195 bp
4	KK11	KK14	195 bp
5	KK13	P156	132 bp

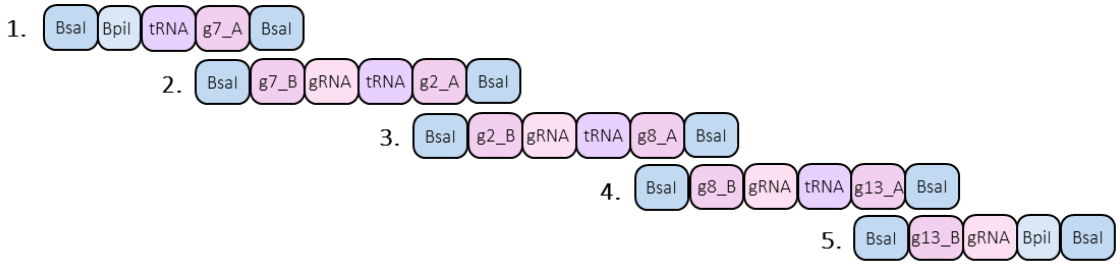

Figure 2.4 Schematic representation of PTG fragments created by amplification of VEC423 with primers from Tab. 2.18.

Furthermore, PCR products 1-5 were loaded onto an agarose gel. Following electrophoresis, the respective bands were excised, and DNA was eluted according to the previously described protocol. In the next step, the amplified t-RNA-gRNA fragments were assembled into a PTG array via a restriction-ligation reaction. BsaI was used to generate compatible sticky ends, allowing T7 DNA ligase to join the digested PTG fragments into a single array. Equal amounts of eluted DNA fragments were used for this reaction, which was set as follows.

Table 2.20 Restriction-ligation for assembling PTG array program

TEMPERATURE	TIME	NUMBER OF CYCLES
37 °C 20 °C	5 min 10 min	50 cycles
20 °C	60 min	1
16 °C	∞	-

After approx. 14 hours of restriction-ligation reaction, PCR was performed to amplify the entire PTG array. The ligation mixture was diluted 1:10, and Phusion polymerase was used

with primers P157 and P158, which contain RRS for BsaI at the 5' end, BpiI at the 3' end, and binding sites for the PTG array on both sites. The amplified PTG array was subsequently separated by agarose gel electrophoresis, and a band of ~580 bp was excised and purified. That purified construct was then prepared for cloning into a Level 0 vector.

Cloning into Level 0 Vector

The Level 0 acceptor vector (VEC 219) contains Control of Cell Death B (ccdB) flanked by RS for BpiI. CcdB encodes a toxin that leads to bacterial cell death, therefore enabling negative selection, as only recombinant plasmids (which have the PTG insert replacing ccdB gene) will survive and propagate. Additionally, the ampicillin resistance (Amp^R) gene allows for positive selection of successfully transformed bacteria (Figure 2.5).

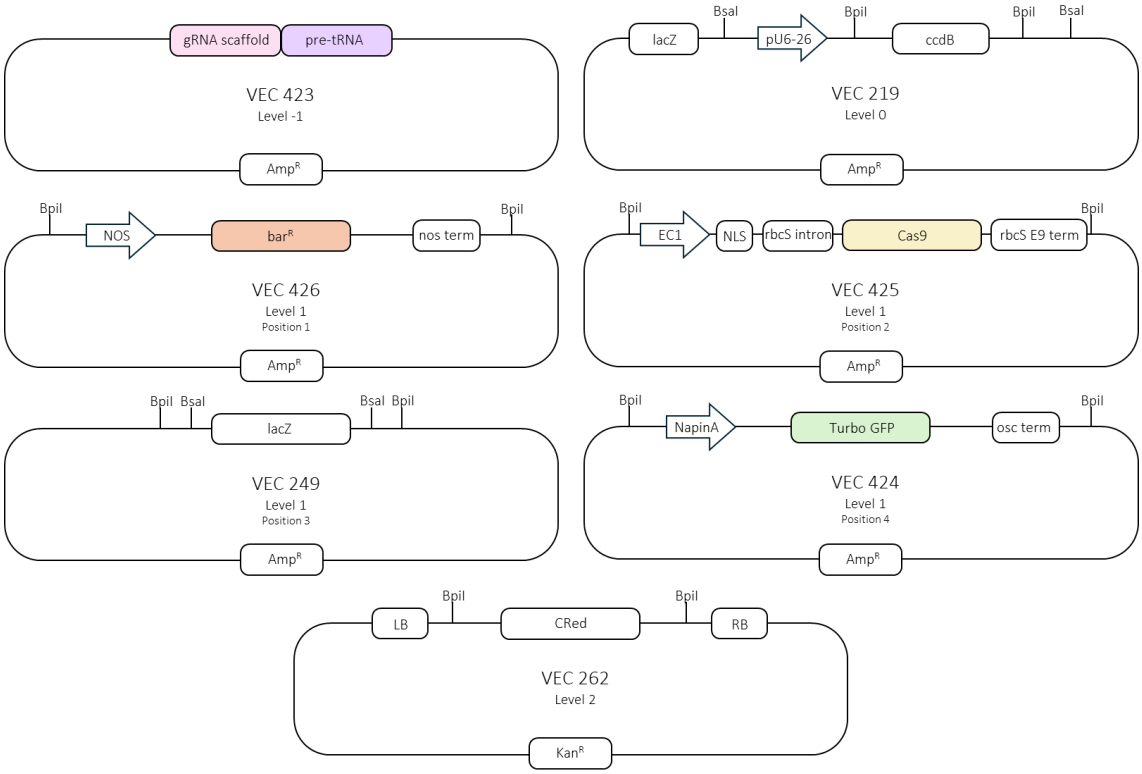

Figure 2.5 Schematic representation of level -1, 0, 1 and 2 Golden Gate Modular Cloning vectors.

Abbreviations: bar – Gene conferring resistance to herbicide phosphinothricin (bialaphos resistance), Cas9 – CRISPR-associated protein 9, Cred – Reporter gene for white/red screening, CmR – Chloramphenicol resistance, CcdB – Control of Cell Death B (toxic gene for negative selection), EC1 – Egg cell-specific promoter 1, LB/RB – left/right border of T-DNA, NapinA – Seed-specific promoter from Brassica napus, NLS – Nuclear localization signal, NOS – Nopaline synthase promoter, nos term – Nopaline synthase terminator, osc term – Terminator from Oryza sativa (rice), pre-tRNA – Precursor transfer RNA, pU6-26 – U6-26 promoter, rbcS intron – Ribulose-1,5-bisphosphate carboxylase small subunit intron, rbcS E9T – Ribulose-1,5-

bisphosphate carboxylase small subunit E9 terminator, TurboGFP – Green fluorescent protein variant used for strong fluorescence.

The PTG array was cloned into a VEC 219 using T4 DNA Ligase and BpiI RE, maintaining a 3:1 molar ratio of the PTG array to the acceptor plasmid (Table 2.21).

Table 2.21 Restriction-ligation reaction for assembling PTG array into level 0 vector

TEMPERATURE	TIME	NUMBER OF CYCLES
37 °C 20 °C	2 min 5 min	45 cycles
50 °C	5 min	1
80 °C	10 min	1
16 °C	∞	-

Therefore, the vector pKK1 (Level 0) was obtained, with the entire PTG array cloned under the pU6-26 promoter, flanked by BsaI RRS, as shown in Figure 2.6.

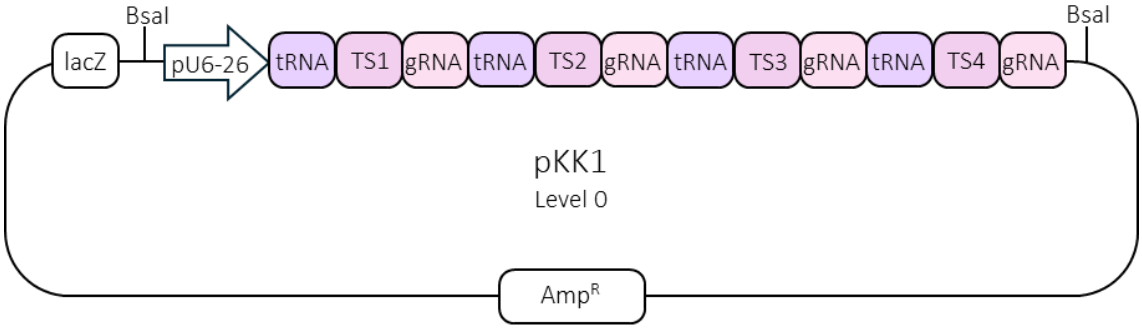

Figure 2.6 pKK1 level 0 vector for Golden Gate Modular Cloning

To amplify the plasmid pKK1 for further cloning, *E. coli* transformation was performed, and the transformed bacteria were placed on selective LB media containing ampicillin. Next, Colony PCR was conducted using primers P001 and P002, which bind to lacZ regions flanking the PTG, to confirm successful transformation. Plasmids isolation followed, and proper insert incorporation was verified by sequencing.

Cloning into Level 1 Vector

Similar to cloning into the Level 0 vector, higher-order constructs were assembled using Level 1 and Level 2 vectors. These vectors contain the Left and Right Border sequences of the T-DNA, facilitating *Agrobacterium*-mediated transformation.

Positive pKK1 plasmids were ligated into the Level 1 vector (VEC 249) at position 3 using T4 DNA Ligase and BsaI, followed by *E. coli* transformation. VEC 249 carries the lacZ gene

allowing α-complementation screening. Colonies that carry the disrupted lacZ gene, (indicating successful cloning) appeared white, while those without an insert remained blue. Additionally, ampicillin selection was used to ensure that only the transformed bacteria grew. This blue-white screening method, in combination with antibiotic selection, allowed for the identification of positive transformants containing the pKK2 Level 1 Vector (Figure 2.7).

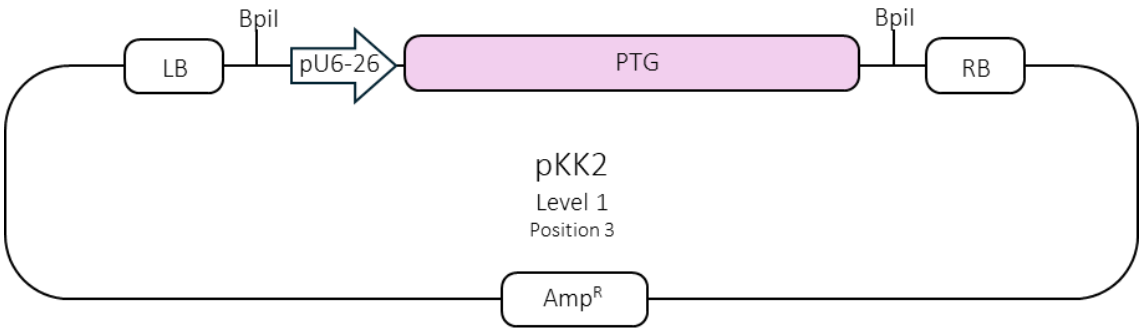

Figure 2.7 pKK2 Level 1, position 3 vector with PTG cassette for Golden Gate Modular Cloning

Colony PCR was performed with primers P142 and P150, which bind outside the PTG array, and the isolated plasmid was confirmed by sequencing.

Cloning into Level 2 Vector

In the final step of the Golden Gate Modular Cloning, five vectors were assembled into the Level 2 Vector in a single reaction. The design of the vectors and their flanking RRS enabled precise positioning of each cassette.

- VEC 426 (Position 1) contains bar resistance gene encoding phosphinothricin acetyltransferase (PAT), conferring resistance to the herbicide phosphinothricin (PPT), also known as glufosinate or BASTA. This vector serves as a selection marker for transformed plants.
- Vector 425 (Position 2) carries Cas9 cassette, facilitating targeted DNA cleavage.
- pKK2 (Position 3) contains PTG array, ensuring proper guide RNA expression
- VEC 424 (Position 4) includes GFP cassette under the control of seed-specific NapinA promoter, enabling selection of fluorescent transgenic seeds.
- VEC 269 functions as a linker between the fourth position and an acceptor Vector 262.

Ligation – restriction reaction into the Level 2 vector was performed using T4 DNA Ligase and BpiI, generating the final construct, pKK3 (Figure 2.8). Each donor plasmid was added

in equal mass of 75 ng. VEC 262 contains CRed cassette, an artificial bacterial operon that enables biosynthesis of canthaxanthin, a red-colored carotenoid pigment. Similar to the lacZ cassette, it allows for visual selection, as successful insertion of foreign DNA disrupts CRed operon, resulting in the formation of white colonies.

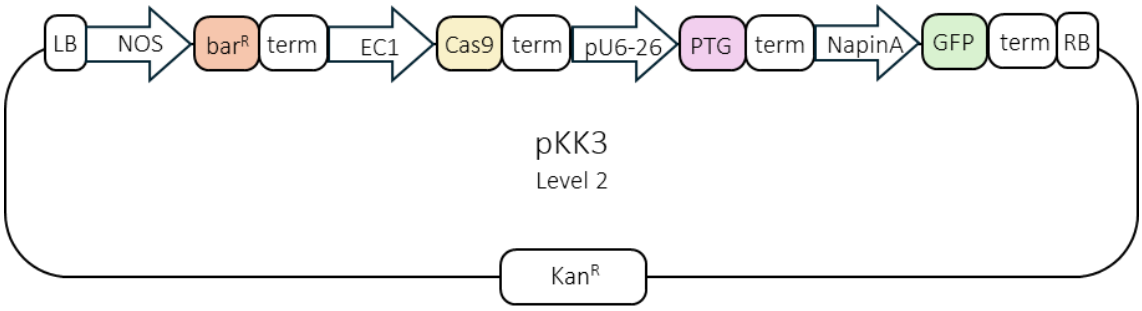

Figure 2.8 pKK3 Level 2 final vector for Agrobacteria-mediated transformation of *Arabidopsis thaliana*

Since Vector 262 also contains kanamycin resistance gene, transformed bacteria were selected on kanamycin- containing media. Subsequently, Colony PCR was performed using the primer pairs listed in Table 2.22.

Table 2.22 Colony PCR set up for all cassettes in Level 2 vector pKK3

LEVEL 1 VECTOR	CASSETTE	PRIMER PAIR	EXPECTED SIZE
VEC 426	Bar	P042/P043	883 bp
VEC 425	Cas9	P167/P168	1090 bp
pKK2	PTG	KK15/KK16	1205 bp
VEC 424	GFP	P151/P166	1156 bp

Positive colonies were then subjected to plasmid isolation, and the purified plasmids were sent for sequencing to verify successful assembly to Level 2 construct – the final pKK3 vector. Once confirmed, pKK3 was ready for *Agrobacterium*-mediated transformation and, eventually, Floral Dip method for transforming *Arabidopsis* buds.

2.2.2.3. Gene expression analysis

2.2.2.3.1. RNA isolation

RNA isolation was carried out using the RNeasy Plant Mini Kit (Qiagen) according to the manufacturer's instructions. Fresh plant material was collected in tubes containing sterile RNase-free metal bead and immediately frozen in liquid nitrogen. Grinding was performed using Retsch Mill (40 s, 28 Hz, twice). RNA extraction was carried out with RLT buffer containing β-mercaptoethanol, and elution was performed with RNase-free water. To

maximize the yield, the eluate was re-applied to the membrane. RNA concentration was measured using a Nanodrop spectrophotometer.

2.2.2.3.2. DNase treatment

To remove any genomic DNA (gDNA) contamination, RNA samples were treated with RQ1 RNase-free DNase (Promega) following the manufacturer's instructions. Each reaction was set up with 1 µg of RNA.

Successful gDNA digestion was assessed by running the samples on a 1% agarose gel. Distinct 28S and 18S rRNA bands indicated intact RNA, while smears or additional bands suggested potential gDNA contamination.

2.2.2.3.3. Complementary DNA (cDNA) synthesis

A complementary cDNA (cDNA) synthesis was performed using the LunaScript RT SuperMix Kit (NEB) according to the manual. To confirm successful reverse transcription, a PCR reaction was performed targeting ACT7 (*ACTIN 7*) gene (At5g09810). PCR was conducted using homemade Taq polymerase with primers P067/P068. The expected product sizes were 734 bp for cDNA and 918 bp for gDNA, allowing for verification of successful reaction.

2.2.2.3.4. Quantitative PCR (qPCR)

To assess transcript abundance of different genes quantitative PCR (qPCR) was performed using the Luna Universal qPCR Master Mix (NEB). This technique follows the standard PCR principles but incorporates the SYBR Green fluorescent dye, which binds to double-stranded DNA (dsDNA), enabling real-time monitoring of the amplicon accumulation during each PCR cycle. Gene expression levels are determined using the cycle threshold (Ct) method, where lower Ct values indicate higher transcript abundance. Data normalization was performed relative to a reference (housekeeping) gene using the following equations:

$$\Delta Ct = Ct_{\,target\,gene} - Ct_{\,reference\,gene}$$

$$\Delta\Delta Ct = \Delta Ct_{sample} - \Delta Ct_{control}$$

$$Fold\ change = 2^{(-\Delta\Delta Ct)}$$

A fold change greater than 1 indicates gene upregulation, while fold change less than 1 indicates downregulation.

Primers for qPCR were designed using PrimerQuest (IDT) and Primer-BLAST (NIH), following these criteria: amplicon length: 70-200 bp; primer melting temperature: ~60 °C; efficiency: ~100% (±20%); specificity: no primer-dimer formation; primer design: spanning two exon-exon junctions, to prevent gDNA amplification. The selected primers and their corresponding target genes are listed in Table 2.23.

Table 2.23 qPCR primer pairs and their corresponding genes

PRIMER PAIR	PRIMERS	GENE
PP7	KK31/KK32	*pertl6* (At1g74240)
PP11	P094/P095	GTP binding elongation factor T4 family protein (At5g60390)
PP13	DG40/DG41	*hsfa1a* (At4g17750)
PP15	DG48/DG49	*hsp90* (At4g24190)

The qPCR reaction was prepared according to the manufacturer's protocol. The reaction was run on Applied Biosystems instrument using StepOne™ Software v2.x, following the cycling program detailed in Table 2.24.

Table 2.24 The qPCR program scheme

CYCLE STEP	TEMPERATURE	TIME	NUMBER OF CYCLES
Initial	50 °C	20 s	1
Denaturation	95 °C	10 min	1
Denaturation	95 °C	15 s	40
Extension	60 °C	1 min	
Melting curve	95 °C	15 s	-
	60 °C	-	-
	95 °C	Incremental increase (0.5 °C/s)	-

2.2.3. Microbiological methods

The microorganisms and their respective genotypes used in this thesis are listed in Table 2.5. in the Materials section.

2.2.3.1. Bacterial strains and Growth Conditions

Escherichia coli (E. coli) MACH 1 was used for plasmid amplification during cloning. The cells were cultivated overnight at 37 °C in either liquid Lysogeny Broth (LB) (Bertani, 1951) with shaking at 150 rpm or on solid LB agar plates supplemented with appropriate antibiotic for selection (Cultures were grown overnight at 30 °C, either in liquid medium with shaking at 200 rpm or on solid YEP medium plates.

Table 2.25, Table 2.26). *Agrobacterium tumefaciens* GV3101 was used for vector introduction into Arabidopsis and tobacco plants. The bacteria were cultivated on YEP medium supplemented with Rifampicin and Gentamycin, as the strain carries resistance genes for these antibiotics (Table 2.8, Table 2.26) (Koncz & Schell, 1986). Cultures were grown overnight at 30 °C, either in liquid medium with shaking at 200 rpm or on solid YEP medium plates.

Table 2.25 Lysogeny broth (LB) medium

SOLUTE	CONCENTRATION
Tryptone (or peptone)	1% (w/v)
Yeast Extract	0.5% (w/v)
NaCl	1% (w/v)
Agar (for solid media)	1.5% (w/v)

Table 2.26 Antibiotic concentration for cultivating bacteria

ANTIBIOTIC	CONC. FOR *E.COLI*	CONC. FOR A.TUMEFACIENS
Ampicillin	200 µg/mL	-
Kanamycin	30 µg/mL	50 µg/mL
Spectinomycin	100 µg/mL	100 µg/mL
Rifampicin	-	150 µg/mL
Gentamycin	-	50 µg/mL

2.2.3.2. Transformation Techniques

2.2.3.2.1. Transformation of *E.coli* via heat shock

To introduce exogenous DNA into *E.coli*, the heat shock method was used. First, a 100 µL aliquot of competent cells was thawed on ice. For re-transformation, 1 µL of plasmid was added, whereas for ligation or Gibson assembly transformations, 10-20 µL reaction mix was used. The mixture was incubated on ice for 10 minutes, followed by a 90-second heat shock at 42 °C. Immediately after, the tubes were placed on ice for 2 minutes. Subsequently, 800 µL of room temperature LB medium was added, and the sample was incubated at 37 °C with constant shaking at 150 rpm for 1 hour. Finally, 20 µL of the cell culture was spread onto LB agar plates supplemented with the appropriate antibiotic and incubated overnight at 37 °C.

2.2.3.2.2. Transformation of *A.tumefaciens* via Electroporation

To introduce exogenous DNA into *A. tumefaciens*, electroporation was used. Similar to the *E.coli* transformation, a 50 µL aliquot of *Agrobacterium* competent cells was thawed on ice. Then, 1 µg of the plasmid DNA was added, and the mixture was transferred to a pre-cooled

2-mm electroporation cuvette. Electroporation was performed using an Eppendorf Electroporator 2510 with the following settings: capacitance 25 of μF, voltage of 2,4 kV, resistance of 200 Ohm and pulse length of 5 ms. Immediately after electroporation, 1 mL of YEP medium was added to the cuvette, and the entire mixture was transferred to a fresh tube. The culture was incubated at 30 °C with constant shaking at 200 rpm for 2 hours. Finally, 20 μL of the cell culture was spread onto YEP agar plates supplemented with the appropriate antibiotics and incubated at 30 °C for two nights.

2.2.3.3. Plasmid Manipulation

2.2.3.3.1. Colony PCR

Colony PCR was performed to rapidly verify the presence of the plasmid to confirm successful bacterial transformation. A single colony was picked and either directly used for PCR master mix or first resuspended in 50 μL of nuclease-free water to lyse the cells during denaturation in 90 °C for 10 minutes. Subsequently, 1 μL of the lysate was used as a template for PCR, employing homemade Taq DNA polymerase and appropriate primers.

2.2.3.3.2. Plasmid isolation

Following successful Colony PCR, plasmids from positive colonies were isolated using the Wizard® Plus SV Minipreps DNA Purification System (Promega), according to the manufacturer's instructions. DNA was eluted with 30 μL of nuclease-free water preheated to 55 °C to enhance yield. The concentration of purified plasmid was measured using a Nanodrop Spectrophotometer.

2.2.4. Metabolomics

2.2.4.1. Sample Collection and Preparation

To assess how plant responses to stress affect metabolic pathways, metabolite profiling was performed. Fresh plant material, either leaves or whole seedlings, was collected in tubes containing a sterile metal bead and immediately froze in liquid nitrogen to stop the metabolic activity. Grinding was performed using Retsch Mill (40 s, 28 Hz, twice) or FastPrep-24 instrument with a CoolPrepAdapter (20 s, 9 times). Afterward, the samples were weighed on a precision scale to ensure a similar weight within each experimental batch.

2.2.4.2. Metabolites extraction

The two-phase extraction method was chosen, as it enables the separation of metabolites based on their polarity. A methanol:chloroform solvent mixture (7:3 (v/v)) was used. Internal standards were selected according to the analytical technique: for Gas Chromatography-Mass Spectrometry (GC-MS), 5 µM ribitol and 10 µM of trichloroacetic acid (TCA) or 5 µM norleucine were used; for Liquid Chromatography-Mass Spectrometry (LC-MS), a stable isotope-labeled mix of 5 µM Valine-d8 and Phenylalanine – d5 was employed. In the first step, 350 µL of pre-cooled methanol/chloroform solvent was added to the sample and vortexed for 1 minute, followed by incubation at -20 °C for 2 hours with vortexing every 30 minutes. Subsequently, 560 µL of ice-cold HPLC-grade water containing internal standard was added to the sample, mixed for 1 minute, and incubated on ice for 10 minutes. Samples were then centrifugated at maximum speed for 4 minutes at 4 °C. After phase separation, the upper aqueous (polar) phase was transferred to a fresh tube and the extraction step was repeated using an additional 560 µL of ice-cold HPLC-grade water. Following the final collection of samples, ice-cold HPLC-grade water was added to a final volume of 1700 µL to prevent bubbling during the subsequent lyophilization step. Samples were dried in CHRIST Lyophilizer for at least 24 hours and then resuspended in 500 µL of ice-cold HPLC-grade water. Finally, samples were stored at -70 °C.

2.2.4.3. Sample derivatization and Analysis

To improve detection, stability, ionization and volatility of certain metabolites, samples underwent derivatization process. All samples, except those from salt stress treatment, were derivatized at the CEPLAS Metabolomics and Metabolism Laboratory.

For salt stress treatment samples, methoximation was performed by adding 50 µL of methoxyamine hydrochloride in dry pyridine, followed by vortexing and overnight incubation at room temperature. The next day, 50 µL of N,O-Bis (trimethylsilyl) trifluoroacetamide with 1% trimethylchlorosilane (BSTFA) was added and incubated at 60 °C for 1 hour, resulting in trimethylsilyl (TMS) derivatives. Samples were then centrifuged for 2 minutes in a SpeedVac, and 50 µL of the supernatant was transferred into a glass inlet placed inside an autosampler glass vial.

GC-MS and LC-MS analysis were performed by CEPLAS Metabolomics and Metabolism Laboratory at HHU and by Michigan State University Mass Spectrometry and Metabolomics Core Facility. GC-MS analysis of the derivatized samples was performed using an Agilent

7890A single quadrupole mass spectrometer with 5975C inert XL MSD (Agilent, Santa Clara, CA). One microliter of the derivatized sample was injected in a split mode (1:10) with an injector temperature of 230 °C and a helium flow rate of 1 mL/min. Separation was achieved using an Agilent J&W VF5-ms column (30 m x 0.25 mm x 0.25 mm) (Agilent, Santa Clara, CA) using the following temperature program: 40 °C for 1 min; 40 °C min^{-1} to 80 °C; 10 °C min^{-1} to 240 °C; 20 °C min^{-1} to 320 °C; 320 °C for 5 min. Ionization employed 70 eV electron ionization, and the mass spectrometer was operated in scanning mode with a m/z scan range of 50-600. Data files were converted to MassHunter data format, and peaks were identified based on background-subtracted spectrum matches to the NIST17 library. A quantifier and qualifier ion were used to quantify the peak areas for each compound.

2.2.5. Imaging and phenotyping

2.2.5.1. Microscopy and subcellular localization

Microscopy was performed to determine the subcellular localization of PERTL6. For this, the tobacco plant was transiently transformed with *Agrobacterium* carrying vectors with the appropriate cassettes obtained via Gibson Cloning, as previously described. Fragments of tobacco leaves were used for imaging epidermal cells on the abaxial side using an Olympus FluoView FV1000 Confocal Laser Scanning Microscope, configured on an Olympus IX81 inverted microscope, using FV10-ASW software (version 4.2) at the Center for Advanced Microscopy at Michigan State University. Fluorescence images were acquired using 60x objective with 2x magnification under the following excitation/emission settings:

Table 2.27 Excitation and emission wavelengths used for microscopy

FLUOROPHORE	EXCITATION WAVELENGTH	LASER WAVELENGTH	EMISSION WAVELENGTH	DICHROIC MIRROR
Chlorophyll a	430, 460	559	670	BA 655-755
Chlorophyll b	455, 640	559	650	BA 655-755
mCerulean	433	458	475	SDM 510 (475-500)
mCherry	587	559	610	BA 600-620

The images were then processed using Fiji.

2.2.5.2. Photosynthetic measurements

Photosynthetic measurements were performed to evaluate the impact of stress on photosynthesis. Chlorophyll fluorescence imaging was conducted using a FluorCam (PSI)

system to assess photosynthetic efficiency. Before the measurement, plants were dark-adapted for 30 minutes. The maximum quantum efficiency of Photosystem II (PSII) was then determined using the Fv/Fm equation, where Fm represents the maximum fluorescence yield under light-saturated conditions, and Fv = Fm - F0, with F0 being the minimal fluorescence yield. FluorCam 7 software was used to calculate the parameters.

2.2.5.3. Gas exchange measurements

Net carbon assimilation (A) under ambient (21%) and photorespiratory (2%) oxygen conditions were measured using the LI-6800 portable photosynthesis system (LI-COR).

For ambient conditions, plants were placed into the small plant chamber and acclimating to the following conditions: flow: flow rate: 300 μmol s^{-1}, water vapor pressure deficit (VPD) 1.2 kPa, CO_2 concentration: 420 μmol^{-1}, fan speed: 10 000 rpm, leaf temperature: 22 °C and a light source composed of 50% red and 50% blue light (r50b50) at 1000 PAR μmol m^{-2} s^{-1} to reach the photosynthetic steady state.

The CO_2 response curve was obtained using the Dynamic Assimilation Technique (DAT) under the following conditions: initial CO_2 concentration: 50 ppm, waiting time: 3 min, final CO_2 concentration: 1800 ppm, ramp rate: 100 μmol min^{-1}, and logging interval: 5 s. After completion of the CO_2 ramp, chamber CO_2 was restored to 420 $\mu mol\, mol^{-1}$. The CO_2 response curves were fitted to estimate the V_{cmax} (the maximum carboxylation rate of Rubisco), J_{max} (the maximum rate of electron transport for the given light intensity, representing RuBP regeneration) and TPU (the maximum rate of triose phosphate utilization) using an R-based A/C_i fitting tool (https://github.com/poales/msuRACiFit), with the following parameters: respiration in the light (R_L) = 0.51, photorespiratory CO_2 compensation point (CCP) (Γ^*) = 4.83, and mesophyll conductance to CO_2 transfer g_m = 1.83.

CO_2 assimilation under photorespiratory (40% O_2) conditions was measured using manual CO_2 control at 420 ppm, with either high (40% O_2/60% N_2) or low (2% O_2/98% N_2) oxygen concentrations. Once steady-state conditions in 2% of O_2 were reached, the following program was applied: oxygen concentration 2%, 40%, 2% with a 2 s interval and a 5 min duration. An R-based fitting tool (https://github.com/codexf/oxygenTransientFit) was used to model the time course data using one-phase exponential decay functions.

For rapid, non-steady-state measurements of plants exposed to prolonged warming stress stomatal conductance and photosynthesis were measured using a portable Porometer/Fluorometer Model LI-600 (LI-COR). Three oldest leaves of each plant were selected for the assessment to better evaluate the plant's physiological state.

2.2.6. Computational Analysis and Data Processing

2.2.6.1. Phylogenetic Studies

Phylogenetic analysis was performed to identify orthologs of the PERTL6 protein in other species. Protein sequences from various Archaeplastida species were retrieved in FASTA format from Phytozome (https://phytozome-next.jgi.doe.gov/), a plant genomic database (Goodstein et al., 2012). OrthoFinder (https://github.com/davidemms/OrthoFinder) was used to identify orthologs by performing all-versus-all sequence comparisons and clustering genes into orthogroups based on sequence similarity (Emms & Kelly, 2019). Additionally, BLAST was used to identify homologous sequences in red algal species that were not available in Phytozome. Multiple Sequence Alignment of the identified orthogroups was performed using MUSCLE within the MultAlin tool (Corpet, 1988) (http://multalin.toulouse.inra.fr/multalin/). The phylogenetic tree was constructed using Maximum Likelihood method in MEGA X (https://www.megasoftware.net/) with JTT substitution model, 1000 bootstrap replications, 4 threads, and 150 graduations steps (Kumar et al., 2018). Tree visualization and annotation was performed using iTOL: interactive Tree Of Life (https://itol.embl.de/)(Letunic & Bork, 2024).

Additionally, SHOOT.bio (https://shoot.bio/) was used to complement the ortholog analysis across different domains of life besides plants, including Metazoa, Bacteria, Archaea, and Fungi. The tool identifies homologous genes and classifies them into families based on sequence similarity, providing insights into their potential biological functions.

3. Results

3.1. Subcellular localization studies of PERTL6

Identifying the correct subcellular compartment is essential to hypothesize which metabolic processes PERTL6 may influence. To verify the peroxisomal localization of PERTL6, despite its classification as a member of the MCF, subcellular localization studies of fluorescent fusion proteins were performed in plants. Using the Gibson Assembly method (2.2.2.2.4), the CDS of PERTL6 from pHHU 431 vector was fused to the fluorescent marker protein mCherry at the C-terminus, to enable the visualization of the protein. Additionally, the fluorescent marker mCerulean was fused to a PTS1 to serve as peroxisomal matrix marker. Both expression cassettes were cloned into one binary vector to guarantee the same expression level in the same cells and simplify the transformation. To balance expression levels, the two cassettes were under two different strong and constitutive promoters, the UBQ10 for the PERTL6 and the CaMV 35S for the organelle marker. This setup enabled stable co-expression in all cells while lowering the risk of overexpression artifacts or silencing. The resulting construct (pUBQ10::PERTL6-mCherry and 35S::mCerulean-PTS1) in the pKK4 vector (Figure 2.1) was used to transform *E. coli* and subsequently *A. tumefaciens*. Successful transformation was confirmed by Colony PCR (Suppl. Figure 6.18).

Vectors used as negative controls carried either just mCherry alone (pMG2) or mCerulean fused with PTS1 alone (pMG43), are detailed in Appendix 6.5.

Positively transformed *A. tumefaciens* colonies were inoculated and used for transient transformation of *Nicotiana tabacum* by leaf infiltration (2.2.1.1.1). Two days after, transformed leaves were visualized using Confocal Laser Scanning Microscopy (2.2.5.1). Localization studies were performed in replicates, and representative images are presented in Figure 3.1 and Figure 3.2.

As shown in Figure 3.1, mCerulean-PTS1 appears as cyan punctate structures, confirming its localization in peroxisomes within the *N.tabacum* epidermal cells. In the red fluorescence channel, mCherry-PERTL6 was observed in punctate and/or ring-like structures surrounding the peroxisomes. The merged image (third panel) confirms their colocalization.

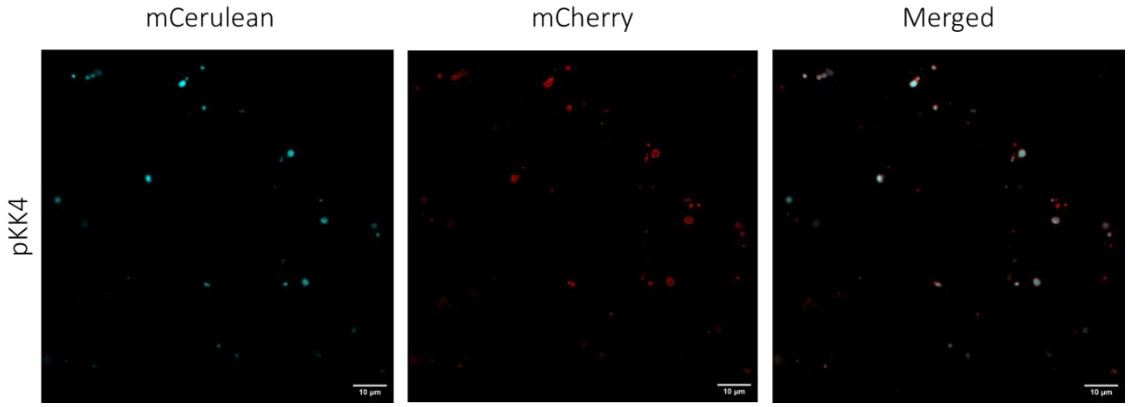

Figure 3.1 Subcellular localization of PERTL6 in tobacco epidermal cells

PERTL6 fused to mCherry, along with mCerulean fused to PTS1 (pKK4 vector), was transiently expressed in *A.tumefacines*-infiltrated *N.tabacum* leaves. Imaging was performed on epidermal cells from the abaxial side of the leaves. In the left panel, cyan fluorescence signal represents mCerulean-PTS1, serving as peroxisomal marker. In the middle panel, red fluorescence signal corresponds to mCherry-PERTL6, while the right panel shows a merged image of both channels. Scale bars = 10 µm.

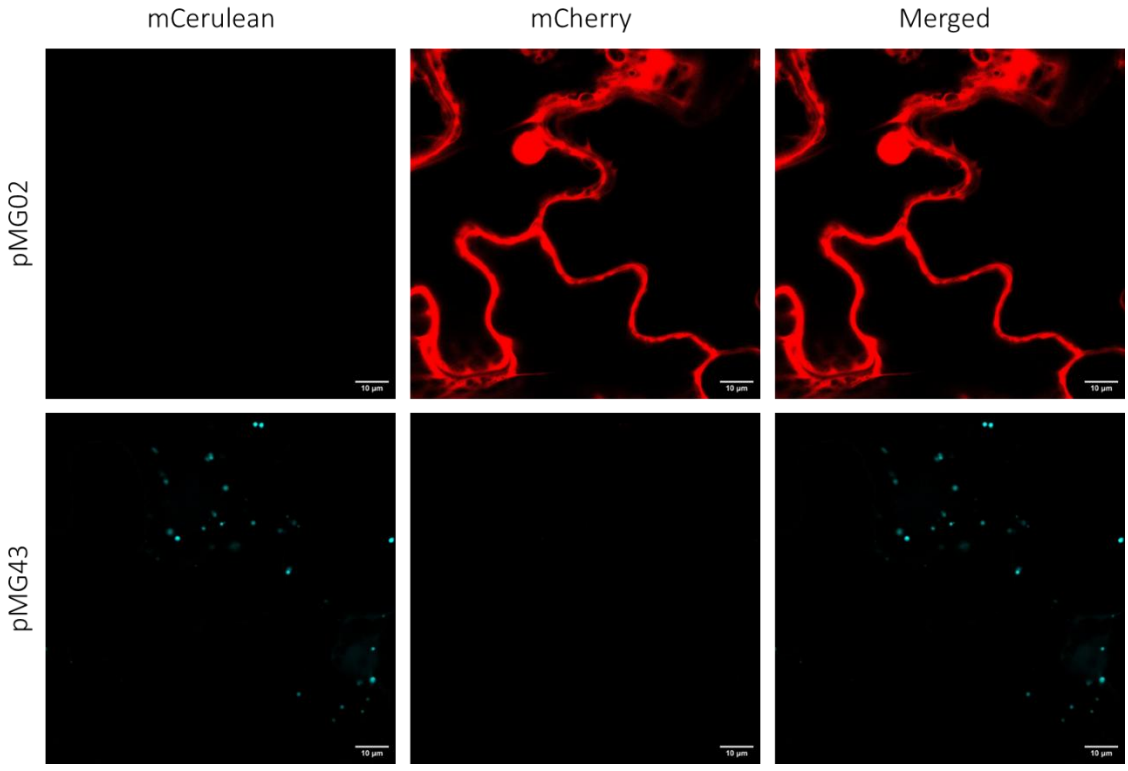

Figure 3.2 Negative controls for subcellular localization studies in tobacco epidermal cells

Tobacco leaves were transiently transformed, and epidermal cells were imaged. The upper panel presents fluorescence from the pMG02 vector, which expresses only mCherry, resulting in signal diffusion in the apoplast. The lower panel shows fluorescence from the pMG43 vector, where mCerulean-PTS1 marks peroxisomes. Scale bars = 10 µm.

In the negative control, vector pMG02, where only mCherry was expressed, the fluorescence signal was diffusely localized in the apoplast of epidermal cells. No mCerulean signal was detected. Conversely, in the negative control vector pMG43, which expresses only mCerulean-PTS1, fluorescence was exclusively observed in peroxisomes (Figure 3.2).

To verify the experimental results, the Subcellular Localization Database for Arabidopsis Proteins (SUBA5; suba.live) was used (Hooper et al., 2017). The prediction data indicated that PERTL6 localizes to mitochondria. As some proteins are known to be dual-localized to mitochondria and peroxisomes (Carrie et al., 2009), co-infiltration with mitochondrial marker fused to YFP was performed in tobacco leaves to further experimentally confirm the subcellular PERTL6 localization in peroxisomes.

Upon co-infiltration with pKK4 and the mitochondrial marker, the mCerulean channel showed cyan puncta corresponding to peroxisomes, while the mCherry channel confirmed a ring-like structure red signal representing PERTL6 in the peroxisomal membrane. The YFP channel however showed smaller yellow puncta indicating mitochondria. In the overlayed images, mCerulean signal co-localizes with mCherry, as observed previously with the single infiltration with pKK4 vector. However, the yellow mitochondrial puncta did not overlap with neither the PERTL6 signal nor the peroxisomal signal, suggesting that PERTL6 localizes predominantly in peroxisomes, not in mitochondria (Figure 3.3).

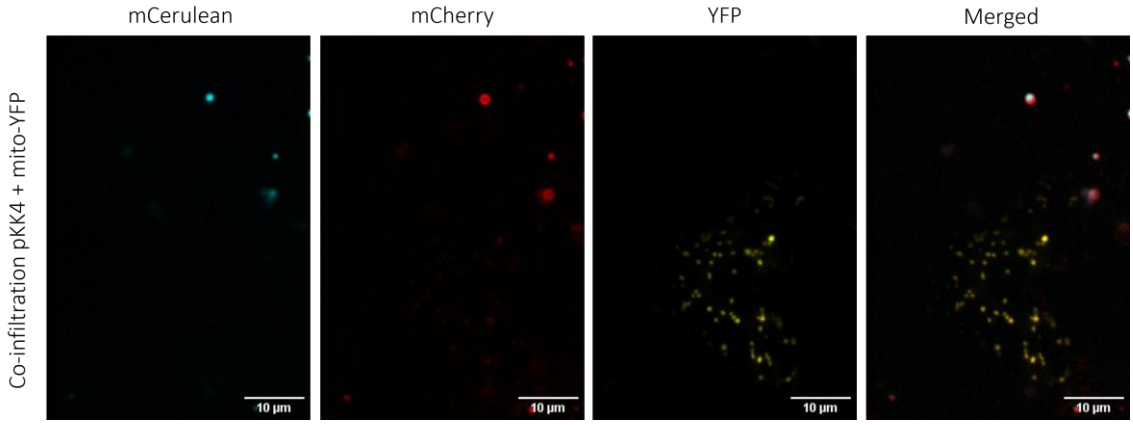

Figure 3.3 Co-infiltration of pKK4 with mitochondrial marker-YFP in *Nicotiana tabacum* leaves

Tobacco leaf epidermal cells co-infiltration with the pKK4 and a mitochondrial marker fused to YFP. From left to right, the panel shows: mCerulean fluorescence representing peroxisomes; mCherry signal corresponding to PERTL6; YFP signal marking mitochondria; and the merged image of all three fluorescence channels. Scale bars = 10 µm.

3.2. Phylogenetic analyses

To annotate the function of the PERTL6 protein by identifying its orthologs and to determine its evolutionary relationship with other proteins, a phylogenetic analysis was performed. Various protein sequences from Archaeplastida were used to identify orthologs. The results from OrthoFinder are shown in Figure 3.3. The phylogenetic tree illustrates all orthologs found in representative plants from Viridiplantae (green plants). Different colors indicate the clade or a plant group, to which each species belong, as indicated on the right side of the tree. The numerical values along the tree represent the branch length, which represents the evolutionary distance between nodes, substitutions per site, where 0 means identical sequences with no changes between them. Bootstrap values are shown as pink circles at key branches, with larger circles corresponding to higher bootstrap values, reflecting greater statistical robustness and confidence in the branch.

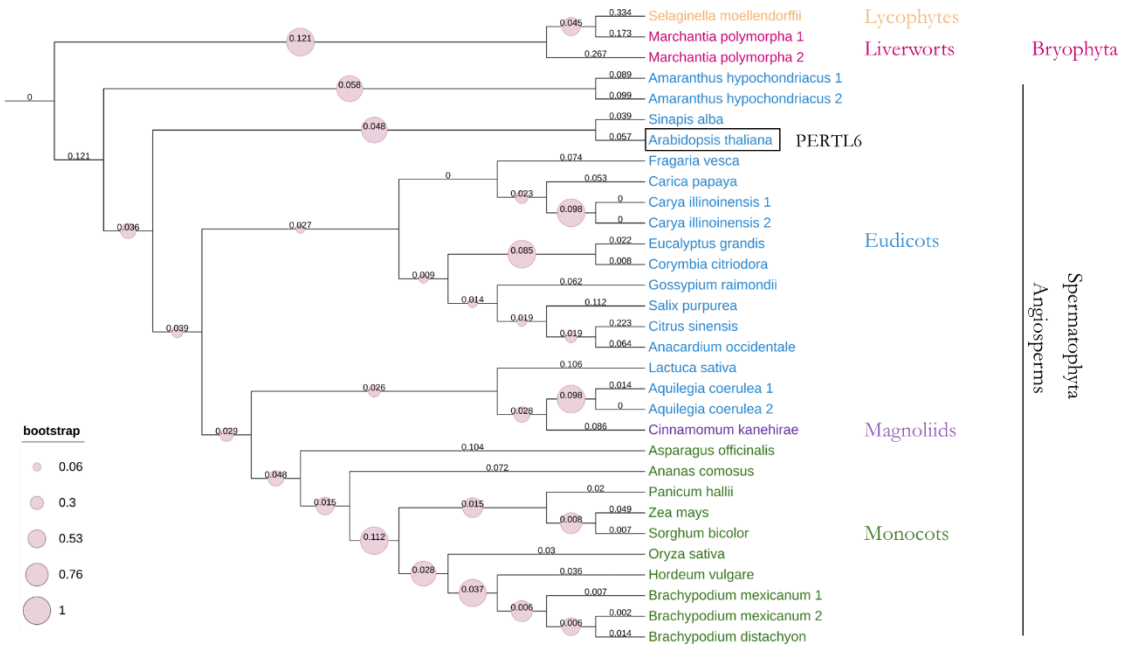

Figure 3.4 Phylogenetic tree of PERTL6 orthologs within Viridiplantae species from OrthoFinder

Different colors correspond to various plant clades and groups. Numerical values along the tree represent branch lengths, rounded to three decimals Bootstrap values are shown as pink circles, with the legend located on the left. The PERLT6 protein sequence in Arabidopsis thaliana is highlighted in black box for visibility.

The PERTL6 protein sequence was found only as a one protein-coding sequence (in black box), indicating At1g74240 is a single-copy gene in *Arabidopsis thaliana*. Orthologs for PERLT6 were identified in other Angiosperms species from all clades (Eudicots, Magnoliids, Monocots), and in representative species from Bryophyta (Liverworts) and Lycophytes. Low

branch length values suggest high similarity between many sequences and evolutionary relationships. That suggests protein functional conservancy between these species. High bootstrap values separating Angiosperms from Lycophytes and Liverworts support the statistical reliability of these distinctions.

Interestingly, OrthoFinder did not identify any orthologs in green algae *Chlamydomonas reinhardtii* and *Dunaliella salina* (Chlorophyta), nor in the red algae *Porphyra umbilicalis* (Rhodophyta). To confirm that result, BLAST search was used, confirming no orthologs for any algal species available. This absence may suggest that *pertl6* gene is land-plant specific that either evolved after the divergence from algal species in land plants in response to new terrestrial challenges, or it was lost independently in these organisms.

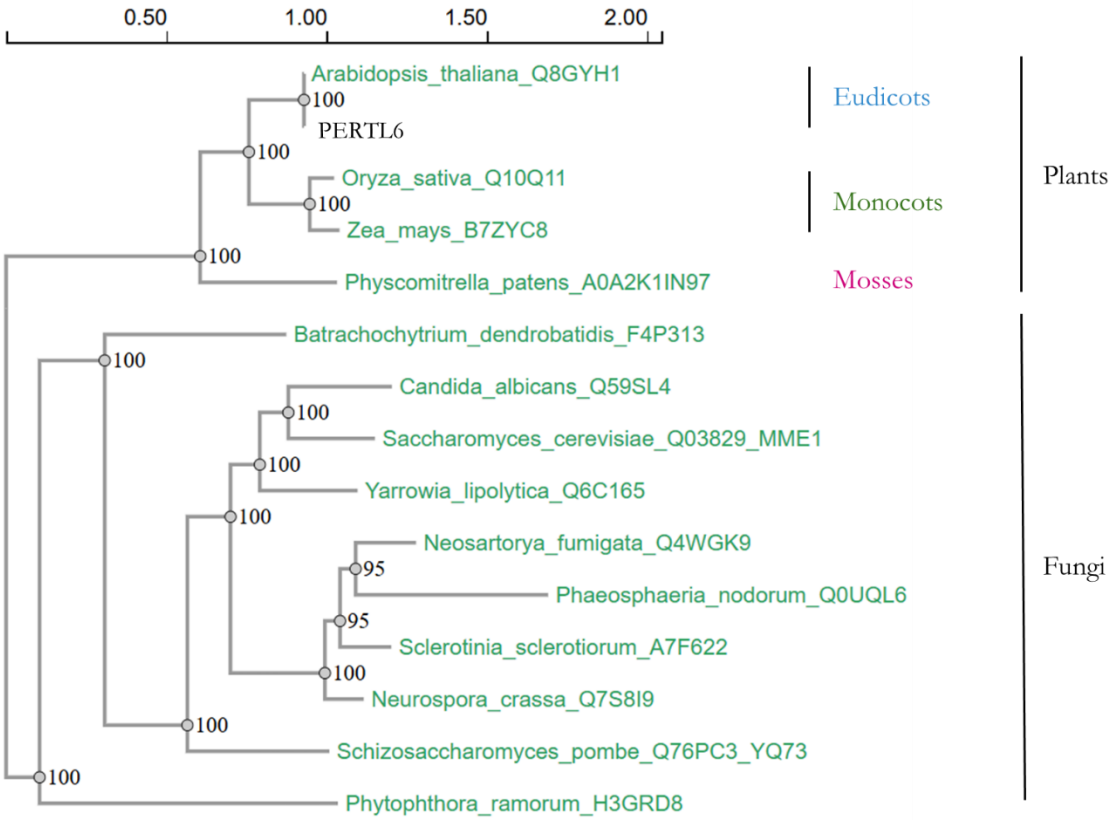

Figure 3.5 Phylogenetic tree of PERTL6 orthologs within all domains of life from SHOOT.BIO

This tree presents green-colored results, indicating most likely PERLT6 orthologs identified in SHOOT.BIO database. The numbers along the tree represent bootstrap support values, with 100 meaning high confidence in that branching. The scale above the tree shows the branch length.

To further investigate species specificity of PERTL6, a broader database was used, including not only photosynthetic eucaryotes (Archaeplastida), but also other domains of life. The SHOOT.BIO was chosen for this analysis, as it allows for an easy search of a query sequence

against a database combining all domains of life like Animals, Fungi, Bacteria and Archaea (Emms & Kelly, 2022). OrthoFinder and the maximum likelihood method were applied to build an ortholog tree.

The ortholog search result from SHOOT.BIO (Figure 3.5) revealed that PERTL6 orthologs were found only in Plants and Fungi species. Among these fungal orthologs, two mitochondrial transporters were annotated according to UniProt database like thiamine pyrophosphate carrier 1 and magnesium exporter 1 (MME1, Cui et al., 2015). The results are supported with very high bootstrap values (>95). However, the long branch lengths separating fungal and plant orthologs suggest distinct evolutionary relationships, which may indicate functional divergence between these groups or orthologs. No orthologs were identified in Animals, Bacteria, or Archaea, indicating significant divergence in these domains.

3.3. *PERTL6* promoter region *in silico* analysis

To further investigate the potential function of PERTL6, promoter analysis was carried out. Researching the regulatory elements that control gene expression may provide valuable insights into its biological role. For that purpose, a 1000 bp upstream of the Transcription Start Site (TSS) of the *PERTL6* gene was retrieved using EnsemblPlants (https://plants.ensembl.org/index.html). This sequence was then used to identify the Transcription Factors (TF) and their corresponding cis-elements (motifs) using multiple databases: PLACE https://www.dna.affrc.go.jp/PLACE/?action=newplace) (Higo et al., 1999), PlantPAN (https://plantpan.itps.ncku.edu.tw/plantpan4/index.html) (Chow et al., 2024), JASPAR (https://jaspar.elixir.no/) (Rauluseviciute et al., 2024), and AGRIS (https://agris-knowledgebase.org/) (Yilmaz et al., 2011). Subsequently, the sense-strand cis-elements were further investigated using Transcription Factor database PlantTFDB (https://planttfdb.gao-lab.org/) (Tian et al., 2020) and TAIR.

Figure 3.6 Nucleotide sequence of the *PERTL6* promoter region (700 bp upstream of the TSS)

The numbers on the right side indicate the distance from the TSS. The cis-elements are underlined and color-coded according to their corresponding TF functional group. For the descriptions of each element, see Table 3.1

Promoter analysis of the 700 bp upstream of the TSS revealed the presence of eighteen transcription factor-binding sites associated with various environmental signals. The cis-elements were underlined and color-coded based on their corresponding primary biological functions: Abiotic stress response (brown), Salt, drought, osmotic stress response (blue), Heat stress response (red), Light response (yellow), Immune response (violet), Growth and development regulation (green), as shown in Figure 3.6. A more detailed description of the identified transcription factors is provided in Table 3.1.

Table 3.1 Summary of selected Transcription Factors (TFs), their cis-elements, associated biological functions, and supporting literature references.

TRANSCRIPTION FACTOR	CIS-ELEMENT	BIOLOGICAL FUNCTION	REFERENCE
ATERD1	ACGT	Abiotic stress response (osmotic stress, nitrogen starvation)	(Dhatterwal et al., 2022)
AP2/ERF	ATTTTGGCGGCGGCG	Abiotic stress response (ethylene, osmotic stress)	(Z. Xie et al., 2019)
ASF-1	TGACG	Abiotic stress response	(Devi et al., 2006; Redman et al., 2002)
AZF1	GGTGGAAGTGA	Growth inhibition under abiotic stress (cold and salt stress)	(Kodaira et al., 2011)
CCAAT - BOX1	CCAAT	Heat shock response; transcriptional regulation	(Haralampidis et al., 2002)
GATA15	TTTGATCAA	Light-responsive regulation	(Manfield et al., 2007)
HRS1	ATCGAATATTTT	Growth and development regulation	(Wu et al., 2012)
HSFA1B	GAATCTCC	Heat shock response	(Albihlal et al., 2018)
HSFA6B	TTCTGAAA	Heat shock response	(Huang et al., 2016)
HSFB2A	GAACTTTCTTAA	Heat shock response	(Wunderlich et al., 2014)
I-BOX	GATAAG	Light-responsive regulation	(Berry et al., 2013)
MYB13	CAACCAACCA	Salt stress response	(Sukumaran et al., 2023)
MYB70	AAACTGTAATAACT	Growth and development regulation	(Wan et al., 2021)
MYBCORE	CTGTTG	Drought response; flavonoid biosynthesis	(Guo et al., 2016; Yu et al., 2017)
NAC2	TGTGCCGTGTAT	Abiotic stress response (high light, salt, and drought stress)	(Borgohain et al., 2019; Morishita et al., 2009)
SURE	GAGAC	Sulfur deficiency response	(Maruyama-Nakashita et al., 2005)
TGA2	TTACGTCATG	Biotic stress response (Systemic Acquired Resistance (SAR) via salicylic acid)	(Zander et al., 2010)
WRKY71	TGAC	Salt stress response; ethylene-mediated senescence	(Yu et al., 2018, 2021)

The majority of the identified transcription factors are associated with stress response. Among the most frequently observed motifs were those related to salt, drought and osmotic stress – such as ATERD1, MYBCORE, WRKY71, MYB13, AZF1 and AP2/ERF – highlighting an important role of *PERTL6* in salt stress adaptation. Transcription factors associated with heat stress response were also identified, including HSFA6B, HSFA1B, CCAAT-BOX1, and HSFB2A indicating a possible involvement of *PERTL6* gene in heat stress adaptation. Additionally, light responsive elements (I-BOX and GATA15) were

identified, which also links the gene with circadian clock regulation. TFs such as ASF-1, SURE and NAC2 – involved in general abiotic stress response, but also nutrient deficiency, sulfur (SURE) or nitrogen (ATERD1) – give a potential connection role of PERTL6 to nutrient stress signaling. Other TFs involved in growth and development regulation (HRS1 and MYB70) further point the *PERTL6* regulatory role in hormonal signaling and growth-related stress responses. Finally, the presence of TGA2, a TF involved in Systemic Acquired Resistance (SAR) through salicylic acid pathway, along with ethylene-regulated elements (AP2/ERF and WRKY71) suggest also a potential role in biotic stress response and senescence regulation.

Overall, all the identified TF-binding cis-elements are related to a wide range of stress responses, support possible role of *PERTL6* in stress adaptation, homeostasis and growth regulation in plants.

3.4. Co-expression analysis of *PERTL6*

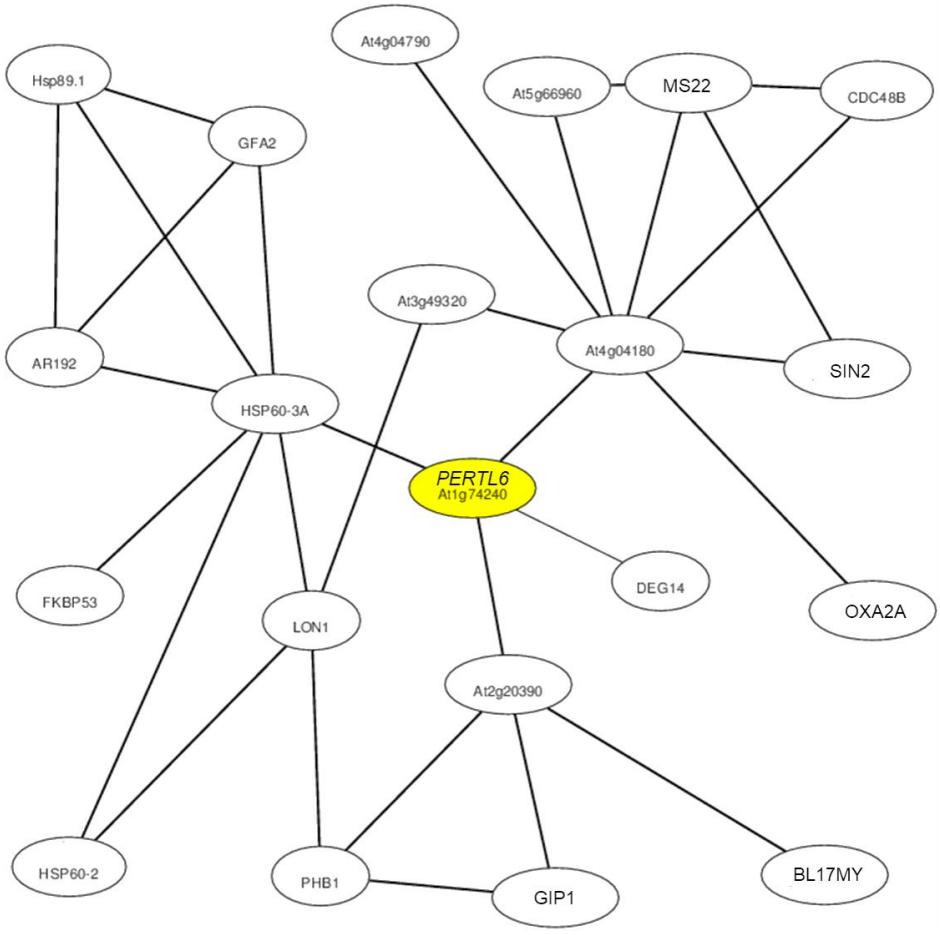

Figure 3.7 *PERTL6* co-expression network obtained from ATTED-II database (edited)

Table 3.2 List of 20 co-expressed genes together with their Gene Ontology information

GENE ID	NAME	BIOLOGICAL PROCESS	MOLECULAR FUNCTION	CELLULAR COMPARTMENT	CLASSIFICATION
At3g13860	*HSP60-3A*	Protein folding	ATP-dependent protein folding chaperone	Chloroplast, Cytosol, Mitochondrion	Stress response, Protein folding
At4g04180	-	Proteasome-mediated ubiquitin-dependent protein catabolic process	Proteasome-activating activity	Chloroplast, Mitochondrion	Proteolysis, Ubiquitin-proteasome system
At2g20390	-	Cytochrome oxidase complex assembly	-	Chloroplast, Mitochondrion	Mitochondrion organization
At5g26860	*LON1*	ATP-dependent protein homeostasis	ATP binding, Protein binding	Chloroplast, Mitochondrion	Proteolysis
At3g49320		Metal-dependent protein hydrolysis	-	Cytoplasm, Nucleus	Proteolysis
At5g27660	*DEG14*	Heat response	Peptidase activity, Serine-type endopeptidase activity	Mitochondrion, Nucleus	Stress response, Protein degradation
At4g28510	*PHB1*	Mitochondrion organization	-	Chloroplast, Mitochondrion, Vacuole	Mitochondrion organization
At4g26780	*AR192*	Heat response and acclimation, Protein folding, Mitochondrial import	ATP binding, Adenyl-nucleotide exchange factor activity, Copper ion binding	Chloroplast, Cytosol, Mitochondrion	Stress response, Protein folding
At4g04790	-	Unknown	Unknown	Mitochondrion	Unknown
At5g48030	*GFA2*	Female gametophyte development	Protein folding chaperone, Unfolded protein binding	Chloroplast, Mitochondrion	Development, Protein folding
At1g64600	*MS22*	Translation	-	Mitochondrion	Translation
At2g33210	*HSP60-2*	Protein folding	ATP binding, Protein folding chaperone, RNA binding, Copper ion binding	Chloroplast, Cytosol, ER, Mitochondrion, Vacuole	Stress response, Protein folding
At3g07770	*HSP89.1*	Heat response, Protein folding, Protein stabilization	ATP binding, ATP hydrolysis activity, Protein binding, Unfolded protein binding	Cell wall, Chloroplast, Cytosol, Mitochondrion,	Stress response, Protein folding
At3g53630	*GIP1*	Response to abiotic stimulus	Protein binding	Chloroplast, Cytosol, Nucleus	Abiotic stress response
At2g41670	*SIN2*	Mitochondrial translation	GTPase activity	Chloroplast, Mitochondrion	Translation
At2g03670	*CDC48B*	-	ATP hydrolysis activity	Cell membrane	Protein processing
At5g66960	-	Unknown	Unknown	Unknown	Unknown
At5g64650	*BL17MY*	Translation	Structural constituent of ribosome	Mitochondrion	Translation
At1g65080	*OXA2.4*	Cytochrome c oxidase assembly	Membrane insertase activity	Chloroplast, Mitochondrial inner membrane	Mitochondrial protein insertion
At4g25340	*FKBP53*	Nucleosome assembly	Histone binding, Isomerase activity, Protein binding	Nucleus	Chromatin remodeling

Co-expression analysis in *Arabidopsis* was performed to gain insight into the possible molecular function of PERTL6 (At1g74240). Co-expressed genes often participate in similar biological processes or share regulatory mechanisms, thus identifying them can help elucidate PERTL6' function. The analysis was carried out using ATTED-II database (https://atted.jp/) (Obayashi et al., 2022) while the Gene Ontology (GO) annotations were retrieved from TAIR (https://www.arabidopsis.org/). ATTED-II uses publicly available Arabidopsis RNAseq and microarray data to identify highly co-expressed genes and build a gene network, as presented on Figure 3.7. A list of the top twenty co-expressed genes along with their GO annotations is provided in Table 3.2.

In the co-expression network, there are four genes directly connected to *PERTL6* mRNA. These genes are involved in heat shock response, mitochondrial organization and protein folding, and proteolysis. Most of the top twenty co-expressed genes are associated with stress response, protein homeostasis, and mitochondrial function.

Notably, several well-characterized heat shock chaperones, such as *HSP60-3A* (At3g13860), *HSP60-2* (At2g33210), *HSP89.1* (At3g07770) are co-expressed with *PERTL6,* with *HSP60-3A* displaying the highest co-expression score. These chaperones are involved in ATP-dependent protein folding and localize to chloroplast, cytosol and mitochondria, suggesting their role in cellular stress response and protein quality control. Another major group of co-expressed genes consists of genes involved in protein degradation, such as *LON1* (At5g26860), *DEG14* (At5g27660), *CDC48B* (At2g03670), At3g49320, and At4g04180. Several other genes like *PHB1* (At4g28510) and *OXA2A* (At1g65080), maintain the mitochondrial homeostasis. Genes such as *MS22* (At1g64600), *BL17MY* (Att5g64650), and *SIN2* (Att2g41670) are involved in translation indicating their role in gene expression regulation. Few genes from the network (At4g04790, At5g66960) remain so far uncharacterized, potentially representing novel components of the PERTL6 functional network.

3.5. Cell-specific expression analysis of *PERTL6* in leaves

To determine whether expression of *PERTL6* varies depending on the cell type, single-cell RNA sequencing data from the Plant Single Cell Browser and the Leaf scRNA-Seq Atlas was analyzed (Ma et al., 2020). The results obtained showed that *PERTL6* is expressed at low levels in nearly all *Arabidopsis* leaf cell types under non-stress conditions (Figure 3.8).

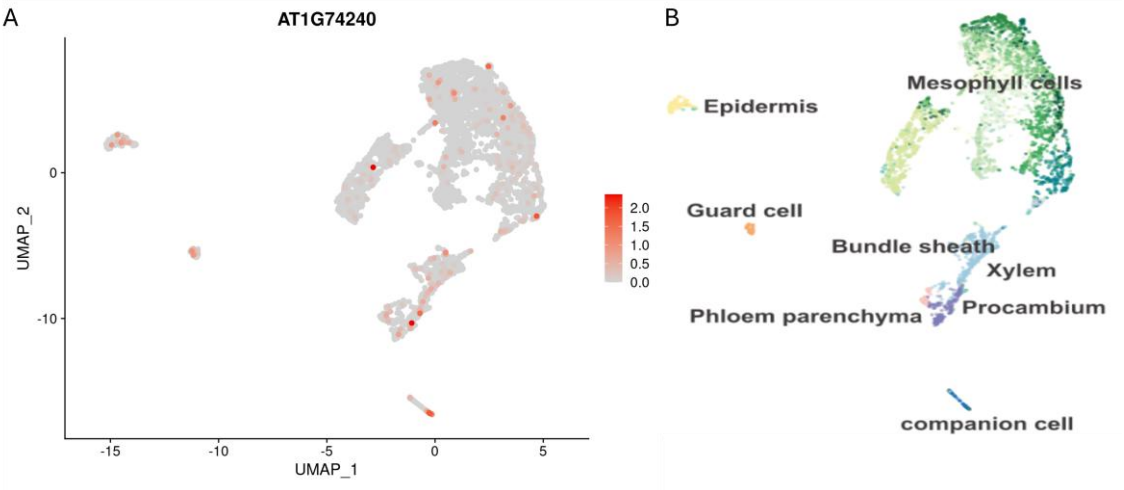

Figure 3.8 Single-cell RNA-seq expression of *PERTL6* in *Arabidopsis* leaf cell

Expression of *PERTL6* mapped across clusters derived from *Arabidopsis thaliana* leaf single-cell transcriptome data from Plant Single Cell Browser (A) with the corresponding legend (B). Red dots represent detected *PERTL6* transcripts in individual cells.

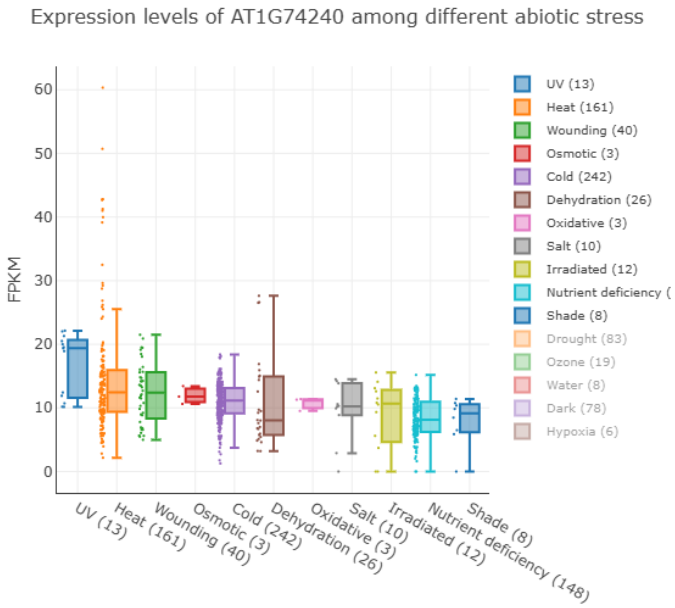

Figure 3.9 Expression levels of *PERTL6* under various abiotic conditions from Arabidopsis RNA-seq Database

Expression levels were retrieved from Arabidopsis RNA-seq Database. Each dot represents a separate RNA-seq library or experiment, reflecting transcript abundance under specific conditions marked by different colors with corresponding legend on the right.

Overall, although *PERTL6* is expressed at low levels under non-stress conditions, the co-expression network points to the potential role for PERTL6 in stress adaptation and mitochondrial maintenance, regulated by translation and proteolysis. Notably, its association

with stress response is consistent with earlier observations of *PERTL6* upregulation during heat stress (D. Winter et al., 2007b). Moreover, the RNA-seq data from the Arabidopsis RNA-seq Database (https://plantrnadb.com/athrdb/) indicate that *PERTL6* transcript levels increase upon various abiotic stresses, with particularly strong induction during heat (Figure 3.9), further strengthening the hypothesis that PERTL6 contributes to antioxidative mechanisms in plant cells (H. Zhang et al., 2020).

3.6. Plant lines

Based on promoter analysis, co-expression patterns, tissue-specific single-cell RNA-seq data, and transcript upregulation under heat stress suggesting PERTL6's potential role in stress response, further *in planta* studies were conducted to investigate its function. This section provides an overview of all the *Arabidopsis* lines that were generated or utilized to characterize the function of PERTL6. The confirmation of the T-DNA insertions or mutations in these lines was performed via PCR using primers listed in Table 2.9.

3.6.1. *pertl6* plant lines

3.6.1.1. T-DNA insertion line *pertl6-1*

The *pertl6-1* (SALK_030104) mutant line carries a tandem insertion in the fifth exon of the *pertl6* gene, as presented on Figure 3.10 A. Homozygous plants were identified by genotyping with gene-specific and T-DNA specific primers on genomic DNA extracted from the leaves of *pertl6-1* plants (lane 2), WT plants (lane 3) and a water as a negative control (lane 4). A 1 kb DNA ladder (lane 1) was used to determine the band sizes. Additionally, as positive control for successful gDNA extraction, primers specific to the housekeeping gene *ACT7* were used. The presence of T-DNA tandem insertions was confirmed (712 bp and 841 bp bands) while the absence of gene specific (1165 bp) band confirmed homozygosity of the line (Figure 3.10 B).

To validate if the T-DNA insertions in *perlt6-1* line disrupts the DNA transcription, RT-PCR was performed. Primers binding to first exon (KK33) and last 9th exon (KK35) were used to amplify the gene. cDNA from WT was used as positive control with expected band size 939 bp (lane 2) and water was used as negative control (lane 4). Obtained result showed no PCR product for *perlt6-1* line (lane 3), indicating premature transcription termination due to the T-DNA insertions within the *PERLT6* gene (Figure 3.11).

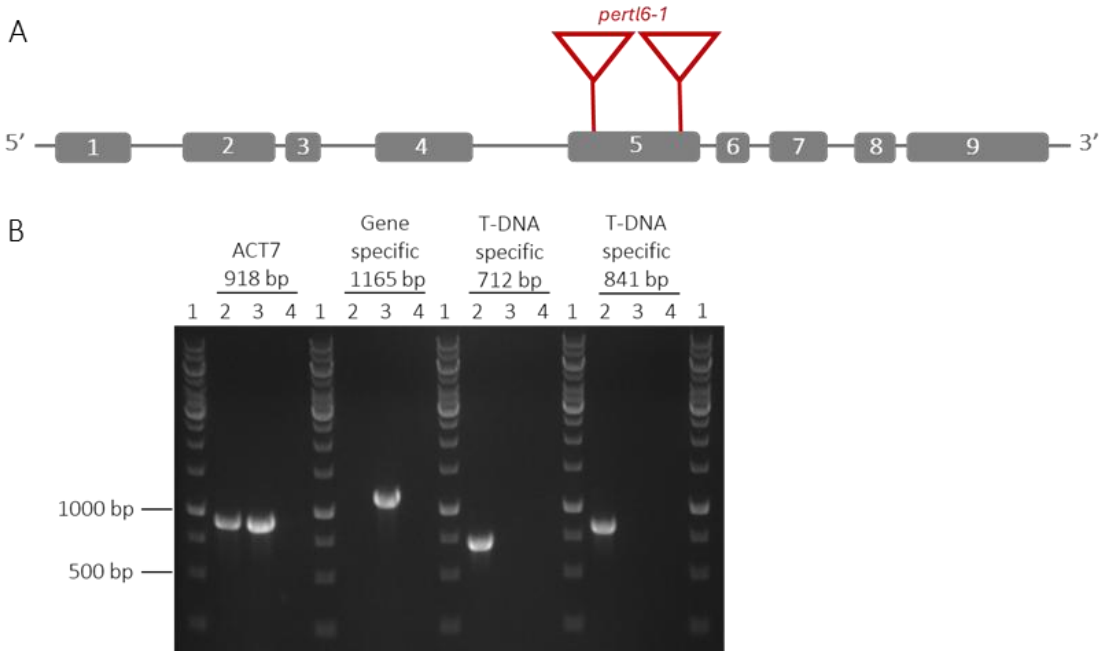

Figure 3.10 T-DNA tandem insertion in pertl6-1 mutant line and corresponding genotyping results

A. Schematic representation of a pertl6-1 T-DNA tandem insertion in exon 5 of At1g74240. Exons are depicted as numbered gray boxes, introns as gray lines, and T-DNA insertions as red triangles. B. PCR analysis of genomic DNA isolated from homozygous perlt6-1 mutant plants (lane 2), WT plants (lane 3) and water as negative control (lane 4). A 1 kb ladder (lane 1) was used for size comparison. Primers used for the PCR are listed in Table 2.9.

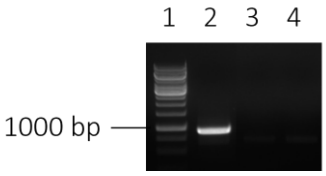

Figure 3.11 RT-PCR on cDNA spanning the whole PERTL6 gene in WT and *pertl6-1* line

RT-PCR on cDNA from WT (lane 2), pertl6-1 (lane 3) and water (lane 4) as negative control. 1 kb ladder (lane 1) was used for size comparison. Primers KK33 and KK35 are listed in Table 6.1.

To assess the effect of T-DNA insertions on the *pertl6* expression level in *pertl6-1* line, qPCR was conducted. Figure 3.12 presents the positions of the qPCR primers binding sites relative to the T-DNA insertions.

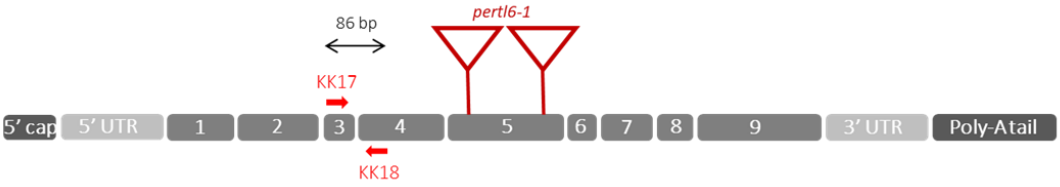

Figure 3.12 Primer binding sites for qPCR within the *pertl6* mRNA

Schematic diagram of a qPCR primer binding sites within pertl6 gene (At1g74240) in the *pertl6-1* mutant line. Exons are indicated as numbered gray boxes. The 5' cap, 5' UTR, 3'UTR, and Poly-A tail are shown as corresponding gray boxes. The T-DNA insertions are marked with red triangles, and primer binding sites are indicated by red arrows (primers KK17 and KK18). The expected qPCR amplicon length is 86 bp.

The relative *PERTL6* transcript abundance was measured compared to WT using qPCR. Six-week-old WT and *perlt6-1* plants grown under LD conditions were used for RNA extraction. Five biological replicates per genotype were analyzed. The GTP binding elongation factor T4 family protein (At5g60390) was used as a reference gene. As presented in Figure 3.13, the *PERTL6* transcript level in *pertl6-1* is reduced by 74% compared to WT. This highly significant difference ($p = 0.0003$, t-test) confirms that *pertl6-1* is a strong knock-down line, suitable for functional studies of the gene.

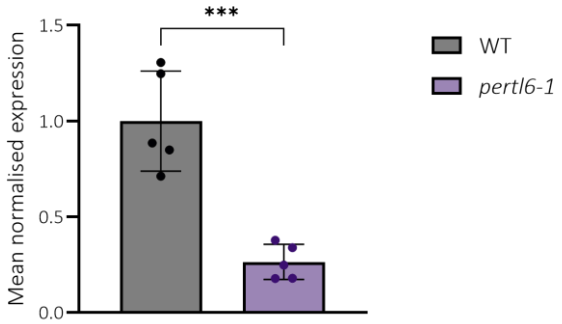

Figure 3.13 Relative gene expression of At1g74240 in WT and *pertl6-1* mutant line

Mean normalized expression (MNE) of At1g74240 in 6-week old WT and pertl6-1 plants grown under LD conditions. Expression was normalized to the reference gene GTP binding elongation factor T4 family protein (At5g60390). Bars represent means of five biological replicates ± SD (WT MNE was normalized to 1). Asterisks denote a highly significant difference based on t-test ($p = 0.0003$).

3.6.1.2. CRISPR/Cas9 *perlt6-6* line

To better study the PERTL6 function, another independent mutant line (*pertl6-6*) was created using CRISPR/Cas9 genome editing via Golden Gate Modular Cloning. This approach enables obtaining stable gene knock out and, using a multiplex gRNA expression system, allows for expression of multiple gRNA from a single polycistronic gene (Engler et al., 2014;

Marillonnet & Grützner, 2020). Four different target sites were selected within exons 1, 3, 4, and 5, as marked in Figure 2.3. Homozygous, Cas9-free mutant plants were identified thanks to BASTA resistance cassette, GFP cassette and RRS incorporated in the vector. Out of over 230 screened plants, one line was identified with a single thymine (T) insertion in the first exon. To confirm that this insertion mutation happened not only on gDNA but also on transcript level, RNA was isolated from 11-week-old *pertl6-6* and WT plants grown under SD conditions. Primers flanking the T insertion were used to amplify cDNA and sequenced (Figure 3.14).

Figure 3.14 Primer binding positions for confirmation of mutation in *PERTL6* cDNA in *pertl6-6* CRISPR/Cas9 line

Schematic diagram showing PCR primer binding sites within pertl6 gene (At1g74240) in the pertl6-6 CRISPR/Cas9 mutant line. Exons are indicated as numbered gray boxes. The 5' cap, 5' UTR, 3'UTR, and Poly-A tail are shown as corresponding gray boxes. The thymine (T) insertion is marked as a blue triangle, and primer binding sites are indicated by red arrows (primers KK72 and KK73). The expected PCR amplicon length is 297 bp.

Sequencing of the *perl6-6* cDNA confirmed the presence of one thymine insertion, causing a frameshift mutation that leads to premature stop codon and translation termination. This results in truncated, likely non-functional protein (Figure 3.15).

3.6.1.1. Complementation *pertl6-1* line

The better study the role of PERTL6, a complementation line (*perlt6-1* CL) was used. The line was created by Maximilian Trippelsdorf (MSc thesis, 2014) and Lennart Charton (MSc thesis, 2015) by introducing pUBQ10::PERTL6-YFP construct (vector pHHU 431) into the *pertl6-1* background. Transgenic homozygous plants were identified via genotyping. PCR was performed with genomic DNA extracted from the leaves of *pertl6-1 CL* plants (lane 2), WT plants (lane 3) and water as a negative control (lane 4). A 1 kb DNA ladder (lane 1) was used to estimate the fragment sizes. *ACT7* was used as a positive control for successful gDNA extraction. The presence of PERTL6 CDS (1611 bp) along with the T-DNA-specific insertions (712 bp and 841 bp), and the absence of gene-specific (1165 bp) WT band, confirmed the homozygosity of the complementation line (Figure 3.16). Additionally, the

expression of PERTL6 was confirmed by YFP signal visible in leaves (in trichomes) under fluorescence microscope.

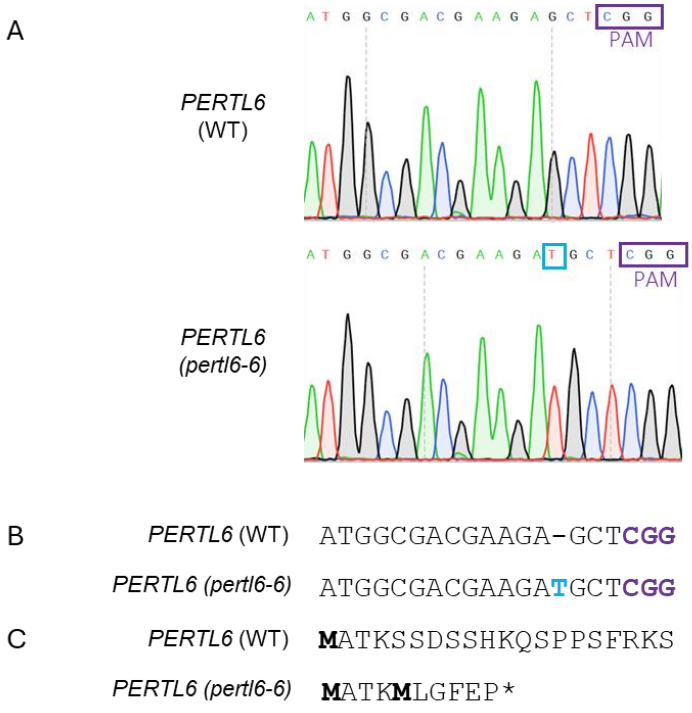

Figure 3.15 Generation of *pertl6-6* mutant

A cDNA sequencing chromatogram of pertl6 gene, highlighting PAM sequences (purple) and thymidine insertion (blue box) in the perlt6-6 mutant line compared to WT. B Nucleotide sequence with marked PAM sequences (purple) and thymine insertion (blue). C Translated amino acid sequence with methionine as the translation start and an asterisk indicating premature stop codon.

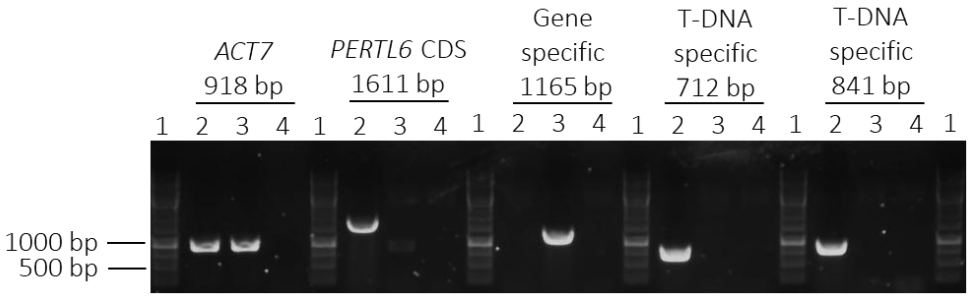

Figure 3.16 PCR results of genotyping complementation line *pertl6-1* (CL)

PCR analysis of genomic DNA from homozygous perlt6-1 CL plants (lane 2), WT (lane 3) and water (lane 4). A 1 kb ladder (lane 1) was used for size comparison. Primers are listed in Table 2.9.

3.6.1.2. *PERTL6* overexpressor line

The *PERTL6* overexpressor line (OEX) was also generated by Maximilian Trippelsdorf and Lennart Charton using the same pUBQ10::PERTL6-YFP genetic construct (vector pHHU 431), but introduced into a WT background. Homozygous transgenic lines were identified by PCR genotyping (Figure 3.17) and YFP signal detection confirmed the PERTL6 expression.

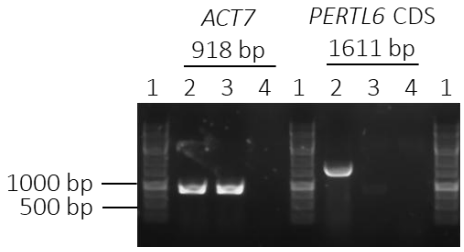

Figure 3.17 PCR results of genotyping the *PERTL6* overexpressor line (OEX)

PCR analysis of genomic DNA from homozygous PERTL6 OEX plants (lane 2), WT (lane 3) and water as negative control (lane 4). A 1 kb ladder (lane 1) was used for size comparison. Primers used for the PCR are listed in Table 2.9.

3.6.2. *cat2-1* and the *pertl6-1 x cat2-1* double mutant

Catalase is a key enzyme to scavenge hydrogen peroxide in peroxisomes. There are three isoforms of this enzyme described in *Arabidopsis thaliana*, with *CAT2* being the one mostly abundant in photosynthetic tissues. *CAT1* is expressed in pollen and seed and *CAT3* in vascular tissues and senescent leaves. Thus, to study its effect on physiology in *Arabidopsis*, the major isoform *CAT2* was chosen. The mutant lacking this isoform is known to accumulate hydrogen peroxide, especially under stress conditions, which makes it good candidate to study PERTL6 responses to oxidative stress. (Bueso et al., 2007; W. C. Liu et al., 2017; Mhamdi, Queval, et al., 2010; Su et al., 2018). Thus, the well characterized *cat2-1* catalase mutant (SALK_076998) with T-DNA insertion in the 4th exon of At4g35090 (Bueso et al., 2007), was used to generate the double mutant with *pertl6-1* line. Including *cat2-1* in the study helps to elucidate the function and interaction of PERTL6 by comparing the phenotypic responses. Additive phenotypes would suggest that the two genes act in parallel pathways, operating independently, but contributing to the same outcome. In contrast, lack of additional effect in the double mutant may indicate involvement in the same pathway, while stronger phenotype in double mutant may suggest cumulative effects indicating involvement in related or interacting pathways.

PCR genotyping confirmed the homozygosity of *cat2-1* T-DNA specific gel band (338 bp) and lack of gene specific WT band (1019 bp) (Figure 3.18).

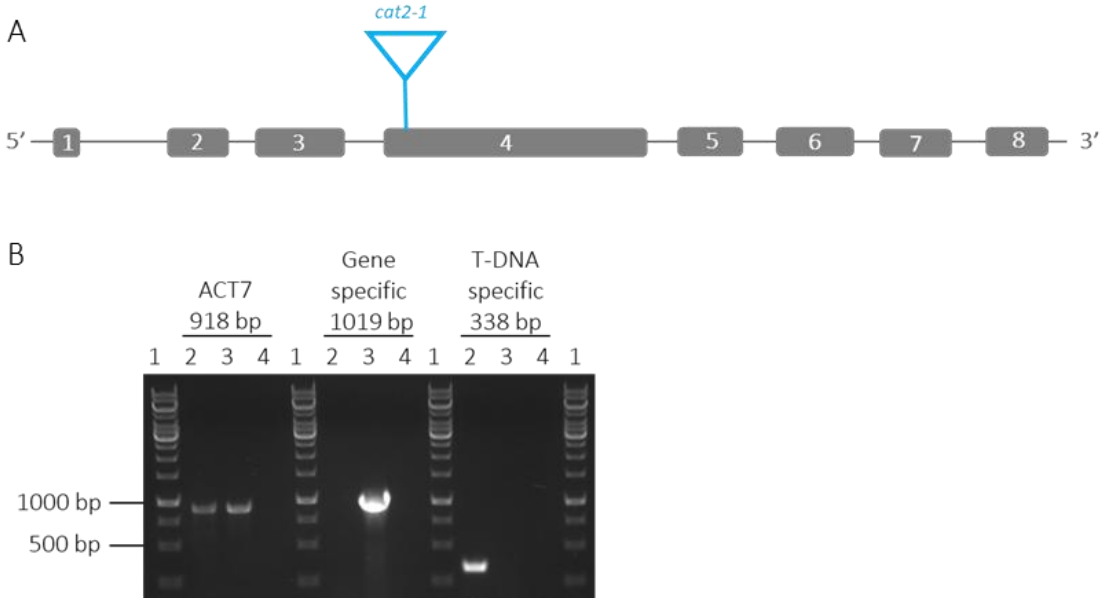

Figure 3.18 T-DNA insertion in *cat2-1* line and corresponding genotyping results

A. Schematic representation of a cat2-1 T-DNA tandem insertion in exon 4 of At4g35090. Exons are shown as numbered gray boxes, introns as gray lines, and T-DNA insertion is marked by a blue triangle. B. PCR analysis of genomic DNA from homozygous cat2-1 mutant plants (lane 2), WT (lane 3) and water as negative control (lane 4). A 1 kb ladder (lane 1) was used for size comparison. Primers used for the PCR are listed in Table 2.9.

The *pertl6-1 x cat2-1* double mutant line was generated by crossing homozygous *perlt6-1* and *cat2-1* plants. Second generation progeny were screened via PCR in order to select homozygous line (Figure 3.19).

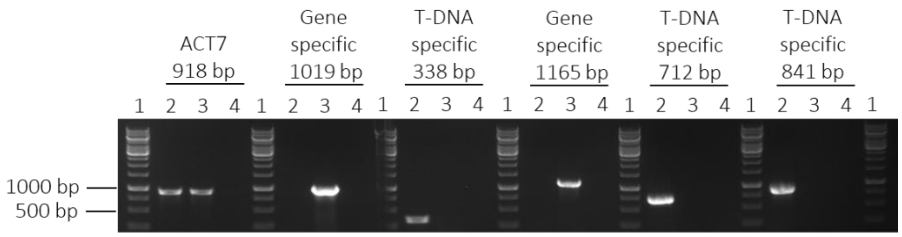

Figure 3.19 PCR results of genotyping the *pertl6-1 x cat2-1* double mutant line

PCR analysis of genomic DNA from second generation homozygous perlt6-1 x cat2-1 plants (lane 2), WT (lane 3) and water (lane 4). A 1 kb ladder (lane 1) was used for size comparison. Primers are listed in Table 2.9.

3.6.3. *gr1-1* and the *pertl6-1 x gr1-1* double mutant

Glutathione reductase is a key enzyme in ascorbate-glutathione cycle, which helps maintain cellular redox balance. This protein has two isoforms in *Arabidopsis*: *GR1* in peroxisomes, cytosol and nucleus, and a dual-targeted *GR2* in plastids and mitochondria. *Gr1* mutants exhibit increased accumulation of oxidized glutathione and enhances sensitivity to oxidative stress. To explore the potential role of PERTL6 in stress response via redox regulation, through a distinct mechanism than catalase, the *gr1-1* glutathione reductase mutant (SALK_105794), with a T-DNA insertion in the 4th intron of At3g24170 was used in this study (Marty et al., 2009a, 2019; Mhamdi, Hager, et al., 2010). The double mutant with *pertl6* may help to investigate whether the peroxisomal transporter contributes to the antioxidant capacity or stress tolerance. Homozygosity was confirmed via PCR, showing a T-DNA-specific band (676 bp) and absence of the gene-specific band (1224 bp) (Figure 3.20).

Figure 3.20 T-DNA insertion in *gr1-1* line and corresponding genotyping results

A. Schematic representation of a gr1-1 T-DNA tandem insertion in intron 4 of At3g24170. Exons are depicted as numbered gray boxes, introns as gray lines, and T-DNA insertion as a violet triangle. B. PCR analysis of genomic DNA isolated from homozygous gr1-1 mutant plants (lane 2), WT plants (lane 3) and water as negative control (lane 4). A 1 kb ladder (lane 1) was used for size comparison. Primers used for the PCR are listed in Table 2.9.

The *pertl6-1 x gr1-1* double mutant line was generated by crossing homozygous *pertl6-1* and *gr1-1* plants. PCR genotyping was used to confirm the genotype of the second-generation progeny (Figure 3.21).

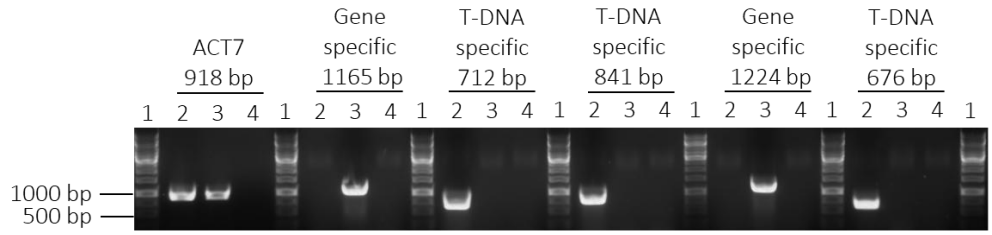

Figure 3.21 PCR results of genotyping the *pertl6-1 x gr1-1* double mutant line

PCR analysis of genomic DNA from second-generation homozygous *perlt6-1 x gr1-1* plants (lane 2), WT (lane 3) and water (lane 4). A 1 kb ladder (lane 1) was used for size comparison. Primers are listed in Table 2.9.

3.7. Phenotyping

To investigate the developmental and physiological consequences of PERTL6 mutation, phenotypic characterization of the available plant lines was performed. These analyzes, included assessment of autotrophic growth such as morphological assessment, response to photoperiod and carbon assimilation, as well as heterotrophic processes including storage oil utilization and germination efficiency. These experiments were first conducted without the application of abiotic stress to assess the effect of the mutation itself.

3.7.1. General phenotype – rosette size

Plants used in the phenotyping experiment were grown for 4 weeks under normal day (ND, 12 h light / 12 h dark) (Figure 3.22) and short day (SD, 8 h light / 16 h dark) (Figure 3.23) conditions (day temperature 22 °C, night temperature 20 °C, 410 ppm CO_2, 65% humidity) and rosette area was measured using ImageJ.

Under ND conditions both *pertl6* T-DNA insertion line and CRISPR/Cas9 line were expected to exhibit similar rosettes growth. The *pert6-1* line was significantly smaller than the *pertl6-6,* while the *pertl6-6* line rosette size was similar to WT. This result could be attributed to several factors, including the potential impact of T-DNA insertions on other genes or differences in expression levels, which may regulate the rosette growth differently. Double mutants of *pert6-1 x cat2-1* showed significantly inhibited grow compared to the single *pertl6-1* line, but not compared to *cat2-1*, suggesting epistatic effect. In another double mutant, *pertl6-1 x gr1-1*, the phenotype was not significantly different from either of the single mutants (*pertl6-1* or *gr1-1).* All of them show similar rosette area under the ND, suggesting that both genes may be involved in similar biological pathways regulating the development of rosettes

and the combination of them did not produce more severe phenotype than the single mutations (Figure 3.22).

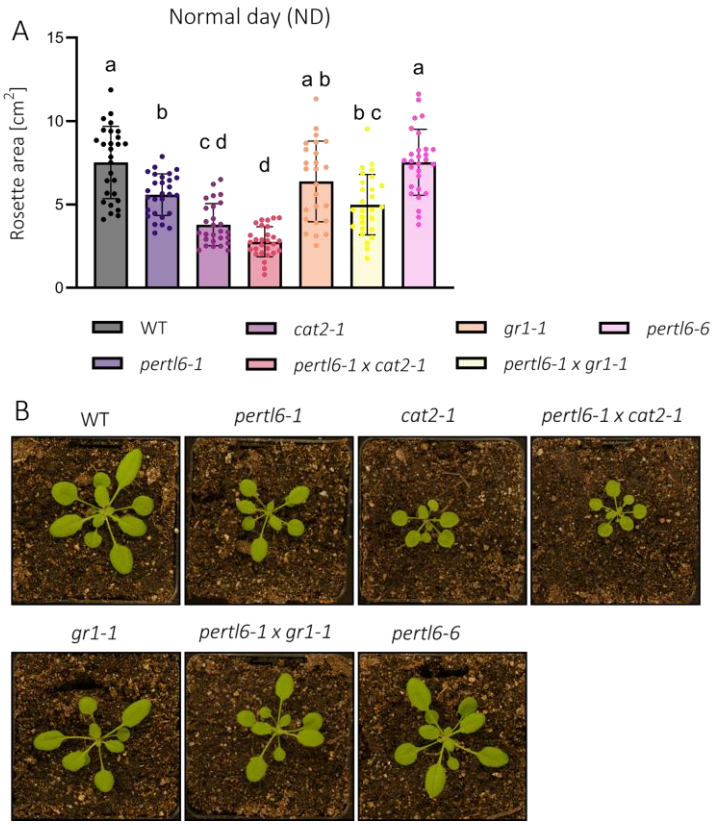

Figure 3.22 Rosette area measurements and phenotype in 4-week-old plants grown under normal day conditions

Rosette area was measured in 4-week-old plants grown under ND conditions (A) and the representative images of the *Arabidopsis* plants (B). Different genotypes are represented by colored bars as indicated in the legend. Values are presented as means ± SD (n = 25-28) with individual data points displayed (A). Bars labelled with same letter within each graph do not differ significantly from each other. Different letters indicate significant differences based on Tukey's multiple comparison test, following a one-way ANOVA ($p < 0.05$). Outliers were identified using the ROUT method (Q = 5%) and excluded from the statistical analysis.

Under SD conditions, all *pertl6-1, pertl6-6* and *pertl6-1 CL* show similar growth to WT, indicating no influence on development under this light regime and successful complementation of the *perlt6* gene in the mutant line *perlt6-1 CL*. However, the OEX line displayed significantly reduced rosette size, suggesting that overexpression of *PERTL6* leads to growth inhibition. It highlights the importance of gene expression level, with the optimal being crucial for proper plant development. The rosette size of *cat2-1* and *perlt6-1 x cat2-1* was not significantly different, as observed in the ND conditions, again suggesting that there

is no strong additive effect, and the reduced rosette size in the double mutant is primarily driven by CAT2 mutation (Figure 3.23).

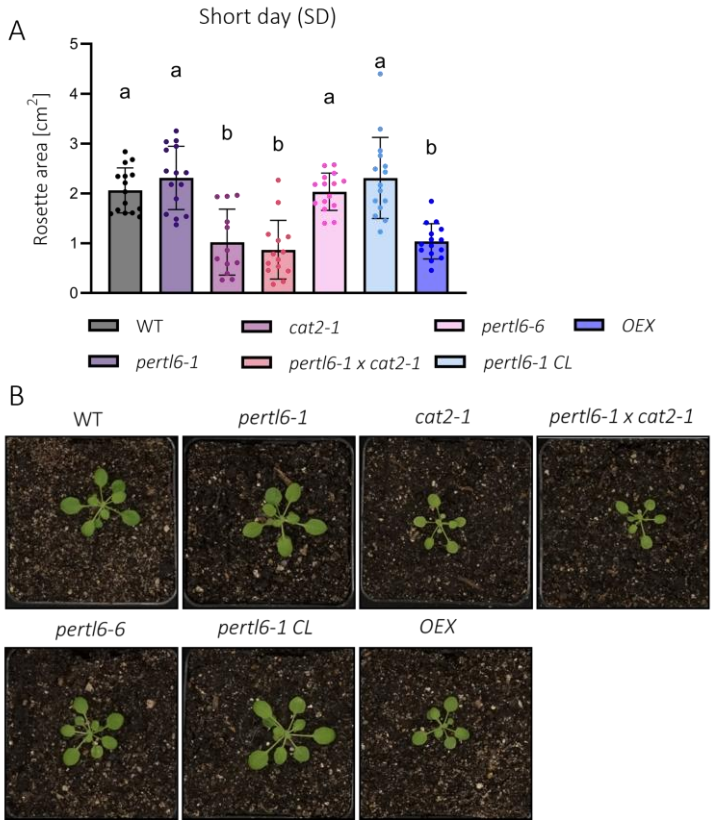

Figure 3.23 Rosette area measurements and phenotype in 4-week-old plants grown under short day conditions

Rosette area was measured in 4-week-old plants grown under SD conditions (A) and the representative images of the *Arabidopsis* plants (B). Different genotypes are represented by colored bars as indicated in the legend. Values are presented as means ± SD (n = 12-15) with individual data points displayed (A). Bars labelled with same letter within each graph do not differ significantly from each other. Different letters indicate significant differences based on Tukey's multiple comparison test, following a one-way ANOVA ($p < 0.05$). Outliers were identified using the ROUT method (Q = 5%) and excluded from the statistical analysis.

3.7.2. Photoperiod and sucrose influence

Building on previous results on 4-week-old plants (WT, *pertl6-1, cat2-1, pertl6-1 x cat2-1*) grown under different light regimes, which revealed differences in rosettes sizes, additional growth experiments focusing on younger developmental stages were conducted. *Arabidopsis* seedlings were grown on sterile minimal half-strength MS medium, with and without sucrose supplementation, under various photoperiods. These experiments aimed to evaluate how external carbon sources, like sucrose, impacts plant growth and photosynthesis under various light regimes in young one week old plants. It is well established that mutant plants with

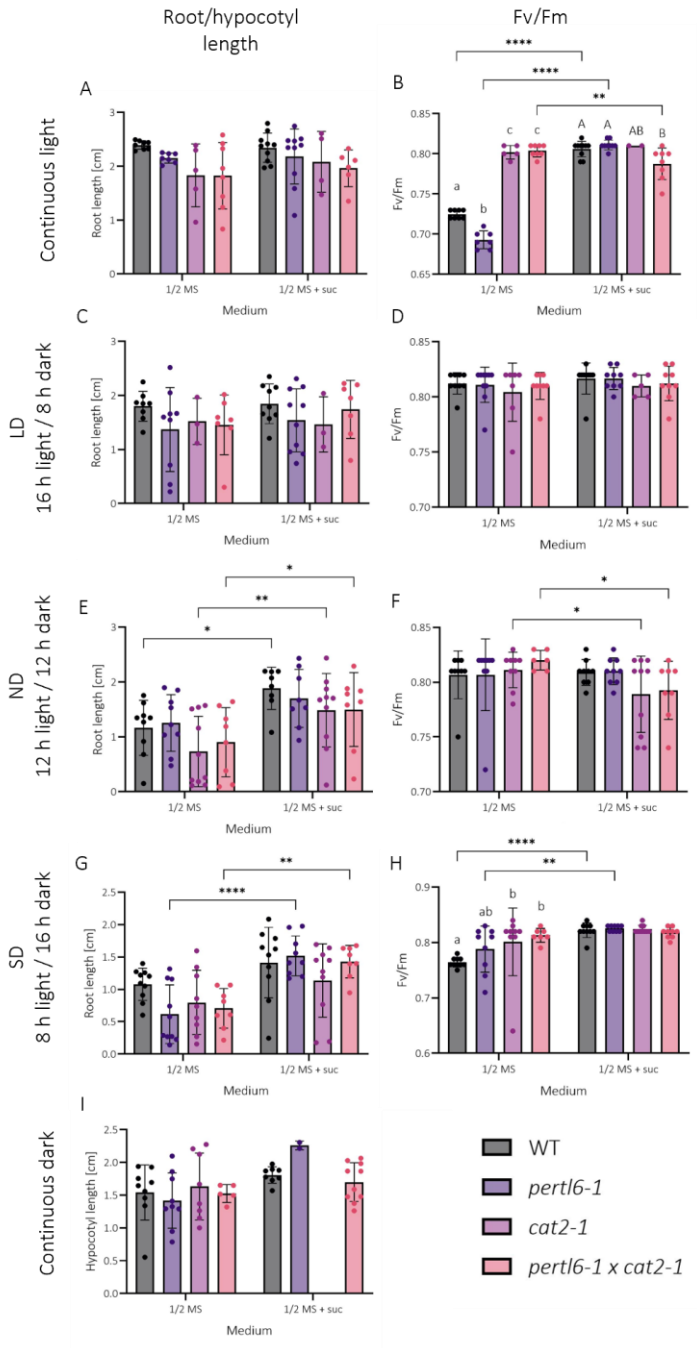

Figure 3.24 Photoperiod and sucrose influence on phenotype and photosynthetic efficiency

Root, hypocotyl length and Fv/Fm were measured in 1-week-old plants grown under various light conditions in media with or without sucrose. Different genotypes are represented by colored bars as indicated in the legend. Data is presented as means ± SD, with individual data points displayed ($n \leq 10$). Significant differences based on Sidak's multiple comparison test, following a two-way ANOVA are displayed as asterisks (* $p < 0.05$; ** $p < 0.01$; *** $p < 0.001$; **** $p < 0.0001$), comparing sucrose treatment between the same line, or by letters above the bars, indicating the differences between genotypes grown in the same medium. Statistical comparisons were made within each photoperiod and for all genotypes within one medium, as well as between the same genotype grown in different media.

impaired β-oxidation need external carbon source for proper seedling establishment, as they are unable to efficiently mobilize the lipids through fatty acids breakdown. This manifests by sucrose-dependent phenotype (Bernhardt et al., 2012; Graham, 2008a; Kelly et al., 2011; Quettier & Eastmond, 2009). Furthermore, since carbon availability and photosynthetic activity are linked to redox balance, these experiments may allow for assessment of how PERTL6 mutation influences the development under varying media and light conditions.

The photoperiod tested included the following light regimes: continuous light, LD, ND, SD, and continuous dark. Plants were grown for 7 days in either ½ MS or ½ MS + 1% sucrose media. Root (or hypocotyl) length was measured together with Fv/Fm, which assesses the photosynthetic efficiency of photosystem II (PSII). Statistical analysis was performed to compare the influence of added sucrose to media (marked with asterisks) and to compare the genotypes within one media type (marked with letters) (Figure 3.24).

Under continuous light conditions (Figure 3.24 A, B), no significant differences in root length were observed between the genotypes or the media. However, the Fv/Fm results showed that on ½ MS medium *perlt6-1* exhibited significantly the lowest PSII efficiency, which was restored to WT levels when grown on medium supplemented with sucrose. This indicates that *perlt6-1* is sugar-dependent, as sucrose supports its growth when photosynthesis is impaired. A similar increase in Fv/Fm was observed for WT plants, suggesting that continuous light photoperiod my limit photosynthetic capacity, which can be restored by addition of external carbon source. Lower than typical Fv/Fm values (between 0.79-0.84) of WT and *pertl6-1* line suggest these plants experienced higher stress level due to the constant lighting that specifically impacts photosystem II efficiency (Velez-Ramirez et al., 2011). In *cat2-1* and the *perlt6-1 x cat2-1* double mutant, the photosynthetic performance was not affected in ½ MS medium, but on ½ MS + sucrose medium the double mutant showed significantly lower Fv/Fm compared to ½ MS medium, possibly due to the photodamage of PSII. This higher Fv/Fm of *cat2-1* and *pertl6-1 x cat2-1* than WT might be possibly due to the elevated H_2O_2 level acting as signaling molecule inducing acclimation responses, thereby enhancing PSII stability. Under LD conditions (Figure 3.24 C, D), no significant differences in root length nor Fv/Fm were observed between plant lines or media. Under ND conditions (Figure 3.24 E, F), plant growth was unaffected across genotypes. However, the addition of sucrose significantly increased root length in all genotypes, except for the *pertl6-1* line, which showed no change. This suggests that *pertl6-1* responds differently to sucrose under ND light conditions. For photosynthetic efficiency, Fv/Fm remained unchanged for WT and *perlt6-1*

when sucrose was added, but *cat2-1* and *pertl6-1 x cat2-1* exhibited significantly lower Fv/Fm on media with sucrose. Under SD conditions (Figure 3.24 G, H), the root length of *pertl6-1* was extremely significantly increased on medium containing sucrose. A highly significant increase was also observed in *perlt6-1 x cat2-1*. No statistically significant difference was observed between *cat2-1* mutant grown in media without or with sucrose. Although the phenotype suggests that *perlt6-1* is responsible for observed changes, there were no significant differences in root length between the genotypes in either medium. Photosynthetic measurements showed that both WT and *perl6-1* lines performed better with sucrose, further indicating sugar-dependency. In contrast, in the medium without sucrose, *cat2-1* and *perlt6-1 x cat2-1* performed better than WT, suggesting that the light regime together with their mutations may induce stress responses that facilitate photosynthesis. Under continuous dark conditions (Figure 3.24 I), hypocotyl length was measured, but no significant differences between genotypes or media were observed.

3.7.3. Carbon assimilation

After switching from photoautotrophic growth (driven by storage oil mobilization) to autotrophic growth, plants rely on photosynthesis. Gas exchange measures can therefore determine whether PERTL6-lacking mutants differ in their capacity for CO_2 assimilation. Knowing the key biochemical parameters like V_{cmax} (the maximum carboxylation rate of Rubisco), J_{max} (the maximum rate of electron transport for the given light intensity, representing RuBP regeneration) and *TPU* (the maximum rate of triose phosphate utilization) provide insights into the photosynthetic efficiency and potential limitations in the mutant lines (Sharkey, 1985, 2016). A/C_i response curves were measured using LI-COR gas exchange system on 9-week-old plants (WT, *pertl6-1, cat2-1, pertl6-1 x cat2-1*, and *pertl6-6*) grown under SD conditions and the parameters were derived by fitting the data to a model using Shiny app (Figure 3.25)(Gregory et al., 2021).

The results showed that all genotypes exhibit WT-like values for V_{cmax}, J_{max}, and TPU indicating no significant differences in rubisco carboxylation rate, electron transport, or downstream triose phosphate metabolism. Only the *cat2-1* mutant displayed significantly lower V_{cmax} and J_{max} values, compared to *pertl6-6*, suggesting impaired CO_2 fixation and electron transport capacity, potentially due to the increased oxidative stress sensitivity (Figure 3.26).

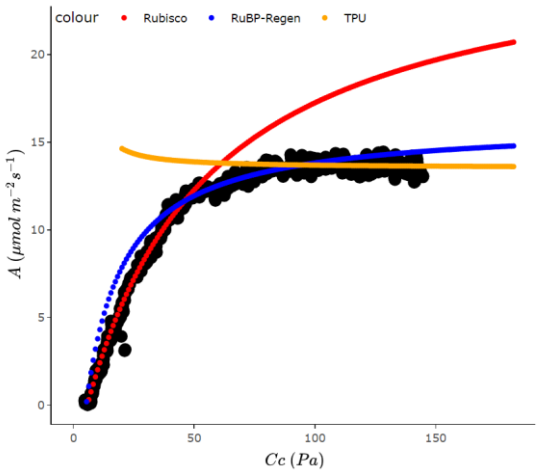

Figure 3.25 *A/Ci* curve fitting using R-based fitting tool

Representative example of A/Ci curve fitting generated using R script with a user-friendly interface Shiny app interface. The fitted curves correspond to different photosynthetic limitation phases: red indicates rubisco-limited, blue the RuBP regeneration–limited, and gold represents TPU-limited conditions.

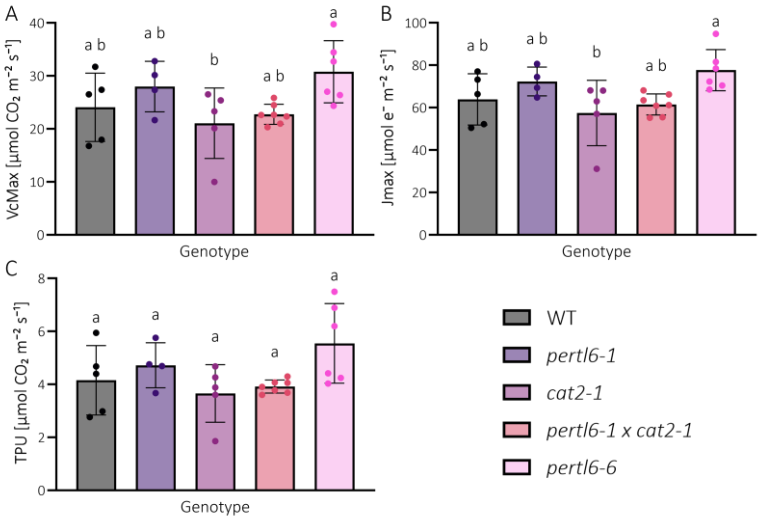

Figure 3.26 Gas exchange parameters

Plants were grown under SD light condition for 9 weeks and the gas exchange measurements were taken. Fitted A/Ci curves and the derived parameters are presented as bar graphs. Different genotypes are represented by colored bars as indicated in the legend. Data is presented as means ± SD, with individual data points displayed (n = 4-7). Statistical significance was determined using Tukey's multiple comparison test, following a one-way ANOVA and is marked by different letters above the bars, indicating the differences between genotypes (* $p < 0.05$).

3.7.4. Seedling development and storage oil mobilization

Plant lines with disturbed fatty acid β-oxidation cannot efficiently convert stored oil into sugars and exhibit sucrose-dependent phenotypes, as they need exogenous carbon supply for seedling establishment. Peroxisomal β-oxidation is, however, coupled to the redox state, as during this process H_2O_2 is produced by acyl-CoA oxidase and must be detoxified (Bussell et al., 2013; Eastmond, 2007; Graham, 2008b; Quettier & Eastmond, 2009). Therefore, disrupted peroxisomal redox homeostasis or defective transportation of redox equivalents can reduce β-oxidation efficiency and limit carbon supply during early seedling development. Consequently, seedlings may need an external carbon source like sucrose to support grow (Graham, 2008). Therefore, investigating the differences in seedling growth under varying carbon supply allow may indicate altered storage oil mobilization.

Seeds were sown on ½ MS media with or without sucrose, and root length was measured on the 4th, 5 th, 6 th and 7 th day after sowing (DAS).

Under SD conditions (Figure 3.27 A, B), the growth curves across the 4-day period of measurements showed linear growth in root length for all genotypes, with no significant differences in growth rates. However, analysis of the absolute root length at individual time points revealed a significant influence of sucrose supplementation for *pertl6-1,* which was the only genotype to exhibit significantly longer roots on sucrose-containing media compared to media without sucrose. This sucrose-induced growth enhancement was not observed in WT, *cat2-1* or *pertl6-1 x cat2-1*, suggesting that *pertl6-1* exhibited enhanced sensitivity to exogenous sucrose that might be linked to impairment in β-oxidation. Notably, on day 5th *perlt6-1 x cat2-1* seedlings grown on ½ MS media exhibited significantly shorter roots than WT, however, this difference was transient and was not present at other time points or in sucrose-containing medium. Aside from these observations, there were no other significant differences in root length between genotypes grown on the same medium at any time point.

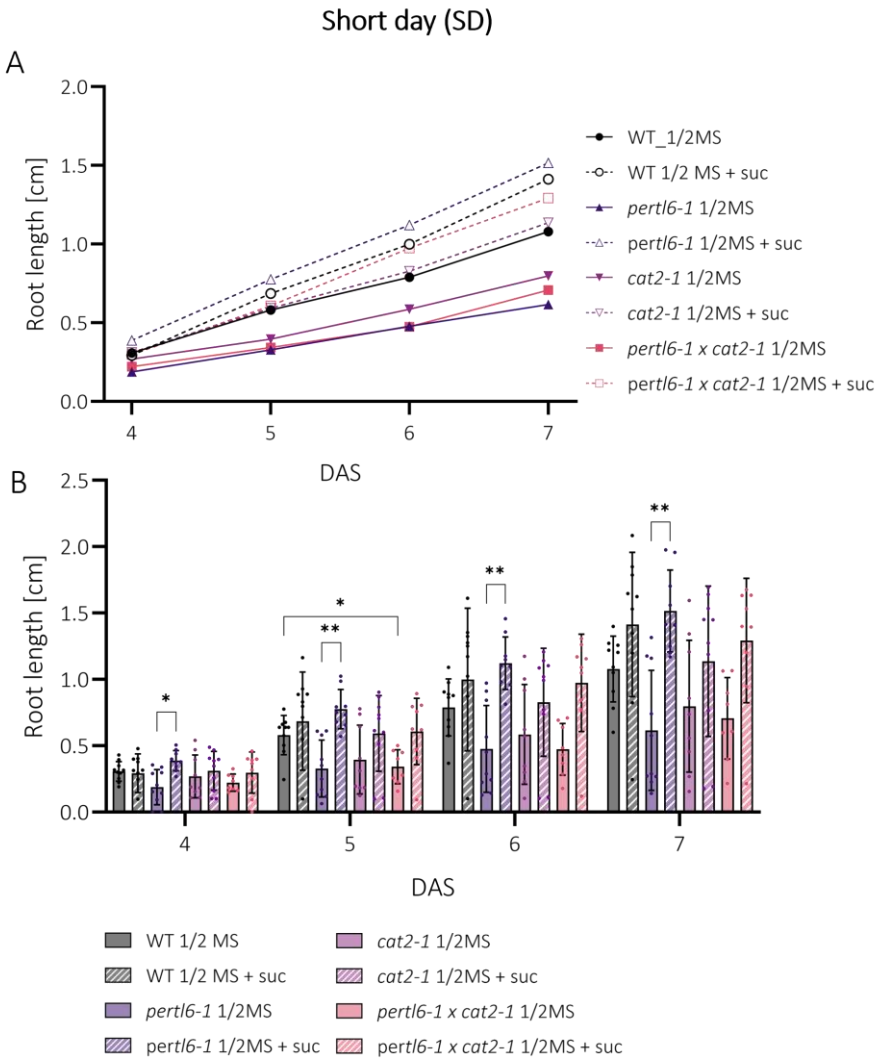

Figure 3.27 Root growth variation as growth curves and absolute length measurements across four days of early seedling development

Seedlings were grown under either SD light condition (A, B) on media with or without sucrose. Root length was measured on the 4th, 5th, 6th and 7th DAS. Different genotypes are represented by colored lines/bars as indicated in the legend, with dotted/hatched lines/bars representing media with sucrose. Data in the growth curves (A) is presented as means; bar chart show means ± SD, with individual data points displayed (n = 8-10). Statistical significance was determined using Tukey's multiple comparison test, following a two-way ANOVA. Asterisks indicate significant differences (* $p < 0.05$; ** $p < 0.01$), comparing sucrose treatment withing the same genotype or differences between genotypes grown on the same medium at the same DAS.

3.7.5. Seed germination assay

Peroxisomes are important organelles for seed germination, as fatty acid β-oxidation, which occurs in them, breaks down lipids stored in seeds to provide carbon and energy necessary for seedlings establishment before the photosynthetic tissues develop and photosynthesis

begins. Additionally, during β-oxidation peroxisomes help regulate redox balance, which can become disturbed (Bussell et al., 2013; J. Li et al., 2022). If PERTL6 is involved in maintaining redox homeostasis, studying germination can shed a light on its function. Delayed or impaired seed germination may indicate impaired β-oxidation or redox regulation, possibly caused by defective substrate transport through the peroxisomal membrane. Therefore, to complement seedling development measurements taken from 4 to 7 DAS, the germination assay (1-4 DAS) was used to assess seed viability during the very early developmental phase.

Seedlings were grown on ½ MS medium under ND conditions, and the stage of radical emergence was assessed every 24 hours for 4 consecutive days. Different germination developmental stages are depicted on Figure 3.28 A. Four different genotypes were assessed: *WT, pertl6-1, cat2-1* and *pertl6-1 x cat2-1* (Figure 3.28).

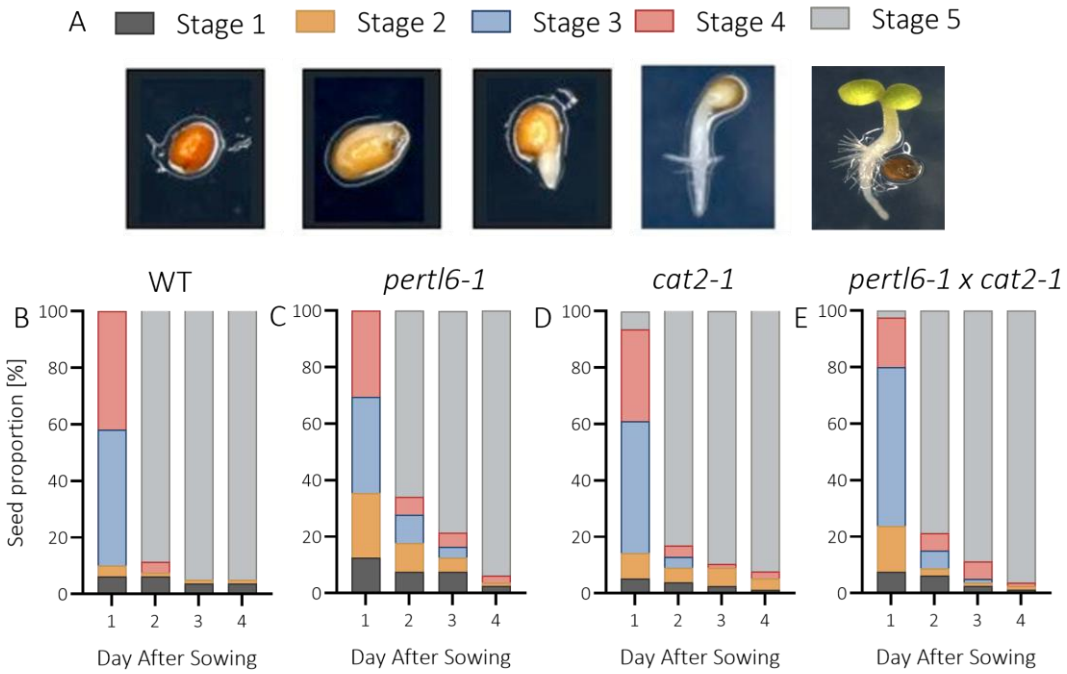

Figure 3.28 Germination assay

Seedlings were grown under ND light conditions on ½ MS media. The developmental stages were assessed every 24 hours for four days based on pictures (A) and are represented as the percentage of total seed proportions depicted as colored bars (n = 77-80).

On 1 DAS, in WT, 6% were in Stage 1, 4% in Stage 2, 48% in Stage 3, and 42% in Stage 4, with the majority still in early stages. On DAS 2, 89 % of WT seeds had already reached the last Stage 5, indicating full radical emergence. On DAS 3 and DAS 4, 95% of all WT seeds

were in Stage 5, completing the germination process (Figure 3.28 B). In *perlt6-1* however, on 1 DAS, 13% of seeds were in Stage 1, 23 % in Stage 2, 34 % in Stage 3 and 30% in Stage 4, showing a delay in radical emergence compared to WT. On DAS 2, only 66% of all seeds reached the last Stage 5, and by DAS 3, this proportion increased to 78%. On DAS 4, 94% of seeds were in Stage 5, nearly reaching the WT-like level, indicating *pertl6-1* mutant has a delayed germination phenotype in the early steps, possibly related to metabolic regulation. (Figure 3.28 C). In *cat2-1* mutant, on 1 DAS, 5% of total seeds were in Stage 1, 9% in Stage 2, 47% in Stage 3, 32% in Stage 4, and 6% in Stage 5, showing a similar pattern to WT. On DAS 2, 83 % of total *cat2-1* seeds were already in Stage 5, indicating a faster germination rate than *pertl6-1* but slower than WT. On DAS, 3 90% of seeds reached Stage 5, and by DAS 4, 92% were in Stage 5. These results indicate that *cat2-1* exhibit a moderate germination rate, slightly slower than WT, possibly due to the altered antioxidative activity and metabolic processes affecting germination speed, in which *CAT2* might be involved (Figure 3.28 D). In the *pertl6-1 x cat2-1* double mutant, on DAS 1, the proportions were as follows: 8% in Stage 1, 16% in Stage 2, 56% in Stage 3, 18% in Stage 4 and 3% in Stage 5, showing a slower start than either of the single mutants. By DAS 2, 79% of the seeds had reached Stage 5, 89%, and by DAS 3, 96% were in Stage 5, with 96% reaching Stage 5 by DAS 4, showing that *pertl6-1 x cat2-1* exhibits an additive phenotype with a delayed start, but ultimately shows no difference in the final germination rate by DAS 4 compared to the single mutants or WT (Figure 3.28 E).

3.8. Abiotic stress response

Considering the previous *in silico* results on the promoter region or co-expressed gene network, as well as the available data of PERTL6 response to abiotic stress, a series of experiments were conducted to investigate its potential role in stress adaptation. Tested conditions included temperature, salt, photorespiratory, dark, and oxidative stress, resemble challenges plants encounter in their natural environment. Different plant lines were assessed at multiple levels: phenotypic (root length rosette size), molecular (transcript level), physiological (photosynthetic efficiency, germination), and biochemical (metabolites). Together, these experiments allow for a comprehensive evaluation of PERTL6 role to plant acclimation and sensitivity under abiotic stress.

3.8.1. Temperature stress

To investigate PERTL6 response to temperature, plants were subjected to heat stress (HS, short-term temperature stress) and prolonged warming (PW, long-term temperature stress) conditions. These treatments are different in terms of temperature and duration, allowing for short and longer-term response with or without acclimation.

3.8.1.1. Heat stress

PERTL6 expression under heat stress

To quantify *PERTL6* upregulation upon heat stress, plants were exposed to a 40 °C heat shock (HS) for four hours, and the transcript levels were measured. This experiment aimed to determine whether *perlt6* is indeed directly regulated by elevated temperature and potentially involved in heat stress response. Additionally, the expression levels of the master regulator heat shock transcription factor a 1a *(HSFA1A)* (Mishra et al., 2002), and another abiotic stress responsive heat shock protein 90 (*HSP90)* (Song et al., 2009), were analyzed as markers of heat stress activation. The expression was normalized to the reference gene At5g60390 (GTP binding elongation factor T4 family protein) and monitored through time: before heat treatment (control), immediately after the 4 h of heat stress (0 h recovery) and post-heat recovery (4 h HS + 1 h, + 2 h, + 4 h). Relative transcript abundance was normalized to the control levels (set to 1) (Figure 3.29).

Expression level of *PERTL6* increased by approximately 30 % immediately after the heat shock and reached a statistically significantly higher 40 % increase after 1 h of recovery. Expression continued to rise, reaching 50 % increase over control levels by the 4 h of recovery phase. This upregulation of *PERTL6* upon heat stress indicates rather later adaptation to heat stress (Figure 3.29 A). In contrast, *HSFA1A* expression level dropped down by approx. 70 % immediately following heat shock and gradually returned to the control levels by the 4 h recovery (Figure 3.29 B). This shows very quick response of *HSFA1A* to heat stress, indicating its activation of expression of other heat shock proteins like *HSP90*, which shows strong upregulation after 4 h of heat stress, with approx. 11-fold higher levels than control. These results comply with previously described models as *HSFA1A* under heat stress is activated and induces strong expression of other genes, like *HSP90* (Yoshida et al., 2011a). Elevated expression was maintained during the whole recovery phase, suggesting *HSP90* responded to heat stress (Figure 3.29 C).

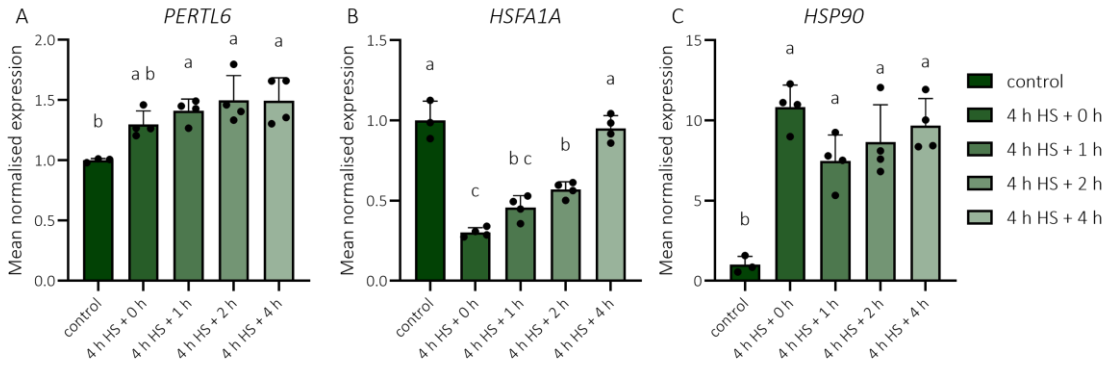

Figure 3.29 Expression levels of *PERTL6, HSFA1A* and *HSP90* in WT under heat stress

Mean normalized expression (MNE) levels of *PERTL6* (At1g74240) (A), *HSFA1A* (At4g17750) (B), *HSP90* (At4g24190) (C) in 2 week-old WT plants grown under ND conditions and exposed to 40 °C heat stress for 4 hours. Samples were collected at five time points: before the HS (control), immediately after the 4 h HS, 1 h, 2 h and 4 h after the HS. Expression values were normalized to the reference gene At5g60390 (GTP binding elongation factor T4 family protein). Bars represent the means of four biological replicates ± SD (control MNE was normalized to 1). Statistical significance was determined using Tukey's multiple comparison test, following a one-way ANOVA and is marked by different letters above the bars, indicating the differences between measuring time points ($p < 0.05$).

Photosynthetic efficiency of PSII under heat stress

As the previous experiment confirmed the *PERTL6* upregulation upon heat stress, further experiments were conducted to compare the stress response of the *pertl6-1* mutant to that of the WT. Here, PSII efficiency was measured in plants exposed to heat stress. Five-day-old WT and *pertl6-1* seedlings were subjected to 1-hour heat stress at 40 °C, and Fv/Fm was assessed at four time points: before the treatment (control), immediately after heat stress (0 h recovery), and after 1 h, and 4 h of recovery.

Before the treatment, both genotypes exhibited similar PSII efficiencies (Figure 3.30 A). However, immediately after 1 hour of HS, Fv/Fm values decreased in both plant lines, with a significantly lower decrease in *pertl6-1* compared to WT (Figure 3.30 B). In contrast, after 1 h of recovery, the Fv/Fm of *pertl6-1* increased from 0.58 to 0.65 and was significantly higher than that of WT at this time point (Figure 3.30 C). By 4 h of recovery, both genotypes reached similar Fv/Fm values, although still lower than at the initial pre-stress levels (0.71 before stress vs 0.65 after the 4 h of recovery) indicating incomplete recovery (Figure 3.30 D, E). These results indicate that *pertl6-1* shows an altered response to heat stress, with a lower initial drop, a fast rebound and then reaching equilibrium as WT. This supports the

hypothesis that PERTL6 plays an important role in heat stress response that reflects in photosynthetic performance.

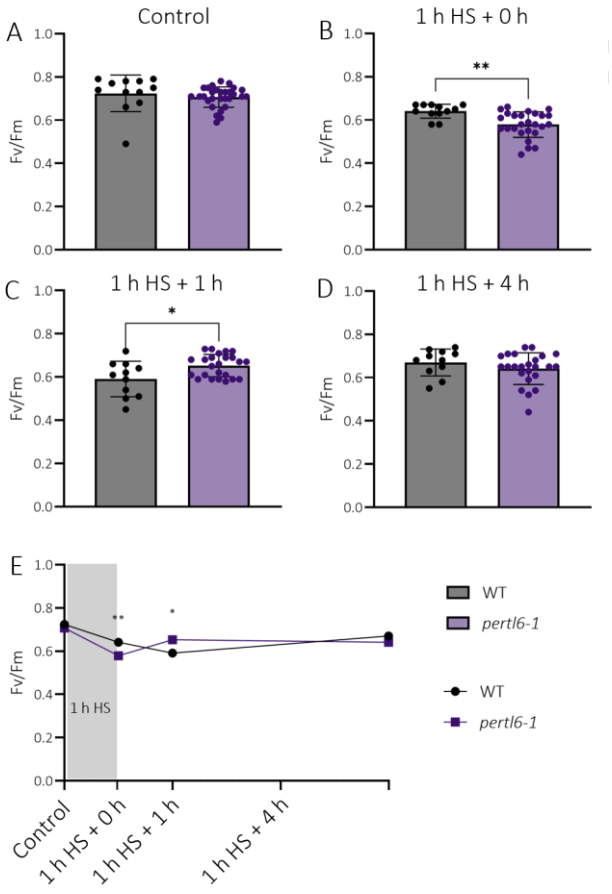

Figure 3.30 Photosynthetic efficiency (Fv/Fm) in response to heat stress in WT and *pertl6-1* seedlings

Five-day-old WT and *pertl6-1* seedlings were subjected to a 1-hour heat stress at 40 °C, and the maximum efficiency of photosystem II (Fv/Fm) was assessed at four time points: before the treatment (control), immediately after heat stress (0 h recovery), and after 1 h, and 4 h of recovery. Different genotypes are represented by colored bars or lines as indicated in the legend. Data is presented as means ± SD, with individual data points displayed (n = 11-24) in bar plots (A-D), and as connected means values over time in the line graph (E). The gray shaded area in panel E indicates 1 h heat stress period. Significant differences between genotypes were determined using a two-tailed unpaired t-test and are displayed as asterisks (* $p < 0.05$; ** $p < 0.01$).

Heat stress and its influence on phenotype and metabolism

To further investigate *PERTL6* response to heat, phenotypic response and metabolic profiles were assessed. While transcriptomic and photosynthetic measurements indicated upregulation of *PERLT6* and alteration in PSII efficiency, the downstream processes affecting metabolism remained unclear. Therefore, phenotypic observations were carried out

as a preliminary confirmation of heat stress activation pathway, followed by metabolite sampling for GCMS and LCMS analysis.

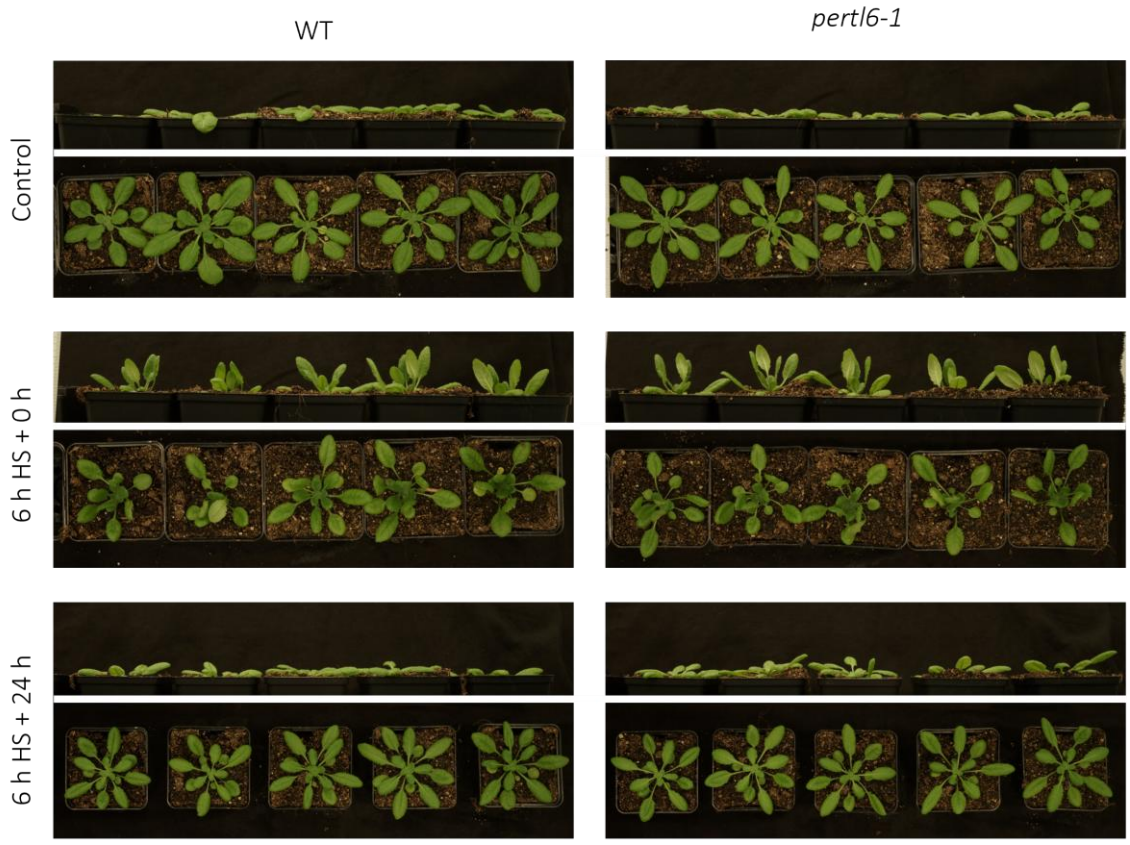

Figure 3.31 Heat shock phenotype in 5-week-old plants

Representative images of 5-week-old plants (WT and pertl6-1) before heat treatment (control panel), immediately after 6 hours of heat shock (40 °C) treatment (6 h HS + 0 h), and after one day of recovery (6 h HS + 24 h). Side and top views are presented to visualize leaves movement upon heat.

Plants of various genotypes (WT, *pertl6-1, pertl6-6*) were grown under ND conditions for approx. 5 weeks before being subjected to a 6-hour heat treatment at 40 °C. Phenotypic observations and metabolic sampling were conducted on control (not treated) and treated plants, immediately after the heat shock (6 h HS + 0 h) and 24 hours of recovery (6 h HS + 24 h).

Phenotypic observations revealed that all the genotypes bent their rosette leaves upwards in response to heat stress. This nastic movement, called hyponastic response, is a typical avoidance strategy of *Arabidopsis* to cope with stress (van Zanten et al., 2009). After 24 h of recovery, most plants returned their leaves to a downward position, however, in some genotypes, including *pertl6-1*, full recovery of leaf orientation was not observed. This suggests

a possible delay in recovery kinetics compared to WT, potentially reflected in metabolic level (Figure 3.31).

Metabolite profiling is presented as log_2 fold changes (log_2FC) calculated by normalizing the mean values (n = 5) of heat stressed samples to their corresponding mock-treated controls at two time points: after the heat shock (6 h + 0 h; panels A, B), and after 24 hours of recovery (6 h HS + 24 h; panels C and D) (Figure 3.32).

Heat stress led to widespread changes in metabolites level across all genotypes (WT, *pertl6-1* and *pertl6-6*), with a general trend toward increased accumulation. After 6 hours of heat shock, several amino acids were elevated in all the genotypes, particularly in *perlt6-6* line, which showed increased levels of proline, arginine, aspartate, and glycine. Accumulation of amino acids, especially proline, may suggest enhanced stress mitigation in *pertl6-6* line. While ornithine levels remained slightly decreased but similar in all lines, citrulline showed the strongest reduction in WT, suggesting disruption in nitrogen metabolism in mutants. All genotypes exhibited strong accumulation of raffinose, a sugar known for its protective role during abiotic stress. Among organic acids, most showed decrease upon heat stress, with citrate + isocitrate displaying a pronounced reduction in *pertl6-1* line indicating impairment in TCA cycle. All lines showed low levels of glycerate. Additionally, *pertl6-6* line exhibited higher levels of ethanolamine and DMPA compared to WT or *pertl6-1,* which may indicate altered lipids turnover in *pertl6* mutants (Figure 3.32 A, B).

After 24 hours of recovery following heat stress, some metabolites returned to control (mock) levels, while many remained altered, indicating sustained metabolic shifts. Among amino acids, *pertl6-1* and *pertl6-6* exhibited higher levels of arginine, lysine, valine, leucine, phenylalanine, and tyrosine compared to WT, whereas methionine remained elevated only in WT. The most pronounced increases were observed in glycine and alanine in both mutants compared to WT. Ornithine level was notably reduced in *pertl6-1* line, while WT and *pertl6-6* showed similar levels. A comparable pattern was also observed for citrulline contrasting with the acute response (6 h HS + 0 h) where citrulline decreased more strongly than ornithine. This may indicate different alteration in urea cycle after recovery. LL-2,6-diaminopimelic acid accumulated only *pertl6-1* line, while L-2-aminoadipic acid and pipecolic acid were reduced in both mutants compared to WT. Putrescine slightly increased only in *pertl6-1* line, while GABA decreased in both WT and *pertl6-1,* but increased in *pertl6-6*. These results indicate different GABA and polyamines responses in mutants. Raffinose levels remained strongly elevated in *perlt6-6* line, which also showed higher levels of other sugars compared to the

other lines. Within the TCA cycle, citrate + isocitrate were again most strongly reduced in *perlt6-1* line. WT showed mild reductions or unchanged levels of TCA cycle metabolites and organic acids, while *pertl6-1* showed reduction, whereas *pertl6-6* levels increased, indicating alteration in energy metabolism. Ethanolamine levels were highly reduced in *pertl6-6* line, moderately reduced in *perlt6-1*, and remained unchanged in WT relative to the mock-treated controls. DMPA levels remained stable in *pertl6-6*, while both *pertl6-1* and WT showed reductions.

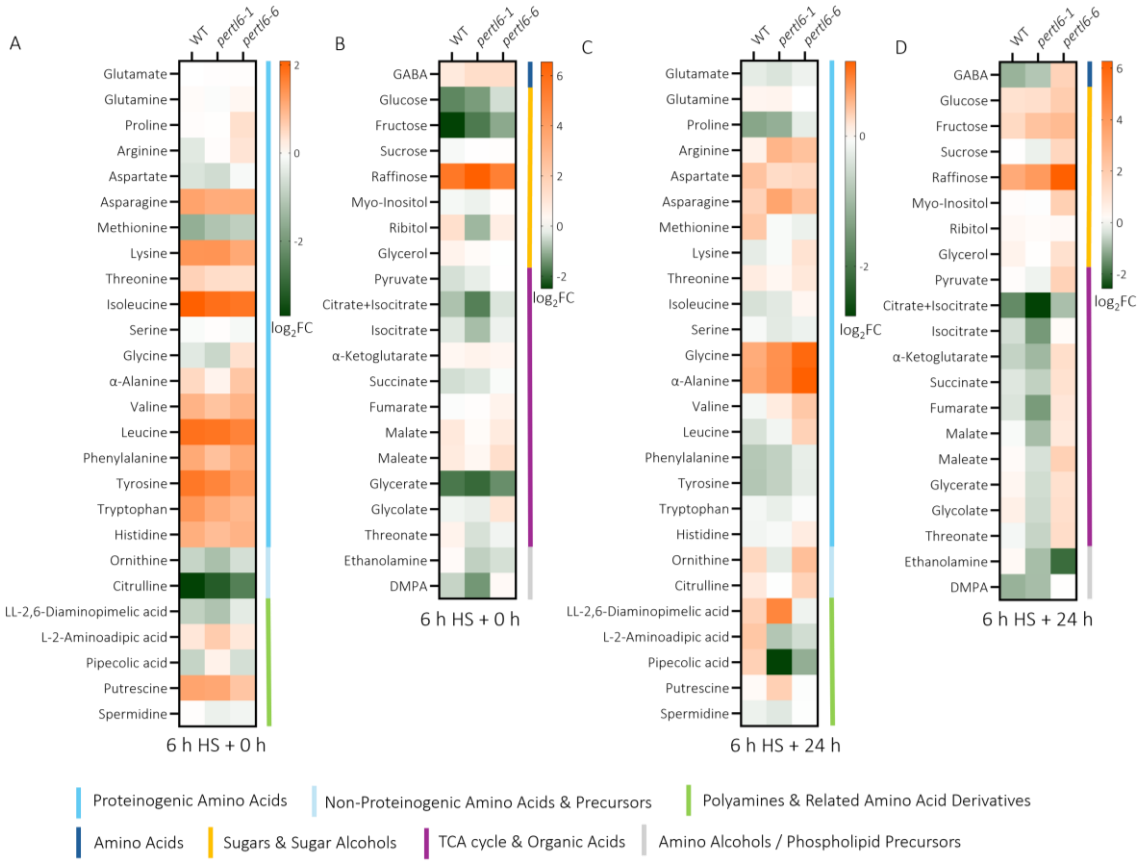

Figure 3.32 Metabolic profiling of plants exposed to heat stress

Metabolic profiles of plants subjected to a 6-hour heat stress at 40 °C presented as heat maps. Panel A and B show metabolite changes immediately after the heat shock (6 h + 0 h), while panels C and D represent changes after 24 hours of recovery (6 h HS + 24 h). Relative metabolite levels were determined using LCMS (A, C) and GCMS (B, D). The log_2 fold changes (log_2FC) were calculated by normalizing the mean values (n=5) of heat stressed samples to their corresponding mock-treated controls at each time point. Orange boxes indicate metabolites that accumulated in response to heat, while green boxes reflect reductions compared to controls. For easier interpretation, metabolites were grouped into functional classes (e.g. amino acids, organic acids, sugars), marked by colored bars to the right of each metabolite name, with the legend at the bottom of the figure.

3.8.1.2. Prolonged warming

In another experiment, moderately elevated temperature influence was assessed rather than acute stress. In prolonged warming experiment, 6 °C higher temperature was applied to plants during the day and night (28 °C/26 °C) for period of seven days. Studying this allows to investigate sustaining stress effects and recovery dynamics or adaptation to thermal resilience, essential for understanding plant performance under climate change.

Photosynthetic and metabolic changes in plants exposed to prolonged warming

Plants of various genotypes (WT, *pertl6-1, cat2-1, pertl6-1 × cat2-1, gr1-1, pertl6-1 × gr1-1, pertl6-6*) were grown under ND conditions for approx. 5 weeks before being subjected to a 7-day long warming treatment at elevated temperature of 6 °C both day and night. Physiological state of the plants was assessed, and metabolic sampling were conducted on control (not treated) and treated plants, on the seventh day of prolonged warming.

Portable LI-600 was used to measure parameters presented on Figure 3.33: A Stomatal conductance (g_{sw}), B Transpiration rate (E), C Leaf vapor pressure deficit (VPD), D Actual Photosynthetic efficiency (ΦPSII), E Electron transport rate (ETR), and F Intrinsic Water use efficiency (iWUE) was calculated by dividing ΦPSII/ g_{sw}. Knowing these parameters give insights into the CO_2 uptake, water loss and photosynthetic capacity.

Under control conditions, the *pertl6-1 × cat2-1* exhibited the highest stomatal conductance, suggesting enhanced gas exchange capacity. The single *cat2-1* mutant showed moderate g_{sw}, while all other genotypes including *pertl6-1, pert6-6, gr1-1,* and *pertl6-1 × gr1-1* have WT-like values. Under prolonged warming (PW) conditions, all genotypes have significantly lower stomatal conductance than under control, indicating strong response in stomatal closure, likely aimed to limit water loss. Moreover, under PW conditions, even *pertl6-1 × cat2-1* and *cat2-1* drop to the similar level as other genotypes, suggesting that the temperature stress response dominates over genotype-specific differences (Figure 3.33 A). Transpiration rate under control conditions mirrors the patterns observed in stomatal conductance, with *pertl6-1* and *cat2-1* showing the most elevated water loss consistent with highest gas exchange capacity. Moderate transpiration rates were observed in *pertl6-1, gr1-1*, and *pertl6-6*, while *pertl6-1 × gr1-1* and WT showed the lowest transpiration rate under non-stressful conditions. Under PW, similarly, like in stomatal conductance, drop in transpiration rate was observed across all genotypes, suggesting protective mechanisms in response to elevated temperature to limit to water loss (Figure 3.33 B). Leaf vapor pressure deficit (VPD) indicates the

evaporation demand from the leaf to the air. Under control conditions VPD all genotypes showed similar VPD values, indicating stable environmental conditions for all to minimize water evaporation.

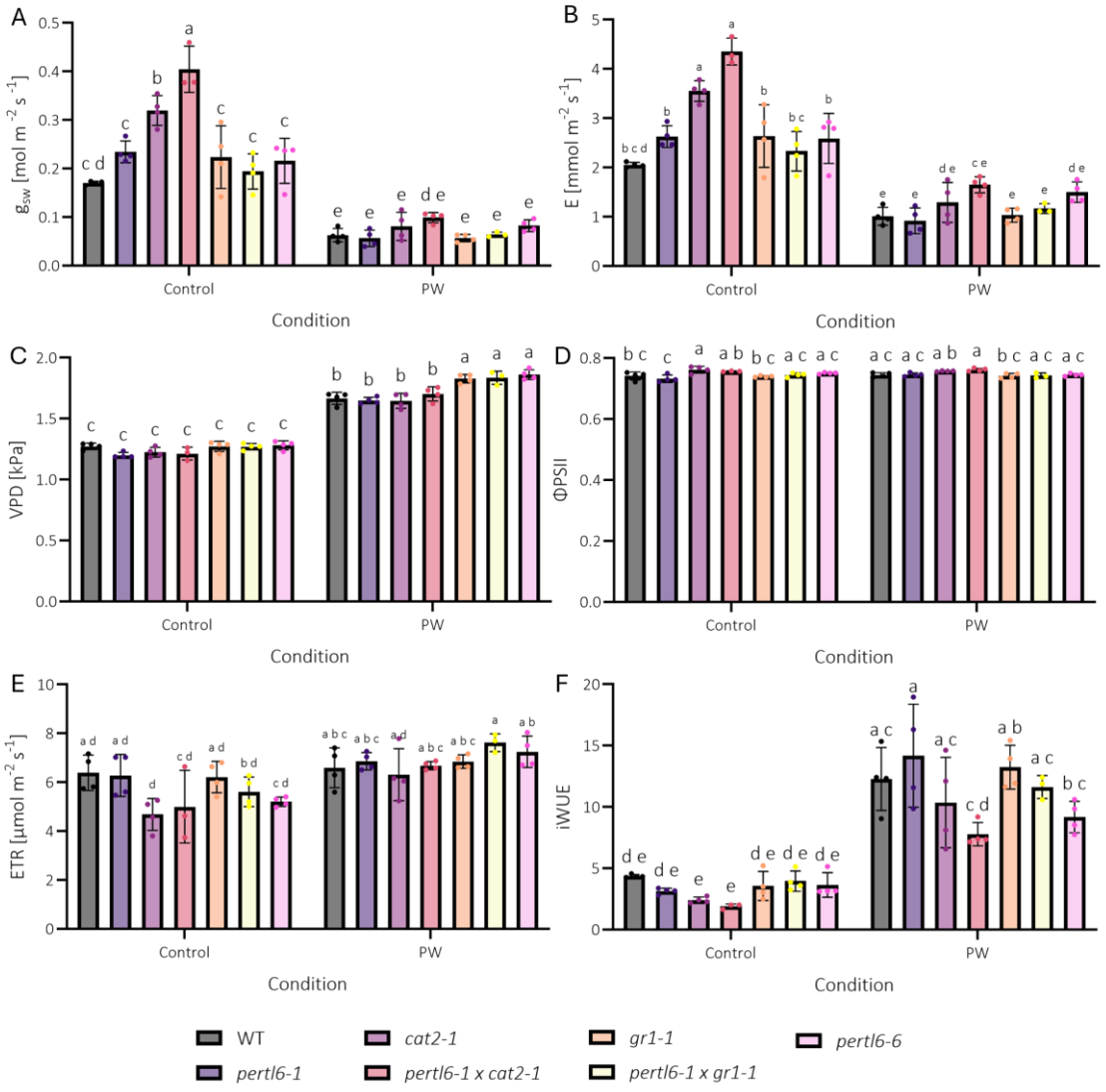

Figure 3.33 Physiological characteristics of plants under prolonged warming

Five-week-old plants were subjected to a 7-day warming treatment (6 °C above ND conditions), after that A Stomatal conductance (gsw), B Transpiration rate (E), C Leaf vapor pressure deficit (VPD), D Actual Photosynthetic efficiency (ΦPSII), E Electron transport rate (ETR) were measured using Li-COR 600. F Intrinsic Water use efficiency (iWUE) was calculated ΦPSII/ g_{sw}. (control) in not-treated plants(control) and those experiencing prolonged warming (PW). Different genotypes are represented by colored bars as indicated in the legend. Data is presented as means ± SD, with individual data points displayed (n = 3-4) in bar plots. Significant differences between genotypes were determined using a two-way ANOVA followed by Tukey's multiple comparison test, and is marked by different letters above the bars, indicating the differences between genotypes $p < 0.05$).

However, under PW conditions, VPD significantly increased in all genotypes, with *gr1-1, pertl6-1 x gr1-1,* and *perlt6-6* having the highest values, indicating stronger transpiration demand in these genotypes in response to PW stress (Figure 3.33 C). Actual photosynthetic efficiency (ΦPSII) informs about the actual effectiveness of PSII measured under actual light-acclimated conditions, without dark adaptation. Under control conditions, all lines exhibited similar ΦPSII values, with *cat2-1* showing slightly elevated efficiency, suggesting higher photosynthetic capacity. Under PW, the overall values of ΦPSII are maintained, with slight improvements observed in some lines. This indicates plant resilience, as all genotypes could maintain or adapt their photosynthetic performance under PW stress (Figure 3.33 D). Electron Transport Rate (ETR) indicates the flow of electrons through the photosynthetic electron transport chain, reflecting the energy conversion driven by light. Under control conditions, all genotypes exhibit WT-like ETR values. PW conditions enhance ETR values across all genotypes, indicating a possible acclimation to the stress conditions (Figure 3.33 E). Intrinsic Water Use Efficiency (iWUE) represents the efficiency of carbon assimilation relative to water loss. Under control conditions, *cat2-1* and *pertl6-1 x cat2-1* exhibited lower iWUE compared to WT, that might be linked to the ROS detoxification capacity in these mutants. Under PW, all genotypes showed higher iWUE compared to control, with WT, *pertl6-1, cat2-1, gr1-1* and *pertl6-1 x gr1-1* showing the highest values, indicating improved water use efficiency under temperature stress. These results suggest that prolonged warming induces plant resilience and acclimation by enhancing water use efficiency in all genotypes (Figure 3.33 F).

On the 7th day of growth under elevated temperature, leaf tissues from WT, *pertl6-1* and *pertl6-6* plants were sampled for metabolite analysis. Relative metabolite levels were determined using LCMS (Figure 3.34 A) and GCMS (Figure 3.34 B). The log_2 fold changes (log_2FC) were calculated by normalizing the mean values (n = 4) of plant grown under elevated temperature to their respective mock-treated controls.

Prolonged warming induced several changes in metabolic responses of *pertl6* mutants compared to WT. Among amino acids, glutamate, lysine, and isoleucine levels were elevated in both mutants relative to WT and their controls. Moreover, *pertl6-6* showed strongly upregulated arginine, asparagine and glycine levels, suggesting upregulation in either protein turnover or nitrogen metabolism. Both mutants exhibited a strong decrease in GABA levels compared to their controls, whereas in WT, GABA levels increased in response to warming. Ornithine accumulated in *pertl6-6*, remained stable in WT, and decreased in *pertl6-1*. In

contrast, citrulline levels dropped in all genotypes, with the strongest reduction observed in *pertl6-1,* potentially suggesting alteration in urea cycle. Putrescine levels were elevated in both mutants, but remained unchanged in WT, suggesting that this polyamine biosynthesis may be enhanced under warming only in mutants. Spermidine levels were comparable across

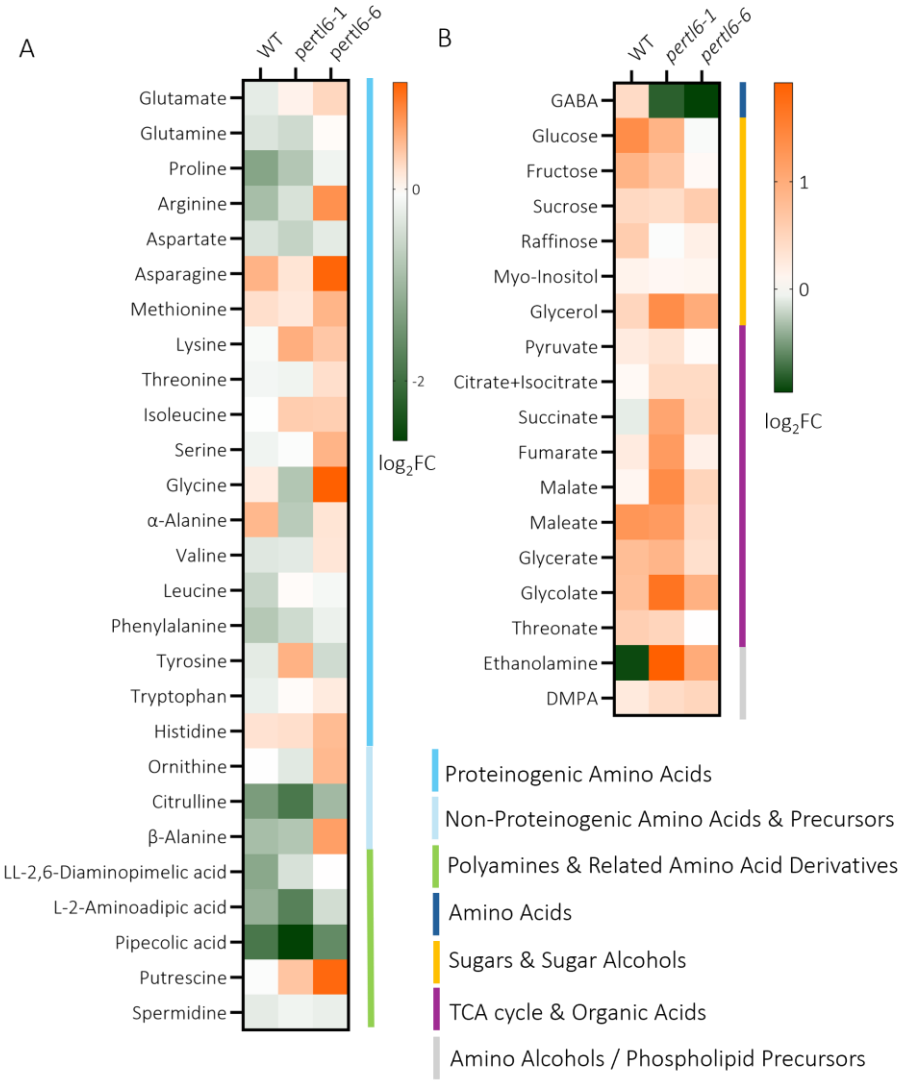

Figure 3.34 Metabolic profiling of plants exposed to prolonged warming

Metabolic profiles presented as heat maps of plants subjected to a 7-day prolonged warming at day and night (28 °C/26 °C) grown in ND. Relative metabolite levels were determined using LCMS (A) and GCMS (B). The log_2 fold changes (log_2FC) were calculated by normalizing the mean values (n = 4) of plant grown in elevated temperature to their corresponding mock-treated controls at the 7th day of warming. Orange boxes indicate metabolites that accumulated in response to temperature, while green boxes reflect reductions compared to controls. For easier interpretation, metabolites were grouped into functional classes (e.g. amino acids, organic acids, sugars), marked by colored bars to the right of each metabolite name, with the legend at the bottom right of the figure.

genotypes. Sugar levels were either elevated or remained similar as in control conditions in all lines. Organic acids were mostly increased in *pertl6-1* mutant, with strong accumulation of glycolate, suggesting enhanced photorespiration. Ethanolamine levels were strongly reduced in WT, whereas both mutants displayed elevated levels of this metabolite, suggesting differences in lipids turnover in mutants (Figure 3.34).

3.8.2. Salt stress

Salt stress impacts plant growth by inducing osmotic and ion imbalance, leading to oxidative stress. To evaluate the influence of salt stress, a combination of phenotypic, molecular and biochemical analyses was conducted. Plants were subjected to NaCl treatment under control conditions, and the following parameters were analyzed: germination rate, growth phenotype, photosynthetic efficiency, transcript level, and metabolic response.

Germination assay with salt stress

The germination assay was used to assess how salt stress affects seed early development. Seeds were grown on MS medium without or with 100 mM NaCl under ND conditions, and radical emergence was assessed every 24 h for five consecutive days (Figure 3.35 A). Four genotypes were analyzed: *WT, pertl6-1, cat2-1* and *pertl6-1 x cat2-1*.

On the first day after sowing (DAS 1), *pertl6-1* showed the highest proportion of seeds still in Stage 1 in both control (24%) and salt-supplemented medium (32%). In contrast, *cat2-1* and *pertl6-1 x cat2-1* had fewer seeds in Stage 1 than WT in MS media, however under salt stress, WT reached Stage 2 in a higher proportion that other lines. By DAS 2, all lines reached Stage 3 and 4 in control conditions, however, *pertl6-1* still displayed a delay, with 15% of seeds still remaining in Stage 1 and Stage 2. This delay persisted under salt stress, where *pertl6-1* seeds distributed as 14% in Stage 1, 67% in Stage 2 and 19% in Stage 3. In contrast, all other genotypes had less than 6% of seeds in Stage 1. On DAS 3, the germination delay of *pertl6-1* under control conditions was reduced, but under salt stress, the difference remained substantial. While in WT only 2% remained in Stage 1, with 68% reaching Stage 4, and 9% reaching Stage 5, in *pertl6-1* the higher distribution is in the early stages: 8% are in Stage 1, 35% in Stage 2, 4% in Stage 3, 49% in Stage 4 and 4% in Stage 5. Both *cat2-1* and *perlt6-1 x cat2-1* exhibited similar, improved germination profiles compared to *pertl6-1* in both media, suggesting the *cat2-1* mutation mitigates the delayed germination phenotype of *pertl6-1* in the double mutant. By DAS 4 and 5, on MS medium, *pert6-1* almost reached WT-like radical emergence into Stage 5. However, under salt-supplemented medium, *pertl6-1* germination

remained delayed, with only 65% seeds reaching Stage 5, compared to 92% in WT and *cat2-1*, and 93% in the double mutant. These results indicate that salt stress delays seed germination in *pertl6-1,* and unlike in control conditions, this delay is not fully compensated by the DAS 5. The rescue of this phenotype in the double mutant points to the dominant role of *cat2-1* in this line (Figure 3.35).

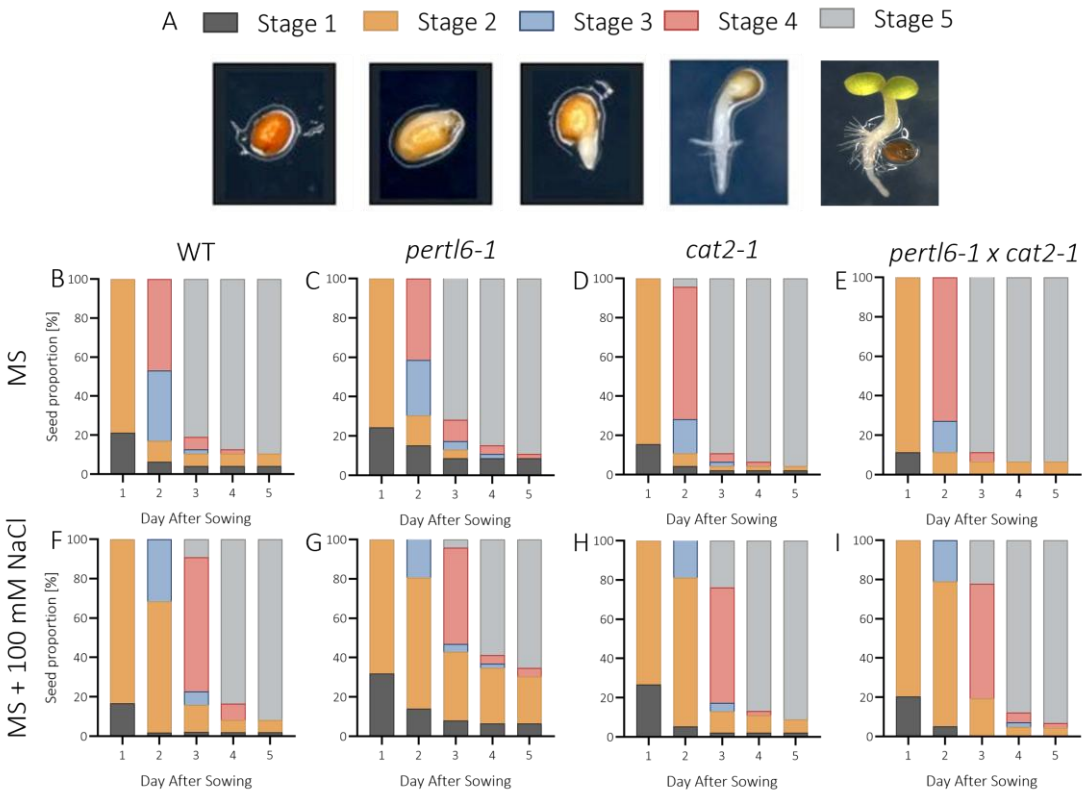

Figure 3.35 Germination assay with salt stress

Seeds were grown on MS medium without (B, C, D, E) or with (F, G, H, I) 100 mM NaCl under ND conditions. The developmental stages were assessed every 24 hours for four days based on pictures (A) and are represented as the percentage of total seed proportions depicted as colored bars (n = 48).

Phenotypic changes under salt stress: root length and rosette area

In another experiment, phenotypic changes like root length and rosette area were analyzed to see how salt stress influences growth and photosynthetic performance.

Plants were grown on MS medium with or without 100 mM NaCl under ND conditions for 2 weeks, after which root length and rosette area were measured. Under control conditions (MS medium) the growth of *pertl6-1*, *perlt6-6, gr1-1* and *pertl6-1 x gr1-1* was comparable to WT. In contrast, *cat2-1* and the double mutant *pertl6-1 x cat2-1* had significantly shorter roots compared to WT, but showed no significant difference from each other, indicating

impairment of ROS detoxification in these lines negatively affected the root growth even under non-stress conditions (Figure 3.36 A). Under salt stress, roots were truncated across all genotypes compared to control. However, the reduction in *pertl6-1* line was stronger than in *pertl6-6*, indicating these lines vary in their sensitivity to NaCl. The *cat2-1* showed most severely reduced root length, whereas *pertl6-1 x cat2-1* exhibited significantly longer roots, although significantly shorter form WT, suggesting partial rescue. While *gr1-1* maintained roots comparable to WT, the double mutant of *pertl6-1 x gr1-1* resembled *pertl6-1* line, suggesting that the *gr1-1* mutation does not compensate for the phenotype in these salt conditions (Figure 3.36 B). Rosette area of *pertl6-1* and *pertl6-6* lines did not differ significantly from WT in each condition (Figure 3.36 C).

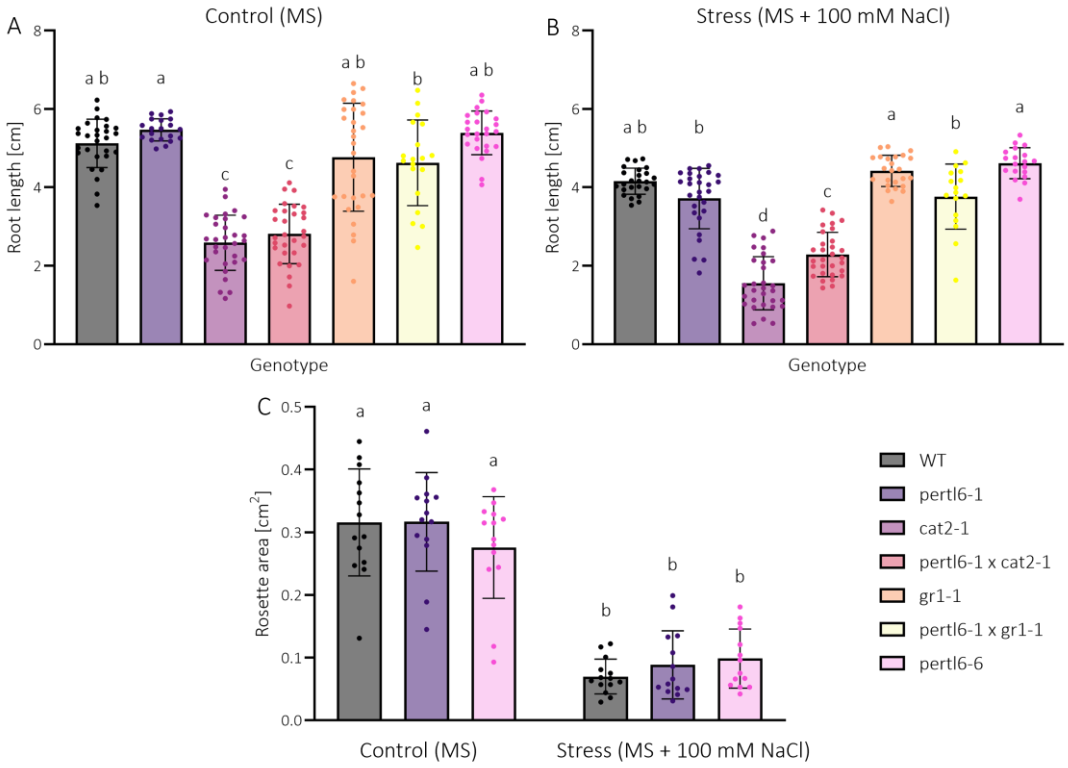

Figure 3.36 Root length and rosette area of plants exposed to salt stress

Root length and rosette area were measured in 2-week-old plants grown on MS medium with or without 100 mM NaCl under ND conditions. Different genotypes are represented by colored bars as indicated in the legend. Values are presented as means ± SD (n = 19-30 for A, B and n = 14 for C) with individual data points displayed. Bars labelled with same letter within each graph do not differ significantly from each other. Different letters indicate significant differences based on Tukey's multiple comparison test following a one-way ANOVA ($p < 0.05$). Outliers were identified using the ROUT method (Q = 5%) and excluded from the statistical analysis.

Growth and photosynthetic performance under combined salt and sucrose conditions

Since *pertl6* lines did not exhibit a strong phenotype under previous conditions, an additional experiment was conducted to further explore response to salt stress. Plants were grown on MS media without or with sucrose, supplemented with 50 mM or 100 mM NaCl under LD conditions. After 2 weeks, rosette area, fresh weight and maximum quantum efficiency of PSII (Fv/Fm) were assessed.

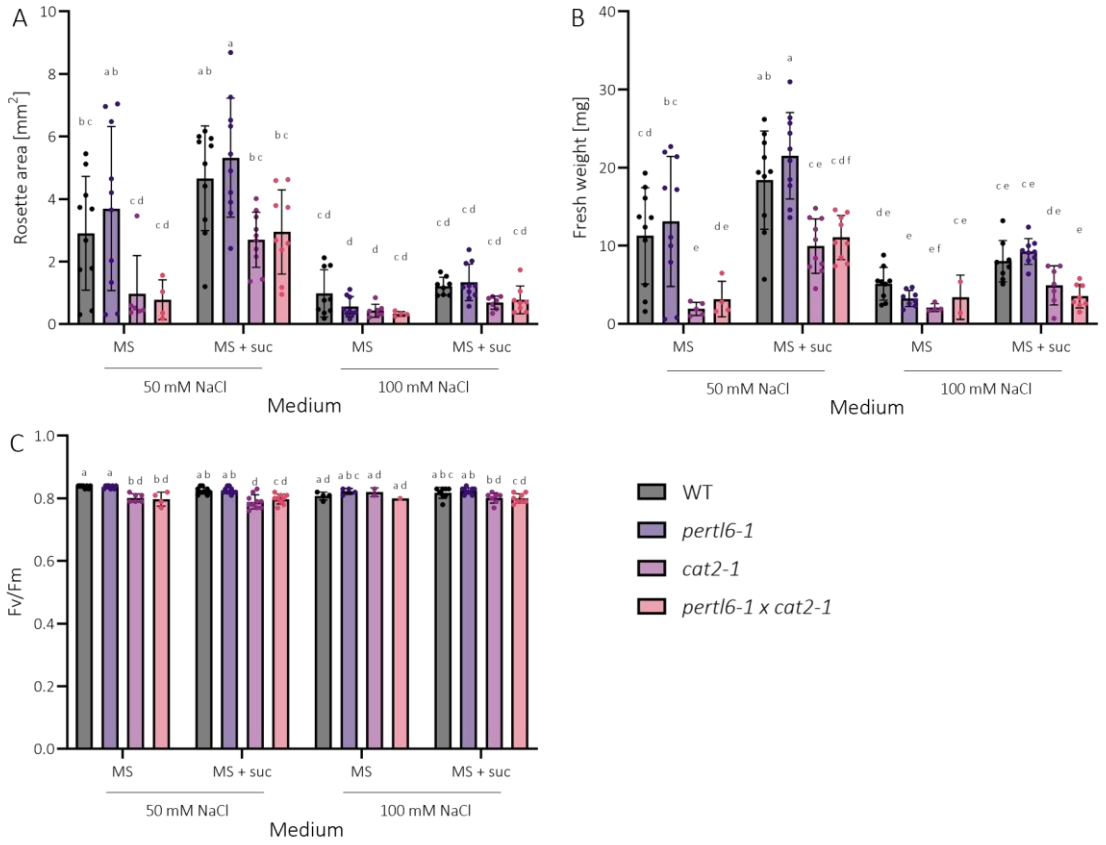

Figure 3.37 Growth and photosynthetic performance under combine salt and sucrose conditions

Rosette area (A), fresh weight (B) and Fv/Fm (C) were measured in 2-week-old plants grown on MS media without or with sucrose, supplemented with 50 mM or 100 mM NaCl under LD conditions. Different genotypes are represented by colored bars as indicated in the legend. Values are presented as means ± SD (n = 10) with individual data points displayed. Bars labelled with same letter within each graph do not differ significantly from each other. Different letters indicate significant differences based on Tukey's multiple comparison test following a one-way ANOVA ($p < 0.05$). Outliers were identified using the ROUT method (Q = 5%) and excluded from the statistical analysis.

In MS medium containing 50 mM NaCl, *pertl6-1* showed no significant differences in rosette area, fresh weight, or Fv/Fm compared to WT. Both *cat2-1* and *pertl6-1 x cat2-1* mutants exhibited reduced growth, although their values did not differ from each other. The addition

of sucrose to the medium enhanced growth across all lines but did not amplify the differences between genotypes. Sucrose also had a minimal influence on photosynthetic efficiency of PSII. In the MS medium supplemented with 100 mM NaCl, growth effects were more pronounced. Both rosette area and fresh weigh of *pertl6-1* decreased compared to WT, reaching levels comparable to *cat2-1* and *perlt6-1 x cat2-1*, in contrast to the 50 mM NaCl condition, where *pertl6-1* retained WT-like growth. The Fv/Fm remained similar across the lines. Supplementation with sucrose increased rosette growth and fresh weight in all lines under high salt, but no significant differences were observed, neither in Fv/Fm.

Metabolite profile under salt stress

To assess whether salt stress triggers metabolic adjustments e.g. increase in osmoprotectants, metabolite assay was performed. Plants were grown for two weeks on ND on MS medium supplemented with sucrose, without or with 100 mM NaCl. Metabolites were analyzed using GCMS and results are presented as $\log_2$ fold changes ($\log_2$FC) calculated by comparing the salt-treated samples to their corresponding mock-treated controls (n = 4).

Salt stress induced changes in metabolites level, with the majority of metabolites downregulated in both WT and *pertl6-1* line. Among the few metabolites that increased in response to salt stress were proline, ornithine and serine. Proline, known as osmoprotectant, was substantially higher in WT than in *pertl6-1*, indicating that *pertl6-1* might have reduced capacity to respond to salt stress in same way as WT. In contrast, ornithine accumulated to much higher levels in *pertl6-1*, which could be linked to altered nitrogen metabolism and urea cycle. Several amino acids including glutamate, GABA, oxoproline, aspartate, glycine, β-alanine, leucine, and phenylalanine were also more abundant in WT than in *pertl6-1*, reinforcing the idea of different reactions of the mutant to salt stress. In addition, all measured TCA cycle metabolites exhibited decrease in *pertl6-1* compared to WT, suggesting potential implication in central energy metabolism under stress. Similarly, the decrease in glycerate and glycolate levels suggest altered photorespiratory flux. These results indicate that *pertl6-1* is less effective in response to salt stress at the metabolic level, as it accumulates less proline, but also exhibits general repression in amino acids and organic acids under stress (Figure 3.38).

Transcript level under salt stress

To further understand the basis of altered salt stress response in *pertl6*, transcript levels of *PERTL6*, *HSFA1A* and *HSP90* were measured in various plant lines (WT, *pertl6-1, cat2-1,*

pertl6-1 x cat2-1, and *pertl6-6*) grown under ND conditions for two weeks on MS medium supplemented with or without 100 mM NaCl. The transcript abundance was normalized to the reference gene At5g60390 (GTP binding elongation factor T4 family protein) and values were presented relative to WT levels (set to 1).

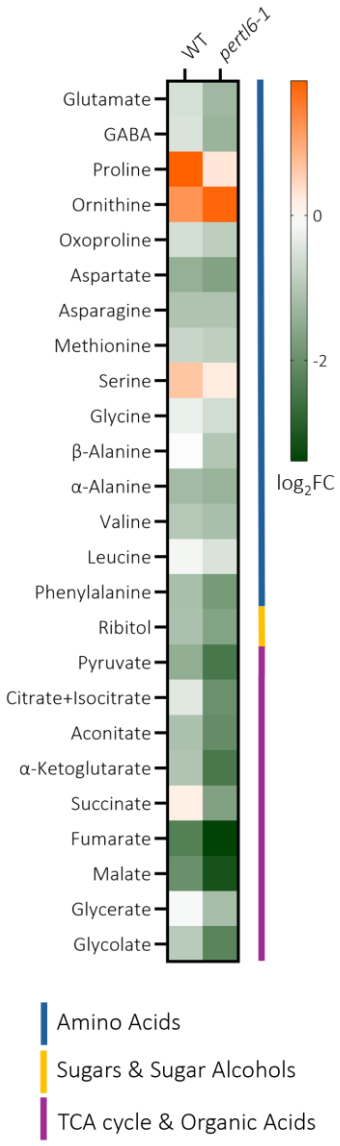

Figure 3.38 Metabolic profile under salt stress

Metabolic profiles presented as heat maps of plants subjected to a 14-day long salt stress grown in ND. Relative metabolite levels were determined using GCMS. The log_2 fold changes (log_2FC) were calculated by normalizing the mean values (n=4) of plant grown in salt stress to their corresponding mock-treated controls. Orange boxes indicate metabolites that accumulated in response to temperature, while green boxes reflect reductions compared to controls. For easier interpretation, metabolites were grouped into functional classes (e.g. amino acids, organic acids, sugars), marked by colored bars to the right of each metabolite name, with the legend at the bottom of the figure.

Under control conditions, expression of *PERTL6* gene in *cat2-1* was comparable to WT. As expected, *pertl6-1* and *pertl6-1 x cat2-1* showed approx. 75% reduced transcript levels, confirming successful knock-down in both backgrounds. The *pertl6-6* CRISPR line also exhibited reduction in transcript abundance, likely due to nonsense-mediated decay, as premature stop codon trigger transcript degradation (Raxwal & Riha, 2023) (Figure 3.39 A). Under salt-supplemented medium, a slight upregulation of *PERTL6* gene was observed in *cat2-1*, which might be a compensatory response to impaired ROS detoxification (Figure 3.39 D). Expression of *HSFA1A* under control conditions remained low across all genotypes, however salt stress triggered moderate upregulation in all lines, suggesting this master regulator is slightly induced in response to salt stress (Figure 3.39 B, E). Under control conditions, *HSP90* expression was significantly upregulated in *cat2-1* compared to other lines, which remained similar to WT (Figure 3.39 C). This upregulation might be linked to the oxidative stress sensitivity in the *cat2-1* mutant itself. Under salt stress, *HSP90* transcript levels were elevated in all lines compared to WT, with *cat2-1* and *pertl6-1* showing a moderate increase. Notably, the double mutant exhibited even higher *HSP90* expression than either

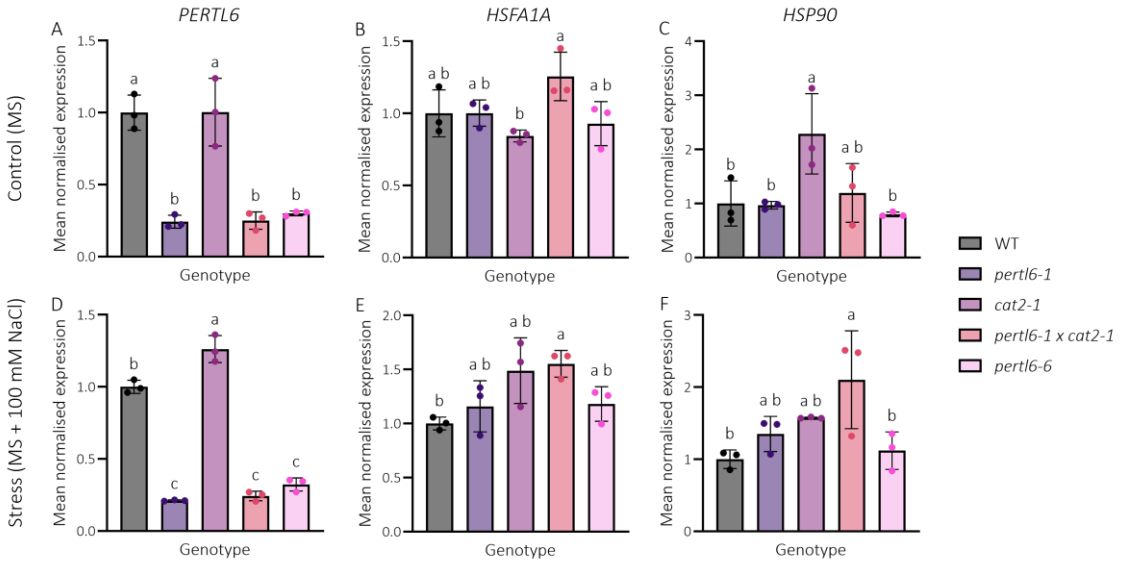

Figure 3.39 Expression levels of *PERTL6, HSFA1A* and *HSP90* under salt stress

Mean normalized expression (MNE) levels of PERTL6 (At1g74240) (A,D), HSFA1A (At4g17750) (B, E), HSP90 (At4g24190) (C, F) in 2 week-old WT plants grown in MS media without (A, B, C) or with (D, E, F) 100 mM NaCl under ND condition. Expression values were normalized to the reference gene At5g60390 (GTP binding elongation factor T4 family protein). Bars represent the means of three biological replicates ± SD (WT MNE was normalized to 1). Statistical significance was determined using Tukey's multiple comparison test, following a one-way ANOVA and is marked by different letters above the bars, indicating the differences between measuring time points ($p < 0.05$).

single mutant, suggesting an additive or synergistic effect. These results may reflect a more pronounced cellular stress in the double mutant (Figure 3.39 F).

3.8.3. Photorespiratory stress

Photorespiratory stress is closely linked to environmental stress, particularly when oxygen concentration is high and CO_2 availability is low. To assess the photorespiratory responses, a CO_2 shift experiment was performed to induce photorespiration and analyze metabolic changes and gas exchange measurements of plants exposed to a shift from high to low O_2 concentrations to evaluate CO_2 assimilation capacity of rubisco.

Shift from high to ambient CO_2 and its influence on metabolism

To investigate metabolic changes associated with photorespiration, plants were grown in ND conditions under elevated CO_2 concentration (3000 ppm) on ½ MS medium for eleven days, followed by shift to ambient CO_2 concentration (390 ppm) for another three days and samples were harvested for GCMS analysis. Results are presented as $\log_2$ fold changes ($\log_2$FC) relative to WT controls (n = 4-8).

Following the CO_2 shift, most amino acids were upregulated in *pertl6-1, cat2-1,* and *perlt6-1 x cat2-1*. However, both serine and glycine were sharply reduced in all lines compared to WT, suggesting impairment in photorespiration at the level of glycine-serine conversion, despite glycolate and glycerate remaining slightly elevated. Moreover, ornithine levels decreased only in *pertl6-1*, while proline levels remained elevated in all lines, suggesting that ornithine is consumed faster in this line. A strong increase in branched-chain amino acids (leucine, isoleucine, valine) in all mutants potentially reflects stronger proteolysis or reduced BCAA catabolism under these photorespiratory conditions. In *perlt6-1* line sugar levels were unchanged or decreased relative to WT, while in *cat2-1* and *perlt6-1 x cat2-1,* glycerol-P, hexose-P and gluconate accumulated. These results indicate different stress responses among genotypes, with an activation of oxidative pentose phosphate pathway and a dominant role of *cat2-1* in the double mutant metabolic profile. TCA cycle intermediates were generally increased in *pertl6-1*, except for pyruvate and succinate, suggested enhanced TCA flux as a compensatory response to redox imbalance. Finally, increased tryptamine and 3-amino-2-piperidone were elevated in all lines suggesting a general stress-induced shift in nitrogen metabolism (Figure 3.40).

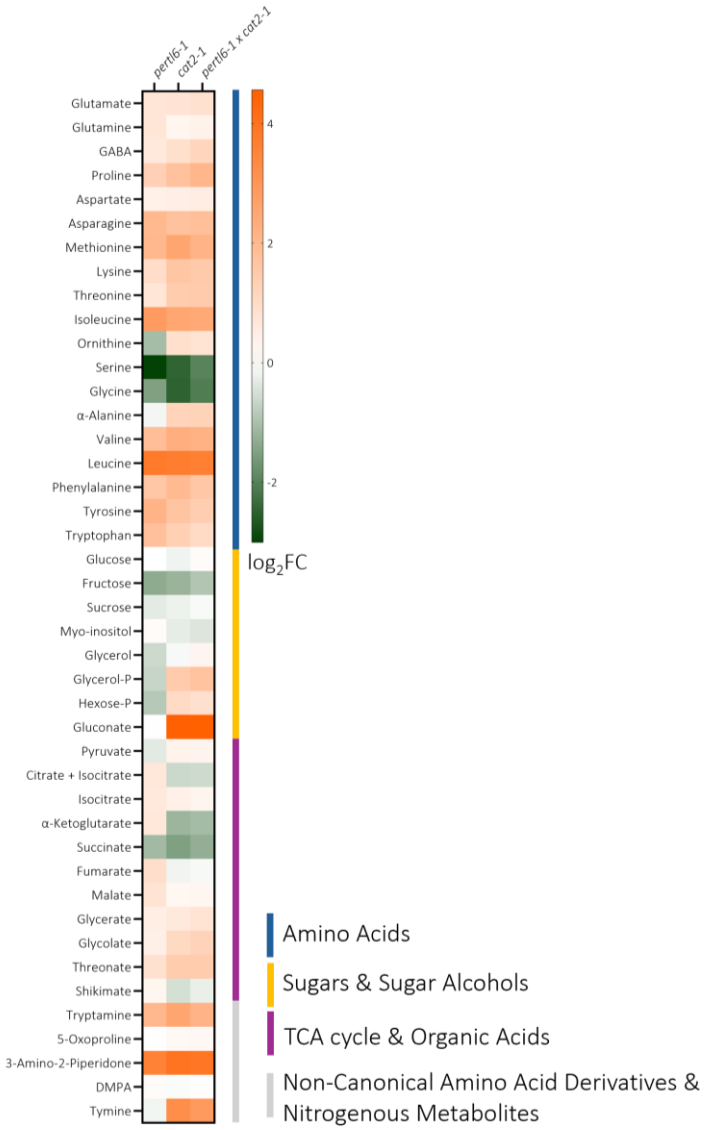

Figure 3.40 Metabolic profile after CO_2 shift

Metabolic profiles presented as heat maps of plants subjected to CO_2 shift form 3000 ppm to 390 ppm grown in ND on ½ MS medium. Relative metabolite levels were determined using GCMS. The log_2 fold changes (log_2FC) were calculated by normalizing the mean values (n = 3-8) to WT. Orange boxes indicate metabolites that accumulated in response to temperature, while green boxes reflect reductions compared to controls. For easier interpretation, metabolites were grouped into functional classes (e.g. amino acids, organic acids, sugars), marked by colored bars to the right of each metabolite name, with the legend on the bottom right of the figure.

Oxygen transient and carbon assimilation dynamics

To assess the photosynthetic response under photorespiratory conditions, CO_2 assimilation was measured during oxygen transient from low (2%) to high (40%) oxygen concentration using the LI-COR system. This shift is known to stimulate photorespiration and thus affects photosynthetic efficiency (Fu et al., 2023).

Following the O_2 increase, a characteristic decrease in carbon assimilation was observed in all genotypes (WT, *pertl6-1, cat2-1, pertl6-1 x cat2-1,* and *pertl6-6*), followed by a transition to steady-state. These dynamic responses were fitted with a one-phase exponential function for individual replicates to compare the rate at which CO_2 assimilation reached steady-state across genotypes. The obtained exponential rate constant (k) representing the speed of the transient recovery was used for comparison. This experiment revealed no significant differences in k among tested genotypes, suggesting comparable response to the elevated oxygen concentrations, even despite previously observed metabolic differences in response to photorespiratory shift (Figure 3.41).

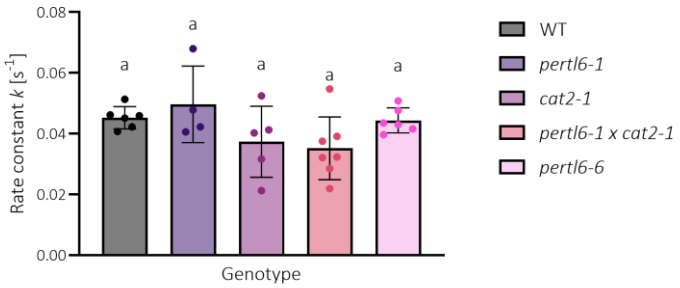

Figure 3.41 Curve fitting of CO_2 assimilation during oxygen transient (2% to 40% O_2)

Net CO_2 assimilation rate was measured in the 9- week old plants grown in SD conditions during the shift from low (2%) to high (40%) oxygen concentration, and a one-phase exponential model was fitted to each biological replicate (n = 4-7). Fitted exponential rate constant (k) was extracted and compared across genotypes. Bars represent means ± SD with individual data points displayed and color-coded as indicated in the legend. Statistical significance was determined using a one-way ANOVA followed by Tukey's multiple comparison test. Identical letters above bars indicate no significant differences between genotypes.

3.8.4. Dark stress

Extended darkness interrupts photosynthesis and triggers broad metabolic reprogramming. Previous metabolic data under various abiotic stresses revealed substantial changes in amino acid levels and alterations in TCA cycle intermediates. This may suggest altered protein turnover and a potential shift in redox balance, particularly in pathways compensating for NADH/NAD^+ during the dark stress. To explore these processes, respiration in the dark, metabolic profiling and photosynthetic efficiency were assessed in dark-treated plants and recovered plants.

Respiration in the dark

Dark respiration is leaf respiration measured in the absence of light, allowing to distinguish between carbon fixed in photosynthesis from the one released by mitochondrial TCA cycle. This measurement helps to assess whether respiration differs across genotypes (Fonseca et al., 2021). Negative assimilation values, reflecting respiratory CO_2 release exceeding any CO_2 fixation, were measured in dark-adapted leaves. No significant differences were observed across WT, *pertl6-1, cat2-1, pertl6-1 x cat2-1*, and *pertl6-6* plants, indicating the basal respiratory activity under darkness is similar in all lines (Figure 3.42).

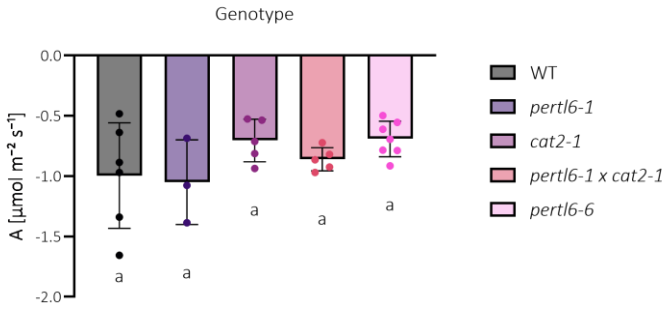

Figure 3.42 Respiration in the dark

Respiration in the dark was measured in the 30-min dark-adapted leaves of 10-week old plants grown in SD conditions using a LI-COR system. Negative values reflect CO_2 release from mitochondrial respiration. Bars represent means ± SD with individual data points displayed (n = 3-7), color-coded as indicated in the legend. Statistical significance was determined using a one-way ANOVA followed by Tukey's multiple comparison test. Identical letters above bars indicate no significant differences between genotypes.

Extended darkness and recovery: effects on metabolic profile and photosynthetic efficiency

Extended darkness followed by recovery provides insights into how primary metabolites fluctuate and how the photosynthetic apparatus functions when photosynthetic carbon assimilation is interrupted and then restored. This sheds light on mechanisms maintaining cellular redox balance under carbon starvation conditions.

Plants (WT, *pertl6-1, pertl6-6, pertl6-1 CL*) were grown under SD conditions for 4 weeks and then transferred to complete darkness for 6 days, followed by recovery for 3 days in SD conditions. Metabolite sampling was performed before the dark stress (control), at the end of dark period and after the recovery phase. Relative metabolite levels were determined by GCMS and are presented as log_2 fold changes (log_2FC) relative to control (n = 5).

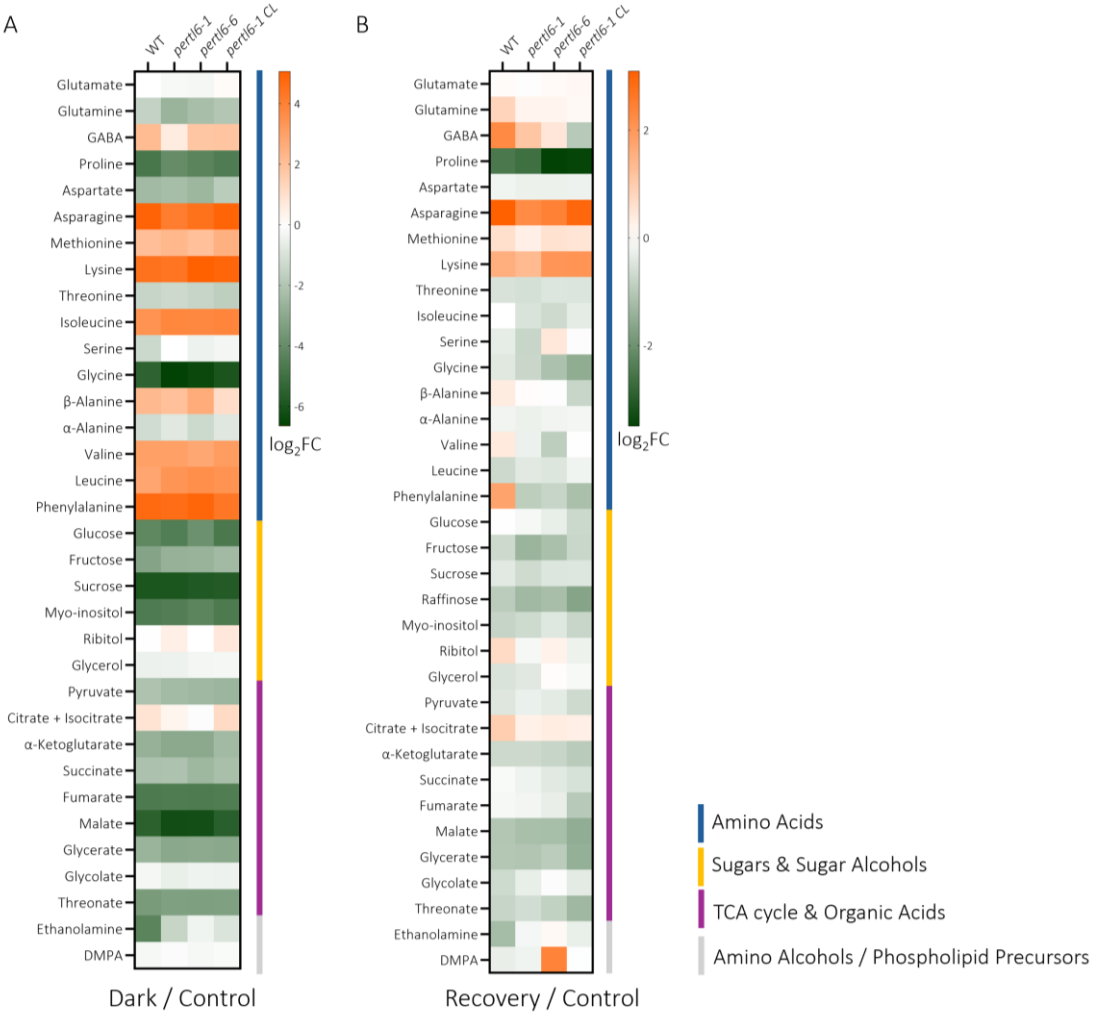

Figure 3.43 Metabolic profiling of plants exposed to dark stress followed by recovery

Metabolic profiles of 10-week old plants grown under SD conditions and exposed to 6 days of darkness followed by 3 days of recovery are presented as heat maps. Panel A shows metabolite changes in dark-treated plants relative to control, while panel B represents changes after recovery relative to control before the darkness. Relative metabolite levels were determined using GCMS and are presented as $\log_2$ fold changes ($\log_2$FC) (n = 5). Orange boxes indicate metabolites that accumulate, while green boxes reflect reductions. For clarity, metabolites were grouped into functional classes (e.g. amino acids, organic acids, sugars), marked by colored bars next to each metabolite name, with the legend at the bottom right of the figure.

Following extended darkness, large metabolic changes were observed across all genotypes. Among amino acids, asparagine, lysine, methionine, GABA, β-alanine, valine, leucine and isoleucine accumulated in all lines, probably reflecting protein degradation. Conversely, glutamine, proline, threonine, α-alanine, and glycine (which decreased about six fold) declined in all lines, suggesting altered nitrogen metabolism. Interestingly, serine levels slightly decreased only in WT but remained stable in other lines after darkness, indicating possible differences in metabolite regulation. No major changes in amino acid responses

were observed between WT and *pertl6* lines overall. Regarding sugars, glucose, fructose, sucrose and myo-inositol were strongly decreased in all lines after darkness, consistent with carbon starvation. Ribitol and glycerol remained stable. TCA cycle intermediates decreased, with malate showing strong reduction in *pertl6-1* and *perlt6-6* lines, suggesting impaired respiratory metabolism in these mutants. Citrate and isocitrate levels were slightly elevated in WT and *pertl6-1* CL, but stable in *pertl6-1* and *pert6-6*. The most notable difference was ethanolamine, which decreased sharply in WT but remained stable in mutants, possibly reflecting altered membrane lipid metabolism or stress signaling in *pertl6* lines (Figure 3.43 A).

After the recovery phase metabolic changes within metabolites were less pronounced compared to the dark treatment, however the differences across genotypes become more apparent, suggesting incomplete recovery compared to control before darkness. Among amino acids, asparagine and lysine showed the highest accumulation in all lines, indicating an ongoing adjustment in nitrogen metabolism. GABA increased markedly in WT, but to a lesser extent in *pertl6-1* and *pertl6-6,* with a decrease observed in *perlt6-1* CL, which may be linked to a different stress response in the mutants. Glutamine, phenylalanine, β-alanine, and valine were elevated only in WT, while the metabolites decreased in *pertl6* lines, suggesting impaired recovery of amino acids metabolism in the mutants. Most sugars remained below control levels, with WT displaying slightly increased levels compared to mutants. TCA cycle intermediates generally decreased, although citrate and isocitrate increased mainly in WT indicating better recovery. Glycolate and ethanolamine levels were higher in mutants than in WT, suggesting altered membrane metabolism. DMPA remained stable in all lines except for a strong increase in *pertl6-6* (Figure 3.43 B).

Photosynthetic efficiency (Fv/Fm) was measured in dark-adapted plants at the end of dark period and after the recovery phase. Data is presented as ratio of Fv/Fm in recovered plants relative to the dark-treated ones. Even though Fv/Fm values dropped after extended darkness, most genotypes recovered to WT-like levels, except for the *cat2-1* mutant, consistent with its sensitivity to oxidative stress. All *pertl6* lines showed no significant differences from WT, however their values were slightly lower. These results suggest that despite the metabolic changes observed, photosynthetic apparatus in *perlt6* mutants restored to WT-like level and remined functionally resilient (Figure 3.44).

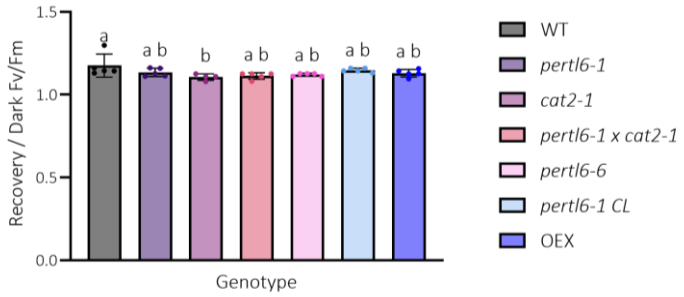

Figure 3.44 Photosynthetic efficiency ratio of recovered to dark-adapted plants

Plants were grown under SD conditions for 4 weeks and then transferred to complete darkness for 6 days, followed by recovery for 3 days in SD conditions. Photosynthetic efficiency (Fv/Fm) was measured in dark-adapted plants at the end of dark period and after the recovery phase. Data is presented as ratio of Fv/Fm in recovered plants relative to the dark-treated ones. Different genotypes are represented by colored bars as indicated in the legend. Values are presented as means ± SD (n = 5) with individual data points displayed. Bars labelled with same letter within each graph do not differ significantly from each other. Different letters indicate significant differences based on Tukey's multiple comparison test following a one-way ANOVA ($p < 0.05$).

3.8.5. Exogenous oxidative stress

Paraquat (methyl viologen) commonly used as a herbicide, induces oxidative stress by catalyzing the ROS formation and thereby inhibiting photosynthesis. Thus, to test how PERTL6 contributes to oxidative stress tolerance, plants were exposed to paraquat-induced ROS stress. Seedlings were grown for two weeks under ND conditions on ½ MS medium supplemented with 0.5% sucrose, with or without 0.05 µM paraquat, and primary root length was measured.

Under control conditions (without paraquat) both *perlt6-1* and *pertl6-6* showed root lengths comparable to WT, while *cat2-1* and the double mutant *pertl6-1 x cat2-1* were significantly shorter (Figure 3.45 A). Upon paraquat treatment, all genotypes had truncated root length, however the reduction showed similar pattern for each genotype (Figure 3.45 B). These results indicate that loss of *PERTL6* does not impair the primary root length under exogenously induced oxidative stress. Moreover, the phenotype of *perlt6-1 x cat2-1* appears to be mostly linked to the *cat2-1* background.

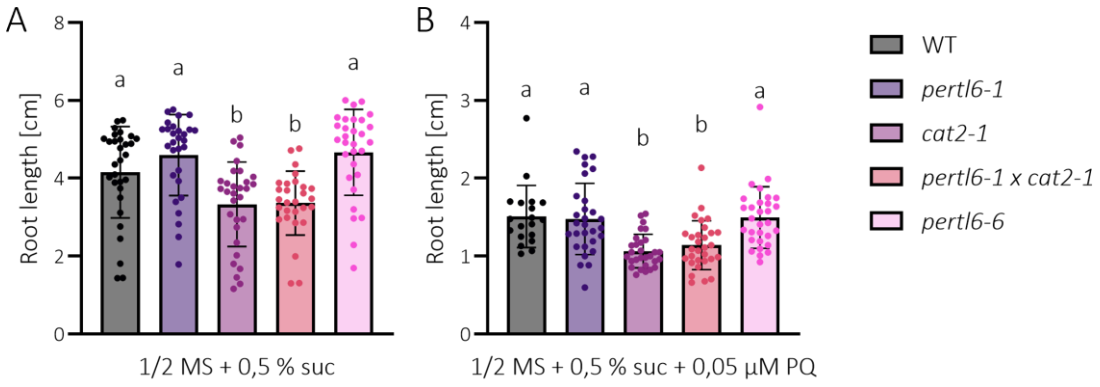

Figure 3.45 Root length of plants grown on media supplemented with paraquat

Root length was measured in 2-week-old plants grown under ND conditions on ½ MS medium supplemented with 0.5 % sucrose, either without (A) or with (B) 0.05 µM paraquat. Different genotypes are represented by colored bars as indicated in the legend. Values are presented as means ± SD (n = 19-30) with individual data points displayed. Bars labelled with same letter within each graph do not differ significantly from each other. Different letters indicate significant differences based on Tukey's multiple comparison test following a one-way ANOVA ($p<0.05$).

4. Discussion

The physiological and phenotypic characterization of Peroxisomal Transport-Like Protein 6 (PERTL6) combined with subcellular localization, phylogenetic, promoter and co-expression studies, points role of PERTL6 in modulating oxidative stress responses in plants. While its precise transport function remains to be elucidated, the observed metabolic alterations and genetic interactions under stress suggest that PERTL6 may influence peroxisomal metabolic balance, potentially linking nitrogen-related pathways to oxidative stress adaptation.

In this discussion chapter, individual experiments are addressed separately, with later sections integrating physiological and metabolic data to provide a broader perspective on the potential transport function of PERTL6 under abiotic stress conditions.

4.1. PERTL6 is localized to peroxisomal membrane

The subcellular localization studies using fluorescent protein fusions in *Nicotiana tabacum* epidermal cells revealed that PERTL6 localizes to peroxisomes, rather than to mitochondria as might be expected from its classification within the mitochondrial carrier family (MCF) or as predicted by *in silico* tools. The PERTL6-mCherry signal showed a characteristic ring-like structure fluorescent pattern surrounding the mCerulean-PTS1 peroxisomal marker punctuates (Figure 3.1). This observation was consistent across independent replicates and was further supported by co-infiltration with a mitochondrial YFP marker, which did not overlap with the PERTL6-mCherry signal (Figure 3.3). Negative controls confirmed the localization specificity where mCherry expression alone was apoplastic and mCerulean-PTS1 correctly localized to peroxisomes (Figure 3.2).

These findings contrast with the data from SUBA5 database, where PERTL6 is predicted to localize to mitochondria. Proteomic studies by Fuchs et al. also identified PERTL6 in *Arabidopsis* mitochondrial membranes (Fuchs et al., 2020). Although dual targeting, especially among MCF, to which PERTL6 belongs, has been reported (Carrie et al., 2009), the data presented here strongly support that PERTL6 predominantly, if not exclusively, localizes to peroxisomes in tobacco epidermal cells. Nevertheless, dual-localization cannot be entirely excluded, as certain proteins such as the dual-targeted Plastidial Glucose-6-Phosphate Transporter GPT1, can alter its localization from plastids to peroxisomes under stress conditions (Baune et al., 2020).

Even though transient expression in tobacco leaves is a widely used and well-established method for studying subcellular localization, it is not entirely equivalent to stable transformation in *Arabidopsis thaliana*. Transient expression systems carry potential disadvantages, including introduction of artifacts such as protein overexpression, which may alter subcellular distribution (Sparkes et al., 2006). Nevertheless, the observed localization is supported by multiple sets of data including distinct separation from mitochondrial signal and strong peroxisomal membrane co-localization. Conflicting proteomic results highlight the importance and need of future validation of PERTL6 localization directly in *Arabidopsis* plants, particularly under oxidative conditions (Fuchs et al., 2020).

The identification of PERTL6 as a peroxisomal membrane protein has important implications for understanding its potential function. Peroxisomes are key hubs for plant metabolism including fatty acid β-oxidation, photorespiration or redox balance. Many other MCF members are involved in transport of small metabolites across the organelle membranes, thus PERTL6 may therefore contribute to maintaining peroxisomal functions potentially in ROS detoxification or redox exchange. This role is explored further in subsequent sections of this discussion chapter, in the context of plant responses to oxidative stress.

4.2. PERTL6 is land plant-specific

Phylogenetic studies showed a clear evolutionary pattern consistent with the hypothesis that PERTL6 evolved in land plants to address the terrestrial-specific physiological challenges. Using Ortho Finder, BLAST and SHOOT.BIO, PERTL6 was identified in a wide range of land plants across all major clades and groups, including Eudicots, Monocots, Magnoliids, Lycophytes, and Liverworts. Moreover, in *Arabidopsis thaliana*, *PERTL6* gene At1g74240 appears to be a single-copy gene, which enables downstream transgenic plant lines studies and suggest evolutionary conservation (Figure 3.4).

Surprisingly, no orthologs were found in green algae (*Chlamydomonas reinhardtii, Dunaliella salina)* and red algae (*Porphyra umbilicalis*), even upon BLAST analysis. This absence suggests that PERTL6 either emerged after the divergence of land plants from algal ancestors or was independently lost in algae. Considering the consistent presence of its orthologs in lower plants like Bryophyta and Lycophyta, it is more likely that PERTL6 evolved during the colonization of terrestrial environment, when plants faced new abiotic stressors like desiccation, enhanced PAR, UV radiation, higher oxygen concentrations and rapid

temperature fluctuations. The land-to-water transition was accompanied by key evolutionary innovations in plants such as cuticle, vascular tissue, stomata and roots (Bowles et al., 2022; Kapoor et al., 2022). These rearrangements in plant evolution together with the emergence of PERTL6 may be supporting adaptation to oxidative stress and other redox-related challenges in new environments.

It has been reported that the number of MCF members, to which PERTL6 belongs, is higher in land plants compared to the number of MCF members in algae such as *Chlamydomonas reinhardtii*, indicating that this transporter family was exploited for novel functions required to conquer land during evolution of life on Earth (Palmieri et al., 2011).

Moreover, the presence of PERTL6 orthologs in Bryophyta and Lycophyta indicates that emergence of the protein occurred early in the evolution of plants during water to land transition, before the divergence of vascular plants. These findings imply that PERTL6 has been retained across diverse clades and groups of green land plants potentially due to its contribution to core cellular function.

In broader orthologs search using SHOOT.BIO, some distant orthologs were found in Fungi, but none in Animals, Bacteria or Archaea (Figure 3.5). Among all the fungal orthologs identified as mitochondrial carriers, two were annotated as thiamine pyrophosphate carrier 1 and magnesium exporter 1 (MME1, Cui et al., 2015). While these orthologs could potentially indicate substate candidates for PERTL6, the long branch lengths separating plants and fungal orthologs suggest quite distinct evolutionary relationships therefore functional specialization. The absence of orthologs in other kingdoms supports the previous result of PERTL6 having its unique evolutionary function within the land plant kingdom.

Comparative studies have investigated the differences in oxidative metabolism in organisms adapted to terrestrial and aquatic environments. In *Chlorella vulgaris,* which colonize both habitats, the terrestrial strains compared to the aquatic one were found to accumulate higher levels of nitrogen-rich metabolites like arginine, asparagine, lysine, as well as osmoprotectants like proline and the polyamine putrescine. These metabolites are associated with enhanced antioxidative defense, suggesting an adaptation to increased terrestrial oxidative stress. In contrast, aquatic strains showed increased sugar levels like trehalose, likely reflecting different stress signaling in water environment (Aigner et al., 2020). A similar trend was observed in vascular plants from terrestrial and palustrine habitats. Terrestrial plants exhibited higher activity of the alternative oxidase (AOX), which plays a critical role in managing excessive

energy dissipation and avoiding ROS generation in mitochondria. Collectively, these findings support the notion that terrestrial environments impose stronger redox pressure compared to aquatic habitats requiring robust antioxidant mechanisms (Del-Saz et al., 2021). Even though antioxidative mechanisms are conserved in aquatic organisms, no dedicated ascorbate or glutathione transporters have been described in algae so far (Rezayian et al., 2019; Yeh et al., 2019).

If PERTL6 facilitates the movement of antioxidants or their precursors through the peroxisomal membrane, it could support the antioxidative pathways involved in ROS detoxification. This function would play an important role in maintaining redox balance for the successful adaptation to terrestrial environment where oxidative stress is more pronounced. Phylogenetic analyzes support the hypothesis that PERTL6 evolved to play a specialized function probably in response to terrestrialization, contributing to peroxisomal redox regulation and stress resilience. Its conservation across diverse plant clades, presence as a single-copy gene in *Arabidopsis* and absence in algae reinforce the idea of PERTL6 contributing to the success of early land plants linked to oxidative stress mitigation during terrestrial adaptation.

4.3. *PERTL6* plays a role in plant stress adaptation

All combined *in silico* analyzes of the promoter region, co-expressed gene networks, single-cell RNA-Seq data collectively suggest that *PERTL6* plays a specialized role in stress adaptation, particularly related to abiotic stresses such as heat, light, salt, drought, and osmotic challenges. The function might involve maintaining peroxisomal redox balance, through regulation of translation and proteolysis, despite its generally low expression across all cell types under non-stressful conditions.

The data from cis-regulatory promoter region from 700 bp upstream of Transcription Start Site revealed multiple cis-regulatory elements predominantly associated with abiotic stress responses. Transcription factors such as those for salt, drought and osmotic stress (ATERD1, MYBCORE, WRKY71, MYB13, AZF1 and AP2/ERF) (Dhatterwal et al., 2022; Guo et al., 2016; Kodaira et al., 2011; Sukumaran et al., 2023; Z. Xie et al., 2019; Yu et al., 2017, 2018, 2021) heat stress (HSFA6B, HSFA1B, CCAAT-BOX1, and HSFB2A) (Albihlal et al., 2018; Haralampidis et al., 2002; Wunderlich et al., 2014; D. L. Xie et al., 2022) or light stress (GATA15, I-BOX) (Berry et al., 2013; Manfield et al., 2007) were identified (Figure 3.6). Although promoter motif annotations may include false positives, the abundance and

diversity of stress related elements strongly suggests a complex transcriptional regulation of PERTL6' expression particularly related to abiotic stress response.

This cis regulatory region of the 700 bp upstream of the TSS analysis was supported by gene co-expression analysis, showing associations with genes encoding heat shock proteins (*HSP60-3A* (At3g13860), *HSP60-2* (At2g33210), *HSP89.1* (At3g07770)), involved in protein degradation (*LON1* (At5g26860), *DEG14* (At5g27660), *CDC48B* (At2g03670), At3g49320, and At4g04180) or regulators of gene expression (*MS22* (At1g64600), *BL17MY* (At5g64650), and *SIN2* (At2g41670)) (Figure 3.7). Although none of the co-expressed genes are directly annotated as peroxisome-localized, *LON1* and *DEG14* have their peroxisome-specific isoforms: *LON2* (At5g47040) and *DEG15* (At1g28320). While *LON1* and *DEG14* are responsible for protein degradation in mitochondria in response to heat stress (*DEG14*) (Basak et al., 2014; L. Li et al., 2017), *LON2* and *DEG15* have been validated as peroxisomal targeted proteases, with *LON2* also facilitating the protein import into peroxisome. These proteases are essential for function during stress (Lingard & Bartel, 2009). Hence, PERTL6 may act in parallel to sustain peroxisomal redox balance.

While previous predictions proposed dual targeting of PERTL6 to mitochondria and peroxisomes (SUBA5), experimental work confirmed the exclusive peroxisomal membrane targeting. The strong co-expression of genes responsible for mitochondrial maintenance, despite that, may suggest some functional interplay between mitochondria and peroxisomes, particularly in stress signaling and redox regulation (Foyer & Noctor, 2003; Noctor et al., 2007).

Single cell RNA-sequencing data indicates that *PERTL6* is expressed at low levels in nearly all types of leaf cells under non-stress conditions (Figure 3.8). Similar low and ubiquitous expression pattern was observed in various *Arabidopsis* organs (Figure 1.4). Interestingly, the expression of PERTL6 elevates under abiotic stress, specifically heat shock conditions (Winter et al., 2007a; Zhang et al., 2020), which was confirmed experimentally (Figure 3.29), suggesting that PERTL6 is needed to alleviate the negative effects of stress. This may suggest basal housekeeping-like role of PERTL6 with inducible upregulation under stress condition.

In summary, integrated cis-regulatory promoter region, co-expression and single-cell transcriptomic data support the narrative that PERTL6 contributes to plant stress adaptation, particularly linked to oxidative stress mitigation and protein homeostasis. Future

experimental studies should validate the functional role of the transporter to fully elucidate its role in plant resilience to oxidative stress.

4.4. Established mutant lines as a tool for studying stress adaptation

To characterize the function of PERTL6 in *Arabidopsis thaliana,* several mutant lines were investigated as a good tool to assess the biological relevance of PERTL6. The *pertl6* lines exhibited sensitivity to oxidative conditions suggesting its role in stress response during abiotic stress. Moreover, the double mutants of *cat2-1*, and *gr1-1*, depending on physiological experiment revealed epistatic effects, suggesting that PERTL6 might act in parallel or downstream to these enzymes regulating redox balance.

Supporting this, the *perlt6-1* line, which carries tandem T-DNA insertions in exon 5th, was confirmed to be a knock down based on RT-PCR and qPCR analyses, showing 74% of transcript reduction. Despite this residual gene expression, no full-length transcript as detected, indicating that the T-DNA insertion led to disruption in gene transcription. However, the non-reliable primer efficiency downstream the insertion disenabled another qPCR measurement.

To overcome this limitation, an independent CRISPR/Cas9-generated *pertl6-6* line was established. After screening hundreds of plants, cDNA sequencing revealed one thymidine insertion in first exon in one plant line. This one nucleotide insertion leads to frameshift mutation, which introduces premature stop codon. While the confirmation on the protein level was not possible due to the lack of specific antibodies against PERTL6, protein sequence analysis suggests the mutation leads to elimination of the N-terminus transmembrane domain. The presence of alternative translation start downstream at the end of the sequence in the first transmembrane domain, would likely lead to a truncated protein lacking an essential structure for membrane docking or substrate transportation (Figure 4.1). Therefore, *pertl6-6* is a very likely functional knock out plant line.

To ensure the observed phenotype in *pertl6* lines are indeed linked to the disruption of a gene, a complementation line was also included in this research, serving as a third independent line to study the gene function.

To evaluate genetic interactions of *pertl6*-1 with oxidative stress lines: *catalase2-1* and *glutathione reductase1-1*, these double mutants were obtained. The rationale behind creating these genetic

crosses was to see whether PERTL6 has a role that as the others influence redox homeostasis.

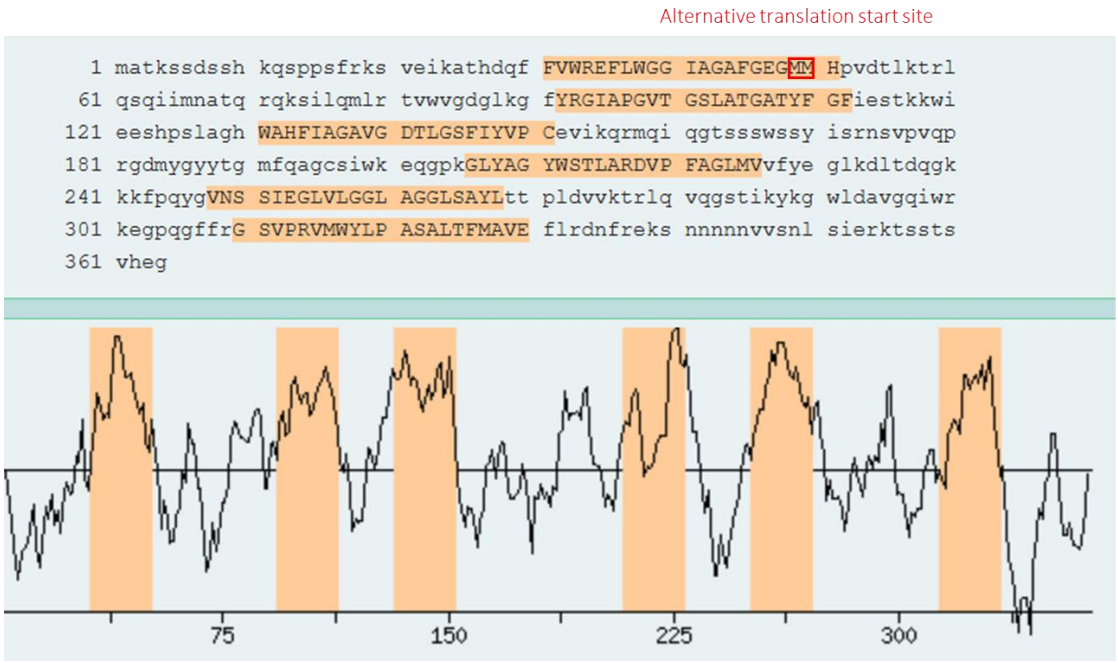

Figure 4.1 Transmembrane domain regions in PERTL6

Transmembrane domain regions in PERTL6 marked in orange. Alternative translation start site marked in red would likely lead to unfunctional protein missing first transmembrane domain in *perlt6-6* line.

Nevertheless, the lack of protein-level validation leaves a gap as well as the absence of functional assays for substrate specificity, making the insights into the PERTL6 redox role rather speculative. Another challenge is the interpretation of all physiological and metabolic results, that not always are consistent with one another. However, as these mutants are stress-sensitive, and PERTL6 was found to have many orthologs with green plant species, therefore they are a valuable tool to study oxidative stress responses and acclimation in plants.

Surprisingly, *perlt6* mutant lines did not show strong phenotype under normal conditions, despite its strong *in silico* connection to stress response. However, this aligns with the low and ubiquitous expression pattern across all tissues and cell types. That might potentially suggest that PERTL6 is not a crucial transporter in stress adaptation but conditionally activated or upregulated upon stress induction to support the existing antioxidative mechanisms. Therefore, PERTL6 might act as a stress-inducible peroxisomal transporter.

4.5. Phenotypic analyses revealed altered sensitivity of *pertl6* mutants to oxidative stress

To gain insight into the physiological role of PERTL6, especially in response to oxidative stress, a range of phenotypic experiments were carried out. Overall, the loss of *PERTL6* function enhanced sensitivity to oxidative stress. This was manifested by photoperiod-dependent rosette size reduction, sucrose-dependent root growth, delayed germination and altered stress-responsive gene expression, while steady-state CO_2 assimilation remained unaffected.

Under SD conditions, *perl6-1, pertl6-6* and complementation line (*perlt6-1* CL) displayed WT-like rosette size in 4-week old plants (Figure 3.23). However, when grown in ND light regime, *pertl6-1* line showed reduced rosette size compared to WT, unlike *pertl6-6* which resembled WT (Figure 3.23). The difference in phenotypes of these lines may be caused by the T-DNA insertion line retaining residual transcript or carrying a background mutation that leads to the reduced growth phenotype. Alternatively, the CRIPSR line may permit for alternative translation retaining partial protein function in the *pertl6-6* CRISPR line. Therefore, *perlt6* CL should be included for future experiments as a control. This reduced growth phenotype observed in *pertl6-1* line under ND is however consistent with the hypothesis that the longer light exposure increases ROS production due to higher photosynthetic and metabolic activity (Shibaeva & Titov, 2025). Therefore, if PERTL6 plays a role in oxidative stress mitigation, its absence may become more detrimental under ND conditions, where ROS production is higher and defense mechanisms must be more active.

Although *pertl6-1* exhibited reduction in rosette size under ND, no significant differences in root length were observed in 2-week-old plants grown on media with and without salt (Figure 3.23, Figure 3.36). Since most ROS in plants is mainly generated during photosynthesis, oxidative stress likely affects leaf peroxisomes more than roots (Eljebbawi et al., 2021). This suggests that PERTL6 may be more critical for supporting antioxidative defenses in leaves than for mitigating salt-induced oxidative stress in roots. Moreover, developmental stage and metabolic reserves may also have an impact, as younger seedlings may still rely on seed-derived oils as a carbon source, providing metabolic flexibility that helps buffer stress effects. Consequently, root measurements may not be the most suitable tissue for studying redox sensitivity – consistent with paraquat assay, in which no differences were observed neither (Figure 3.45). These results are not necessarily contradictory but rather point to a context

dependent role of PERTL6. Future studies should measure ROS accumulation in roots versus shoots under matched developmental stages and stress intensities to pinpoint where the PERTL6 function is more essential. Redox-sensitive biosensors like ro-GFP2 should be used to assess redox state in peroxisomes versus cytosol, as they enable for compartment-specific redox measurements in living plans during stress conditions (Müller-Schüssele et al., 2021).

Peroxisomal β-oxidation is central to converting stored lipids into acetyl-CoA for the TCA cycle, for further energy production. This process, however, alters redox state, as acyl-CoA oxidase produces hydrogen peroxide and downstream reactions produce NADH (Lismont et al., 2015). Mutants defective in β-oxidation (e.g. *pxn, mdar4, pxa1, mfp2*) show arrested seedling growth, that can be rescued by external carbon source such as sucrose (Bernhardt et al., 2012; Eastmond, 2007; Rylott et al., 2006). Therefore, functional fatty acid breakdown is essential for seedling establishment and disrupted redox homeostasis in *pertl6* lines may affect β-oxidation, limiting carbon availability during early seedling development, which may be restored with sucrose. Indeed, *pertl6-1* exhibited sucrose-dependent root growth under SD conditions (Figure 3.24) and early seedling development (4-7 DAS) confirmed that sucrose addition enhanced growth specifically in *pertl6-1* line (Figure 3.27). Combined sucrose-dependency and salt stress experiments revealed that higher salt concentrations (100 mM) had stronger impact on rosette area and fresh weight. Without sucrose *pertl6-1* showed reduced growth, whereas sucrose supplementation eliminated the differences from WT (Figure 3.37). This suggests that the absence of PERTL6 limits carbon availability under stress, but this deficit can be externally compensated.

Germination was delayed in *pertl6-1* under control conditions, suggesting that PERTL6 function is supporting timely seed germination (Figure 3.28). Salt stress further prolonged this delay and unlike in the control conditions it was not compensated by the DAS 5 (Figure 3.35). These results indicate that PERTL6 contributes to early stage stress tolerance, potentially through modulating redox homeostasis during germination, as ROS scavenging capacity is critical for seeds and elevated ROS can inhibit germination (Bykova & Igamberdiev, 2025; Lee & Park, 2010). To assess whether PERTL6 directly alters lipid mobilization, triacylglycerol quantification under both stressed and non-stressed conditions should be performed in future studies.

Measurements of net CO_2 assimilation under control and stress conditions revealed no significant differences between *pertl6* and WT (Figure 3.26, Figure 3.33, Figure 3.41). This

indicates that PERTL6 does not directly affect steady-state carbon assimilation processes such as photorespiration. However, chlorophyl fluorescence analyses under continuous light indicated lower Fv/Fm than WT (Figure 3.24), potentially reflecting mild photoinhibition. However, similar trend was also visible in WT and as no exact equivalent data exists for comparison, these findings should be interpreted cautiously. Under heat stress *pertl6-1* showed drop in photosynthetic efficiency of PSII, followed by increase within 1 h to even the WT level after 4 h (Figure 3.30). These fluctuations indicate that PERTL6 may play an important role in dynamic regulation of photosynthetic performance under acute heat stress. This effect may be mediated by buffering the redox state through the supply of nitrogen-rich amino acids or antioxidants, supporting polyamine synthesis, when canonical antioxidative pathways like catalase or ascorbate-glutathione are under high demand. The mechanism could explain the transient drop and subsequent recovery in PSII efficiency observed in *pertl6-1*. To test this hypothesis, future experiments could combine peroxisome-targeted ro-GFP2 redox sensor with simultaneous monitoring of Fv/Fm under heat stress to directly determine whether PERTL6-dependent peroxisomal redox regulation affects photosynthetic performance.

Expression analysis confirmed *PERTL6* upregulation upon heat, along with 11-fold induction of *HSP90* and decrease of *HSFA1A* (Figure 3.29). *HSFA1A* as a master regulator of heat responses in plants triggers strong expression of other transcription factors, HS-responsive genes such as *HSP90*. The *HSP90* high upregulation confirms effective heat perception and signaling consistent with previous studies (Ohama et al., 2016; Yamada et al., 2007; Yoshida et al., 2011b). The transient downregulation of *HSFA1A* after 4 h of HS matches the documented negative feedback regulation after 1 h of HS at 37°C of *HSP90* (Yamada et al., 2007; Yoshida et al., 2011b). Therefore, these results align with canonical heat stress reposes supportive PERTL6 putative role in broader stress adaptation.

In contrast, salt stress caused only mild *HSP90* and *HSFA1A* upregulation in both *pertl6-1* and *pertl6-6* mutant lines compared to WT (Figure 3.39). This is likely due to the moderate stress intensity (100 mM NaCl) and the early developmental stages of the seedlings, which may allow for better metabolic flexibility and capacity for stress mitigation. Moreover, salt stress predominantly activates osmotic and ion signaling pathways, rather than strongly inducing chaperone expression as observed during heat stress. Another limitation is that the current dataset does not allow for direct comparison of the salt stress effect on between WT

and *perlt6* lines, in terms of PERTL6 upregulation, making is impossible to determine whether the gene itself is upregulated upon these specific stress conditions.

Collectively, these phenotypic analyses indicate that PERTL6 is not essential for elementary growth, but becomes important under stressful conditions, where ROS levels increase or carbon mobilization is critical. This suggests a link between PERTL6, peroxisomal metabolism and redox state. This data, however, should be interpreted with caution, as most evidence is correlative. Physiological experiments revealed some differences between the T-DNA (*pertl6-1*) and CRISPR/Cas9 (*pertl6-6*) lines, which might arise from residual transcript, background mutations in *perlt6-1*, off-target effects, compensatory mechanisms, or incomplete loss-of-function in the CRIPSR/Cas9 line. The complementation line generally restored the phenotype toward WT, but interestingly the overexpression line (OEX) showed a reduction in growth, suggesting that PERTL6 might be dosage sensitive, as excessive PERTL6 may lead to perturbation in redox balance, metabolic homeostasis or signaling pathways, highlighting the importance of proper expression for its physiological function. As these independent mutants are not always equivalent, generating another independent stable line is recommended. Furthermore, metabolic experiments were performed from the whole rosettes or leaves at a single time point that could mask peroxisome-specific temporal changes. Future experiments should include tissue-specific kinetic experiments, ideally using organelle specific ro-GFP redox sensors and assays directly measuring PERTL6 transport activity.

4.6. Genetic interaction of *pertl6-1* with oxidative stress mutants (*cat2-1* and *gr1-1*)

Crossing *pertl6-1* with oxidative stress-sensitive mutants was performed to evaluate whether PERTL6 contributes to antioxidative mechanisms. In theory, if PERTL6 has a role in mitigating oxidative stress, the double mutant with *cat2-1* would be expected to exhibit exacerbated phenotype due to the combined inability to efficiently detoxify ROS. However, genetic crosses of *pertl6-1* with mutants impaired in antioxidative systems (*cat2-1* and *gr1-1*) revealed that loss of PERTL6 does not always modify the oxidative stress responses, suggesting a PERTL6 role in redox homeostasis is parallel or downstream catalase or ascorbate-glutathione cycle, possibly by supporting the redox homeostasis through alternative mechanisms. Distinct interaction patterns between *cat2-1* and *gr1-1* indicate that

PERTL6 may have more specific function in supporting antioxidative mechanisms, rather than broadly substituting for role of major ROS-scavenging systems.

The *cat2-1* mutant line is a well-studied model to study oxidative stress in *Arabidopsis thaliana*. Previous studies reported that CAT activity increases under stress conditions via the peroxisomal small heat shock protein Hsp17.6CII (G. Li et al., 2017). Under ambient air, *cat2-1* exhibits reduced rosette biomass, disruption of intracellular redox balance, and activation of oxidative stress signaling pathway. Interestingly, these phenotypes may be mitigated under high CO_2 conditions, when photorespiration is limited (Queval et al., 2007). Consistent with previous research, *cat2-1* exhibited limited rosette growth under ND and SD conditions, however no necrotic lesions were observed (Mhamdi, Hager, et al., 2010; Queval et al., 2007). Notably, the double mutants of *pert6-1 x cat2-1* showed inhibited rosette growth compared to the single *pertl6-1* line, but not relative to *cat2-1* (Figure 3.23). This suggests *pertl6* expression is masked by expression of the stronger *cat2* phenotype, implying that PERTL6 functions in the same or converging pathway as CAT2, possibly downstream or parallel.

Previous work demonstrated enhanced root growth of *cat2-1* under LD conditions with sucrose supplementation (Yang et al., 2019), however this was not observed in younger plants (Figure 3.24). Under ND conditions, however, both *cat2-1* and the double mutant exhibited root growth improvement when sucrose was added, while under SD*, pertl6-1* and the double mutant also showed increased roots length after sucrose supplementation (Figure 3.24). This suggests that photoperiod-dependent regulation influence root growth responses in these lines by affecting the interaction between ROS and carbohydrate availability. This photoperiod-dependent phenotype is consistent with the role of CAT2 in redox homeostasis which is tightly linked to day-night cycle, as *CAT2* transcript is upregulated upon light (McClung, 1997). Interestingly, under salt supplementation, the double mutant showed an additive phenotype, with root length differing form both single mutants, unlike in control conditions where its roots resembled that of *cat2-1* (Figure 3.36). This contrasts with the epistatic pattern seen under sucrose and paraquat supplementation, where double mutant resembled only *cat2-1* alone (Figure 3.45). This suggests that the relationship between CAT2 and PERTL6 depends on the type of stress encountered. Since CAT2 is known to be activated upon salt stress, leading to enhanced ROS detoxification (Selma, 2025; Zhuang et al., 2025), its absence in *cat2-1* likely contributes to oxidative stress and impaired root growth. It is important to consider that in *cat2* mutant, two other isoforms of catalase are still active. The finding that PERTL6 may partially alleviate the impairment in double mutant, suggests

that perturbation in metabolite transport across the peroxisomal membrane may elevate ROS levels to a degree that enhances stress signaling and activates alternative detoxification processes. Thus, PERTL6 may balance between ROS detoxification and ROS signaling and its absence can modify the phenotype of CAT2 deficiency under salt stress.

Glutathione reductase (GR1) catalyzes the reduction of oxidized glutathione disulfide (GSSG) to reduced glutathione (GSH) using NADPH, as a part of glutathione-ascorbate cycle that operates in multiple cellular compartments (Marty et al., 2009b). GSH is a key antioxidant that buffers cellular redox status and maintains the thiol state of proteins. In *Arabidopsis*, GR1 isoform responsible for ~ 65% of total GR activity, is in cytosol and peroxisomes (Marty et al., 2009a). If PERTL6 facilitates transport of GSH (or GSH against GSSG) to support the ASC-GSH cycle or to enable GSH-S transferases catalyze the glutathionylation of reactive molecules, then a cytosolic GR1 would be essential for regenerating GSH pools (Dixon et al., 2002). Alternatively, if GR1 within peroxisomes primarily maintains the GSH/GSSG ration, PERTL6 might function as a uniporter to preload peroxisomes ensuring proper redox buffering and sustaining peroxisomal antioxidant capacity.

While *gr1-1* mutants alone do not exhibit oxidative stress phenotype, their redox state becomes more oxidized, particularly when combined with mutants that have impaired ROS scavenging, like *cat2-1* (Han et al., 2013; Marty et al., 2009; Mhamdi, Hager, et al., 2010). This makes *gr1-1* a useful genetic background to test if PERTL6 contributes to oxidative stress defense analogously to *cat2* and the genetic interaction may reveal overlapping or complementary functions. While previous studies confirmed that *gr1-1* alone shows no phenotype, the double mutants of *gr1-1 x cat2-1* exhibited more severe growth reduction than *cat2-1* alone (Mhamdi, Hager, et al., 2010), suggesting additive effects when both ASC-GSH and catalase functions are compromised. However, a detailed analysis of *gr1-1* single mutants under different conditions is still missing in the literature, leaving uncertainties for interpretation of the results and the contribution to redox homeostasis.

In this context, the interaction between *pertl6-1* and *gr1-1* mutants may provide insights into PERTL6 function. Under ND conditions rosette size the single *gr1-1*, *pertl6-1* and the double mutant (*pertl6-1 x gr1-1*) did not differ significantly (Figure 3.23), in line with earlier work (Mhamdi, Hager, et al., 2010). *Gr1-1* resembled WT in rosette growth, whereas *pertl6-1* and the double mutants were slightly smaller, but remained comparable to *gr1-1*, suggesting that the absence of PERTL6 rather than GR1 may underline the minor growth differences.

Interestingly, this shifted under salt treatment. The *gr1-1* roots were significantly longer than that of *pertl6-1* or *pertl6-1 x gr1-1*, suggesting the enhanced root growth under salt stress in *gr1-1* benefits from PERTL6 (Figure 3.36). The growth of *gr1-1* under salt conditions is dependent on the presence of PERTL6, suggesting that PERTL6 may provide metabolites of cofactors necessary for the protective mechanisms when GR1 is missing. Therefore, if PERTL6 transports GSH or GSSG, these findings imply that PERTL6 becomes critical under stress when GR-mediated GSH recycling is impaired, supporting the hypothesis that PERTL6 contributes to maintaining redox balance under stress conditions.

Parameters indicative of photosynthetic capacity (Vcmax, Jmax, TPU) did not differ among genotypes (Figure 3.26), suggesting that the core photosynthetic machinery remains unaffected by the loss of CAT2 or PERTL6. However, stomatal conductance and transpiration rate were elevated in *cat2-1* and the *pertlt6-1 x cat2-1* double mutant compared to WT, with double mutant displaying the highest values (Figure 3.33). This supports the thesis that CAT2 deficiency affects guard cells leading to increased stomatal opening independently on photosynthetic demand, as supported by unchanged Fv/Fm and ETR. The further increase in gsw in double mutant implies that loss of PERTL6 exacerbated this dysregulation, possibly by impairing the ROS homeostasis or signaling pathways that control stomatal closure. CO_2 assimilation measurements showed no differences between the double mutants of *pertl6-1 x gr1-1* and single mutants, while under prolonged warming VPD of the double mutants resembled *gr1-1* rather than *pertl6-1*, suggesting that for certain traits, *gr1-1* is dominant, whereas under salt stress *pertl6* plays the decisive role (Figure 3.33).

Chemical inhibition of CAT activity by 3-aminotriazole (3-AT) impairs seed germination in WT (Bi et al., 2017). Similarly, *cat2-1* mutants showed delayed germination under control and salt stress conditions compared to WT, with the double mutant resembling *cat2-1* rather than *perlt6-1* (Figure 3.28, Figure 3.35). This reinforces the dominant role of CAT2 in germination-related oxidative stress tolerance. Probable cause of their delay is the accumulation of H_2O_2 during imbibition, as function of CAT2 is abolished.

Expression analysis revealed elevated *PERTL6* transcript levels in *cat2-1* under salt stress, but not under control conditions. Notably, *HSFA1A* expression was higher in double mutant even under control conditions, suggesting a possible antagonistic or compensatory effect between these two pathways (Figure 3.39). Metabolic profiling data following CO_2 shift, further support epistasis, as the double mutant *pertl6-1 x cat2-1* resembled *cat2-1* (Figure 3.40). While *pertl6-1* line exhibited rather increased TCA cycle intermediates, probably

suggesting enhanced mitochondrial metabolite flux in response to stress and redox imbalance, *cat2-1* and the *pertl6-1 x cat2-1* accumulated sugars, suggesting activation of oxidative pentose phosphate pathway. The selective drop in ornithine levels only visible in *pertl6-1* mutant highlights a unique role of PERTL6 in nitrogen metabolism, possibly linked to polyamine or proline pathways. These findings also suggest that CAT2 plays the dominant role in determining the metabolic stress phenotype in the double mutant with *pertl6-1* and PERTL6 may contribute to maintaining the nitrogen and redox homeostasis under stress.

Taken together, the genetic interaction analyses between PERTL6 and CAT2/GR1 highlights that PERTL6 contributes to oxidative stress responses in *Arabidopsis* that are probably independent and secondary to major ROS scavengers like CAT2 and GR1. The dominant phenotype of CAT in the double mutant suggests that PERTL6 either acts in the same redox regulatory pathway parallel or downstream CAT2. In the parallel pathway, PERTL6 alone cannot mitigate ROS effectively when CAT2 is missing, so its contribution becomes irrelevant for the observed phenotype in the double mutant. Alternately, if PERTL6 operates downstream CAT2, possibly by transporting redox cofactors to support the antioxidative metabolism, its function is masked in the absence of CAT2. This positions PERTL6 as a peroxisomal transporter that is not a primary scavenger, but a modulator of peroxisomal balance.

4.7. Metabolic signatures highlight PERTL6's role in stress adaptation

Metabolic profiling across diverse abiotic stresses like heat shock, prolonged warming, salt stress, photorespiratory shift and extended darkness revealed consistent alterations in *pertl6* mutant lines compared to WT. The absence of PERTL6 altered amino acid metabolism, modified polyamine levels, disrupted TCA cycle, and changed metabolites levels linked to lipid turnover, suggesting PERTL6 plays a crucial role in abiotic stress responses by modulating metabolic plasticity and redox balance in *Arabidopsis thaliana*.

Amino acids are central metabolites in plant stress physiology, functioning as osmoprotectants, signaling molecules and nitrogen reservoirs – often reflecting increased protein degradation under stress. Proline, a well-known osmoprotectant accumulated substantially in WT as expected (Sánchez-Vicente & Lorenzo, 2021; G. Winter et al., 2015), under salt stress but not in *perlt6-1* (Figure 3.38), suggesting altered stress perception or proline metabolism. Proline is also a precursor for ornithine synthesis, which feeds into the

polyamine synthesis pathway through putrescine, spermidine and spermine. Notably, *pertl6-1* exhibited elevated ornithine level relative to WT, supporting the idea that proline may be converted toward ornithine and PAs synthesis in mutants as part of the stress response, given polyamines critical signaling role under stress (Buezo et al., 2025). Moreover, ornithine, citrulline, fumarate and arginine are also key intermediates in urea cycle (Buezo et al., 2025). During prolonged warming, the urea cycle intermediates showed opposing trends, as arginine, ornithine and fumarate were more abundant in mutants than in WT, whereas citrulline was reduced (Figure 3.34). Under heat stress ornithine levels were similar in WT and mutants (Figure 3.32). These dynamic shifts suggest that PERTL6 might be involved in nitrogen metabolism or urea cycle regulation, critical under stress when nitrogen mobilization is essential. Elevated levels of BCAAs (valine, leucine and isoleucine) after heat and extended darkness (Figure 3.32, Figure 3.43) suggests enhanced proteolysis, a common response to oxidative stress as an adaptive mechanism (Palma et al., 2002).

Polyamines and GABA act as stress signaling molecules connected to ROS scavenging (Blázquez, 2024; Ramos-Ruiz et al., 2019). Putrescine levels were markedly higher in mutants compared to WT after prolonged warming, yet not after heat shock (Figure 3.32, Figure 3.34). Elevated level only after recovery, suggests a role in acclimation rather than immediate stress response. GABA, typically accumulating under stress (Ramos-Ruiz et al., 2019; Xu et al., 2022), was surprisingly lower in *pertl6* lines under prolonged warming compared to WT (Figure 3.34). These altered PA and GABA levels suggest that PERTL6 affects pathways crucial for maintaining redox balance and stress signaling.

The TCA cycle and photorespiratory intermediates were altered by PERTL6 disruption, particularly under stress, suggesting impact on redox-related metabolism and energy conversion. Citrate and isocitrate levels decreased upon heat stress (Figure 3.32) but increased upon prolonged warming and darkness, pointing to a complex alteration in the TCA cycle possibly linked to crosstalk with the urea cycle. Photorespiratory intermediates glycine and serine were strongly reduced in *pertl6-1* relative to WT following photorespiratory shift (Figure 3.40). Given that photorespiration in peroxisomes generates hydrogen peroxide, these findings imply disturbed photorespiration in *perlt6* mutants potentially exacerbating oxidative stress. Slight changes in glycolate and glycerate levels further support this.

Ethanolamine, a precursor for phospholipid synthesis (Kwon et al., 2012) showed marked difference between *pert6* line and WT under heat, prolonged warming, and darkness (Figure 3.32, Figure 3.34, Figure 3.43). Elevated ethanolamine in mutants under warming but

decreased after heat and stable levels after darkness (vs. WT decrease) suggest altered membrane lipid turnover or stress signaling in *pertl6* mutants, consistent with the confirmed subcellular localization of PERTL6.

These metabolic changes detected in PERTL6 partially overlap with those reported in other oxidative stress metabolic profiling experiments (Savchenko & Tikhonov, 2021) where TCA cycle intermediates decreased and ornithine increased upon stress. Overall, the results obtained support the hypothesis that PERTL6 is involved in stress response by modulating redox homeostasis, nitrogen metabolism and stress signaling pathways.

It is important to note that these metabolic analyses were conducted on whole rosettes or leaf tissues, which may mask peroxisome-specific metabolic dynamic critical for PERTL6's function. Moreover, metabolite profiling represents snapshots at specific time points, thus kinetic studies using stable isotopes labelling under stress exposure would clarify the timing and metabolic fluxes. Some metabolic changes, such as amino acid increases due to protein turnover, could represent general stress responses rather than PERTL6-specific roles. Finally, differences observed between *pertl6-1* and *pertl6-6* mutants highlight the need for inclusion of another line in further studies.

In summary, the metabolic profile of PERTL6 places it on the crossroad of nitrogen metabolism, redox homeostasis and membrane dynamic – all critical for plant stress resilience. Consistent alterations in amino acids, polyamines and organic acids across heat, warming, salt, photorespiratory and dark stress position PERTL6 as an important player in abiotic stress adaptation. Arginine and ornithine emerged as promising candidate substrates for PERTL6, providing a further focus direction for biochemical characterization to test the specificity of PERTL6.

4.8. PERTL6 as putative arginine/ornithine transporter

Considering all the above presented results with their interpretation aimed to characterize PERTL6, a putative peroxisomal transporter in *Arabidopsis,* particularly its involvement in oxidative stress response, arginine and ornithine emerged as potential metabolic candidates for substrates for PERTL6.

One of the most consistent findings across stressed and non-stress conditions was the alteration in metabolic pathway in the arginine-ornithine-proline pathway. Excessive accumulation of ornithine and arginine in *perlt6* lines upon stress could implicate its impaired

catabolism, possibly due to reduced transport or arginine or ornithine through peroxisomal membrane. Arginine stands out among amino acids for its highest nitrogen to carbon ratio, making it a good nitrogen reservoir. It's synthesized via ornithine pathway and used for proline biosynthesis as well as a precursor for peroxisomal NO and PAs. Therefore, arginine is very important in activating these related defense mechanisms as well as serves as nitrogen supply (Funck et al., 2008; L. Palmieri et al., 1997; G. Winter et al., 2015). Ornithine is a precursor for proline, which acts as osmoprotectant and ROS scavenger. Interestingly, proline did not consistently accumulate, suggesting a metabolic bottleneck on this pathway between ornithine and proline synthesis.

This observed alterations in ornithine and arginine levels are closely connected to disturbance in urea cycle reactions in plants. Although the urea cycle in plants is distinct from this in animals that take place in mitochondria, peroxisomes are indeed involved in arginine catabolism and nitrogen recycling (Buezo et al., 2025). Accumulation of upstream intermediates of urea cycle suggests disrupted cycle, potentially leading to impaired production of urea. This has implications on nitrogen thus energy metabolism, under stress when efficient recycling is critical for sustaining robust metabolism and ROS detoxification.

Thus, organic acid profile was affected, notably TCA cycle intermediates were decreased. This is connected to peroxisomal metabolism through production of acyl-CoA during β-oxidation in peroxisomes, which are later used in TCA cycle for energy production. However, tested alteration of TCA by measuring carbon release during dark respiration (Figure 3.42) did not show any changes under non-stressful conditions, indicating the perturbations are mostly occurring during stress, and especially after salt stress. The decrease in fumarate, malate and succinate could indicate a shift in carbon metabolism, potentially a downstream effect of impaired nitrogen metabolism given the interaction between urea cycle and TCA intermediates via fumarate.

Another important molecules connected to disturbed ornithine and arginine are polyamines. Putrescine, spermidine and spermine are synthesized from them and closely related to oxidative stress responses (Blázquez, 2024). In *pertl6* PA levels increases after warming, which could be an effect of impaired ROS scavenging. Polyamine oxidases also contribute to ROS production, by generating H_2O_2 as by-products, thus if PERTL6 lacks transporter responsible for importing or exporting PAs precursors, it can disrupt PAs homeostasis and ROS balance. Furthermore, GABA a product of catabolism of PAs decreased in stress in *pertl6* lines, supporting this thesis.

Comparing acute heat stress and prolonged warming, they both revealed some overlapping but distinct metabolic signatures. Heat stress triggered increase of osmoprotectant like raffinose, proline and amino acids like GABA, isoleucine, while under prolonged warming led to more pronounced shifts in organic acids, possibly in response to prolonged stress adaptation. When integrating the results from all oxidative conditions tested, a consistent pattern emerges: *perlt6* mutants accumulate nitrogen-rich amino acids, this supports a model in which PERTL6 would act as arginine/ornithine transporter across the peroxisomal membrane. This would directly connect the peroxisomal metabolism in both urea-cycle pathway and TCA cycle via fumarate.

In the model PERTL6 supports the antioxidative system with the import of nitrogen-rich amino acids such as arginine or ornithine, into peroxisomes. The absence of PERTL6 in algae and its conservation in land plants, where oxidative stress is predominant, supports the idea that PERTL6 plays a tuning role in redox regulation, complementing the major ROS scavengers like CAT or ASC-GSH cycle. This also explains why the physiological phenotype of *pertl6* mutants under stress is mild, despite clear metabolic alterations.

Exclusion of other potential substrates such as ASC and GSH is based on the lack of clear metabolic connection and lack of experimental evidence for their uptake. Unpublished data (Ferdinando Palmieri, Laboratory of Biochemistry and Molecular Biology, Department of Pharmaco-Biology, University of Bari; personal communication) indicate slow Arg transport activity in reconstituted PERTL6 expressed in *E.coli,* suggesting potential specificity, however, requires further optimization. Additional unpublished data (Francisco Javier Corpas, Group of Antioxidant, Free Radical and Nitric Oxide in Biotechnology, Food and Agriculture, Department of Biochemistry, Cell and Molecular Biology of Plants, Estación Experimental del Zaidín, CSIC; personal communication) showed that dehydrogenases involved in NADPH generation (NADP-ICDH, NADP-ME, G6PDH, 6PGDH) showed higher difference of enzymatic activity in *perlt6-1* under salt stress/control compared to WT, suggesting that when *pertl6* is under stress need to increase NADPH concentration meaning that loss of PERTL6 is compensated by increase of activity of dehydrogenases. NADP transport into peroxisomes is not required as peroxisomes have OPPP pathway that can regenerate the substrate for ASC-GSH cycle. Additionally, NAD imported through PXN can be phosphorylated by NAD kinase inside peroxisomes to support antioxidative activity. This aligns with the hypothesis that PERTL6 loss disrupts urea cycle associated with energy metabolism.

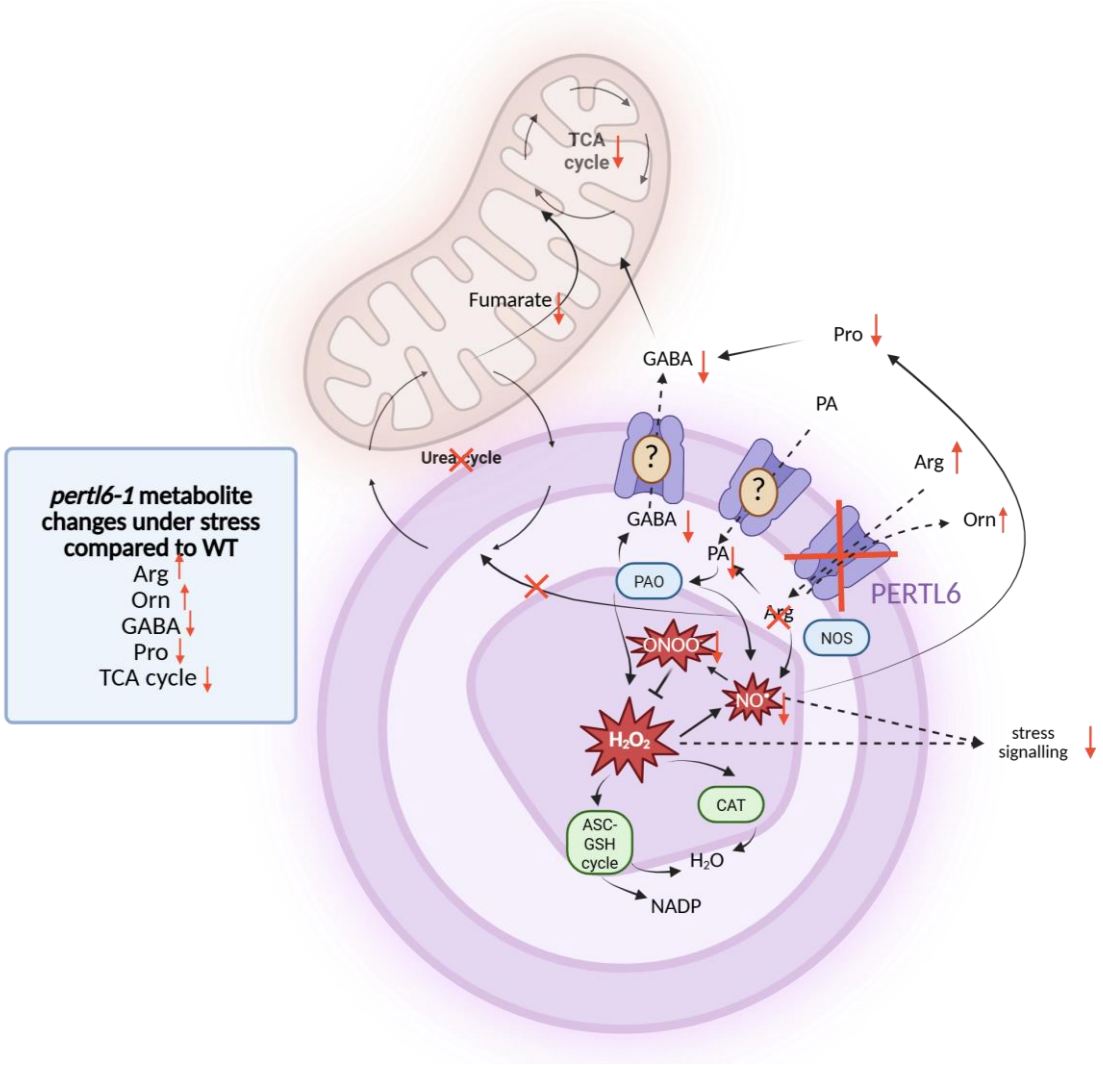

Figure 4.2 Model of loss of PERTL6 as an arginine /ornithine transporter and its consequences on metabolic network compared to WT

Red arrows indicate increase (arrow up) and decrees (arrow down) of metabolites in *perlt6* lines compared to WT under stress. Abbreviations: ASC - ascorbate, AOX – acyl-CoA oxidase, Arg – arginine, CAT – catalase, GABA - γ-aminobutyric acid, GOX – glycolate oxidase, GSH - glutathione, GSNO - S-nitrosoglutathione, NADP - nicotinamide adenine dinucleotide phosphate, NO• – nitric oxide, NOS – nitric oxide synthase, $ONOO^-$ – peroxynitrite, Orn – ornithine, PA – polyamines, PAO – polyamine oxidase, Pro – proline, TCA cycle – tricarboxylic acid cycle.

Key aspects of the model:

- Under normal conditions: PERTL6 facilitates the antiport of substrates for polyamine synthesis and urea-like cycle in peroxisomes, supporting the antioxidative signaling pathways and ROS scavenging
- Under stress conditions: PERTL6 role become more relevant as Arginine-derived NO and PA are needed for proper stress signaling and redox activation pathways

- Loss of PERTL6: Leads to metabolic disruption, including altered PA levels, disrupted TCA flux and higher sensitivity to oxidative stress. Major ROS scavengers such as CAT and GSH-ASC are less effectively supported due to inefficient substrate transport. Decreased GABA levels result from reduced Pro availability and impaired PAs catabolism. In WT, Orn is converted into Pro, supporting GABA synthesis and maintaining fumarate levels. In *pertl6* mutants this flux is disrupted reducing both urea cycle and TCA intermediates (Figure 4.2).

Future experiments to verify the model should focus on proving the transport activity of arginine/ornithine by reconstituting the protein into a liposome; testing the metabolic fluxes using stable isotope labelling; checking the enzyme activity like PAO and NOS; monitoring the redox state within different cellular compartments using redox biosensors; verifying if PERTL6 might be dual targeted by checking its subcellular localization during stress; phenotyping genetic crosses of *perlt6* with mutants lacking enzymes acting in Arg/PAO pathways.

Together, this thesis integrates the PERTL6 function into the broader understanding of stress adaptation, directly addressing the aim and elucidating its contribution to peroxisomal metabolic resource allocation and oxidative stress tolerance in *Arabidopsis thaliana*. It emphasizes the connection between nitrogen metabolism, polyamine signaling, redox homeostasis demonstrating how single transporter can influence stress adaptation and metabolic network.

5. Reference list

Aigner, S., Glaser, K., Arc, E., Holzinger, A., Schletter, M., Karsten, U., & Kranner, I. (2020). Adaptation to Aquatic and Terrestrial Environments in Chlorella vulgaris (Chlorophyta). *Frontiers in Microbiology*, *11*, 585836. https://doi.org/10.3389/FMICB.2020.585836/FULL

Albihlal, W. S., Irabonosi, O., Blein, T., Persad, R., Chernukhin, I., Crespi, M., Bechtold, U., & Mullineaux, P. M. (2018). Arabidopsis HEAT SHOCK TRANSCRIPTION FACTORA1b regulates multiple developmental genes under benign and stress conditions. *Journal of Experimental Botany*, *69*(11), 2847–2862. https://doi.org/10.1093/JXB/ERY142

Allakhverdiev, S. I., Kreslavski, V. D., Klimov, V. V., Los, D. A., Carpentier, R., & Mohanty, P. (2008). Heat stress: An overview of molecular responses in photosynthesis. *Photosynthesis Research*, *98*(1–3), 541–550. https://doi.org/10.1007/S11120-008-9331-0/METRICS

Apel, K., & Hirt, H. (2004). Reactive oxygen species: Metabolism, oxidative stress, and signal transduction. In *Annual Review of Plant Biology* (Vol. 55, pp. 373–399). https://doi.org/10.1146/annurev.arplant.55.031903.141701

Astier, J., Gross, I., & Durner, J. (2018). Nitric oxide production in plants: An update. In *Journal of Experimental Botany* (Vol. 69, Issue 14, pp. 3401–3411). Oxford University Press. https://doi.org/10.1093/jxb/erx420

Bachhawat, A. K., Thakur, A., Kaur, J., & Zulkifli, M. (2013). Glutathione transporters. *Biochimica et Biophysica Acta (BBA) - General Subjects*, *1830*(5), 3154–3164. https://doi.org/10.1016/J.BBAGEN.2012.11.018

Bao, H., Morency, M., Rianti, W., Saeheng, S., Roje, S., Weber, A. P. M., & Walker, B. J. (2021). Catalase protects against nonenzymatic decarboxylations during photorespiration in Arabidopsis thaliana. *Plant Direct*, *5*(12). https://doi.org/10.1002/pld3.366

Basak, I., Pal, R., Patil, K. S., Dunne, A., Ho, H. P., Lee, S., Peiris, D., Maple-Grødem, J., Odell, M., Chang, E. J., Larsen, J. P., & Møller, S. G. (2014). Arabidopsis AtPARK13, Which Confers Thermotolerance, Targets Misfolded Proteins. *Journal of Biological Chemistry*, *289*(21), 14458–14469. https://doi.org/10.1074/JBC.M114.548156

Baune, M. C., Lansing, H., Fischer, K., Meyer, T., Charton, L., Linka, N., & von Schaewen, A. (2020). The Arabidopsis Plastidial Glucose-6-Phosphate Transporter GPT1 is Dually Targeted to Peroxisomes via the Endoplasmic Reticulum. *The Plant Cell*, *32*(5), 1703–1726. https://doi.org/10.1105/TPC.19.00959

Bernhardt, K., Wilkinson, S., Weber, A. P. M., & Linka, N. (2012). A peroxisomal carrier delivers NAD+ and contributes to optimal fatty acid degradation during storage oil mobilization. *The Plant Journal*, *69*(1), 1–13. https://doi.org/10.1111/J.1365-313X.2011.04775.X

Berry, J. O., Yerramsetty, P., Zielinski, A. M., & Mure, C. M. (2013). Photosynthetic gene expression in higher plants. *Photosynthesis Research*, *117*(1–3), 91–120. https://doi.org/10.1007/S11120-013-9880-8/FIGURES/5

Bertani, G. (1951). *STUDIES ON LYSOGENESIS I. THE MODE OF PHAGE LIBERATION BY LYSOGENIC ESCHERICHIA COLI1*. https://journals.asm.org/journal/jb

Bi, C., Ma, Y., Wu, Z., Yu, Y. T., Liang, S., Lu, K., & Wang, X. F. (2017). Arabidopsis ABI5 plays a role in regulating ROS homeostasis by activating CATALASE 1 transcription in seed germination. *Plant Molecular Biology*, *94*(1), 197. https://doi.org/10.1007/S11103-017-0603-Y

Blázquez, M. A. (2024). Polyamines: Their Role in Plant Development and Stress. *Annual Review of Plant Biology*, *75*(1), 95–117. https://doi.org/10.1146/ANNUREV-ARPLANT-070623-110056,

Borgohain, P., Saha, B., Agrahari, R., Chowardhara, B., Sahoo, S., van der Vyver, C., & Panda, S. K. (2019). SlNAC2 overexpression in Arabidopsis results in enhanced abiotic stress tolerance with alteration in glutathione metabolism. *Protoplasma*, *256*(4), 1065–1077. https://doi.org/10.1007/S00709-019-01368-0/FIGURES/7

Bowles, A. M. C., Paps, J., & Bechtold, U. (2022). Water-related innovations in land plants evolved by different patterns of gene cooption and novelty. *New Phytologist*, *235*(2), 732–742. https://doi.org/10.1111/NPH.17981;PAGE:STRING:ARTICLE/CHAPTER

Brown, L. A., & Baker, A. (2008). Shuttles and cycles: Transport of proteins into the peroxisome matrix (Review). *Molecular Membrane Biology*, *25*(5), 363–375. https://doi.org/10.1080/09687680802130583;REQUESTEDJOURNAL:JOURNAL:IMBC20;WGROUP:STRING:PUBLICATION

Bueso, E., Alejandro, S., Carbonell, P., Perez-Amador, M. A., Fayos, J., Bellés, J. M., Rodriguez, P. L., & Serrano, R. (2007). The lithium tolerance of the Arabidopsis cat2 mutant reveals a cross-talk between oxidative stress and ethylene. *Plant Journal*, *52*(6), 1052–1065. https://doi.org/10.1111/j.1365-313X.2007.03305.x

Buezo, J., Urra, M., González, E. M., Alcázar, R., Marino, D., & Moran, J. F. (2025). The Urea Cycle in Connection to Polyamine Metabolism in Higher Plants: New Perspectives on a Central Pathway. In *Physiologia Plantarum* (Vol. 177, Issue 3). John Wiley and Sons Inc. https://doi.org/10.1111/ppl.70321

Bussell, J. D., Behrens, C., Ecke, W., & Eubel, H. (2013). Arabidopsis peroxisome proteomics. *Frontiers in Plant Science*, *4*(APR), 41930. https://doi.org/10.3389/FPLS.2013.00101/BIBTEX

Bykova, N. V., & Igamberdiev, A. U. (2025). Redox Control of Seed Germination is Mediated by the Crosstalk of Nitric Oxide and Reactive Oxygen Species. *Antioxidants and Redox Signaling*, *42*(7–9), 442–461. https://doi.org/10.1089/ARS.2024.0699/ASSET/IMAGES/ARS.2024.0699_FIGURE8.JPG

Carrie, C., Kühn, K., Murcha, M. W., Duncan, O., Small, I. D., O'Toole, N., & Whelan, J. (2009). Approaches to defining dual-targeted proteins in Arabidopsis. *Plant Journal*, *57*(6), 1128–1139. https://doi.org/10.1111/J.1365-313X.2008.03745.X;SUBPAGE:STRING:FULL

Charton, L., Plett, A., & Linka, N. (2019). Plant peroxisomal solute transporter proteins. In *Journal of Integrative Plant Biology* (Vol. 61, Issue 7, pp. 817–835). Blackwell Publishing Ltd. https://doi.org/10.1111/jipb.12790

Chaudhry, S., & Sidhu, G. P. S. (2021). Climate change regulated abiotic stress mechanisms in plants: a comprehensive review. *Plant Cell Reports 2021 41:1*, *41*(1), 1–31. https://doi.org/10.1007/S00299-021-02759-5

Chow, C. N., Yang, C. W., Wu, N. Y., Wang, H. T., Tseng, K. C., Chiu, Y. H., Lee, T. Y., & Chang, W. C. (2024). PlantPAN 4.0: updated database for identifying conserved non-coding sequences and exploring dynamic transcriptional regulation in plant promoters. *Nucleic Acids Research*, *52*(D1), D1569–D1578. https://doi.org/10.1093/NAR/GKAD945

Clough, S. J., & Bent, A. F. (1998). Floral dip: a simplified method for Agrobacterium -mediated transformation of Arabidopsis thaliana. *The Plant Journal*, *16*(6), 735–743. https://doi.org/10.1046/J.1365-313X.1998.00343.X

Corpas, F. J., & Barroso, J. B. (2018). Peroxisomal plant metabolism - An update on nitric oxide, Ca 2+ and the NADPH recycling network. In *Journal of Cell Science* (Vol. 131, Issue 2). Company of Biologists Ltd. https://doi.org/10.1242/jcs.202978

Corpas, F. J., González-Gordo, S., & Palma, J. M. (2020). Plant Peroxisomes: A Factory of Reactive Species. In *Frontiers in Plant Science* (Vol. 11). Frontiers Media S.A. https://doi.org/10.3389/fpls.2020.00853

Corpas, F. J., González-Gordo, S., & Palma, J. M. (2021). Nitric oxide and hydrogen sulfide modulate the NADPH-generating enzymatic system in higher plants. *Journal of Experimental Botany*, *72*(3), 830–847. https://doi.org/10.1093/jxb/eraa440

Corpet, F. (1988). Multiple sequence alignment with hierarchical clustering. *Nucleic Acids Research*, *16*(22), 10881–10890. https://doi.org/10.1093/NAR/16.22.10881

Crabeel, M., Soetens, O., De Rijcke, M., Pratiwi, R., & Pankiewicz, R. (1996). The ARG11 gene of Saccharomyces cerevisiae encodes a mitochondrial integral membrane protein required for arginine biosynthesis. *Journal of Biological Chemistry*, *271*(40), 25011–25018. https://doi.org/10.1074/jbc.271.40.25011

Cui, Y., Zhao, S., Wang, J., Wang, X., Gao, B., Fan, Q., Sun, F., & Zhou, B. (2015). A novel mitochondrial carrier protein Mme1 acts as a yeast mitochondrial magnesium exporter. *Biochimica et Biophysica Acta - Molecular Cell Research*, *1853*(3), 724–732. https://doi.org/10.1016/J.BBAMCR.2014.12.029

Del Río, L. A., & López-Huertas, E. (2016). ROS generation in peroxisomes and its role in cell signaling. In *Plant and Cell Physiology* (Vol. 57, Issue 7, pp. 1364–1376). Oxford University Press. https://doi.org/10.1093/pcp/pcw076

Del-Saz, N. F., Douthe, C., Carriquí, M., Ortíz, J., Sanhueza, C., Rivas-Medina, A., McDonald, A., Fernie, A. R., Ribas-Carbo, M., Gago, J., Florez-Sarasa, I., & Flexas, J. (2021). Different Metabolic Roles for Alternative Oxidase in Leaves of Palustrine and Terrestrial Species. *Frontiers in Plant Science*, *12*, 752795. https://doi.org/10.3389/FPLS.2021.752795/XML

Devi, S. R., Chen, X., Oliver, D. J., & Xiang, C. (2006). A novel high-throughput genetic screen for stress-responsive mutants of Arabidopsis thaliana reveals new loci involving stress responses. *The Plant Journal*, *47*(4), 652–663. https://doi.org/10.1111/J.1365-313X.2006.02814.X

Dhatterwal, P., Mehrotra, S., Miller, A. J., Aduri, R., & Mehrotra, R. (2022). Effect of ACGT motif in spatiotemporal regulation of AtAVT6D, which improves tolerance to osmotic stress and nitrogen-starvation. *Plant Molecular Biology*, *109*(1–2), 67–82. https://doi.org/10.1007/S11103-022-01256-X/FIGURES/7

Dixon, D. P., Lapthorn, A., & Edwards, R. (2002). Plant glutathione transferases. *Genome Biology*, *3*(3), reviews3004.1. https://doi.org/10.1186/GB-2002-3-3-REVIEWS3004

Eastmond, P. J. (2007). Monodehyroascorbate reductase4 is required for seed storage oil hydrolysis and postgerminative growth in Arabidopsis. *Plant Cell*, *19*(4), 1376–1387. https://doi.org/10.1105/tpc.106.043992

Eljebbawi, A., Guerrero, Y. del C. R., Dunand, C., & Estevez, J. M. (2021). Highlighting reactive oxygen species as multitaskers in root development. *IScience*, *24*(1), 101978. https://doi.org/10.1016/J.ISCI.2020.101978

Emms, D. M., & Kelly, S. (2019). OrthoFinder: Phylogenetic orthology inference for comparative genomics. *Genome Biology*, *20*(1), 1–14. https://doi.org/10.1186/S13059-019-1832-Y/FIGURES/5

Emms, D. M., & Kelly, S. (2022). SHOOT: phylogenetic gene search and ortholog inference. *Genome Biology*, *23*(1), 1–13. https://doi.org/10.1186/S13059-022-02652-8/FIGURES/4

Engler, C., Kandzia, R., & Marillonnet, S. (2008). A one pot, one step, precision cloning method with high throughput capability. *PLoS ONE*, *3*(11). https://doi.org/10.1371/journal.pone.0003647

Engler, C., Youles, M., Gruetzner, R., Ehnert, T. M., Werner, S., Jones, J. D. G., Patron, N. J., & Marillonnet, S. (2014). A Golden Gate modular cloning toolbox for plants. *ACS Synthetic Biology*, *3*(11), 839–843. https://doi.org/10.1021/sb4001504

Fiermonte, G., Dolce, V., David, L., Santorelli, F. M., Dionisi-Vici, C., Palmieri, F., & Walker, J. E. (2003). The mitochondrial ornithine transporter: Bacterial expression, reconstitution, functional characterization, and tissue distribution of two human isoforms. *Journal of Biological Chemistry*, *278*(35), 32778–32783. https://doi.org/10.1074/JBC.M302317200,

Fonseca, J. P., Griffiths, M., York, L. M., & Mysore, K. S. (2021). Dark Respiration Measurement from Arabidopsis Shoots. *Bio-Protocol*, *11*(19), e4181. https://doi.org/10.21769/BIOPROTOC.4181

Foyer, C. H., & Noctor, G. (2003). Redox sensing and signalling associated with reactive oxygen in chloroplasts, peroxisomes and mitochondria. *Physiologia Plantarum*, *119*(3), 355–364. https://doi.org/10.1034/J.1399-3054.2003.00223.X

Fu, X., Gregory, L. M., Weise, S. E., & Walker, B. J. (2023). Integrated flux and pool size analysis in plant central metabolism reveals unique roles of glycine and serine during photorespiration. *Nature Plants*, *9*(1), 169–178. https://doi.org/10.1038/s41477-022-01294-9

Fuchs, P., Rugen, N., Carrie, C., Elsässer, M., Finkemeier, I., Giese, J., Hildebrandt, T. M., Kühn, K., Maurino, V. G., Ruberti, C., Schallenberg-Rüdinger, M., Steinbeck, J., Braun, H. P., Eubel, H., Meyer, E. H., Müller-Schüssele, S. J., & Schwarzländer, M.

(2020). Single organelle function and organization as estimated from Arabidopsis mitochondrial proteomics. *Plant Journal*, *101*(2), 420–441. https://doi.org/10.1111/tpj.14534

Funck, D., Stadelhofer, B., & Koch, W. (2008). Ornithine-δ-aminotransferase is essential for Arginine Catabolism but not for Proline Biosynthesis. *BMC Plant Biology*, *8*. https://doi.org/10.1186/1471-2229-8-40

Goodstein, D. M., Shu, S., Howson, R., Neupane, R., Hayes, R. D., Fazo, J., Mitros, T., Dirks, W., Hellsten, U., Putnam, N., & Rokhsar, D. S. (2012). Phytozome: a comparative platform for green plant genomics. *Nucleic Acids Research*, *40*(D1), D1178–D1186. https://doi.org/10.1093/NAR/GKR944

Graham, I. A. (2008a). Seed storage oil mobilization. In *Annual Review of Plant Biology* (Vol. 59, pp. 115–142). https://doi.org/10.1146/annurev.arplant.59.032607.092938

Graham, I. A. (2008b). Seed storage oil mobilization. *Annual Review of Plant Biology*, *59*, 115–142. https://doi.org/10.1146/ANNUREV.ARPLANT.59.032607.092938,

Gregory, L. M., McClain, A. M., Kramer, D. M., Pardo, J. D., Smith, K. E., Tessmer, O. L., Walker, B. J., Ziccardi, L. G., & Sharkey, T. D. (2021). The triose phosphate utilization limitation of photosynthetic rate: Out of global models but important for leaf models. *Plant, Cell & Environment*, *44*(10), 3223–3226. https://doi.org/10.1111/PCE.14153

Guo, H., Wang, Y., Wang, L., Hu, P., Wang, Y., Jia, Y., Zhang, C., Zhang, Y., Zhang, Y., Wang, C., & Yang, C. (2016). Expression of the MYB transcription factor gene BplMYB46 affects abiotic stress tolerance and secondary cell wall deposition in Betula platyphylla. *Plant Biotechnology Journal*, *15*(1), 107. https://doi.org/10.1111/PBI.12595

Halliwell, B., & Foyer, C. H. (1976). Ascorbic acid, metal ions and the superoxide radical. *Biochemical Journal*, *155*(3), 697–700. https://doi.org/10.1042/BJ1550697,

Han, Y., Chaouch, S., Mhamdi, A., Queval, G., Zechmann, B., & Noctor, G. (2013). Functional analysis of arabidopsis mutants points to novel roles for glutathione in coupling H2O2 to activation of salicylic acid accumulation and signaling. *Antioxidants and Redox Signaling*, *18*(16), 2106–2121. https://doi.org/10.1089/ARS.2012.5052/SUPPL_FILE/SUPP_FIG6.PDF

Haralampidis, K., Milioni, D., Rigas, S., & Hatzopoulos, P. (2002). Combinatorial Interaction of Cis Elements Specifies the Expression of the Arabidopsis AtHsp90-1 Gene. *Plant Physiology*, *129*(3), 1138. https://doi.org/10.1104/PP.004044

Hasanuzzaman, M., Nahar, K., Anee, T. I., & Fujita, M. (2017). Glutathione in plants: biosynthesis and physiological role in environmental stress tolerance. *Physiology and Molecular Biology of Plants*, *23*(2), 249. https://doi.org/10.1007/S12298-017-0422-2

Higo, K., Ugawa, Y., Iwamoto, M., & Korenaga, T. (1999). Plant cis-acting regulatory DNA elements (PLACE) database: 1999. *Nucleic Acids Research*, *27*(1), 297–300. https://doi.org/10.1093/NAR/27.1.297

Hooper, C. M., Castleden, I. R., Tanz, S. K., Aryamanesh, N., & Millar, A. H. (2017). SUBA4: The interactive data analysis centre for Arabidopsis subcellular protein locations. *Nucleic Acids Research*, *45*(D1), D1064–D1074. https://doi.org/10.1093/NAR/GKW1041

Hu, J., Baker, A., Bartel, B., Linka, N., Mullen, R. T., Reumann, S., & Zolman, B. K. (2012). Plant peroxisomes: Biogenesis and function. In *Plant Cell* (Vol. 24, Issue 6, pp. 2279–2303). American Society of Plant Biologists. https://doi.org/10.1105/tpc.112.096586

Huang, Y. C., Niu, C. Y., Yang, C. R., & Jinn, T. L. (2016). The Heat Stress Factor HSFA6b Connects ABA Signaling and ABA-Mediated Heat Responses. *Plant Physiology*, *172*(2), 1182–1199. https://doi.org/10.1104/PP.16.00860

Jagadish, S. V. K., Way, D. A., & Sharkey, T. D. (2021). Plant heat stress: Concepts directing future research. In *Plant Cell and Environment* (Vol. 44, Issue 7, pp. 1992–2005). Blackwell Publishing Ltd. https://doi.org/10.1111/pce.14050

Kapoor, B., Kumar, P., Verma, V., Irfan, M., Sharma, R., & Bhargava, B. (2022). How plants conquered land: evolution of terrestrial adaptation. *Journal of Evolutionary Biology*, *35*(5), 5–14. https://doi.org/10.1111/JEB.14062

Kelly, A. A., Quettier, A. L., Shaw, E., & Eastmond, P. J. (2011). Seed storage oil mobilization is important but not essential for germination or seedling establishment in Arabidopsis. *Plant Physiology*, *157*(2), 866–875. https://doi.org/10.1104/PP.111.181784,

Kerchev, P. I., & Van Breusegem, F. (2022a). Improving oxidative stress resilience in plants. *The Plant Journal*, *109*(2), 359–372. https://doi.org/10.1111/TPJ.15493

Kerchev, P. I., & Van Breusegem, F. (2022b). Improving oxidative stress resilience in plants. *Plant Journal*, *109*(2), 359–372. https://doi.org/10.1111/TPJ.15493

Kodaira, K. S., Qin, F., Tran, L. S. P., Maruyama, K., Kidokoro, S., Fujita, Y., Shinozaki, K., & Yamaguchi-Shinozaki, K. (2011). Arabidopsis Cys2/His2 zinc-finger proteins AZF1 and AZF2 negatively regulate abscisic acid-repressive and auxin-inducible genes under abiotic stress conditions. *Plant Physiology*, *157*(2), 742–756. https://doi.org/10.1104/PP.111.182683

Koncz, C., & Schell, J. (1986). The promoter of TL-DNA gene 5 controls the tissue-specific expression of chimaeric genes carried by a novel type of Agrobacterium binary vector. *MGG Molecular & General Genetics*, *204*(3), 383–396. https://doi.org/10.1007/BF00331014/METRICS

Kumar, R., Islinger, M., Worthy, H., Carmichael, R., & Schrader, M. (2024). The peroxisome: an update on mysteries 3.0. *Histochemistry and Cell Biology 2024 161:2*, *161*(2), 99–132. https://doi.org/10.1007/S00418-023-02259-5

Kumar, S., Stecher, G., Li, M., Knyaz, C., & Tamura, K. (2018). MEGA X: Molecular Evolutionary Genetics Analysis across Computing Platforms. *Mol. Biol. Evol.*, *35(6)*, 1547–1549. https://doi.org/10.1093/molbev/msy096

Kwon, Y., Yu, S. in, Lee, H., Yim, J. H., Zhu, J. K., & Lee, B. H. (2012). Arabidopsis Serine Decarboxylase Mutants Implicate the Roles of Ethanolamine in Plant Growth and Development. *International Journal of Molecular Sciences 2012, Vol. 13, Pages 3176-3188*, *13*(3), 3176–3188. https://doi.org/10.3390/IJMS13033176

Lee, S., & Park, C. M. (2010). Modulation of reactive oxygen species by salicylic acid in arabidopsis seed germination under high salinity. *Plant Signaling & Behavior*, *5*(12), 1534. https://doi.org/10.4161/PSB.5.12.13159

Letunic, I., & Bork, P. (2024). Interactive Tree of Life (iTOL) v6: recent updates to the phylogenetic tree display and annotation tool. *Nucleic Acids Research*, *52*(W1), W78–W82. https://doi.org/10.1093/NAR/GKAE268

Li, G., Li, J., Hao, R., & Guo, Y. (2017). Activation of catalase activity by a peroxisome-localized small heat shock protein Hsp17.6CII. *Journal of Genetics and Genomics*, *44*(8), 395–404. https://doi.org/10.1016/J.JGG.2017.03.009

Li, J., Peng, Z., Liu, Y., Lang, M., Chen, Y., Wang, H., Li, Y., Shi, B., Huang, W., Han, L., Ma, Y., Zhang, Y., & Wang, B. (2022). Overexpression of Peroxisome-Localized GmABCA7 Promotes Seed Germination in Arabidopsis thaliana. *International Journal of Molecular Sciences*, *23*(4), 2389. https://doi.org/10.3390/IJMS23042389/S1

Li, L., Millar, A. H., & Huang, S. (2017). Mitochondrial Lon1 has a role in homeostasis of the mitochondrial ribosome and pentatricopeptide repeat proteins in plants. *Plant Signaling & Behavior*, *12*(2), e1276686. https://doi.org/10.1080/15592324.2016.1276686;PAGE:STRING:ARTICLE/CHAPTER

Lingard, M. J., & Bartel, B. (2009). Arabidopsis LON2 is necessary for peroxisomal function and sustained matrix protein import. *Plant Physiology*, *151*(3), 1354–1365. https://doi.org/10.1104/PP.109.142505,

Linka, N., Theodoulou, F. L., Haslam, R. P., Linka, M., Napier, J. A., Neuhaus, H. E., & Webera, A. P. M. (2008). Peroxisomal ATP Import Is Essential for Seedling Development in Arabidopsis thaliana. *The Plant Cell*, *20*(12), 3241–3257. https://doi.org/10.1105/TPC.108.062042

Lismont, C., Nordgren, M., Van Veldhoven, P. P., & Fransen, M. (2015). Redox interplay between mitochondria and peroxisomes. *Frontiers in Cell and Developmental Biology*, *3*(MAY), 145876. https://doi.org/10.3389/FCELL.2015.00035/XML

Liu, T., Arsenault, J., Vierling, E., & Kim, M. (2021). Mitochondrial ATP synthase subunit d, a component of the peripheral stalk, is essential for growth and heat stress tolerance in Arabidopsis thaliana. *Plant Journal*, *107*(3), 713–726. https://doi.org/10.1111/TPJ.15317,

Liu, W. C., Han, T. T., Yuan, H. M., Yu, Z. D., Zhang, L. Y., Zhang, B. L., Zhai, S., Zheng, S. Q., & Lu, Y. T. (2017). CATALASE2 functions for seedling postgerminative growth by scavenging H2O2 and stimulating ACX2/3 activity in arabidopsis. *Plant Cell and Environment*, *40*(11), 2720–2728. https://doi.org/10.1111/pce.13031

Manfield, I. W., Devlin, P. F., Jen, C. H., Westhead, D. R., & Gilmartin, P. M. (2007). Conservation, Convergence, and Divergence of Light-Responsive, Circadian-Regulated, and Tissue-Specific Expression Patterns during Evolution of the Arabidopsis GATA Gene Family. *Plant Physiology*, *143*(2), 941. https://doi.org/10.1104/PP.106.090761

Marillonnet, S., & Grützner, R. (2020). Synthetic DNA Assembly Using Golden Gate Cloning and the Hierarchical Modular Cloning Pipeline. *Current Protocols in Molecular Biology*, *130*(1). https://doi.org/10.1002/cpmb.115

Marty, L., Bausewein, D., Müller, C., Bangash, S. A. K., Moseler, A., Schwarzländer, M., Müller-Schüssele, S. J., Zechmann, B., Riondet, C., Balk, J., Wirtz, M., Hell, R., Reichheld, J. P., & Meyer, A. J. (2019). Arabidopsis glutathione reductase 2 is indispensable in plastids, while mitochondrial glutathione is safeguarded by additional reduction and transport systems. *New Phytologist*, *224*(4), 1569–1584. https://doi.org/10.1111/NPH.16086;PAGEGROUP:STRING:PUBLICATION

Marty, L., Siala, W., Schwarzlä Nder C, M., Fricker, M. D., Wirtz, M., Sweetlove, L. J., Meyer, Y., Meyer, A. J., Reichheld, J.-P., & Diger Hell, R. (2009a). *The NADPH-dependent thioredoxin system constitutes a functional backup for cytosolic glutathione reductase in Arabidopsis*. www.pnas.orgcgidoi10.1073pnas.0900206106

Marty, L., Siala, W., Schwarzlä Nder C, M., Fricker, M. D., Wirtz, M., Sweetlove, L. J., Meyer, Y., Meyer, A. J., Reichheld, J.-P., & Diger Hell, R. (2009b). *The NADPH-dependent thioredoxin system constitutes a functional backup for cytosolic glutathione reductase in Arabidopsis*. www.pnas.orgcgidoi10.1073pnas.0900206106

Maruyama-Nakashita, A., Nakamura, Y., Watanabe-Takahashi, A., Inoue, E., Yamaya, T., & Takahashi, H. (2005). Identification of a novel cis-acting element conferring sulfur deficiency response in Arabidopsis roots. *The Plant Journal : For Cell and Molecular Biology*, *42*(3), 305–314. https://doi.org/10.1111/J.1365-313X.2005.02363.X

McClung, C. R. (1997). Regulation of Catalases in Arabidopsis. *Free Radical Biology and Medicine*, *23*(3), 489–496. https://doi.org/10.1016/S0891-5849(97)00109-3

Mhamdi, A., Hager, J., Chaouch, S., Queval, G., Han, Y., Taconnat, L., Saindrenan, P., Gouia, H., Issakidis-Bourguet, E., Renou, J. P., & Noctor, G. (2010). Arabidopsis GLUTATHIONE REDUCTASE1 plays a crucial role in leaf responses to intracellular hydrogen peroxide and in ensuring appropriate gene expression through both salicylic acid and jasmonic acid signaling pathways. *Plant Physiology*, *153*(3), 1144–1160. https://doi.org/10.1104/pp.110.153767

Mhamdi, A., Queval, G., Chaouch, S., Vanderauwera, S., Van Breusegem, F., & Noctor, G. (2010). Catalase function in plants: A focus on Arabidopsis mutants as stress-mimic models. In *Journal of Experimental Botany* (Vol. 61, Issue 15, pp. 4197–4220). Oxford University Press. https://doi.org/10.1093/jxb/erq282

Michaeli, S., & Fromm, H. (2015). Closing the loop on the GABA shunt in plants: Are GABA metabolism and signaling entwined? *Frontiers in Plant Science*, *6*(June), 145458. https://doi.org/10.3389/FPLS.2015.00419/BIBTEX

Mishra, S. K., Tripp, J., Winkelhaus, S., Tschiersch, B., Theres, K., Nover, L., & Scharf, K. D. (2002). In the complex family of heat stress transcription factors, HsfA1 has a unique role as master regulator of thermotolerance in tomato. *Genes & Development*, *16*(12), 1555–1567. https://doi.org/10.1101/GAD.228802

Mittler, R. (2017a). ROS Are Good. *Trends in Plant Science*, *22*(1), 11–19. https://doi.org/10.1016/J.TPLANTS.2016.08.002

Mittler, R. (2017b). ROS Are Good. *Trends in Plant Science*, *22*(1), 11–19. https://doi.org/10.1016/j.tplants.2016.08.002

Mittler, R., Zandalinas, S. I., Fichman, Y., & Van Breusegem, F. (2022). Reactive oxygen species signalling in plant stress responses. *Nature Reviews. Molecular Cell Biology*, *23*(10), 663–679. https://doi.org/10.1038/S41580-022-00499-2

Miyaji, T., Kuromori, T., Takeuchi, Y., Yamaji, N., Yokosho, K., Shimazawa, A., Sugimoto, E., Omote, H., Ma, J. F., Shinozaki, K., & Moriyama, Y. (2015). AtPHT4;4 is a chloroplast-localized ascorbate transporter in Arabidopsis. *Nature Communications*, *6*. https://doi.org/10.1038/NCOMMS6928,

Morishita, T., Kojima, Y., Maruta, T., Nishizawa-Yokoi, A., Yabuta, Y., & Shigeoka, S. (2009). Arabidopsis NAC Transcription Factor, ANAC078, Regulates Flavonoid Biosynthesis under High-light. *Plant and Cell Physiology*, *50*(12), 2210–2222. https://doi.org/10.1093/PCP/PCP159

Müller-Schüssele, S. J., Schwarzländer, M., & Meyer, A. J. (2021). Live monitoring of plant redox and energy physiology with genetically encoded biosensors. *Plant Physiology*, *186*(1), 93–109. https://doi.org/10.1093/PLPHYS/KIAB019

Nadarajah, K. K. (2020). ROS Homeostasis in Abiotic Stress Tolerance in Plants. *International Journal of Molecular Sciences*, *21*(15), 1–29. https://doi.org/10.3390/IJMS21155208

Noctor, G. (2025). Hydrogen peroxide, ascorbate, and glutathione: building the Foyer–Halliwell–Asada pathway. *Planta*, *261*(6), 1–11. https://doi.org/10.1007/S00425-025-04702-4/FIGURES/3

Noctor, G., De Paepe, R., & Foyer, C. H. (2007). Mitochondrial redox biology and homeostasis in plants. *Trends in Plant Science*, *12*(3), 125–134. https://doi.org/10.1016/J.TPLANTS.2007.01.005/ASSET/CE69ACA9-0DF5-44BB-A8A8-BC5DCE48C45F/MAIN.ASSETS/GR1B3.JPG

Obayashi, T., Hibara, H., Kagaya, Y., Aoki, Y., & Kinoshita, K. (2022). ATTED-II v11: A Plant Gene Coexpression Database Using a Sample Balancing Technique by Subagging of Principal Components. *Plant and Cell Physiology*, *63*(6), 869–881. https://doi.org/10.1093/PCP/PCAC041

Ohama, N., Kusakabe, K., Mizoi, J., Zhao, H., Kidokoro, S., Koizumi, S., Takahashi, F., Ishida, T., Yanagisawa, S., Shinozaki, K., & Yamaguchi-Shinozaki, K. (2016). The transcriptional cascade in the heat stress response of arabidopsis is strictly regulated at the level of transcription factor expression. *Plant Cell*, *28*(1), 181–201. https://doi.org/10.1105/tpc.15.00435

Pál, M., Szalai, G., & Janda, T. (2015). Speculation: Polyamines are important in abiotic stress signaling. *Plant Science*, *237*, 16–23. https://doi.org/10.1016/j.plantsci.2015.05.003

Palma, J. M., Sandalio, L. M., Javier Corpas, F., Romero-Puertas, M. C., McCarthy, I., & Del Río, L. A. (2002). Plant proteases, protein degradation, and oxidative stress: role of peroxisomes. *Plant Physiology and Biochemistry*, *40*(6–8), 521–530. https://doi.org/10.1016/S0981-9428(02)01404-3

Palmieri, F., Pierri, C. L., De Grassi, A., Nunes-Nesi, A., & Fernie, A. R. (2011). Evolution, structure and function of mitochondrial carriers: A review with new insights. *Plant Journal*, *66*(1), 161–181. https://doi.org/10.1111/j.1365-313X.2011.04516.x

Palmieri, L., De Marco, V., Iacobazzi, V., Palmieri, F., Runswick, M. J., & Walker, J. E. (1997). Identification of the yeast ARG-11 gene as a mitochondrial ornithine carrier involved in arginine biosynthesis. *FEBS Letters*, *410*(2–3), 447–451. https://doi.org/10.1016/S0014-5793(97)00630-3

Pan, R., Liu, J., Wang, S., & Hu, J. (2020). Peroxisomes: versatile organelles with diverse roles in plants. In *New Phytologist* (Vol. 225, Issue 4, pp. 1410–1427). Blackwell Publishing Ltd. https://doi.org/10.1111/nph.16134

Plett, A., Charton, L., & Linka, N. (2020). Peroxisomal Cofactor Transport. *Biomolecules 2020, Vol. 10, Page 1174*, *10*(8), 1174. https://doi.org/10.3390/BIOM10081174

Quettier, A. L., & Eastmond, P. J. (2009). Storage oil hydrolysis during early seedling growth. *Plant Physiology and Biochemistry*, *47*(6), 485–490. https://doi.org/10.1016/j.plaphy.2008.12.005

Queval, G., Issakidis-Bourguet, E., Hoeberichts, F. A., Vandorpe, M., Gakière, B., Vanacker, H., Miginiac-Maslow, M., Van Breusegem, F., & Noctor, G. (2007). Conditional oxidative stress responses in the Arabidopsis photorespiratory mutant cat2 demonstrate that redox state is a key modulator of daylength-dependent gene expression, and define photoperiod as a crucial factor in the regulation of H2O2-induced cell death. *Plant Journal*, *52*(4), 640–657. https://doi.org/10.1111/J.1365-313X.2007.03263.X;SUBPAGE:STRING:FULL

Ramos-Ruiz, R., Martinez, F., & Knauf-Beiter, G. (2019). The effects of GABA in plants. In *Cogent Food and Agriculture* (Vol. 5, Issue 1). Informa Healthcare. https://doi.org/10.1080/23311932.2019.1670553

Rauluseviciute, I., Riudavets-Puig, R., Blanc-Mathieu, R., Castro-Mondragon, J. A., Ferenc, K., Kumar, V., Lemma, R. B., Lucas, J., Chèneby, J., Baranasic, D., Khan, A., Fornes, O., Gundersen, S., Johansen, M., Hovig, E., Lenhard, B., Sandelin, A., Wasserman, W. W., Parcy, F., & Mathelier, A. (2024). JASPAR 2024: 20th anniversary of the open-access database of transcription factor binding profiles. *Nucleic Acids Research*, *52*(D1), D174–D182. https://doi.org/10.1093/NAR/GKAD1059

Raxwal, V. K., & Riha, K. (2023). The biological functions of nonsense-mediated mRNA decay in plants: RNA quality control and beyond. *Biochemical Society Transactions*, *51*(1), 31–39. https://doi.org/10.1042/BST20211231,

Redman, J., Whitcraft, J., Johnslon, C., & Arias, J. (2002). Abiotic and biotic stress differentially stimulate as-1 element activity in Arabidopsis. *Plant Cell Reports*, *21*(2), 180–185. https://doi.org/10.1007/S00299-002-0472-X

Reumann, S., & Bartel, B. (2016). Plant peroxisomes: recent discoveries in functional complexity, organelle homeostasis, and morphological dynamics. *Current Opinion in Plant Biology*, *34*, 17–26. https://doi.org/10.1016/j.pbi.2016.07.008

Rezaei, E. E., Webber, H., Asseng, S., Boote, K., Durand, J. L., Ewert, F., Martre, P., & MacCarthy, D. S. (2023). Climate change impacts on crop yields. *Nature Reviews Earth & Environment 2023 4:12*, *4*(12), 831–846. https://doi.org/10.1038/s43017-023-00491-0

Rezayian, M., Niknam, V., & Ebrahimzadeh, H. (2019). Oxidative damage and antioxidative system in algae. *Toxicology Reports*, *6*, 1309–1313. https://doi.org/10.1016/J.TOXREP.2019.10.001

Rosenwasser, S., Rot, I., Sollner, E., Meyer, A. J., Smith, Y., Leviatan, N., Fluhr, R., & Friedman, H. (2011). Organelles contribute differentially to reactive oxygen species-related events during extended darkness. *Plant Physiology*, *156*(1), 185–201. https://doi.org/10.1104/PP.110.169797,

Rylott, E. L., Eastmond, P. J., Gilday, A. D., Slocombe, S. P., Larson, T. R., Baker, A., & Graham, I. A. (2006). The Arabidopsis thaliana multifunctional protein gene (MFP2) of peroxisomal β-oxidation is essential for seedling establishment. *Plant Journal*, *45*(6), 930–941. https://doi.org/10.1111/J.1365-313X.2005.02650.X,

Sami, F., Faizan, M., Faraz, A., Siddiqui, H., Yusuf, M., & Hayat, S. (2018). Nitric oxide-mediated integrative alterations in plant metabolism to confer abiotic stress tolerance, NO crosstalk with phytohormones and NO-mediated post translational modifications in modulating diverse plant stress. *Nitric Oxide*, *73*, 22–38. https://doi.org/10.1016/J.NIOX.2017.12.005

Sánchez-Vicente, I., & Lorenzo, O. (2021). Nitric oxide regulation of temperature acclimation: A molecular genetic perspective. *Journal of Experimental Botany*, *72*(16), 5789–5794. https://doi.org/10.1093/jxb/erab049

Savchenko, T., & Tikhonov, K. (2021). Oxidative Stress-Induced Alteration of Plant Central Metabolism. *Life 2021, Vol. 11, Page 304*, *11*(4), 304. https://doi.org/10.3390/LIFE11040304

Scalera, V., Giangregorio, N., De Leonardis, S., Console, L., Carulli, E. S., & Tonazzi, A. (2018). Characterization of a novel mitochondrial ascorbate transporter from rat liver and potato mitochondria. *Frontiers in Molecular Biosciences*, *5*(JUN), 370328. https://doi.org/10.3389/FMOLB.2018.00058/BIBTEX

Selma, S. (2025). When the CAT wants to play: The role of interaction between CRCK3 and CAT2 in Arabidopsis salt stress tolerance. *Plant Physiology*, *197*(2), 50. https://doi.org/10.1093/PLPHYS/KIAF050

Sharkey, T. D. (1985). 02-Insensitive Photosynthesis in C3 Plants' ITS OCCURRENCE AND A POSSIBLE EXPLANATION. *Plant Physiol*, *78*, 71–75. https://academic.oup.com/plphys/article/78/1/71/6080221

Sharkey, T. D. (2016). What gas exchange data can tell us about photosynthesis. *Plant, Cell & Environment*, *39*(6), 1161–1163. https://doi.org/10.1111/PCE.12641

Sharma, I., & Ahmad, P. (2014). Catalase: A Versatile Antioxidant in Plants. *Oxidative Damage to Plants: Antioxidant Networks and Signaling*, 131–148. https://doi.org/10.1016/B978-0-12-799963-0.00004-6

Shi, X., Reinstadler, B., Shah, H., To, T. L., Byrne, K., Summer, L., Calvo, S. E., Goldberger, O., Doench, J. G., Mootha, V. K., & Shen, H. (2022). Combinatorial GxGxE CRISPR screen identifies SLC25A39 in mitochondrial glutathione transport linking iron homeostasis to OXPHOS. *Nature Communications*, *13*(1). https://doi.org/10.1038/s41467-022-30126-9

Shibaeva, T. G., & Titov, A. F. (2025). Photoperiod Stress in Plants: A New Look at Plant Response to Abnormal Light-Dark Cycles. *Russian Journal of Plant Physiology*, *72*(4), 1–7. https://doi.org/10.1134/S102144372560165X/FIGURES/4

Smirnoff, N., & Wheeler, G. L. (2024). The ascorbate biosynthesis pathway in plants is known, but there is a way to go with understanding control and functions. In *Journal of Experimental Botany* (Vol. 75, Issue 9, pp. 2604–2630). Oxford University Press. https://doi.org/10.1093/jxb/erad505

Song, H., Zhao, R., Fan, P., Wang, X., Chen, X., & Li, Y. (2009). Overexpression of AtHsp90.2, AtHsp90.5 and AtHsp90.7 in Arabidopsis thaliana enhances plant sensitivity to salt and drought stresses. *Planta*, *229*(4), 955–964. https://doi.org/10.1007/S00425-008-0886-Y/FIGURES/6

Sparkes, I. A., Runions, J., Kearns, A., & Hawes, C. (2006). Rapid, transient expression of fluorescent fusion proteins in tobacco plants and generation of stably transformed plants. *Nature Protocols*, *1*(4), 2019–2025. https://doi.org/10.1038/NPROT.2006.286;KWRD=LIFE+SCIENCES

Su, T., Wang, P., Li, H., Zhao, Y., Lu, Y., Dai, P., Ren, T., Wang, X., Li, X., Shao, Q., Zhao, D., Zhao, Y., & Ma, C. (2018). The Arabidopsis catalase triple mutant reveals important roles of catalases and peroxisome-derived signaling in plant development. *Journal of Integrative Plant Biology*, *60*(7), 591–607. https://doi.org/10.1111/jipb.12649

Sukumaran, S., Lethin, J., Liu, X., Pelc, J., Zeng, P., Hassan, S., & Aronsson, H. (2023). Genome-Wide Analysis of MYB Transcription Factors in the Wheat Genome and Their Roles in Salt Stress Response. *Cells*, *12*(10), 1431. https://doi.org/10.3390/CELLS12101431/S1

Suzuki, N., Koussevitzky, S., Mittler, R., & Miller, G. (2012). ROS and redox signalling in the response of plants to abiotic stress. *Plant, Cell and Environment*, *35*(2), 259–270. https://doi.org/10.1111/J.1365-3040.2011.02336.X;SUBPAGE:STRING:FULL

Tanahashi, R., Nishimura, A., Morita, F., Nakazawa, H., Taniguchi, A., Ichikawa, K., Nakagami, K., Boundy-Mills, K., & Takagi, H. (2023). The arginine transporter Can1 acts as a transceptor for regulation of proline utilization in the yeast Saccharomyces cerevisiae. *Yeast*, *40*(8), 333–348. https://doi.org/10.1002/YEA.3836,

Tian, F., Yang, D. C., Meng, Y. Q., Jin, J., & Gao, G. (2020). PlantRegMap: charting functional regulatory maps in plants. *Nucleic Acids Research*, *48*(D1), D1104–D1113. https://doi.org/10.1093/NAR/GKZ1020

Tong, W., Imai, A., Tabata, R., Shigenobu, S., Yamaguchi, K., Yamada, M., Hasebe, M., Sawa, S., Motose, H., & Takahashi, T. (2016). Polyamine resistance is increased by mutations in a nitrate transporter gene NRT1.3 (AtNPF6.4) in Arabidopsis thaliana. *Frontiers in Plant Science*, *7*(June2016), 195289. https://doi.org/10.3389/FPLS.2016.00834/BIBTEX

van Roermund, C. W. T., Schroers, M. G., Wiese, J., Facchinelli, F., Kurz, S., Wilkinson, S., Charton, L., Wanders, R. J. A., Waterham, H. R., Weber, A. P. M., & Link, N. (2016). The peroxisomal NAD carrier from arabidopsis imports NAD in exchange with AMP. *Plant Physiology*, *171*(3), 2127–2139. https://doi.org/10.1104/pp.16.00540

van Zanten, M., Voesenek, L. A. C. J., Peeters, A. J. M., & Millenaar, F. F. (2009). Hormone- and light-mediated regulation of heat-induced differential petiole growth in Arabidopsis. *Plant Physiology*, *151*(3), 1446–1458. https://doi.org/10.1104/PP.109.144386,

Velez-Ramirez, A. I., Van Ieperen, W., Vreugdenhil, D., & Millenaar, F. F. (2011). Plants under continuous light. *Trends in Plant Science*, *16*(6), 310–318. https://doi.org/10.1016/J.TPLANTS.2011.02.003/ASSET/BE212700-1B23-4264-AC13-0169DECA57B3/MAIN.ASSETS/GR2.JPG

Wan, J., Wang, R., Zhang, P., Sun, L., Ju, Q., Huang, H., Lü, S., Tran, L. S., & Xu, J. (2021). MYB70 modulates seed germination and root system development in Arabidopsis. *IScience*, *24*(11), 103228. https://doi.org/10.1016/J.ISCI.2021.103228

Wang, L., Ma, K. B., Lu, Z. G., Ren, S. X., Jiang, H. R., Cui, J. W., Chen, G., Teng, N. J., Lam, H. M., & Jin, B. (2020). Differential physiological, transcriptomic and metabolomic responses of Arabidopsis leaves under prolonged warming and heat shock. *BMC Plant Biology*, *20*(1). https://doi.org/10.1186/s12870-020-2292-y

Wang, Y., Yen, F. S., Zhu, X. G., Timson, R. C., Weber, R., Xing, C., Liu, Y., Allwein, B., Luo, H., Yeh, H. W., Heissel, S., Unlu, G., Gamazon, E. R., Kharas, M. G., Hite, R., & Birsoy, K. (2021). SLC25A39 is necessary for mitochondrial glutathione import in mammalian cells. *Nature*, *599*(7883), 136–140. https://doi.org/10.1038/s41586-021-04025-w

Winter, D., Vinegar, B., Nahal, H., Ammar, R., Wilson, G. V., & Provart, N. J. (2007a). An "Electronic Fluorescent Pictograph" Browser for Exploring and Analyzing Large-Scale Biological Data Sets. *PLOS ONE*, *2*(8), e718. https://doi.org/10.1371/JOURNAL.PONE.0000718

Winter, D., Vinegar, B., Nahal, H., Ammar, R., Wilson, G. V., & Provart, N. J. (2007b). An "electronic fluorescent pictograph" Browser for exploring and analyzing large-scale biological data sets. *PLoS ONE*, *2*(8). https://doi.org/10.1371/journal.pone.0000718

Winter, G., Todd, C. D., Trovato, M., Forlani, G., & Funck, D. (2015). Physiological implications of arginine metabolism in plants. *Frontiers in Plant Science*, *6*(JULY). https://doi.org/10.3389/fpls.2015.00534

Wu, C., Feng, J., Wang, R., Liu, H., Yang, H., Rodriguez, P. L., Qin, H., Liu, X., & Wang, D. (2012). HRS1 acts as a negative regulator of abscisic acid signaling to promote timely germination of Arabidopsis seeds. *PloS One*, *7*(4). https://doi.org/10.1371/JOURNAL.PONE.0035764

Wunderlich, M., Groß-Hardt, R., & Schöffl, F. (2014). Heat shock factor HSFB2a involved in gametophyte development of Arabidopsis thaliana and its expression is controlled by a heat-inducible long non-coding antisense RNA. *Plant Molecular Biology*, *85*(6), 541–550. https://doi.org/10.1007/S11103-014-0202-0

Xie, D. L., Huang, H. M., Zhou, C. Y., Liu, C. X., Kanwar, M. K., Qi, Z. Y., & Zhou, J. (2022). HsfA1a confers pollen thermotolerance through upregulating antioxidant capacity, protein repair, and degradation in Solanum lycopersicum L. *Horticulture Research*, *9*, uhac163. https://doi.org/10.1093/HR/UHAC163

Xie, Z., Nolan, T. M., Jiang, H., & Yin, Y. (2019). AP2/ERF transcription factor regulatory networks in hormone and abiotic stress responses in Arabidopsis. *Frontiers in Plant Science*, *10*, 437723. https://doi.org/10.3389/FPLS.2019.00228/XML/NLM

Xu, Y., Freund, D. M., Hegeman, A. D., & Cohen, J. D. (2022). Metabolic signatures of Arabidopsis thaliana abiotic stress responses elucidate patterns in stress priming, acclimation, and recovery. *Stress Biology*, *2*(1). https://doi.org/10.1007/s44154-022-00034-5

Yamada, K., Fukao, Y., Hayashi, M., Fukazawa, M., Suzuki, I., & Nishimura, M. (2007). Cytosolic HSP90 Regulates the Heat Shock Response That Is Responsible for Heat Acclimation in Arabidopsis thaliana. *Journal of Biological Chemistry*, *282*(52), 37794–37804. https://doi.org/10.1074/JBC.M707168200

Yang, Z., Mhamdi, A., & Noctor, G. (2019). Analysis of catalase mutants underscores the essential role of CATALASE2 for plant growth and day length-dependent oxidative signalling. *Plant Cell and Environment*, *42*(2), 688–700. https://doi.org/10.1111/pce.13453

Yeh, H. L., Lin, T. H., Chen, C. C., Cheng, T. X., Chang, H. Y., & Lee, T. M. (2019). Monodehydroascorbate Reductase Plays a Role in the Tolerance of Chlamydomonas reinhardtii to Photooxidative Stress. *Plant and Cell Physiology*, *60*(10), 2167–2179. https://doi.org/10.1093/PCP/PCZ110

Yilmaz, A., Mejia-Guerra, M. K., Kurz, K., Liang, X., Welch, L., & Grotewold, E. (2011). AGRIS: the Arabidopsis Gene Regulatory Information Server, an update. *Nucleic Acids Research*, *39*(Database issue). https://doi.org/10.1093/NAR/GKQ1120

Yoshida, T., Ohama, N., Nakajima, J., Kidokoro, S., Mizoi, J., Nakashima, K., Maruyama, K., Kim, J. M., Seki, M., Todaka, D., Osakabe, Y., Sakuma, Y., SchöZ, F., Shinozaki, K., & Yamaguchi-Shinozaki, K. (2011a). Arabidopsis HsfA1 transcription factors function as the main positive regulators in heat shock-responsive gene expression. *Molecular Genetics and Genomics*, *286*(5–6), 321–332. https://doi.org/10.1007/S00438-011-0647-7

Yoshida, T., Ohama, N., Nakajima, J., Kidokoro, S., Mizoi, J., Nakashima, K., Maruyama, K., Kim, J. M., Seki, M., Todaka, D., Osakabe, Y., Sakuma, Y., SchöZ, F., Shinozaki, K., & Yamaguchi-Shinozaki, K. (2011b). Arabidopsis HsfA1 transcription factors function as the main positive regulators in heat shock-responsive gene expression. *Molecular Genetics and Genomics*, *286*(5–6), 321–332. https://doi.org/10.1007/S00438-011-0647-7/FIGURES/7

Yu, Y., Ni, Z., Chen, Q., & Qu, Y. (2017). The wheat salinity-induced R2R3-MYB transcription factor TaSIM confers salt stress tolerance in Arabidopsis thaliana. *Biochemical and Biophysical Research Communications*, *491*(3), 642–648. https://doi.org/10.1016/J.BBRC.2017.07.150

Yu, Y., Qi, Y., Xu, J., Dai, X., Chen, J., Dong, C. H., & Xiang, F. (2021). Arabidopsis WRKY71 regulates ethylene-mediated leaf senescence by directly activating EIN2, ORE1 and ACS2 genes. *The Plant Journal : For Cell and Molecular Biology*, *107*(6), 1819–1836. https://doi.org/10.1111/TPJ.15433

Yu, Y., Wang, L., Chen, J., Liu, Z., Park, C. M., & Xiang, F. (2018). WRKY71 Acts Antagonistically Against Salt-Delayed Flowering in Arabidopsis thaliana. *Plant and Cell Physiology*, *59*(2), 414–422. https://doi.org/10.1093/PCP/PCX201

Zander, M., La Camera, S., Lamotte, O., Métraux, J. P., & Gatz, C. (2010). Arabidopsis thaliana class-II TGA transcription factors are essential activators of jasmonic acid/ethylene-induced defense responses. *The Plant Journal*, *61*(2), 200–210. https://doi.org/10.1111/J.1365-313X.2009.04044.X

Zhang, H., Zhang, F., Yu, Y., Feng, L., Jia, J., Liu, B., Li, B., Guo, H., & Zhai, J. (2020). A Comprehensive Online Database for Exploring ~20,000 Public Arabidopsis RNA-Seq Libraries. In *Molecular Plant* (Vol. 13, Issue 9, pp. 1231–1233). Cell Press. https://doi.org/10.1016/j.molp.2020.08.001

Zhang, X., Henriques, R., Lin, S. S., Niu, Q. W., & Chua, N. H. (2006). Agrobacterium-mediated transformation of Arabidopsis thaliana using the floral dip method. *Nature Protocols 2006 1:2*, *1*(2), 641–646. https://doi.org/10.1038/nprot.2006.97

Zhou, G., Liu, C., Cheng, Y., Ruan, M., Ye, Q., Wang, R., Yao, Z., & Wan, H. (2022). Molecular Evolution and Functional Divergence of Stress-Responsive Cu/Zn Superoxide Dismutases in Plants. *International Journal of Molecular Sciences*, *23*(13), 7082. https://doi.org/10.3390/IJMS23137082/S1

Zhou, H., Shi, H., Yang, Y., Feng, X., Chen, X., Xiao, F., Lin, H., & Guo, Y. (2024). Insights into plant salt stress signaling and tolerance. *Journal of Genetics and Genomics*, *51*(1), 16–34. https://doi.org/10.1016/J.JGG.2023.08.007

Zhuang, Y., Zhang, Y., Shi, H., Pang, Y., Feng, X., Fan, W., Chang, D., Lin, H., & Zhou, H. (2025). CALMODULIN-BINDING RECEPTOR-LIKE CYTOPLASMIC KINASE 3 regulates salt tolerance through CATALASE 2 in Arabidopsis. *Plant Physiology*, *197*(1). https://doi.org/10.1093/plphys/kiae669

6. Appendix

6.1. List of Abbreviations

35S	CaMV 35S promoter
A	Adenine
A. thaliana	Arabidopsis thaliana
A. tumefaciens	Agrobacterium tumefaciens
Amp	Ampicillin
ATP	adenosine triphosphate
BASTA	Glufosinate Ammonium
BCAA	Branched-chain amino acids
bp	Base pairs
C	Cytosine
Cas9	CRISPR-associated protein 9
cat2	Catalase 2
CcdB	Control of Cell Death B (toxic gene for negative selection
cDNA	Complementary DNA
CDS	Coding sequence
CFU	Colony-Forming Unit
CL	pertl6-1 complementation line
Cm^R	Chloramphenicol resistance
CO_2	Carbon dioxide
Col-0	Columbia
CRISPR	Clustered Regularly Interspaced Short Palindromic Repeats
DAS	Days After Sowing
DNase	Deoxyribonuclease
dNTPs	deoxynucleotide triphosphates
dsDNA	double-stranded DNA
E. coli	Escherichia coli
EC1	Egg cell-specific promoter 1
EDTA	Ethylenediamintetraacetic acid
G	Guanine
GC-MS	Gas Chromatography-Mass Spectrometry
gDNA	Genomic DNA
Gent	Gentamycin
GFP	Green fluorescent protein
GOI	Gene of Interest
Gr1	Glutathione reductase 1
gRNA	Guide RNA
GSNO	S-nitrosoglutathione
H2O2	Hydrogen peroxide
HS	Heat shock
Hyg	Hygromycin
Kan	Kanamycin
kb	kilobases
LB	Lysogeny Broth (Luria Bertani) medium
LB/RB	Left/Right border (T-DNA)
LC-MS	Liquid Chromatography-Mass Spectrometry
LD	Long day (16 h light / 8 h dark)
Methyl viologen	N,N'-dimethyl-4,4'-bipyridinium dichloride
MNE	Mean normalized expression

MS	Murashige & Skoog medium
NaCl	Sodium chloride
NADP	nicotinamide adenine dinucleotide phosphate
ND	Normal day (12 h light / 12 h dark)
NLS	Nuclear localization signal
NO•	nitric oxide
NOS	Nopaline synthase promoter
nos term	Nopaline synthase terminator
nt	nucleotides
OD_{600}	Optical Density at 600 nm
OEX	pertl6 overexpressor line
$ONOO^-$	peroxynitrite
OPPP	oxidative pentose phosphate pathway
p35S	promoter 35 S
PAM	protospacer adjacent motif
Paraquat	N,N'-dimethyl-4,4'-bipyridinium dichloride
PCR	Polymerase chain reaction
pertl6	Peroxisomal transport-like protein 6
PF	Primer Forward
ppm	Parts per million
PR	Primer Reverse
pre-tRNA	Precursor transfer RNA
PTG	polycistronic tRNA-gRNA
PTS1	Peroxisomal Targeting Signal 1
pU6-26	U6-26 promoter
pUBQ10	Ubiquitin 10 promoter
qPCR	Quantitative Polymerase Chain Reaction
rbcS E9T	Ribulose-1,5-bisphosphate carboxylase small subunit E9 terminator
rbcS intron	Ribulose-1,5-bisphosphate carboxylase small subunit intron
RE	Restriction enzyme
Rif	Rifampicin
RNase	Ribonuclease
RNase	Ribonuclease
ROI	Region of Interest
ROS	Reactive Oxygen Species
rpm	revolutions per minute
RRS	restriction recognition sites
RT	Room temperature
SAR	Systemic Acquired Resistance
SD	Short day (8 h light / 16 h dark)
Spec	Spectinomycin
T	Thymine
Taq	*Thermus aquaticus* (DNA polymerase)
TCA	Trichloroacetic acid
T-DNA	Transfer DNA
term	Terminator
TF	Transcription factor
TSS	Transcription Start Site
UV	ultraviolet
WT	Wild type

6.2. List of Figures

6.3. List of Tables

6.4. Primer sequences

Table 6.1 Primers

PRIMER NAME	SEQUENCE	APPLICATION
DG40	GAATATCGGCGAGGCTGTGA	qPCR
DG41	CACGAGAAAACTCCGGTGGA	qPCR
DG48	GGTCCTGCTGTCCGAGTTTA	qPCR
DG49	AGGTGGCCAAATTAGCTAAAGAGA	qPCR
KK03	TAGGTCTCCAACTGTCTGGGTGTTTTAGAGCTAGAA	Golden Gate MoClo
KK04	ATGGTCTCAAGTTCGGAGCATTGCACCAGCCGGGAA	Golden Gate MoClo
KK09	TAGGTCTCCCGACGAAGAGCTGTTTTAGAGCTAGAA	Golden Gate MoClo
KK10	ATGGTCTCAGTCGCCATTTCCTGCACCAGCCGGGAA	Golden Gate MoClo
KK11	TAGGTCTCCTCCCAGCTTAGCGTTTTAGAGCTAGAA	Golden Gate MoClo
KK12	ATGGTCTCAGGGATGAGACTCTGCACCAGCCGGGAA	Golden Gate MoClo
KK13	TAGGTCTCCTGGAAAGAGCAAGTTTTAGAGCTAGAA	Golden Gate MoClo
KK14	ATGGTCTCATCCATATTGAGCTGCACCAGCCGGGAA	Golden Gate MoClo
KK15	GCCAATTGATTGACAACCGCT	PCR & Sequencing
KK16	AGCAAATGGAACCATCCGATAGA	PCR & Sequencing
KK31	GGATTAGCTGGTGGACTAAGTG	qPCR
KK32	TACAAGGGATGGTTGGATGC	qPCR
KK33	AGAGCGTCGAAATCAAAGCC	PCR & Sequencing
KK35	GGAACTCAACGGCCATGAAG	PCR & Sequencing
KK38	TGAGTTTTTCTGATTAACACATGGCGACGAAGAGCTCG	Gibson Assembly, subcellular localization
KK39	GCGTAGATCTCCGCGGACGTTAGACCTTCATGCACTGAAGTAGAAG	Gibson Assembly, subcellular localization
NL0509	TCCTGAGGAGACATACATGGG	Genotyping plants
NL0510	CGCATTTTATAGCAGGAGCAG	Genotyping plants
NL1062	CCTCGTGGTTTTGCAGTCAA	Genotyping plants
NL1063	TCTCAGCATGACGAACCTGG	Genotyping plants
NL1064	TATCGATCGGGTTTGTTTTTG	Genotyping plants
NL1065	GTTGCGGAAAAATATCAATGC	Genotyping plants

P001	GTAAAACGACGGCCAG	PCR & Sequencing
P002	CAGGAAACAGCTATGAC	PCR & Sequencing
P042	GCACCATCGTCAACCACTAC	PCR & Sequencing
P043	GAAGTCCAGCTGCCAGAAAC	PCR & Sequencing
P067	TTCAATGTCCCTGCCATGTA	PCR & Sequencing
P068	TGAACAATCGATGGACCTGA	PCR & Sequencing
P094	TGAGCACGCTCTTCTTGCTTTCA	qPCR
P095	GGTGGTGGCATCCATCTTGTTACA	qPCR
P097	ATTTTGCCGATTTCGGAAC	Genotyping plants
P098	CGATTTTCTGGGTTTGATCG	PCR & Sequencing
P142	GGCATGCACATACAAATGGA	PCR & Sequencing
P149	CTTGGTCACCTTCAGCTTGG	PCR & Sequencing
P150	ACTGATGGGCTGCCTGTATC	PCR & Sequencing
P151	TCATAAGATGCCATGCCAGA	PCR & Sequencing
P155	CGGGTCTCAGGCAGAAGACTAATTGAACAAAG CACCAGTGG	Golden Gate MoClo
P156	TAGGTCTCCAAACGAAGACAAAAACAAAAAAA AAAGCACCGACTCG	Golden Gate MoClo
P157	CGGGTCTCAGGCAGAAGACTAATTG	Golden Gate MoClo
P158	TAGGTCTCCAAACGAAGACAAAAAC	Golden Gate MoClo
P166	TTATCATTCCTCACCAGCATC	PCR & Sequencing
P167	CGCTCACATGATCAAGTTCC	PCR & Sequencing
P168	GTAGACAGTGAAGTACTCGTAC	PCR & Sequencing
P178	AAGTCGTGCTGCTTCATGTG	Genotyping plants

6.5. Vectors and vector maps

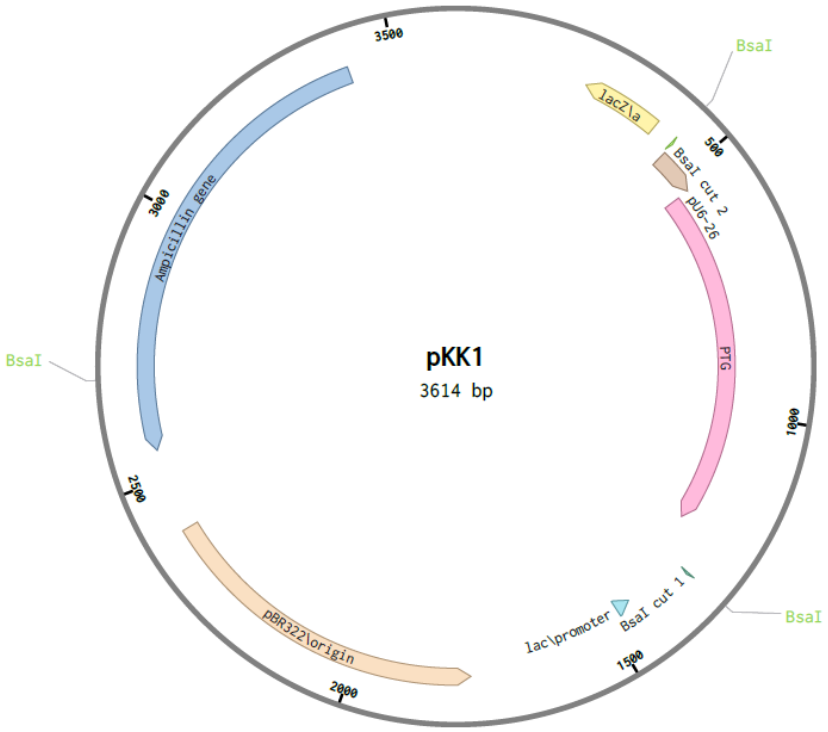

Figure 6.1 pKK1 CRISPR vector: VEC 219 (pU6-26::tRNA-gRNA(PTG) with flanking RRS for BsaI)

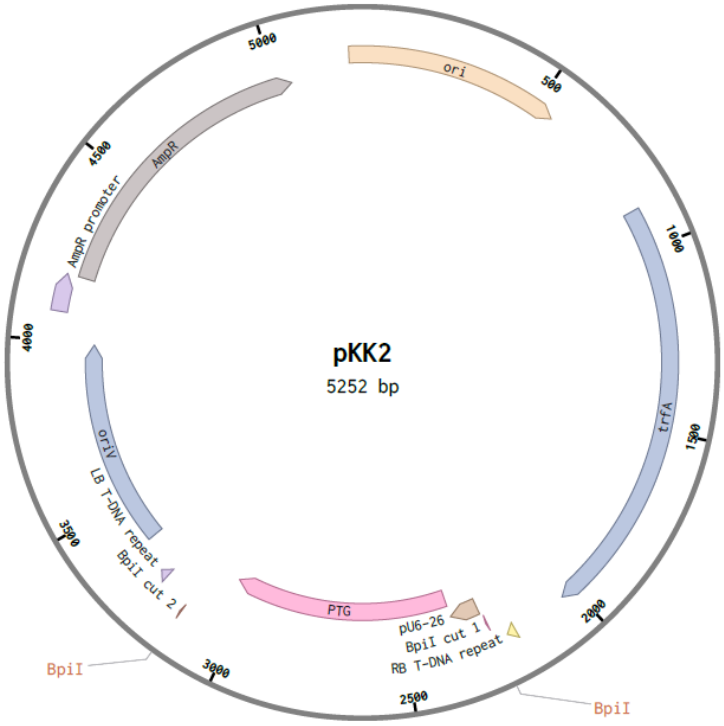

Figure 6.2 pKK2 CRISPR vector: VEC 249 (pU6-26::tRNA-gRNA(PTG) with flanking RRS for BpaI)

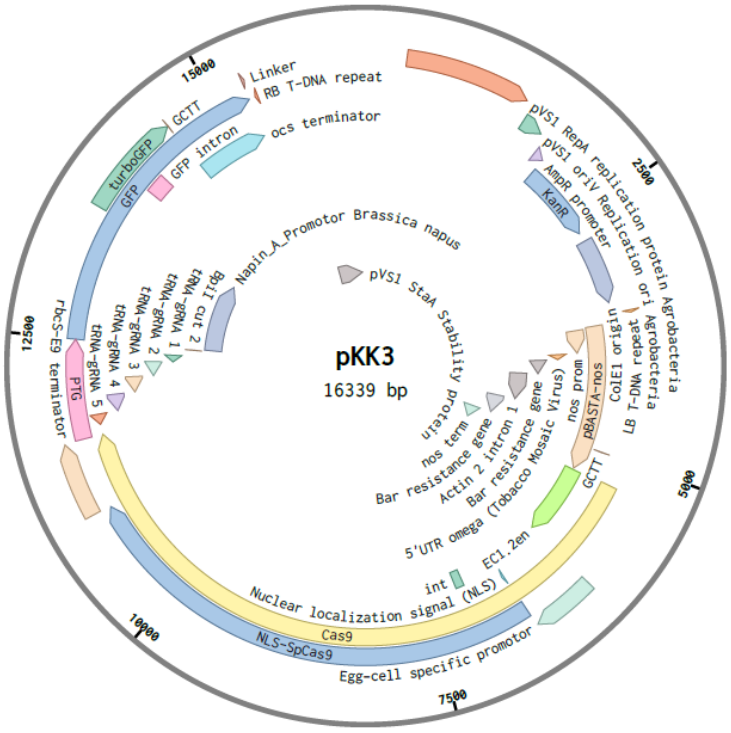

Figure 6.3 pKK3 CRISPR binary vector: VEC 262 (NOS::barR::nos term, EC1::NLS::Cas9::rbcS E9 term, pU6-26::tRNA-gRNA(PTG), NapinA::Turbo GFP::osc term)

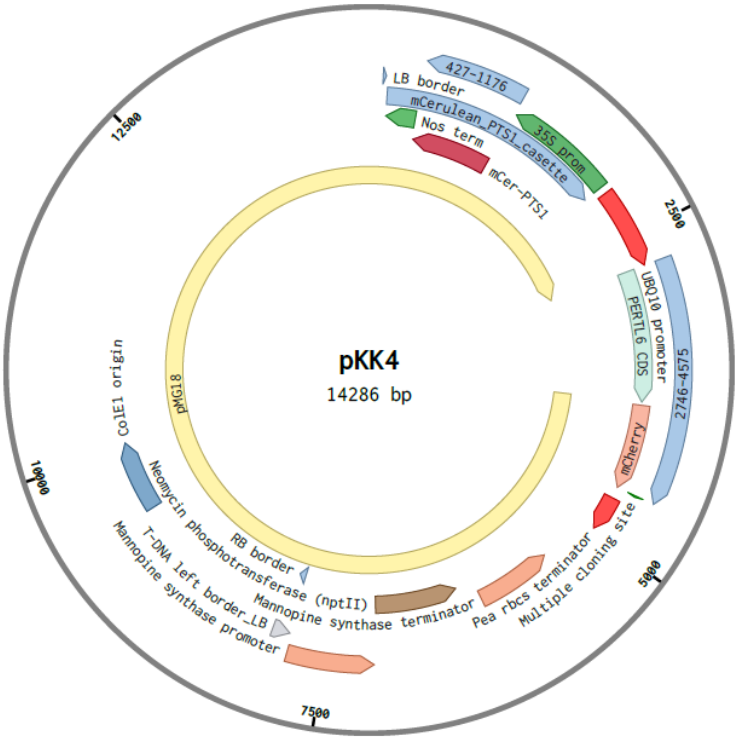

Figure 6.4 pKK4 binary vector pUBQ10::PERTL6-mCherry and 35S::mCerulean-PTS1

Table 6.2 Other vectors

VECTOR NAME	FEATURE	SELECTION MARKER	BACTERIA RESISTANCE	APPLICATION
pGEM-T Easy (Promega)	SP6/T7 promoter::lacZα:: MCS::T-overhangs	none	AmpR	Genotyping plants
pHHU 431	pUBQ10::PERTL6-YFP	Hyg^R	KanR	Subcellular localization studies; CL/OEX lines
pMG02	pUBQ10::C-mCherry	KanR	SpecR	Subcellular localization studies
pMG18	pUBQ10::C-mCherry, 35S::mCerulean-PTS1	KanR	SpecR	Subcellular localization studies
pMG43	35S::mCerulean-PTS1	KanR	SpecR	Subcellular localization studies
VEC 219	Golden Gate Level 0, attR1-CmR-ccdB-attR2	none	AmpR	CRISPR/Cas9 line
VEC 249	Golden Gate level 1, p3, acceptor vector, lacZ	none	AmpR	CRISPR/Cas9 line
VEC 262	Golden Gate Level 2, acceptor vector, CRed	none	KanR	CRISPR/Cas9 line
VEC 269	End-link 4 for assembling 4 Level 1 parts into a Level 2 acceptor (VEC 262)	none	SpecR	CRISPR/Cas9 line
VEC 423	Golden Gate Level -1, pre-tRNA-gRNA fusion fragment	none	AmpR	CRISPR/Cas9 line
VEC 424	Golden Gate Level 1, p4 NapinA , turboGFP with intron	none	AmpR	CRISPR/Cas9 line
VEC 425	Golden Gate Level 1, p2, EC1, SpCas9 with intron	none	AmpR	CRISPR/Cas9 line
VEC 426	Golden Gate Level 1, p1, NOS, barR	none	AmpR	CRISPR/Cas9 line

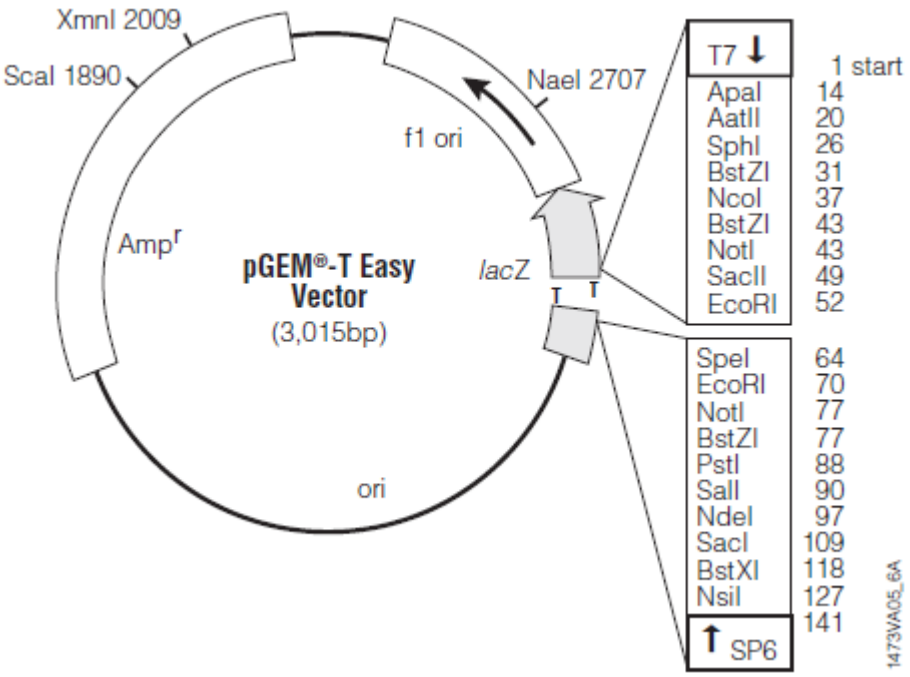

Figure 6.5 pGEM-T Easy Vector for TA cloning and plants genotyping

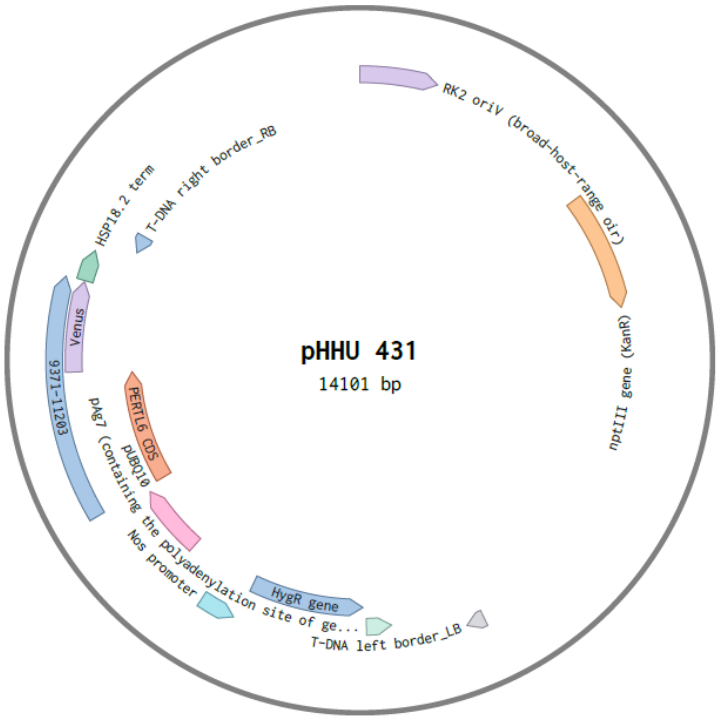

Figure 6.6 pHHU431 binary vector with pUBQ10::PERTL6

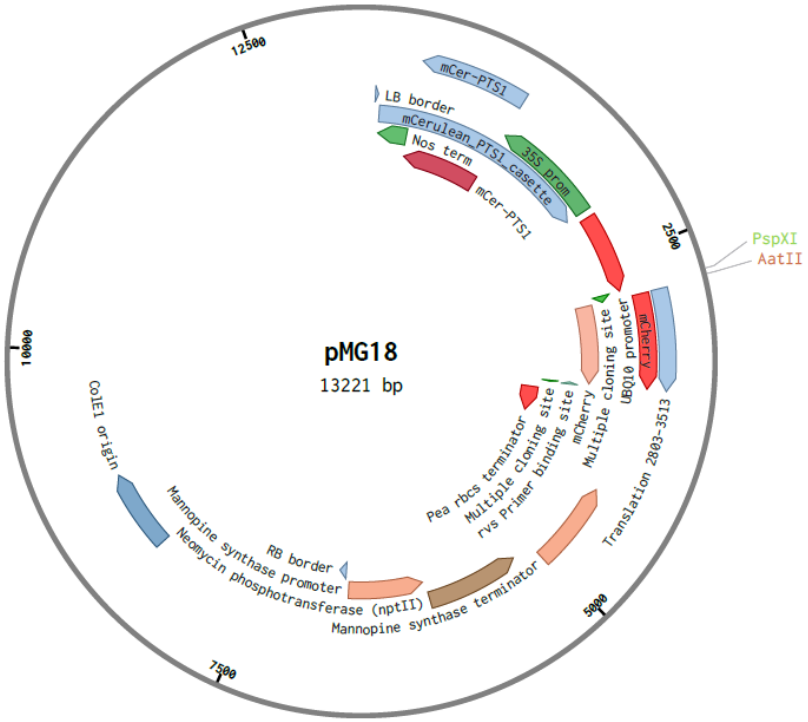

Figure 6.7 pMG18 binary vector with pUBQ10::C-mCherry and 35S::mCerulean-PTS1

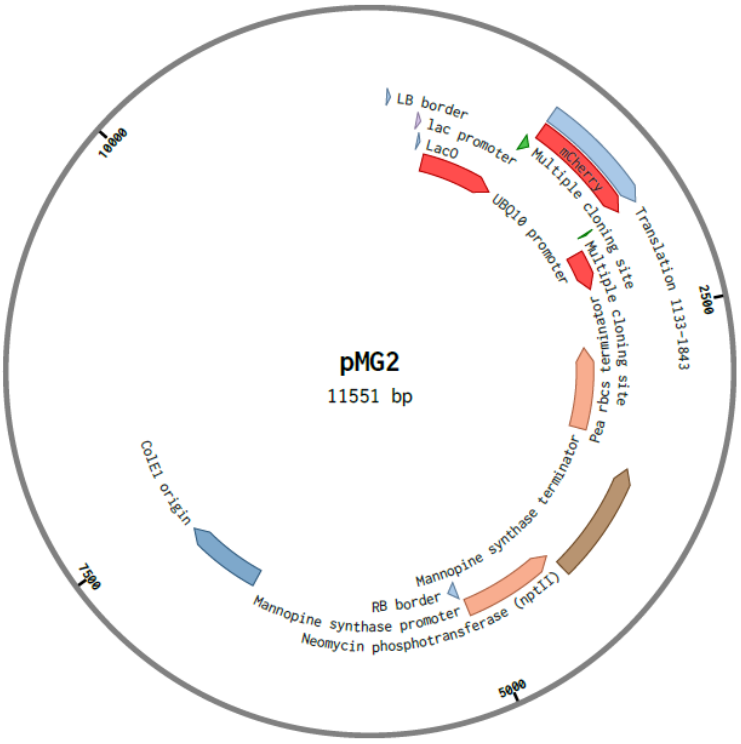

Figure 6.8 pMG2 binary vector with UBQ10::C-mCherry

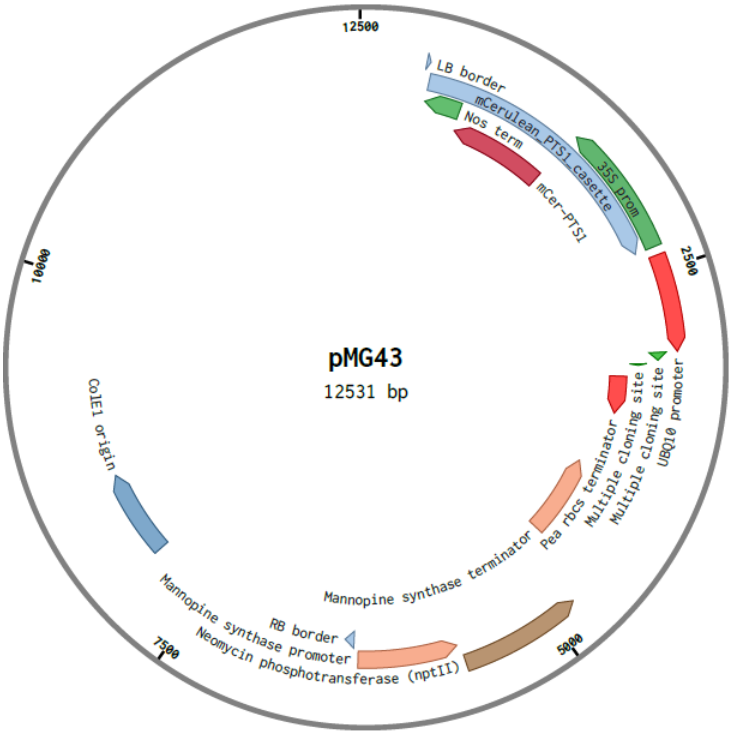

Figure 6.9 pMG43 binary vector with 35S::mCerulean-PTS1

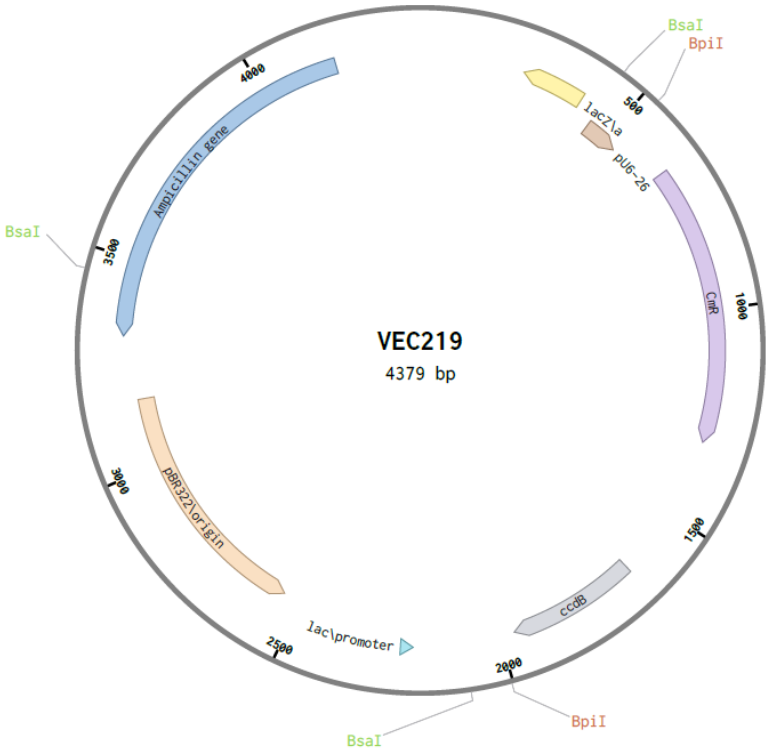

Figure 6.10 VEC219 level 0 vector for Golden Gate Modular Cloning

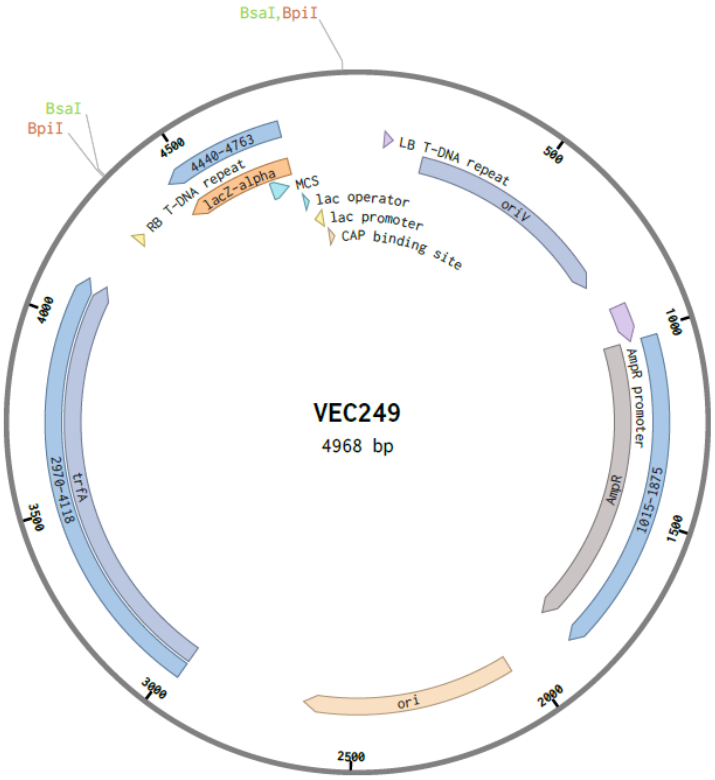

Figure 6.11 VEC249 level 1 vector for Golden Gate Modular Cloning

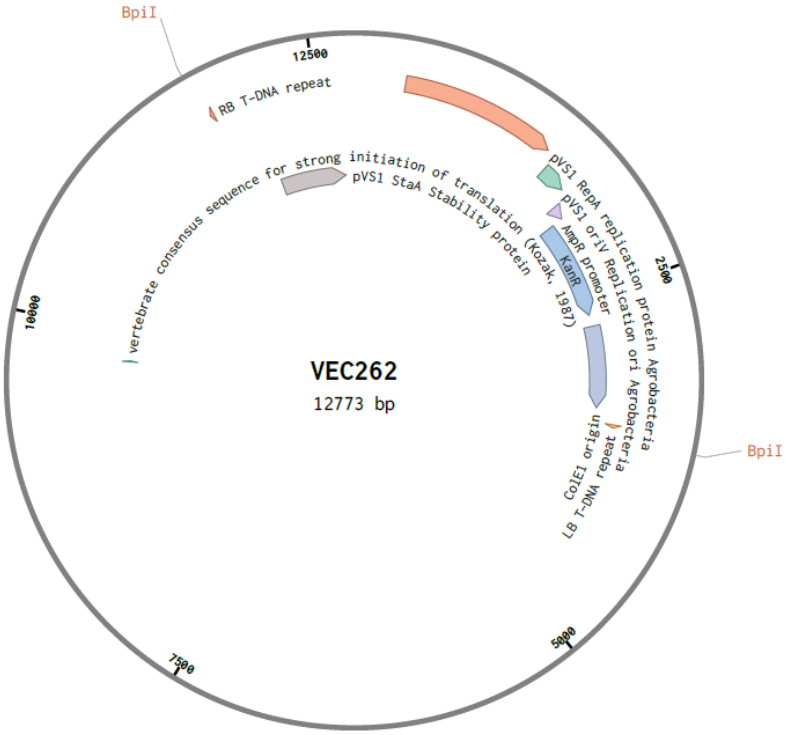

Figure 6.12 VEC262 level 2 vector for Golden Gate Modular Cloning

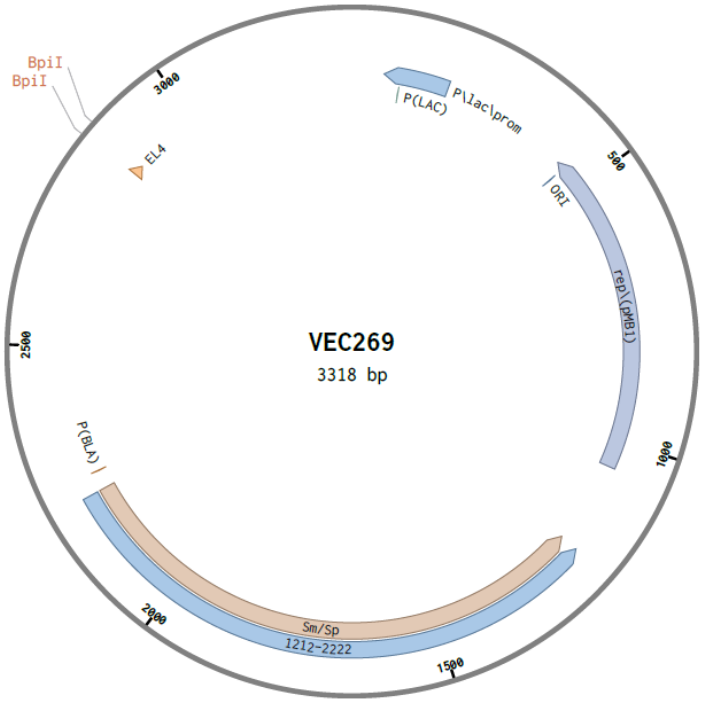

Figure 6.13 VEC269 End link 4 vector for Golden Gate Modular Cloning

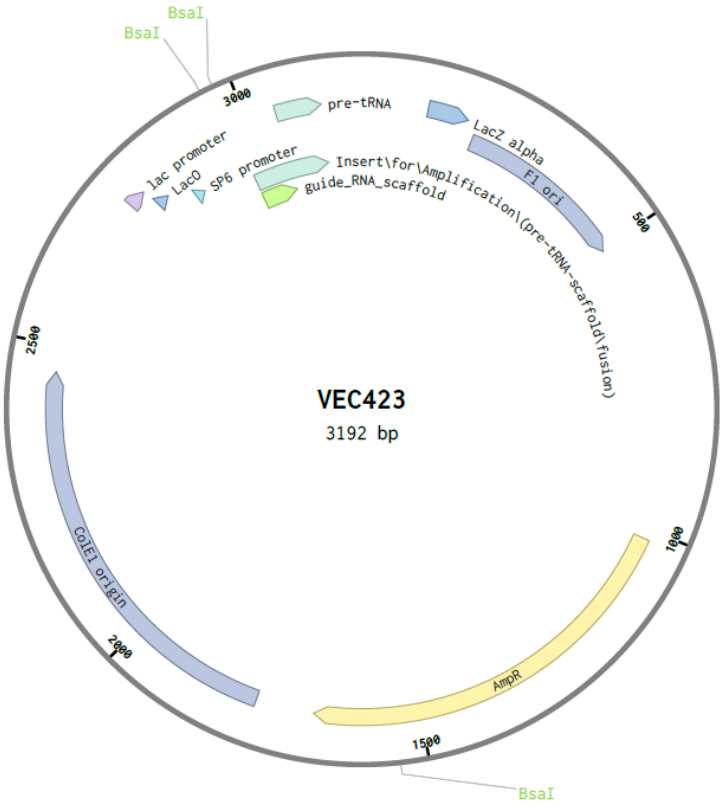

Figure 6.14 VEC423 level -1 vector for Golden Gate Modular Cloning

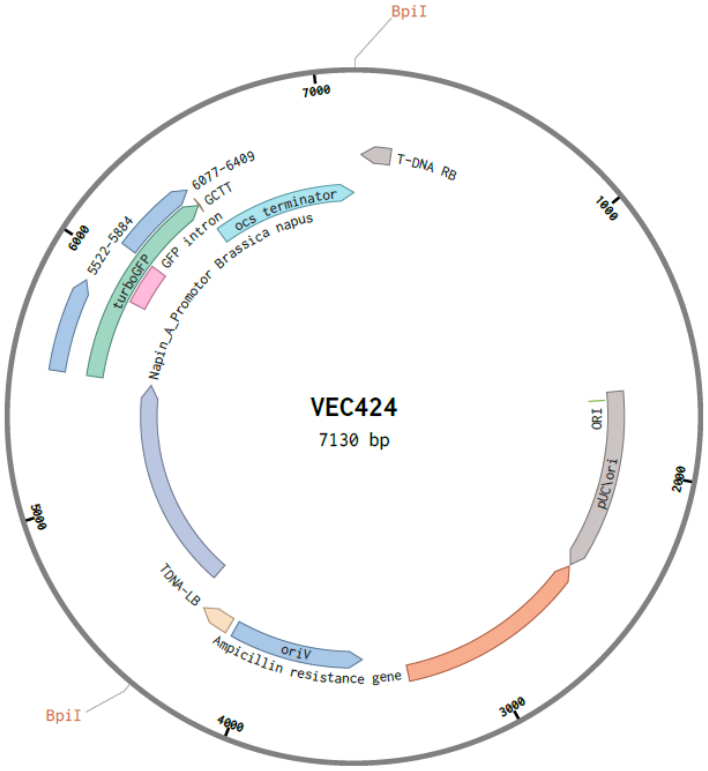

Figure 6.15 VEC424 level 1 vector for Golden Gate Modular Cloning

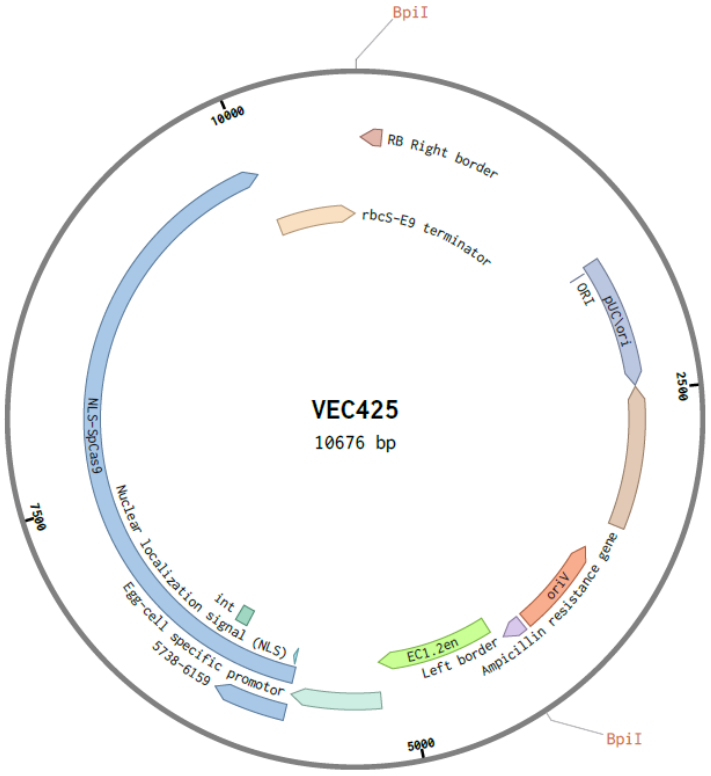

Figure 6.16 VEC425 level 1 vector for Golden Gate Modular Cloning

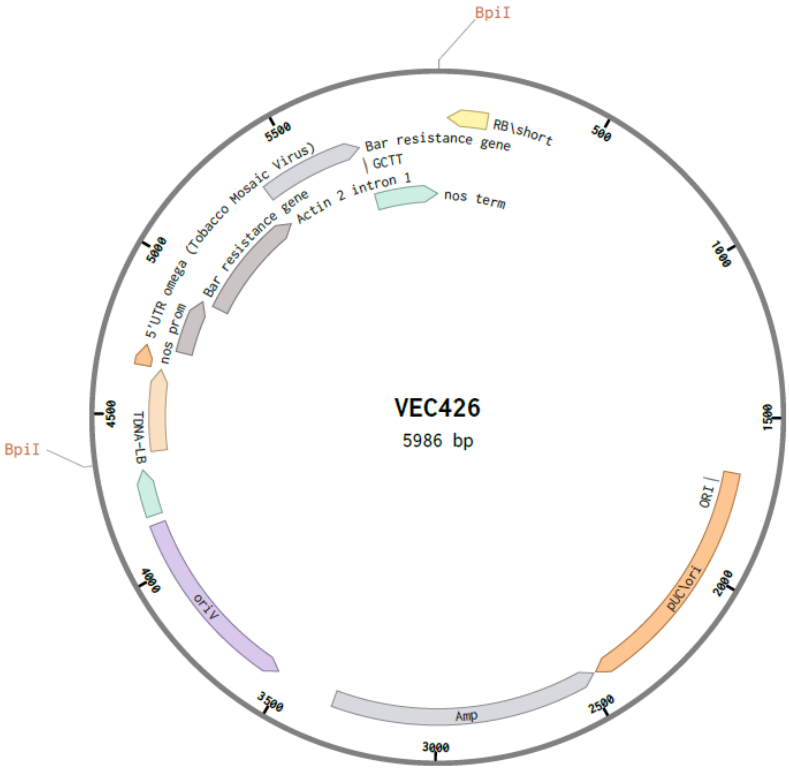

Figure 6.17 VEC426 level 1 vector for Golden Gate Modular Cloning

6.6. Supplemental figures

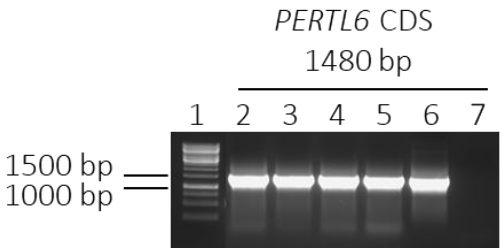

Figure 6.18 Colony PCR of A. tumefaciens transformed with pKK4 vector for subcellular localization studies

PCR was performed with homemade Taq DNA polymerase and P098/P149 primers flanking PERLT6 CDS and separated on 1% agarose gel. Well 1 – 1 kb DNA ladder, wells 2-4 – four colonies with pKK4, well 6 – positive control with CDS of PERTL6 from pHHU 431 vector, well 7 – negative control without DNA. Expected size 1480 bp.

Figures were created with BioRender